

# Liquid Crystalline Behaviour of Semi-Flexible Polymer-Coated Nanoparticles



Jessie Wong, Department of Chemistry

McGill University, Montreal

A thesis submitted to McGill University in partial fulfilment of the requirements of  
the degree of Doctor of Philosophy

© Jessie Wong, 2024

# Table of Contents

Statement of Objectives .....	vi
Abstract .....	vii
Abrégé .....	ix
Acknowledgements .....	xi
Contribution of Authors .....	xiv
Contribution to Original Knowledge .....	xvi
Lists of Figures.....	xviii
Lists of Tables.....	xxiv

## Chapter 1: Introduction

<b>1.1 Polymer Nanocomposites.....</b>	<b>1</b>
1.1.1 Background .....	1
1.1.2 Polymer Matrix Composites (PMCs) .....	2
1.1.3 Surface Modification of Particulates/Nanoparticles .....	4
<b>1.2 Liquid Crystals.....</b>	<b>7</b>
1.2.1 Liquid Crystal Terminology and Classifications.....	7
1.2.2 Optical Microscopy of Liquid Crystals.....	10
1.2.3 X-Ray Scattering of Liquid Crystals.....	13
1.2.4 NMR of Liquid Crystals.....	18
<b>1.3 Liquid Crystal-Based Composites .....</b>	<b>20</b>
1.3.1 Nanoparticle Dispersed Liquid Crystals .....	20
1.3.2 Polymer-Dispersed Liquid Crystals and Other Polymer-LC Composites .....	24
1.3.3 Liquid Crystal Polymer Coated Nanoparticles .....	27
<b>1.4 Lyotropic Nanocomposites .....</b>	<b>29</b>
<b>1.5 Semi-Flexible Polymers and Liquid Crystal Formation .....</b>	<b>32</b>

<b>1.6 Conclusions and Future Outlook .....</b>	<b>35</b>
<b>1.7 References .....</b>	<b>38</b>

## **Chapter 2: Lyotropic Nematic Phases of Isotropic Phases of Isotropic Nanoparticles via Semiflexible Polymer Ligands**

<b>2.1 Abstract.....</b>	<b>55</b>
<b>2.2 Introduction .....</b>	<b>56</b>
<b>2.3 Results.....</b>	<b>58</b>
2.3.1 Preparation of ZrO <sub>2</sub> -PHIC Nanoparticles.....	58
2.3.2 Optical Microscopy .....	63
2.3.3 Transmission Electron Microscopy .....	64
2.3.4 Deuterium NMR Spectroscopy .....	66
<b>2.4 Discussion.....</b>	<b>69</b>
<b>2.5 Experimental Methods .....</b>	<b>73</b>
2.5.1 Materials .....	73
2.5.2 Synthesis of Initiator-Functionalized 23K MW Poly-(Hexyl Isocyanate) (PHIC <sub>180</sub> ) .....	73
2.5.3 ZrO <sub>2</sub> Nanoparticle Synthesis .....	74
2.5.4 PHIC Functionalization of ZrO <sub>2</sub> Nanoparticles .....	74
2.5.5 Polarized Optical Microscopy .....	74
2.5.6 Molecular Weight Determination by GPC and <sup>1</sup> H NMR .....	75
2.5.7 <sup>2</sup> H NMR Spectroscopy .....	75
2.5.8 Transmission Electron Microscopy (TEM) .....	75
2.5.9 Thermogravimetric Analysis (TGA) .....	76
2.6.10 Acknowledgements .....	76
<b>2.6 References.....</b>	<b>77</b>
<b>2.7 Supporting Information .....</b>	<b>80</b>

## **Chapter 3: Cholesteric Behaviour of Poly( $\gamma$ -Benzyl-L-Glutamate) Functionalized Nanoparticles**

<b>3.1 Abstract</b> .....	<b>96</b>
<b>3.2 Introduction</b> .....	<b>96</b>
<b>3.3 Experimental</b> .....	<b>98</b>
3.3.1 Materials .....	98
3.3.2 Measurements .....	98
3.3.3 Synthesis of [DPPA][TBA] .....	98
3.3.4 Synthesis of PBLG-PO(OEt) <sub>2</sub> .....	99
3.3.5 Synthesis of PBLG-PO(OH) <sub>2</sub> .....	99
3.3.6 Functionalization of PBLG onto Bz@ZrO <sub>2</sub> - PBLG@ZrO <sub>2</sub> .....	99
3.3.7 Liquid Crystal Sample Preparation.....	100
3.3.8 SAXS Sample Preparation .....	100
<b>3.4 Results</b> .....	<b>101</b>
3.4.1 Synthesis and Characterization of PBLG Ligands .....	101
3.4.2 Functionalization of Zirconia Nanoparticles .....	103
3.4.3 LC Behaviour .....	104
3.4.4 SAXS Experiments .....	108
<b>3.5 Discussion</b> .....	<b>111</b>
<b>3.6 Conclusion</b> .....	<b>116</b>
<b>3.7 References</b> .....	<b>118</b>
<b>3.8 Supplementary Information</b> .....	<b>128</b>

## **Chapter 4: Thermotropic and Lyotropic Phase Behaviour of Cholesteric Poly( $\gamma$ -Stearyl-L-Glutamate) Functionalized Nanoparticles**

<b>4.1 Abstract</b> .....	<b>138</b>
<b>4.2 Introduction</b> .....	<b>138</b>
<b>4.3 Experimental</b> .....	<b>141</b>

4.3.1 Materials .....	141
4.3.2 Synthesis of tetrabutylammonium-diethylphosphonopropanoic acid (TBA-DPPA) (1).....	141
4.3.3 Synthesis of Stearyl glutamate N-carboxyanhydride (SLG-NCA) (2).. .....	142
4.3.4 Synthesis of PSLG-PO(OEt) <sub>2</sub> from SLG-NCA (3) .....	143
4.3.5 Preparation of Benzyl Alcohol Functionalized ZrO <sub>2</sub> Nanoparticles, Bz@ZrO <sub>2</sub> (4) .....	143
4.3.6 Deprotection of PSLG and Functionalization of ZrO <sub>2</sub> Nanoparticles, PSLG@ZrO <sub>2</sub> (5).....	143
4.3.7 LC and NP/LC Sample Preparation.....	144
4.3.8 Measurements.....	144
<b>4.4 Results.....</b>	<b>145</b>
4.4.1 Synthesis of PSLG Ligands .....	145
4.4.2 Characterization .....	145
4.4.2.1 Nanoparticle Characterization .....	145
4.4.2.2 Lyotropic LC Characterization .....	147
4.4.2.3 Thermotropic LC Characterization .....	151
<b>4.5 Discussion.....</b>	<b>155</b>
4.5.1 Synthesis of the PSLG Ligands.....	155
4.5.2 Characterization of PSLG and PSLG@ZrO <sub>2</sub> .....	156
4.5.3 Lyotropic Behaviour .....	156
4.5.4 Thermotropic Behaviour .....	159
<b>4.6 Conclusion .....</b>	<b>161</b>
<b>4.7 References.....</b>	<b>163</b>
<b>4.8 Supporting Information .....</b>	<b>169</b>

## Chapter 5: Discussions, Conclusions and Future Outlook

5.1 Discussion.....	175
5.2 Conclusions .....	179

<b>5.3 Future Outlook .....</b>	<b>181</b>
<b>5.4 References.....</b>	<b>183</b>

## Statement of Objectives

The main objective of this thesis was to explore the effect of nanoparticle anchoring on liquid crystal polymers. While several literature examples report nanoparticles effectively dispersed within a liquid crystalline matrix, examples of polymer grafted nanoparticles exhibiting liquid crystalline behaviour has not been reported prior to the present work. In general, the objective of each chapter was to explore the design and synthesis of a different semi-flexible polymer ligand as well as its anchoring onto spherical zirconia nanoparticles. Each polymer was chosen for its ability to self-assemble into different liquid crystal phases and the goal upon successful synthesis of these nanoparticles was the preparation and characterization of its resulting liquid crystalline phases. The self-assembly of poly hexyl isocyanate grafted nanoparticles into lyotropic nematic phases were explored in chapter 2. In chapter 3, poly( $\gamma$ -benzyl-L-glutamate), a “model” semi-flexible rod was similarly functionalized onto zirconia nanoparticles to explore its lyotropic cholesteric properties. Chapter 4 explores the thermotropic and lyotropic properties of poly( $\gamma$ -stearyl-L-glutamate) grafted zirconia nanoparticles to self-assemble into lyotropic/thermotropic cholesteric liquid crystals.

# Abstract

## Liquid Crystalline Behaviour of Semi-Flexible Polymer-Coated Nanoparticles

In summary, this thesis explores the liquid crystalline phases enabled by semi-flexible polymers grafted onto spherical zirconia nanoparticles, which is a culmination of advances in several separate fields. Previous examples have been reported of liquid crystal (LC) ligands being synthesized and subsequently attached to a nanoparticle core, however this strategy of LC functionalization proves to be costly, difficult and time-consuming. However, colloidal stabilization of the nanoparticles is crucial in designing LC nanocomposites. For this reason, polymer ligands were examined as potential candidates towards imparting colloidal stability, however several reports of polymer stabilized nanoparticles do not explore LC behaviour. Towards self-assembly of polymer grafted nanoparticles, flexible and rigid polymer grafted nanoparticles have been successfully synthesized, however these particles tend to organize into cubic phases (ie. face-centered and body-centered), while semi-flexible polymers as nanoparticle coatings have been largely unexplored, despite the multiple established theories surrounding the ability of semi-flexible polymers to self-assemble into liquid crystalline phases. Few literature examples of semi-flexible polymer-grafted nanoparticles exist, however, of these examples, none have reported liquid crystalline behaviour. For this reason, the objective of this thesis was to explore phase behaviour of semi-flexible polymer grafted nanoparticles, with each chapter dedicated to a different semi-flexible polymer with unique self-assembly behaviour.

Chapter 2 outlines preparation of poly (hexyl isocyanate) (PHIC) grafted nanoparticles as well as the lyotropic nematic phases enabled by these particles. The major findings were that compared to the PHIC in solution, PHIC coated nanoparticles exhibited lower critical concentrations required for liquid crystal assembly as well as anisotropic ordering of these particles into linear assemblies. Given that the zirconia nanoparticles were spherical, and consequently isotropic, the ability of these isotropic particles to self-assemble into anisotropic structures was a surprising result. We propose that concentration-dependent splaying of the polymer corona into a rod-like structure enables nematic ordering. Following this major finding,

the same general nanoparticle preparation method was extended to two other semi-flexible polymers with unique liquid crystal properties. In chapter 3, poly( $\gamma$ -benzyl-L-glutamate) (PBLG), was chosen for its ability to self-assemble into lyotropic cholesteric phases, which was subsequently also seen in the corresponding functionalized nanoparticles. Functionalized nanoparticles were prepared across a wide molecular weight range, as to explore the effect of molecular weight on LC formation, LC structure and PBLG aggregation. It was found that MW appeared to have a role in the onset of LC formation, as low MW PBLG-grafted NPs exhibited a drastic reduction in the critical concentration, while high MW PBLG-grafted NPs had no noticeable effect. Similarly, Chapter 4 explores LC formation of nanoparticles coated with another synthetic polypeptide, Poly( $\gamma$ -stearyl-L-glutamate) (PSLG), which is unique due to thermotropic and lyotropic cholesteric behaviour. In comparison to untethered PSLG, the LC phases formed from the corresponding nanoparticles were similarly observed to exhibit reduced lyotropic critical concentrations in addition to organizing into LC structures with similar dimensions, despite the small core size/high curvature of the nanoparticles. This suggests that self-assembly of the PSLG coated nanoparticles persists despite the presence of the zirconia cores, which potentially act as a hindrance in the kinetics/structure of LC formation, as seen in the increased LC structure sizes. In summary, the LC phases formed from semi-flexible polymer-grafted nanoparticles reveal that nanoparticle functionalization could prove to be an effective strategy towards altering LC size/structure in addition to enabling LC formation at reduced lyotropic concentrations.

## Abrégé

En résumé, cette thèse explore les phases cristallines liquides permises par des polymères semi-flexibles greffés sur des nanoparticules sphériques de zircon, ce qui est un point culminant des progrès réalisés dans plusieurs domaines distincts. Des exemples antérieurs ont été rapportés de ligands de cristaux liquides (CL) synthétisés puis attachés à un noyau de nanoparticules, mais cette stratégie de fonctionnalisation des CL s'est avérée coûteuse, difficile et chronophage. Cependant, la stabilisation colloïdale des nanoparticules est cruciale dans la conception de nanocomposites à base de cristaux liquides. C'est pourquoi les ligands polymères ont été examinés en tant que candidats potentiels pour conférer une stabilité colloïdale, mais plusieurs rapports sur les nanoparticules stabilisées par des polymères n'explorent pas le comportement de la CL. En ce qui concerne l'auto-assemblage des nanoparticules greffées de polymères, des nanoparticules greffées de polymères flexibles et rigides ont été synthétisées avec succès, mais ces particules ont tendance à s'organiser en phases cubiques (c'est-à-dire centrées sur la face et centrées sur le corps), tandis que les polymères semi-flexibles en tant que revêtements de nanoparticules ont été largement inexplorés, malgré les multiples théories établies entourant la capacité des polymères semi-flexibles à s'auto-assembler dans des phases cristallines liquides. Il existe peu d'exemples bibliographiques de nanoparticules greffées de polymères semi-flexibles, mais aucun de ces exemples n'a fait état d'un comportement cristallin liquide. C'est pourquoi l'objectif de cette thèse était d'explorer le comportement de phase des nanoparticules greffées de polymères semi-flexibles, chaque chapitre étant consacré à un polymère semi-flexible différent ayant un comportement d'auto-assemblage unique.

Le chapitre 2 décrit la préparation des nanoparticules greffées de poly (hexyl isocyanate) (PHIC) ainsi que les phases nématiques lyotropes permises par ces particules. Les principales conclusions sont que, par rapport au PHIC en solution, les nanoparticules enrobées de PHIC présentent des concentrations critiques plus faibles requises pour l'assemblage des cristaux liquides, ainsi qu'un ordonnancement anisotrope de ces particules en assemblages linéaires. Étant donné que les nanoparticules de zircon étaient sphériques et donc isotropes, la capacité de ces particules isotropes à s'auto-assembler en structures anisotropes était un résultat

surprenant. Nous proposons que l'évasement dépendant de la concentration de la couronne de polymère en une structure en forme de tige permette une mise en ordre nématique. Suite à cette découverte majeure, la même méthode générale de préparation de nanoparticules a été étendue à deux autres polymères semi-flexibles aux propriétés cristallines uniques. Dans le chapitre 3, le poly( $\gamma$ -benzyl-L-glutamate) (PBLG) a été choisi pour sa capacité à s'auto-assembler en phases cholestériques lyotropes, ce qui a ensuite été également observé dans les nanoparticules fonctionnalisées correspondantes. Des nanoparticules fonctionnalisées ont été préparées dans une large gamme de poids moléculaires, afin d'explorer l'effet du poids moléculaire sur la formation de CL, la structure de CL et l'agrégation de PBLG. Il a été constaté que le poids moléculaire semblait jouer un rôle dans le début de la formation des CL, car les NP greffées de PBLG de faible poids moléculaire présentaient une réduction drastique de la concentration critique, tandis que les NP greffées de PBLG de poids moléculaire élevé n'avaient pas d'effet perceptible. De même, le chapitre 4 étudie la formation de CL de nanoparticules recouvertes d'un autre polypeptide synthétique, le Poly( $\gamma$ -stearyl-L-glutamate) (PSLG), qui est unique en raison de son comportement cholestérique thermotrope et lyotrope. Par rapport au PSLG non lié, les phases CL formées à partir des nanoparticules correspondantes présentent des concentrations critiques lyotropes réduites et s'organisent en structures CL de dimensions similaires, malgré la petite taille du noyau et la forte courbure des nanoparticules. Cela suggère que l'auto-assemblage des nanoparticules recouvertes de PSLG persiste malgré la présence des noyaux de zircon, qui agissent potentiellement comme un obstacle dans la cinétique/structure de la formation de CL, comme le montre l'augmentation de la taille des structures CL. En résumé, les phases de CL formées à partir de nanoparticules semi-flexibles greffées de polymère révèlent que la fonctionnalisation des nanoparticules pourrait s'avérer être une stratégie efficace pour modifier la taille/structure de la CL en plus de permettre la formation de la CL à des concentrations lyotropes réduites.

# Acknowledgements

McGill's chemistry department hosts some of the most unique, interesting, kindest, considerate, and funniest people I have ever met in my life, and I think that grad school would be a lot less bearable without such wonderful people. I really appreciate that a brief "hi" in the hallways could potentially turn into an hour-long conversation which is why my acknowledgements section was by far the hardest part of the thesis to write, due to everyone I want to thank, that has made my life easier or better.

I am deeply grateful to Prof. Reven for their unwavering support, invaluable guidance, and expertise throughout this journey. I am truly fortunate to have had the opportunity to learn from your wisdom and mentorship. Your encouragement and feedback have been invaluable in refining my ideas and improving my research. Thank you for your patience as well!

Thank you, Violeta, for effectively being a second unofficial supervisor. Research-wise, you taught me everything I know, and your guidance and guidance has been immensely helpful. You are always great at keeping our lab in order, even though I was the only person in our lab that needed to be kept in order. Life-wise, thanks for being a great friend; you're always fun to talk to and you always encouraged me, helped me overcome my obstacles, always made me feel better when I cried, and you always provided low calorie snacks.

Thank you, Prof. Barrett, for being my third adoptive supervisor and for swooping in during my last year to help me with all the editing, thesis work and the life talks.

Thank you, also, to all past and present members of the Reven lab. Brenda, especially, thank you for being my best friend, for helping me break out of my shell, for being a shoulder to

cry on, and just always being there for me. Thank you, Sarah, for being my other best friend; you're always fun to be around and I appreciate it that we can effortlessly talk for hours. Thank you, also, for all the times you stayed late with me, for all the compliments you give and how you always keep my ego boosted, and also for always forcing me to have a social life. Thank you also to Roy, Maria, Amanpreet, Jamie, Rodrigo, Adaline, Oscar, Stephane, and both Gabriella's, for letting me talk at you when you wanted to work.

To everyone in the office, thanks for contributing to such a fun and friendly environment. Thanks for the company and the late nights as well! If I am ever frustrated with lab work, I can always come inside and procrastinate the problem away. Thank you: Kayrel, Misha, all Alex's, Brandon, Vahid, Kadence, Nathan, Antranik, Elliot, JD, Marc, Michael, Stephanie, Marzieh, Nooshin, Ethan, and Michelle.

Thank you also to the boys, Evan, and Hariz, for the high calorie dinners that I didn't ask for and to my next-door neighbors/friends: Durbis and Alida, Juan, JM, Anne, Inna, Tom I guess, Benedetta, and Arthur. Thanks for including me in all your adventures!

Thank you to everyone in and around the department as well, as you were all great company and procrastinating with me. Thank you, Mathieu, Sandra, JP, Taleah, Quentin, Joyce, JP, Kirill, Robin, Hatem, Petr, Alex, Mohini. Thank you also for the help!

And lastly thank you to my family: mom, dad, and sister, for supporting me, the life advice, in telling me to keep on truckin', for the periodic visits and for letting me come back home without paying rent and with all utilities included. Your love has made this journey feel effortless, and it gives me the confidence to believe that I can achieve anything. Thanks for never giving up on me and thanks for believing that I can live up to my potential.

To anyone reading this that I forgot to mention, sorry! It was difficult trying to list everyone who has had a positive impact in my life, given how many amazing people there are, but know that it keeps me up at night to this day.

# Contributions of authors

## Chapter 1

Chapter 1 was written and researched entirely by Jessie Wong, with editing assistance from Prof. Reven.

## Chapter 2: Lyotropic Nematic Phases of Isotropic Nanoparticles via Semiflexible Polymer Ligands

Reprinted with permission from: J. Wong, V. Toader, L. Reven, Lyotropic Nematic Phases of Isotropic Nanoparticles via Semiflexible Polymer Ligands. *Macromol. Rapid Commun.* 2023, 44, 2200951.

Design, synthesis and characterization of the PHIC ligands in addition to the preparation, measurements, characterization, and interpretation of the resulting liquid crystal behaviour was entirely conducted by Jessie Wong. Synthetic assistance was provided by Dr. Violeta Toader. In addition, the manuscript original draft was written by Jessie Wong, with editing assistance from Prof. Reven.

## Chapter 3: Cholesteric Behaviour of Poly( $\gamma$ -Benzyl-L-Glutamate)Functionalized Nanoparticles

Wong, J., Reven, L.. "Cholesteric Behaviour of Poly( $\gamma$ -Benzyl-L-Glutamate) Functionalized Nanoparticles". Manuscript currently in preparation.

Design, synthesis and characterization of the PBLG ligands in addition to the preparation, measurements, characterization, and interpretation of the resulting liquid crystal behaviour was entirely conducted by Jessie Wong. In addition, the manuscript original draft was written by Jessie Wong, with editing assistance from Prof. Reven and Prof. Barrett.

## Chapter 4: Thermotropic and Lyotropic Phase Behaviour of Cholesteric Poly( $\gamma$ -Stearyl-L-Glutamate) Functionalized Nanoparticles

Wong, J., Toader, V., Reven, L.. "Thermotropic and Lyotropic Phase Behaviour of Cholesteric Poly( $\gamma$ -Stearyl-L-Glutamate) Functionalized Nanoparticles". Manuscript currently in preparation.

Design, synthesis and characterization of the PBLG ligands in addition to the preparation, measurements, characterization, and interpretation of the resulting liquid crystal behaviour was entirely conducted by Jessie Wong. SLG-NCA monomer synthesis was originally conducted by Dr. Violeta Toader. In addition, the manuscript original draft was written by Jessie Wong, with editing assistance from Prof. Reven and Prof. Barrett.

### **Chapter 5: Discussions, Conclusions and Future Outlook**

Chapter 5 was written entirely by Jessie Wong, with editing assistance from Prof. Reven and Prof. Barrett.

## Contributions to Original Knowledge

Several Chapters in this thesis are scholarly contributions to original knowledge. At the time of writing, chapter 2 has been published, with chapters 3 and 4 in preparation and soon to be submitted.

The contributions to original knowledge presented in this thesis lies in the liquid crystal (LC) behaviour enabled by grafting semi-flexible polymers onto spherical nanoparticles (NPs). Examples of functionalized NPs using the same polymers chosen in this thesis exist, however the new contributions lie in proving that the same polymers also impart LC behaviour, while also characterizing the structures formed from the functionalized NPs and comparing them to the untethered polymers.

Chapter 2 outlines the preparation of poly (hexyl isocyanate) (PHIC) coated nanoparticles, which has been reported before, however the functionalization of high molecular weight PHIC ligands, its subsequent functionalization onto zirconia nanoparticles and the resulting liquid crystal (LC) phases enabled by surface grafting of these PHIC ligands stand as novel and original contributions to knowledge. The lyotropic nematic phases formed from these particles were extensively explored using polarized optical microscopy and  $^2\text{H}$  NMR, revealing less anisotropic/efficient ordering in the particles compared to the free PHIC in solution. The ability of isotropic particles to self-assemble into anisotropic structures, at sufficiently high concentrations, has not been reported prior to this work.

Following the surprising result found in chapter 2, the concept of attaching semi-flexible polymers with known LC behaviour to spherical nanoparticles were extended to other semi-flexible polymers with known LC behaviour. The design and synthesis of high molecular weight (MW) poly( $\gamma$ -benzyl-L-glutamate) (PBLG) ligands using ionic liquids was an original contribution to knowledge, as previous PBLG ligands have all been prepared via click chemistry, which typically requires design, synthesis, and purification of each of the two “clickable” molecules, which reduces the number of synthetic steps to two (polymerization and the subsequent deprotection).

The advantage of using ionic liquids in PBLG polymerization is its ease, efficiency, low cost, reduced synthetic steps, and the freedom to extend this strategy towards other functional, synthetic homo-polypeptides. A wide molecular weight range of PBLG ligands was synthesized to explore the molecular weight contribution towards LC assembly as well. In addition, the self-assembly and characterization of the LC phases formed from PBLG coated nanoparticles serve as original contributions as well.

In addition to the thermotropic and lyotropic cholesteric phases enabled by poly( $\gamma$ -stearyl-L-glutamate) (PSLG) functionalized nanoparticles, chapter 4 serves as a compilation/comparison of past literature regarding thermotropic phase behaviour of poly( $\gamma$ -stearyl-L-glutamate) (PSLG). Previous literature on thermal behaviour of PSLG has largely been inconsistent, owing to the predominant method of preparing PSLG at the time of their publication, as PSLG was largely prepared through ester exchange of the side chains. This method, while relatively simple to perform, does not produce homopolymers of PSLG, and the resulting products can more accurately be described as random copolymers of PSLG. Consequently, the thermal behaviour of PSLG random copolymers is dependent on the degree of successful stearyl substitution, which gives rise to inconsistent literature values (ie. transition temperatures, the number of transition peaks, structural phenomena etc.). The second original contribution in this chapter lies in the characterization of the thermal behaviour of PSLG homopolymers, which surprisingly hasn't been discussed in recent decades, and the attempt to consolidate past literature with the present work.

# List of Figures

<b>Figure 1-1:</b> Schematic Representation of particulate fillers dispersed within a polymer matrix at various loading fractions.....	3
<b>Figure 1-2:</b> Relationship between tensile strength and particulate filler loadings for different $\text{CaCO}_3$ particulate sizes.....	4
<b>Figure 1-3:</b> Possible liquid crystal geometries .....	8
<b>Figure 1-4:</b> Common (A) Lyotropic and (B) Thermotropic liquid crystal phases .....	10
<b>Figure 1-5:</b> Polarized optical microscopy (POM) instrument schematic representation...	12
<b>Figure 1-6:</b> Common nematic liquid crystal textures under POM.....	13
<b>Figure 1-7:</b> 2D X-ray Scattering profile of (Left) an isotropic and unaligned sample and (Right) an oriented smectic sample.....	15
<b>Figure 1-8:</b> Examples of fitting X-ray scattering profiles (Left) Fitting to the structural features and (Right) fitting the form factors. ....	17
<b>Figure 1-9:</b> Expected 1D and 2D SAXS profiles of a nematic liquid crystal.....	18
<b>Figure 1-10:</b> Representation of liquid crystalline ligands attached to the surface of a gold nanoparticle, which is subsequently dispersed within a polymer matrix .....	22
<b>Figure 1-11:</b> Optical microscopy images representing the effect of nanoparticle dispersants on the orientation of a cholesteric liquid crystal.....	23
<b>Figure 1-12:</b> Templating of nanoparticles by (Left) cholesteric liquid crystals and (Right) smectic liquid crystals. ....	23

<b>Figure 1-13:</b> Schematic representation of liquid crystal droplets dispersed within a polymer matrix .....	25
<b>Figure 1-14:</b> Possible LC structures adopted by liquid crystal elastomers.....	26
<b>Figure 1-15:</b> Contraction curve of liquid crystal elastomer conformations .....	27
<b>Figure 1-16:</b> Generalized Scheme summarizing the effect of ternary composites on the resulting liquid crystal properties .....	28
<b>Figure 1-17:</b> Examples of lyotropic liquid crystal composites comprised of (Left) hydroxypropylcellulose and (Right) single-walled carbon nanotubes .....	29
<b>Figure 1-18:</b> Poly( $\gamma$ -stearyl -L-glutamate) functionalized nanoparticles dispersed within a polymer matrix of poly( $\gamma$ -stearyl -L-glutamate).....	30
<b>Figure 1-19:</b> Classic example of lyotropic nematic liquid crystal based on vanadium pentaoxide .....	30
<b>Figure 1-20:</b> Example of hexagonal close-packed lattice from self-assembled spherical particles .....	31
<b>Figure 1-21:</b> Examples of lyotropic liquid crystals self-assembled from colloidally stable anisotropic particles (nanodiscs) .....	32
<b>Figure 1-22:</b> Representation of polymer flexibility spectrum, from flexible to rigid polymers .....	33
<b>Figure 2-1:</b> (a) Phase separation of PHIC <sub>180</sub> -ZrO <sub>2</sub> through crossed polarizers and uncrossed polarizers. (b) Lyotropic nematic liquid crystal phases of (top) PHIC functionalized nanoparticles and (bottom) PHIC in chloroform .....	63

<b>Figure 2-2:</b> TEM images highlighting the organizational differences between low and high molecular weight PHIC functionalized nanoparticles.....	64
<b>Figure 2-3:</b> Representative <sup>2</sup> .....	67
<b>Figure 2-4:</b> TGA curve of PHIC <sub>24</sub> -ZrO <sub>2</sub> prepared using scheme 2-1 .....	83
<b>Figure 2-5:</b> TGA curve of PHIC <sub>55</sub> -ZrO <sub>2</sub> prepared using Scheme 2-2 .....	83
<b>Figure 2-6:</b> TGA curve of PHIC <sub>180</sub> -ZrO <sub>2</sub> prepared using Scheme 2-3.....	84
<b>Figure 2-7:</b> <sup>1</sup> H NMR spectra of PHIC <sub>180</sub> -ZrO <sub>2</sub> in CDCl <sub>3</sub> .....	85
<b>Figure 2-8:</b> <sup>31</sup> P NMR spectra of PHIC <sub>180</sub> -ZrO <sub>2</sub> in CDCl <sub>3</sub> .....	86
<b>Figure 2-9:</b> GPC results of PHIC <sub>24</sub> (top), PHIC <sub>55</sub> (middle), and PHIC <sub>180</sub> (bottom) .....	87
<b>Figure 2-10:</b> TEM image of benzyl alcohol functionalized ZrO <sub>2</sub> NPs .....	89
<b>Figure 2-11:</b> TEM comparison of PHIC <sub>180</sub> -ZrO <sub>2</sub> drop casted from (left) dilute and (right) concentrated solutions .....	89
<b>Figure 2-12:</b> TEM and corresponding histogram of PHIC <sub>24</sub> -ZrO <sub>2</sub> .....	90
<b>Figure 2-13:</b> TEM and corresponding histogram of inter-chain distances of PHIC <sub>180</sub> -ZrO <sub>2</sub> .....	90
<b>Figure 2-14:</b> TEM and corresponding histogram of intra-chain distances of PHIC <sub>180</sub> -ZrO <sub>2</sub> .....	91
<b>Figure 2-15:</b> POM phase diagram of PHIC <sub>180</sub> in chloroform .....	92
<b>Figure 2-16:</b> POM phase diagram of PHIC <sub>180</sub> in chloroform .....	93
<b>Figure 3-1:</b> TEM images of prepared NPs: (a) PBLG <sub>89</sub> @ZrO <sub>2</sub> , (b) PBLG <sub>228</sub> @ZrO <sub>2</sub> , (c) PBLG <sub>1237</sub> @ZrO <sub>2</sub> , (d) PBLG <sub>2963</sub> @ZrO <sub>2</sub> .....	105

<b>Figure 3-2:</b> Representative POM images of (left) PBLG <sub>228</sub> and (right) PBLG <sub>228</sub> @ZrO <sub>2</sub> in DCM indicating liquid crystallinity .....	106
<b>Figure 3-3:</b> Representative POM images of (a) PBLG <sub>89</sub> @ZrO <sub>2</sub> , (b) PBLG <sub>228</sub> @ZrO <sub>2</sub> , (c) PBLG <sub>1237</sub> @ZrO <sub>2</sub> , (d) PBLG <sub>2963</sub> @ZrO <sub>2</sub> in DMF, where cholesteric textures were visible .....	108
<b>Figure 3-4:</b> SAXS scattering profile PBLG <sub>89</sub> and PBLG <sub>228</sub> and their corresponding nanoparticles in DMF .....	109
<b>Figure 3-5:</b> SAXS scattering profile of PBLG <sub>1237</sub> and PBLG <sub>2963</sub> and their corresponding nanoparticles in DMF .....	110
<b>Figure 3-6:</b> SAXS scattering profile of gelled samples of PBLG <sub>228</sub> and PBLG <sub>228</sub> @ZrO <sub>2</sub> in THF .....	111
<b>Figure 3-7:</b> FTIR Spectrum of PBLG <sub>190</sub> and PBLG <sub>190</sub> @ZrO <sub>2</sub> .....	128
<b>Figure 3-8:</b> TGA weight loss curves of prepared PBLG@ZrO <sub>2</sub> nanoparticles .....	128
<b>Figure 3-9:</b> Comparison between liquid crystalline samples and gelled samples of PBLG (and PBLG coated nanoparticles) .....	129
<b>Figure 3-10:</b> TEM images of gelled polymer networks of PBLG (a) PBLG <sub>89</sub> @ZrO <sub>2</sub> , (b) PBLG <sub>228</sub> @ZrO <sub>2</sub> , (c) PBLG <sub>1237</sub> @ZrO <sub>2</sub> , (d) PBLG <sub>2963</sub> @ZrO <sub>2</sub> in DMF .....	130
<b>Figure 3-11:</b> Phase diagram of lyotropic liquid crystalline samples of PBLG <sub>89</sub> @ZrO <sub>2</sub> and PBLG <sub>89</sub> in DMF.....	132
<b>Figure 3-12:</b> Phase diagram of lyotropic liquid crystalline samples of PBLG <sub>228</sub> @ZrO <sub>2</sub> and PBLG <sub>228</sub> in DMF.....	133
<b>Figure 3-13:</b> Phase diagram of lyotropic liquid crystalline samples of PBLG <sub>1237</sub> @ZrO <sub>2</sub> and PBLG <sub>1237</sub> in DMF .....	134

<b>Figure 3-14:</b> Phase diagram of lyotropic liquid crystalline samples of PBLG <sub>2963</sub> @ZrO <sub>2</sub> and PBLG <sub>2963</sub> in DMF .....	135
<b>Figure 3-15:</b> Gelled samples of PBLG <sub>228</sub> and PBLG <sub>228</sub> @ZrO <sub>2</sub> in THF, across several concentrations .....	136
<b>Figure 4-1:</b> TEM images of PSLG <sub>141</sub> @ZrO <sub>2</sub> cased from a semi-dilute solution to confirm colloidal stability.....	146
<b>Figure 4-2:</b> POM images of non-annealed samples of (top) PSLG <sub>141</sub> and (bottom) PSLG <sub>141</sub> @ZrO <sub>2</sub> in toluene, across several concentrations .....	147
<b>Figure 4-3:</b> POM images of annealed samples of (top) PSLG <sub>141</sub> and (bottom) PSLG <sub>141</sub> @ZrO <sub>2</sub> in toluene, across several concentrations .....	148
<b>Figure 4-4:</b> SAXS profiles of varying concentrations of (Left) PSLG <sub>141</sub> and (Right) PSLG <sub>141</sub> @ZrO <sub>2</sub> in toluene .....	149
<b>Figure 4-5:</b> POM images of thermally annealed samples of (Left) PSLG <sub>141</sub> and (Right) PSLG <sub>141</sub> @ZrO <sub>2</sub> .....	151
<b>Figure 4-6:</b> SAXS profiles of thermally annealed samples of (Left) PSLG <sub>141</sub> and (Right) PSLG <sub>141</sub> @ZrO <sub>2</sub> .....	152
<b>Figure 4-7:</b> <sup>1</sup> H NMR Spectrum of [DPPA][TBA] .....	169
<b>Figure 4-8:</b> <sup>1</sup> H NMR Spectrum of PSLG <sub>141</sub> .....	170
<b>Figure 4-9:</b> DSC curves of PSLG <sub>141</sub> and PSLG <sub>141</sub> @ZrO <sub>2</sub> upon (top) first heating, (middle) first cooling, and (bottom) second heating.....	171
<b>Figure 4-10:</b> FTIR Spectrum of PSLG <sub>141</sub> and PSLG <sub>141</sub> @ZrO <sub>2</sub> .....	172

**Figure 4-11:** 1D SAXS profiles of lyotropic samples of PSLG<sub>141</sub> prepared in toluene ..... 173

**Figure 4-12:** 1D SAXS profiles of lyotropic samples of PSLG<sub>141</sub>@ZrO<sub>2</sub> prepared in toluene  
..... 174

**Scheme 2-1:** Synthesis of Poly hexyl isocyanate functionalized nanoparticles using click  
chemistry..... 60

**Scheme 2-2:** “Grafting-to” approach using click chemistry towards poly hexyl isocyanate  
functionalized nanoparticles..... 61

**Scheme 2-3:** “Grafting-to” approach using pre-polymerized ligands towards poly hexyl  
isocyanate functionalized nanoparticles ..... 62

**Scheme 2-4:** Synthesis of phosphonic acid-based initiator towards poly hexyl isocyanate  
synthesis ..... 80

**Scheme 3-1:** Synthetic scheme towards PBLG ligands using an ionic liquid-based initiator  
..... 102

**Scheme 4-1:** Synthetic scheme of PSLG functionalized nanoparticles using ionic liquid-based  
initiator..... 140

# List of Tables

<b>Table 2-1:</b> Quadrupolar splittings of PHIC <sub>180</sub> and PHIC <sub>180</sub> -ZrO <sub>2</sub> across as determined through <sup>2</sup> H NMR .....	68
<b>Table 2-2:</b> Comparison of grafting densities between prepared PHIC functionalized nanoparticles .....	85
<b>Table 2-3:</b> Summarized molecular weight results of synthesized PHIC ligands .....	88
<b>Table 3-1:</b> Physical properties of synthesized PBLG ligands.....	102
<b>Table 3-2:</b> Average Cholesteric half-pitch measurements of various PBLG samples and their corresponding functionalized nanoparticles .....	107
<b>Table 3-3:</b> Average interparticle distances of prepared PBLG functionalized nanoparticles, as measured from TEM .....	131
<b>Table 3-4:</b> Summary of surface coverages, as calculated from experimentally obtained TGA weight loss, as well as expected weight loss .....	131
<b>Table 4-1:</b> Measured cholesteric pitches of PSLG <sub>141</sub> and PSLG <sub>141</sub> @ZrO <sub>2</sub> across several concentrations .....	147
<b>Table 4-2:</b> Summary of calculated lattice parameters of PSLG <sub>141</sub> and PSLG <sub>141</sub> @ZrO <sub>2</sub> .....	149
<b>Table 4-3:</b> Measured transition temperatures of PSLG <sub>141</sub> and PSLG <sub>141</sub> @ZrO <sub>2</sub> , as determined from DSC.....	150
<b>Table 4-4:</b> Summary of SAXS data for PSLG <sub>141</sub> and PSLG <sub>141</sub> @ZrO <sub>2</sub> .....	154

# Chapter 1 : Introduction

## 1.1 Polymer Nanocomposites

### 1.1.1 Background

The field of materials science seeks to investigate the structure, properties and applications of materials and the relationship between them. Progress in materials science is essential in advancing virtually every field of science, as understanding the properties of existing synthetic materials or biomaterials could advance our ability to design and engineer complex materials, which in turn, could lead to new and helpful products in everyday life or potentially as solutions toward sustainability and energy challenges.

Polymers are one class of materials that has seen widespread use in modern society due to its high durability, cheap production, and ease of processability. Since the explosion of industrial polymer development in the 1930s, the high processability of polymers/plastics as well as the cheap costs of production led to the widespread use of polymers throughout society.<sup>1, 2</sup> However, due to the lack of natural degradation pathways, the long term impact of the synthesized polymer compounds, produced since the 1940s, is still not fully understood.<sup>3, 4</sup> For example, polyethylene, polystyrene and polyvinylchloride, are currently three of the commonly produced plastics produced in 2021,<sup>5</sup> and in one study, and only low density polyethylene revealed possible biodegradation pathways while the others showed little to no degradation over the course of 32 years.<sup>6</sup> While research into polymer degradation strategies exist,<sup>7-9</sup> humanity as a whole is producing far more plastic (currently 390 million tons per year)<sup>5</sup> than can be sustainably degraded. For this reason, research into sustainable polymer products could prove to be a potential solution to plastic pollution, greenhouse gas emissions, and resource depletion while also simultaneously allowing the current population to maintain their high quality of life.<sup>10-</sup>

13

Alternatively, polymer composite/blend materials are polymers reinforced with one or more components thereby enhancing the mechanical, thermal, dielectrical, or optical properties

of the original polymer. In terms of sustainable materials design, either the polymer or the filler/reinforcer can be green/biodegradable while simultaneously enhancing the physical properties of the material. In general, the advantage of using polymer composites is that complex and quality materials may be produced, by simply introducing a composite material, while also circumventing the need for more polymer production.<sup>14-16</sup> In other words, the amount of polymer required to match the enhanced properties of the polymer composite material is often substantially greater. In some high-performance materials, the properties of the composite vastly out-perform those of the unmodified polymers.<sup>17-20</sup> For this reason, polymer composites could potentially be used towards the next generation of sustainable and high-performance materials.

### **1.1.2 Polymer Matrix Composites (PMCs)**

Composite materials can be further distinguished into composite materials in which the reinforcing material is on a macroscopic length scale, while nanocomposites are instead reinforced by fillers on the nanoscale. In general, the unique properties of composite materials are highly tailored towards the intended application and the choice to use macroscopic fillers compared to nanoscale fillers depend on the desired outcome. Typically polymer matrix composites (PMCs) are reinforced with fibers, primarily carbon, glass, and Kevlar, however particulates have also been dispersed in matrices.<sup>21</sup> In the context of this thesis, only dispersed nano-sized particulates are relevant to the research presented.

The diversity of particulate fillers dispersed in PMCs is vast; metal oxides such as iron oxide,<sup>23,24</sup> titanium dioxide,<sup>25</sup> silica,<sup>26</sup> gold,<sup>27</sup> silver,<sup>27</sup> and fullerenes<sup>28</sup> have been dispersed in various polymer matrices, among many others. In addition to the type of filler used, the size, orientation, and volume fraction of the particles also determines the bulk properties of the material, as shown in Figure 1-1.<sup>21</sup> In general, the particle volume fraction required for enhanced properties is highly tailored to each PMC system; filler addition that is above and below optimal will result in negative enhancements of the material.<sup>29</sup> This phenomena is immediately obvious in Figure 1-2; within a polypropylene matrix, CaCO<sub>3</sub> fillers diminished the tensile strength of the polypropylene matrix, however, for the 0.01 μm sized particles, the reverse occurred. Particulate

loadings above a volume fraction of  $\sim 0.8$  instead enhanced the tensile strength of the composite material. Additionally, the authors state that “[stress analysis] must be further refined... and the effect of interfacial interactions must also be considered”.<sup>30</sup> In other words, the specific composite composition as well as their interactions with each other must be considered as to better predict composite properties and behaviour. This sentiment echoes throughout the field of materials science since the unique interplay between the micro/nanostructures and the atomic/molecular interactions simultaneously influence each other as to produce the specific composite behaviour.

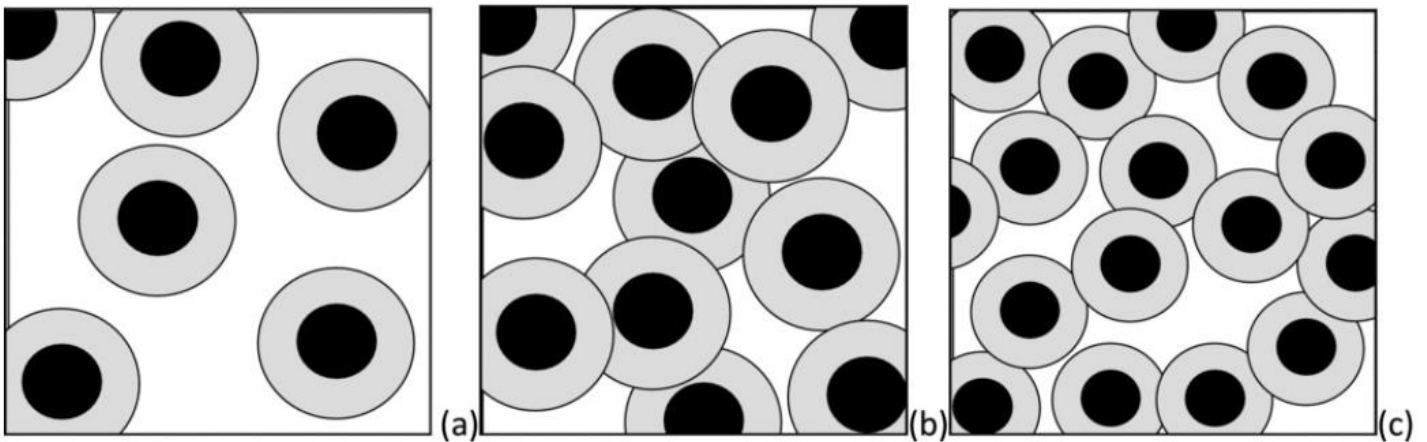


Figure 1-1: In a PMC, the particulate filler (black), is dispersed within a polymer matrix (white), with an interphase region (grey) forming between the two components. The properties of a PMC are dependent on the majority phase. In the case where the polymer matrix is the majority phase (a), the bulk material properties closely resemble the polymer matrix. However, when the volume fraction increases either due to a larger interphase region (b) or due to a larger particulate loading (c). Re-printed with permission.<sup>22</sup>

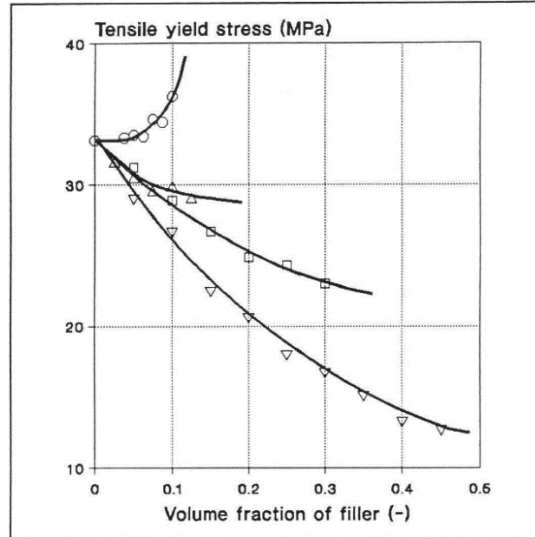


Figure 1-2: The effect of  $\text{CaCO}_3$  nanoparticle size and volume fraction on the tensile strength of a polypropylene matrix.  $0.01 \mu\text{m}$  ( $\circ$ ),  $0.08 \mu\text{m}$  ( $\triangle$ ),  $1.3 \mu\text{m}$  ( $\square$ ),  $58.0 \mu\text{m}$  ( $\nabla$ ) sized particles were used. Upon increasing particle loading, the tensile strength of the composite generally decreased, however, specifically for  $0.01 \mu\text{m}$  sized particles, the tensile strength increased beyond that of the bulk polypropylene material. Printed with permission.<sup>30</sup>

### 1.1.3 Surface Modification of Particulates/Nanoparticles

The compatibility of the particulate filler with the polymer matrix is instrumental in achieving high performance materials. Upon mixing two materials together, interfaces are created where the materials make contact, and in the case where the two materials are poorly compatible, the particles agglomerate and the PMC properties remain unchanged<sup>31</sup> or even degrades.<sup>32</sup> For this reason it becomes essential for the nanoparticles to remain discrete and well-dispersed/compatible within the PMC. One method to improve interfacial compatibility within the PMC is through chemical modification of the nanoparticle surface. Covalent attachment of the necessary functional groups provides surface passivation and allows improved miscibility between the particles and the polymer matrix. For example, it is a common strategy to coat the filler material with the same matrix material to maximize compatibility.<sup>33, 34</sup> In one such example, silicon carbide nanoparticles, which are known to easily agglomerate, which have been coated with a polystyrene corona resulted in improved miscibility within a polystyrene matrix, which in

turn also improved thermal conductivity, increased both the dielectric constant and the DC conductivity, retained tensile strength and improved thermal conductivity.<sup>35</sup> Depending on the application, it becomes necessary that the surface modification strategy does not alter the properties of the filler or the composite.

Several strategies exist for the surface modification of various particulates. Modification strategies generally fall under one of three strategies: chemical treatment, polymerization, or ligand exchange. Chemical treatment typically involves covalent attachment of an organic ligand onto the nanoparticle surface. The only requirement for these organic ligands is that the molecule must contain a “headgroup” which will form a covalent attachment to the nanoparticle surface,<sup>36</sup> molecules with more than one attachment group may risk agglomeration of the nanoparticles through bridging.<sup>37, 38</sup> In the case of noble metal nanoparticles such as gold and silver, the most used attachment groups include amines and ammonium ions, sulfides and disulfides, and polyphosphines.<sup>39-41</sup> Conversely, silanes, carboxylates and phosphonates are all commonly used functional groups for the modification of metal oxide nanoparticles.<sup>39, 42</sup> The primary motivation of chemical modification is to prevent agglomeration of the particles, however it is also possible to introduce several functionalities/properties to the nanoparticle. For example, fluorescent tags have been introduced to non-fluorescent nanoparticles for bioimaging and sensor applications.<sup>43-45</sup> Additionally, through the functionalization of appropriate ligands, the modified nanoparticles are able to self-assemble into various architectures.<sup>46, 47</sup> One particularly important application of chemically modified nanoparticles is within the field of nanomedicine and drug delivery. Macrophages are white blood cells which remove foreign materials from the body, which include functional nanomaterials. For these foreign drugs to bypass the body’s immunity defense mechanism, it is necessary to functionalize the drug with the necessary chemical modifications to prevent uptake by the macrophages, which in turn allows the drug to reach its target destination. This is often done through colloidal carriers (ie. liposomes) coated with hydrophobic ligands thereby preventing macrophage uptake.<sup>48</sup>

Polymerization surface modification strategies involve one of two methods: “grafting-to” and “grafting-from”. In the case of the “grafting-to” method, a pre-synthesized polymer with an appropriate head group is covalently attached to the nanoparticle surface. Conversely, polymers are grown from the nanoparticle surface in “grafting-from” procedures. The primary advantage of “grafting-to” modifications is that the method allows for versatility in that any polymer may be bound to the surface, if it has the correct terminal group. However, “grafting-from” modifications produce nanoparticles higher surface coverages/grafting densities, which is optimal for preventing agglomeration. This is due to the reduced steric hindrance of incoming monomer units compared to large and sterically hindered incoming polymer chains.<sup>49, 50</sup> Furthermore, the “grafting-from” method is more cumbersome in that it requires that the polymer coating must be removed in order to measure its molecular weight (in addition to the polydispersity of the polymerization, which obscures the data). It is also possible to provide colloidal stability through polymer physisorption, however in terms of mechanical properties and thermal stability, physisorption does not compare to polymer grafting.<sup>51, 52</sup> If the goal of surface modification is to prevent agglomeration, polymer grafting is by far the best strategy.<sup>53-</sup>

56

Lastly, in ligand exchange strategies, typically, the nanoparticles are initially synthesized with a weakly bound ligand, which is later replaced by a ligand whose head group has a stronger affinity to the nanoparticle surface. It is also possible for the ligands to be replaced with another with the same head group.<sup>57</sup> This method is sometimes necessary, especially when the nanoparticle preparation procedure is highly rigid. For example, early semi-conducting nanoparticles (ie. quantum dots (QD)) synthetic procedures solely resulted in hydrophobic nanoparticles,<sup>58-61</sup> however, through the pioneering work of Dubois et al., aqueous QDs were achieved using a versatile ligand exchange procedure using dithiocarbamates.<sup>62</sup> In summary, the primary advantage of ligand exchanges is the relatively simple experimental procedures;<sup>36, 63</sup> the pre-synthesized nanoparticles are simply added to a solution alongside the ligand to be exchanged.

## 1.2 Liquid Crystals

### 1.2.1 Liquid Crystal Terminology and Classifications

Liquid Crystals (LCs) exist as a state of matter somewhere between a solid and a liquid; as essentially an ordered fluid, where LC molecules self-assemble into organized structures, and control over this behaviour allows for stimuli-responsive optical materials. In modern society, LCs are primarily used in displays in everyday personal electronic devices, however, recently other technologies have utilized LCs. For example, thermometers,<sup>64</sup> biosensors,<sup>65</sup> some sports equipment,<sup>66</sup> LC light valves,<sup>67</sup> and smart windows<sup>68</sup> all utilize LC materials. The fundamental basis of these applications lies within the anisotropic properties of LCs, where the physical properties of the materials are direction dependent. In contrast, physical properties of isotropic materials are direction independent and will be the same in all orientations.

LC behaviour may be classified as either thermotropic, where the self-assembly behaviour is temperature dependent, or lyotropic, where LCs self-assemble upon reaching a certain critical concentration. Beyond the LC behaviour classifications, LCs can be further distinguished through the organized structures that are formed. It is also important to note that the LC behaviour and the assembled LC phases are not mutually exclusive; it is possible to achieve the same LC phase either through thermotropic or lyotropic means. For example, rod shaped molecules such as 4-cyano-4'-pentylbiphenyl (5CB) and DNA are both able to form nematic LC phases, however, 5CB forms nematic LC phases upon cooling,<sup>69</sup> while DNA forms nematic phases at sufficiently high concentrations in solution.<sup>70, 71</sup>

It is also possible to group together certain LC molecules based on their geometric shape, which allows for some general predictability of the self-assembled phases. Calamitic LCs are the most common of the LC geometries and these molecules are best described as "rod-like". For this reason, calamitic LCs are often known to form nematic, smectic, and cholesteric phases. Discotic LCs are the next most common LC geometry, and as the name implies, these LCs share a "disk-like" geometry and self-assemble into nematic-discotic and nematic columnar phases, with

the possibility of higher order columnar phases ie. right-angled columnar and hexagonal columnar. Additional geometries are also possible, including bent-core, rings, and cones etc.,<sup>72</sup> however in the context of this thesis, only calamitic/rod-like molecules will be discussed, as linear polymers resemble this geometry.

This thesis features several polypeptide-based LCs. In the context of LCs, polypeptides adopt a  $\alpha$ -helical conformation, which in turn results in various self-assembled LCs in organic solvents. LC formation is largely driven by the  $\alpha$ -helix's rigidity, as well as rod-like packing between the polymer chains. It is also important to note that the handedness of the  $\alpha$ -helix is generally independent of the handedness of the LC. Several schematics of polypeptide based-LCs are depicted in Figure 1-3.

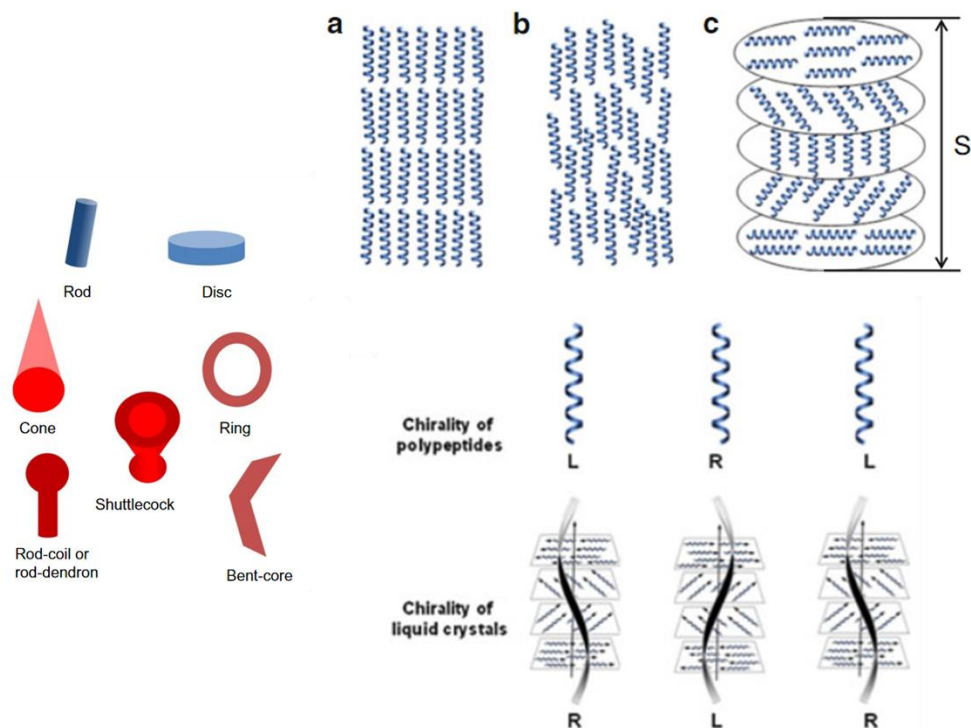


Figure 1-3: Possible LC molecular geometries. Taken with permission from Garbovskiy and Glushchenko.<sup>72</sup> Top Right: Polypeptide-based LCs including a) smectic, b) nematic, c) cholesteric.

Bottom right: Schematic diagram depicting that the handedness of the polypeptide backbone does not necessarily dictate the handedness of the LC. Adapted from Cai et al.<sup>167</sup>

To characterize LCs, it may be useful to define the director, as well as the order parameter. The director,  $\mathbf{n}$ , is used to define the preferred axis of orientation within an LC phase. For simple organized structures such as nematic and smectic LCs, the director would often be parallel to the long axis of the LC molecule. Conversely, the order parameter,  $S$ , describes the tendency for nematic and smectic LCs to align parallel to the director and is a function of temperature. A theoretical fully aligned sample would be assigned  $S = 1$  while a completely isotropic, or unaligned, sample would be assigned  $S = 0$ . While not discussed here, order parameters are instead described as a second rank tensor for biaxial LCs.

For high order organizations such as cholesteric LCs, it becomes more useful to define a helical axis, which is perpendicular to the molecular long axis and describes an axis in which the LC molecules rotate about. The vertical length along the helical axis required for the cholesteric LC molecules to complete rotation is measured by the pitch.

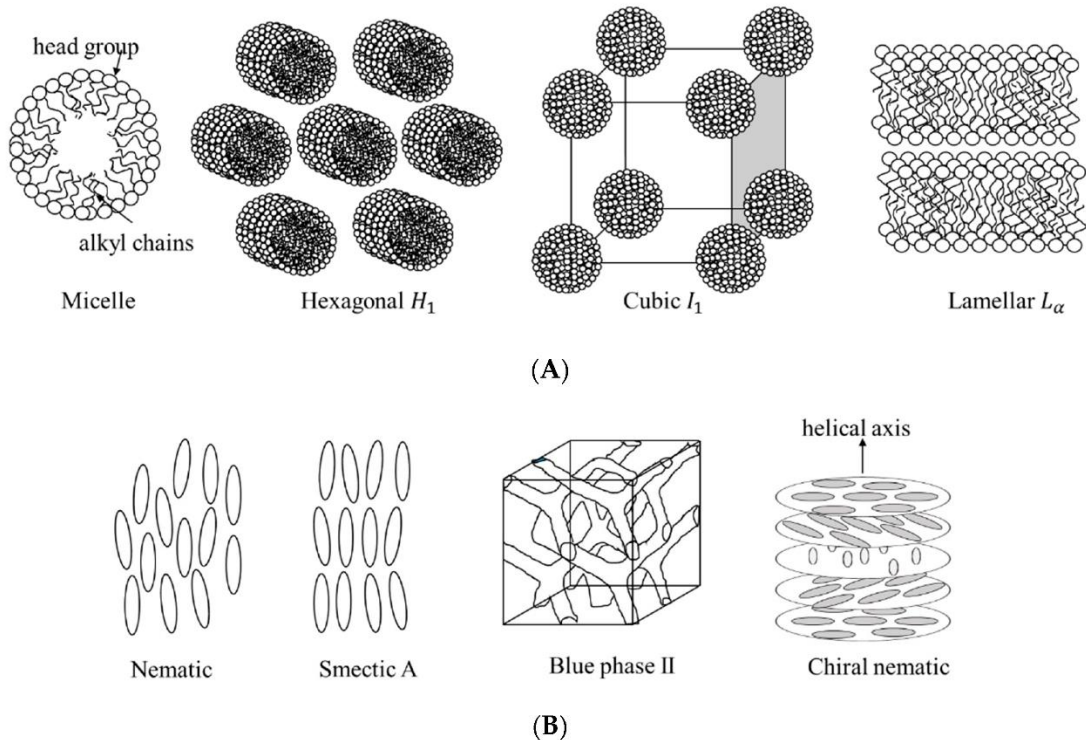


Figure 1-4: Common lyotropic (A) and thermotropic (B) LC phases formed from calamitic molecules. Lyotropic phases are often (but not necessarily) self-assembled from amphiphilic molecules. Here, thermotropic LC phases are formed from rod-shaped molecules and depending on the specific chemical structure, several different ordered phases are possible. It is also important to note that the LC phases listed in (B) are also accessible to rod-like lyotropic molecules. Schematic from ref.<sup>73</sup> and printed with permission, as per open access.

### 1.2.2 Optical Microscopy of Liquid Crystals

When examined under polarized optical microscopy (POM), LCs produce unique and vibrant textures. The origin of this behaviour is complex; however, it can be broken down into two different phenomena: double refraction and birefringence. These terms are often used interchangeably, however, there is a distinction. Double refraction refers to the splitting of unpolarized incident radiation into an ordinary ray and an extraordinary ray. As unpolarized visible light radiation travels through an anisotropic material, the visible light ray interacts with a

symmetric axis (known as the optic axis) differently from how it would interact with an asymmetric axis and simultaneously splits the ray into an ordinary axis (which is parallel to the propagation direction) and an extraordinary axis (which propagates at an angle oblique to the ordinary ray). When viewing images through an anisotropic crystal such as calcite, the image appears doubled, due to the resulting rays (hence double refraction). Normally, visible light radiation propagates forward with two perpendicularly oscillating wave components. When radiation travels through an isotropic medium, the same refractive index is experienced by both wave components. However, in an anisotropic material with one (or more) additional refractive indices, the wave components interact with the refractive indices differently, thereby resulting in birefringence.

While birefringence is normally not visible with the naked eye, it is possible to see birefringence using POM. In a typical setup (Figure 1-5), a light source is placed beneath a birefringent sample, which is sandwiched between two perpendicular polarizers. As radiation is transmitted through the lower polarizer (known as the polarizer), the visible light becomes polarized to propagate in only one direction. After passing through the sample, the light then encounters the upper polarizer (known as the analyzer). In the case of an isotropic sample, the wave components of the polarized incident light will remain unaltered, due to the same refractive index being experienced by all components, and this results in the polarized light being entirely absorbed by the analyzer. However, in an anisotropic material, the polarized light is doubly refracted into two perpendicular wave components, each of which interacts differently with the refractive indices arising from the asymmetry of the material. As a result, the wave component parallel to the analyzer is transmitted and appears as a bright spot through the microscope while the perpendicular wave component is entirely absorbed. This results in the vibrant textures observed in Figure 1-6. For this reason, POM is a useful tool for identifying anisotropic materials, such as LCs.<sup>74, 75</sup>

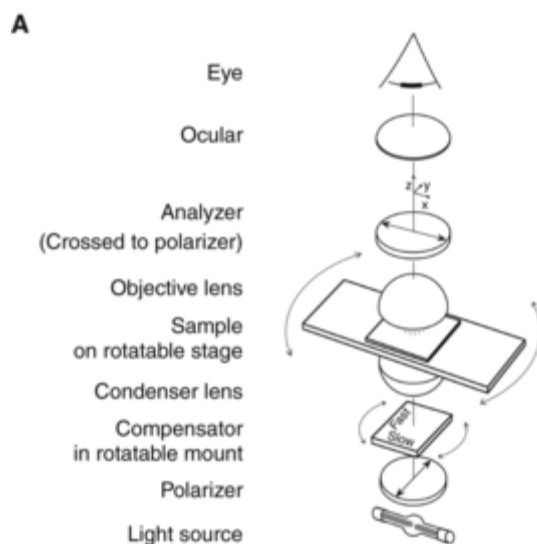


Figure 1-5: Schematic representation of a polarized optical microscope (POM).

In LC materials, birefringence is entirely attributed to how plane polarized light interacts with the LC's director. In anisotropic crystalline samples birefringence occurs as optically homogenous bright spots due to the high periodicity and long-range order. However, due to the fluidity of LC materials, birefringence produces exuberant textures arising from the local fluctuations of the director as well defects within the LC. Since each LC assembly produces a unique optical texture, characterizing these textures requires a highly trained eye to discern the phenomena underlying the images. In the LC field, POM is the primary method of characterization. However, other techniques also exist to supplement and reaffirm the analysis obtained with POM.

To highlight the complexity of analyzing LC POM textures, we can look to nematic LCs as an example. Nematic LCs are relatively simple to analyze due to the simplicity of their molecular shape; the LC textures are largely determined by the orientation of the rod-like LC molecules. In the trivial case where the orientation of the rods is perpendicular to both polarizers (ie. the rods are pointed towards the viewing angle or "optic axis"), due to the recombination of ordinary and extraordinary radiation occurring in the plane of either of the polarizers, a black image appears. In the non-trivial case, three nematic textures arise depending on the circumstances (Figure 1-

6).<sup>76</sup> The first, the Schlieren texture, occurs due to large and continuous fluctuations in the rods, which result in the dark bands when the rods are pointed along the viewing angle, or coloured when the rods are aligned elsewhere. It is also important to note here that in nematic POM textures, the colours produced are determined by the thickness and orientation of the rods. The thread-like texture occurs in nematic samples that have a relatively high concentration of defects, which disrupt nematic ordering as to “link” the defects together, thereby producing the so-called “threads”. Lastly, the marbled texture occurs for thin samples, where the rods fluctuate slowly, resulting in a relatively uniform distribution of rod orientations which results in the marbled texture (like a highly uniform crystalline material).

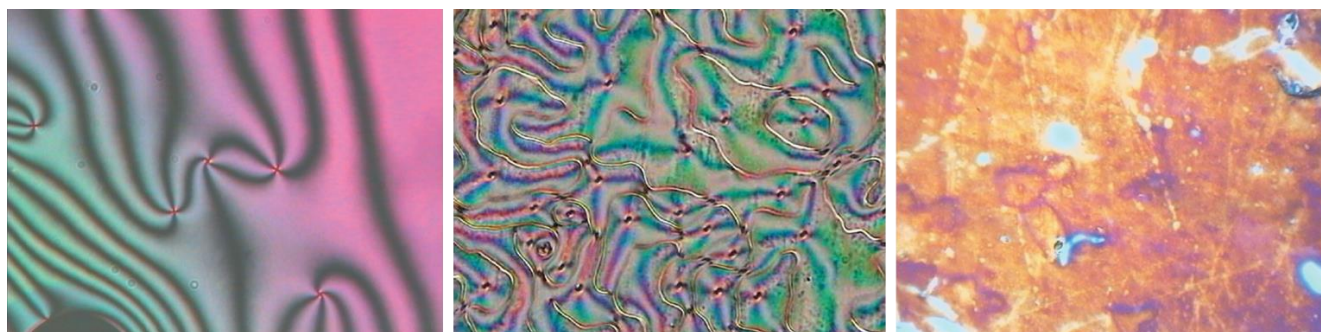


Figure 1-6: Possible nematic textures observed under POM: Schlieren (left), Thread-like (middle), Marbled (right). Reproduced from ref.<sup>76</sup>

### 1.2.3 X-Ray Scattering of Liquid Crystals

While X-ray based techniques are traditionally used on more crystalline materials, it can serve as a valuable tool in characterizing LCs as well. In contrast to crystalline materials, LCs are inherently more disordered, and for this reason, obtained spectra will be less resolved compared to crystalline samples. However, X-ray scattering has still proven to be useful in characterizing several LC phases.

First and foremost, SAXS and WAXS (henceforth collectively abbreviated as SWAXS) as well as X-ray Diffraction (XRD) utilize elastic X-ray scattering to probe different length-scale features of a sample. Depending on the experimental setup, all these techniques

could potentially be performed on one instrument. For crystalline materials, XRD would be the go-to experimental technique, as a detector would collect all angles of scattered radiation, thereby allowing for a high resolution, three-dimensional map of the crystal in question. The drawback, however, is that all angles must be independently scanned, and this results in long experimental times (several hours). Additionally, XRD is limited to crystalline materials, so preparation of the sample is often cumbersome as high-quality crystals are required, thereby rendering this technique unusable towards characterizing LCs.

The difference between SAXS and WAXS is the sample placement, since the scattering angle is inversely proportional to the length of the feature being studied (ie. a smaller feature results in larger scattering angles). For SAXS, the sample is placed further from the detector such that the resulting X-ray scattering profile covers small angles (typically 0.1 to 5°). This set-up probes structural features in the hundreds or thousands of nanometres range, which include intermolecular spacings, nanoparticle shape and sizes, and ordered assemblies. Conversely, WAXS places the sample closer to the detector, resulting in larger scattering angles of the incident X-ray, which allows for probing of smaller features, such as atomic lattices, phase composition and crystallinity. Depending on the LC features being probed, either SAXS or WAXS may be used.

To understand how X-ray scattering is connected to features probed by SWAXS, an understanding of Bragg's law is necessary. The Bragg condition occurs when successive atomic planes scatter X-ray radiation such that the reflected X-radiation interferes constructively and can be described by the following equation (1), where  $n$  is an integral describing the diffraction order (1, 2, 3 etc.),  $\lambda$  is the wavelength of the incident X-ray radiation, and  $\vartheta$  is the angle between the incident beam and the atomic plane. In a lab setting,  $\lambda$  represents Cu K $\alpha$  radiation and corresponds to  $\lambda=1.5418$  Å. from this relationship, we can see the characteristic powder pattern seen in X-ray Diffraction (XRD).

$$n\lambda = 2d\sin\theta \quad (\text{eq. 1})$$

To probe structural features, equation (1) may be rearranged such that the scattering vector,  $q$ , may be used to measure interacting distances through equation (2). From here, the scattering vector can be related to real space through equation (3) and represents the interacting distance ( $d$ ).<sup>2,3</sup> The relationship between equations (2) and (3) explains why larger scattering angles are used to probe small distances and vice versa. For example, a real distance,  $d$ , of 5000 nm would produce a scattering vector of  $0.00126 \text{ nm}^{-1}$  while 50 nm would produce a value of  $0.126 \text{ nm}^{-1}$ .

$$q = \frac{4\pi}{\lambda} \sin\theta \quad (\text{eq. 2})$$

$$d = \frac{2\pi}{q} \quad (\text{eq. 3})$$

While SWAXS collects a two-dimensional map of scattered X-ray radiation, typically the scattering profile is radially integrated to produce a one-dimensional plot as to aid in characterization. The 2D map may also be useful, as the map includes a distribution of all scattering centres that fulfil Bragg Diffraction, which may be useful in identifying highly oriented samples (such as nematics or smectic LCs) as seen in Figure 1-7.

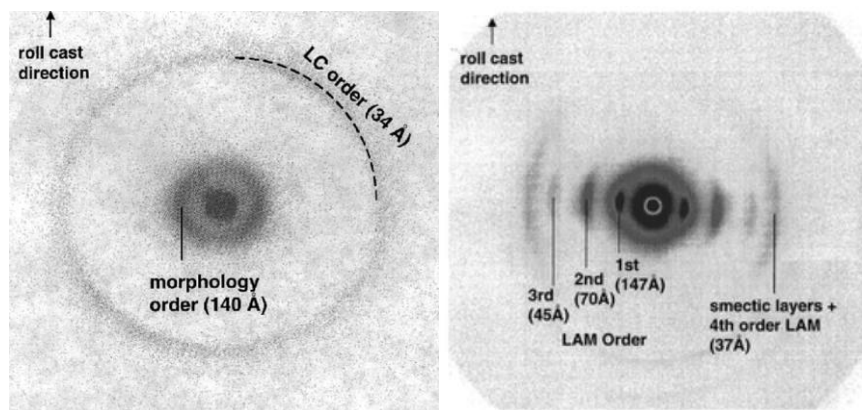


Figure 1-7: (Left) 2D SAXS profile of a non-oriented/isotropic LC sample; peaks appear as concentric circles, as an isotropic sample would scatter equally at all angles around the beam. (Right) 2D SAXS profile of a highly oriented smectic LC. As can be seen, scattered radiation is only caught across the meridional, suggesting anisotropic ordering <sup>77</sup> Reproduced with permission.

In contrast, the 1D profile is also useful in identifying the shape, size, and other structural features. Towards shape and size, specifically, the 1D SAXS profile may be

sorted into separate  $q$  regions (ie. the Guinier and Porod plots). The Guinier region occurs near the origin, is independent of the scattering vector,  $q$ , and is largely concentration dependent. Fitting of this region can give the radius of gyration or molecular weight of the sample.<sup>168</sup> Following the Guinier region, if the 1D scattering data of the Porod region were to be plotted as  $q^2I(q)$  vs  $q$  (known as a Kratky Plot), the shape of the molecule can be extracted. The shape of the resulting bell-like curve will give information about the shape, conformation and flexibility of the sample. This analysis is mostly used in characterizing non-correlated proteins in solution.<sup>169</sup>

It is useful to distinguish the 1D scattering profile into its contributions. The intensity profile of all collected radiation,  $I(q)$ , is a product of a form factor,  $P(q)$ , and a structure factor,  $S(q)$ , which are the contributions arising from molecular and structural contributions, respectively. For this reason, it becomes difficult to identify LC structural features and distinguish these from its molecular features. While it can intuitively be easy to filter out peaks based on their size (since structural peaks will appear at larger distances and lower  $q$  compared to molecular features which occur at smaller distances and higher  $q$ ), this may not be applicable in all situations.

$$I(q) \propto P(q)S(q) \quad (\text{eq. 4})$$

Generally, two methods exist for determining the structure factor. Firstly, the structural contributions can be simulated and fitted to the data as to determine LC dimensions.<sup>78</sup> Alternatively, simulated form factor models are generated based on the shape of the LC molecule (ie. Spheres, rods, disks, etc.)<sup>79</sup>, which allows the structure factor

to be isolated.<sup>80-82</sup> As a result, the remaining contributions from the intensity profile are entirely due to LC features. These methods are exemplified in Figure 1-8.

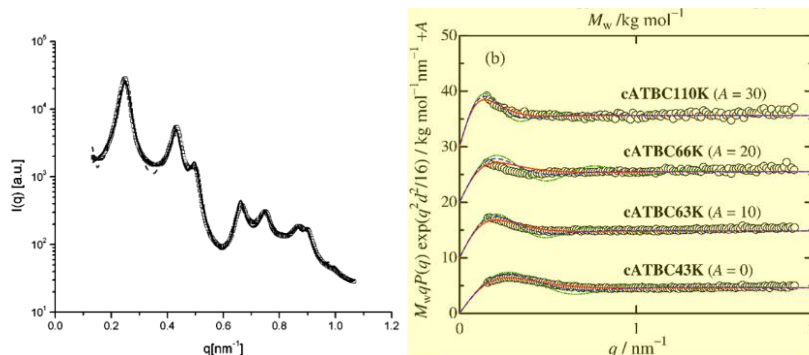


Figure 1-8: Two strategies for fitting SAXS data. (left) Scattering profile of columnar hexagonal liquid crystals fitted to an intensity profile of simulated cylinders.<sup>78</sup>(Right) Fitted form factors fitted from molecular rings, which was subsequently used to identify structural features.<sup>83</sup>

Only two LC structures are relevant within this thesis: nematic and cholesteric. SAXS characterization of both structures are relatively simple in that periodicity arises from either its molecular correlation length ( $l_0$ ), or molecular correlation width ( $w_0$ ) and will occur near  $q=2\pi/w$  or  $q=2\pi/l$  (Figure 1-9).<sup>92,161</sup> Due to the fluid nature of LCs, this naturally produces broad peaks in SAXS, which may not always be above the baseline. Further broadening may also occur in lyotropic LCs, as to accommodate the presence of the solvent molecules.

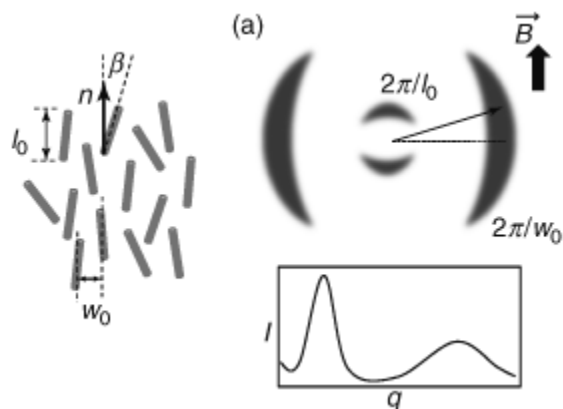


Figure 1-9: Schematic representation of expected peaks observed in nematic and cholesteric LCs.<sup>161</sup> For aligned samples in the direction of  $\vec{B}$ , the expected 2D pattern is depicted in the top right. The scattering direction in the 2D pattern lies along the direction of the structural feature, for example the molecular correlation width ( $w_0$ ) is horizontal in the nematic diagram, hence the larger ring lies horizontally. The 1D profile depicted in the bottom right is misleading in that it simultaneously depicts reflections owing to the long and short axes and does not correspond to the 2D profile, however, 1D profiles may look like this in real, non-aligned LCs.

#### 1.2.4 NMR of Liquid Crystals

The field of NMR characterization of LCs is expansive; numerous experiments exist towards characterizing various types of LCs. In any spin system, its total Hamiltonian,  $\hat{H}$ , is a sum of its individual Hamiltonians and represents the NMR signal for the system. In short, the NMR signal is comprised of individual physical interactions (indicated here by  $H_\lambda$ ), as depicted in eq. 5.<sup>170</sup> In anisotropic environments, such as liquid crystal (LC) systems, additional interaction contributions emerge that would be absent in isotropic systems. These “new” contributions then enable anisotropy-based NMR experiments including residual dipolar couplings (RDCs), residual chemical shift anisotropies (RCSAs), and residual quadrupolar couplings (RQCs).

$$\hat{H} = \sum_{\lambda}^{interactions} H_{\lambda} \quad (\text{eq. 5})$$

Towards characterizing nematic and cholesteric LCs, only RDCs were used in the context of this thesis. Generally, nematic and cholesteric LCs possess positive magnetic susceptibility and align themselves parallel to a strong magnetic field, which introduces high anisotropy into the

system.<sup>171</sup> The dipolar coupling interaction between two NMR active nuclei is dependent on the distance between the nuclei, and the angle of the internuclear vector relative to the external magnetic field.<sup>172</sup> In isotropic environments, this interaction would become zero due to rapid tumbling/Brownian motion of the molecules. Conversely, in anisotropic environments, partial alignment of the internuclear vector results in a splitting of the NMR signal, hence RDCs. Similarly, RQCs also produce a splitting of the NMR signal, but this instead arises from the interaction of the quadrupole moment, of a nucleus with spin  $> \frac{1}{2}$ , with the magnetic field.

Measurement of RDCs or RQCs reveal the extent of alignment of the LCs. In the context of this thesis, only deuterium is considered, however, RDCs prove equally valuable towards the characterization of LCs. This can be achieved either using probe molecules,<sup>173</sup> or selective deuteration of the LC molecule.<sup>174</sup> Both techniques introduce a carbon-deuterium (C-D) bond, and its orientation within the external magnetic field  $(\theta_0, \varphi_0)$  will determine the observed splitting pattern. Hence, the quadrupolar splitting pattern resulting from the C-D bond vector,  $\nu_0$ , can be described through eq. 6, where  $\nu_0^{LC}$  represents the magnitude of quadrupolar splitting in the LC, and  $\eta^{LC}$  represents the asymmetry of the LC matrix.<sup>175</sup> Both of which are represented as components within the quadrupole interaction tensor (eq. 7 and 8). The  $\left(\frac{e^2qQ}{h}\right)$  term is the deuterium quadrupolar coupling constant, which is inherent to the specific deuterated molecule.

$$\nu_0(\theta_0, \varphi_0) = 2\nu_0^{LC} \left[ \frac{1}{2}(3 \cos^2 \theta_0 - 1) + \frac{1}{2}\eta^{LC} \sin^2 \theta_0 \cos 2\varphi_0 \right] \quad (\text{eq. 6})$$

$$\nu_0^{LC} = \frac{3}{4} \left( \frac{e^2qQ}{h} \right) \sum_m f_m C_{m0} \quad (\text{eq. 7})$$

$$\eta^{LC} = \sqrt{6} \frac{\sum_m f_m C_{m2}}{\sum_m f_m C_{m0}} \quad (\text{eq. 8})$$

Towards characterizing LCs, the magnitude of alignment is typically expressed in an order parameter,  $S$ . Rather than polar coordinates, a principal coordinate system is adopted instead, with respect to the field gradient tensor, which gives eq. 7. In the case of uniaxial LCs, where the C-D bond vector lies parallel to the magnetic field, the asymmetry parameter,  $\eta^{LC}$ , becomes zero and eq. 7 can be simplified to eq. 8. This then allows for a direct determination of the order parameter through the quadrupolar splitting.<sup>176,177</sup>

$$\delta v_Q = \frac{e^2 q Q}{h} \left( \frac{3}{2} S_{aa} + \frac{1}{2} \eta^{LC} (S_{cc} - S_{bb}) \right) \quad (\text{eq. 7})$$

$$\delta v_Q = \frac{3}{2} \frac{e^2 q Q}{h} S \quad (\text{eq. 8})$$

## 1.3 Liquid Crystal – Based Composites

### 1.3.1 Nanoparticle Dispersed Liquid Crystals

As can be seen in the previous sections, nanoparticles have tremendous potential within composite materials. Naturally, other nanocomposites comprised of different host materials would be expanded upon. Nanoparticle dispersed liquid crystals (NPLCs) are one such composite material that sees enhanced performance through the presence of a dispersed particulate.

Like PMCs, several factors can affect the properties of the resulting NPLC composite, with each unique blend/composition producing different behaviours. The size, shape, and orientation of the dispersed NPs are all tuneable properties affected by the LC host. Recent advances in NPLCs have largely been based on AuNPs due to plasmonic properties. NPLCS of this type have seen reduced nematic-isotropic transition temperatures,<sup>84, 85</sup> optical non-linearity,<sup>86</sup> altered threshold voltages,<sup>87, 88</sup> increased dielectric anisotropy,<sup>84</sup> and extended memory effects.<sup>89</sup> Additionally, the orientation of the LC host is another parameter that complicates NPLC behaviours. For example, spherical gold nanoparticles (1–3 nm in diameter) when dispersed in a 5CB host (5 wt%), produced conductivity enhancements that were up to two orders in magnitude.<sup>90</sup> Similar conductivity enhancements were seen using nanorod<sup>91-93</sup> and nanodisk systems as well.<sup>94</sup> While there is a lot of nuance to this phenomena, the conductivity enhancement can simply be explained as resulting from a network of conducting nanoparticles, which provides a current pathway through the insulating LC host.<sup>95, 96</sup> In addition, conductivity enhancements are especially pronounced when particles are oriented parallel to the direction of conductivity, due to the improved current pathway.<sup>97, 98</sup> Several NPs have been successfully incorporated into LC matrices with different design features and advantages of each composite.

A non-exhaustive list of dispersed NPs include:<sup>99</sup> AEROSILs,<sup>100, 101</sup> dielectric/semi-conductor NPs,<sup>102-104</sup> carbon nanotubes,<sup>105, 106</sup> and metallic NPs.<sup>87, 107</sup>

In addition to electro-optical enhancements, another major motivation of doping NPs in LCs includes NP templating and LC structural changes induced by the NPs. Depending on the size, shape, and ligand shell of the NPs and how they interact with the LC host, the structural properties will differ. Generally, NPs will either phase separate entirely or concentrate into less ordered regions within the ordered LC phase,<sup>108</sup> as to minimize the total free energy of the system. In a sense, NP inclusion within the LC host matrix destabilizes the LC phase which is why effective colloidal stabilization becomes crucial. Specific methods exist to circumvent this obstacle including NP sputter doping,<sup>108</sup> however custom tailored organic ligand shells are commonly used. Furthermore, optimal compatibility between the NPs and the LC matrix is often attained through custom LC ligands (Figure 1-10) since LC ligands can be easily dispersed within its own LC matrix. Polymer ligands may also be used, however miscibility will depend on the compatibility of the polymer and the matrix.<sup>110, 160</sup>

Despite the compatibility of the organic ligand shell with the LC matrix, even well-dispersed NPs may distort LC structure, a phenomenon which is largely dependent on NP size since smaller NPs are less likely to warp LC ordering compared to larger NPs. Formally, a NP is considered small when the critical radius is below a factor  $\sim K/W$  and does not warp LC director fields (where K represents the Frank Elasticity constant and W represents the polar anchoring energy).<sup>99, 109</sup> For this reason, when designing NPLC composites, it becomes optimal to use smaller NPs as to reduce LC structural deformations.

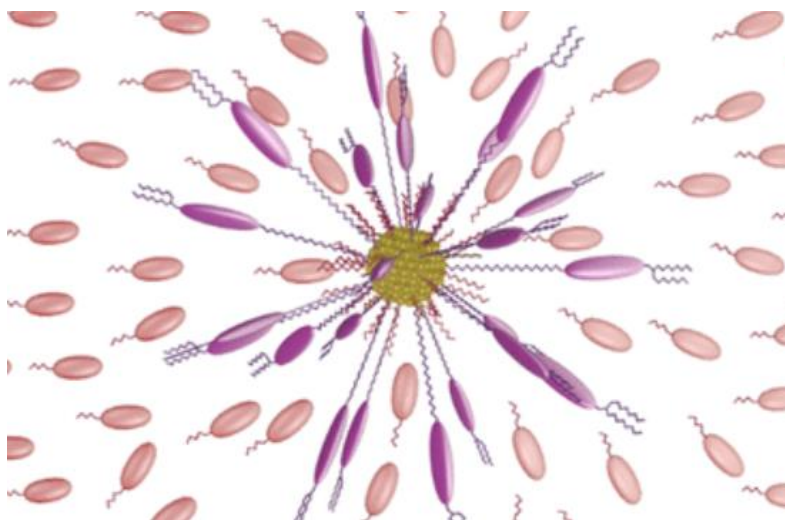


Figure 1-10: Schematic of LC ligands attached to a gold NP core and subsequently dispersed in an LC matrix. This is a common motif seen in LC nanocomposites.

Several examples exist of either LC templating or LC structural changes by NPs. For example, surfactant molecules have been traditionally used to induce either planar or homeotropic alignment in LCs, however, recently, it was recently shown by Zhao et al. that certain NP morphologies can achieve the same effect. They reported that nickel nanospheres produced homeotropic alignment while nickel nanobowls produced planar alignment (Figure 1-11). In cholesteric LCs, NPs become phase separated and map out the cholesteric fingerprint textures.<sup>110</sup> Similarly, in smectic NPLC composites, dispersed NPs trace out the smectic edge dislocations.<sup>107</sup> These examples are featured in Figure 1-12. In summary, nanoparticle doping could prove to be an effective strategy towards altering LC structure/behaviour.

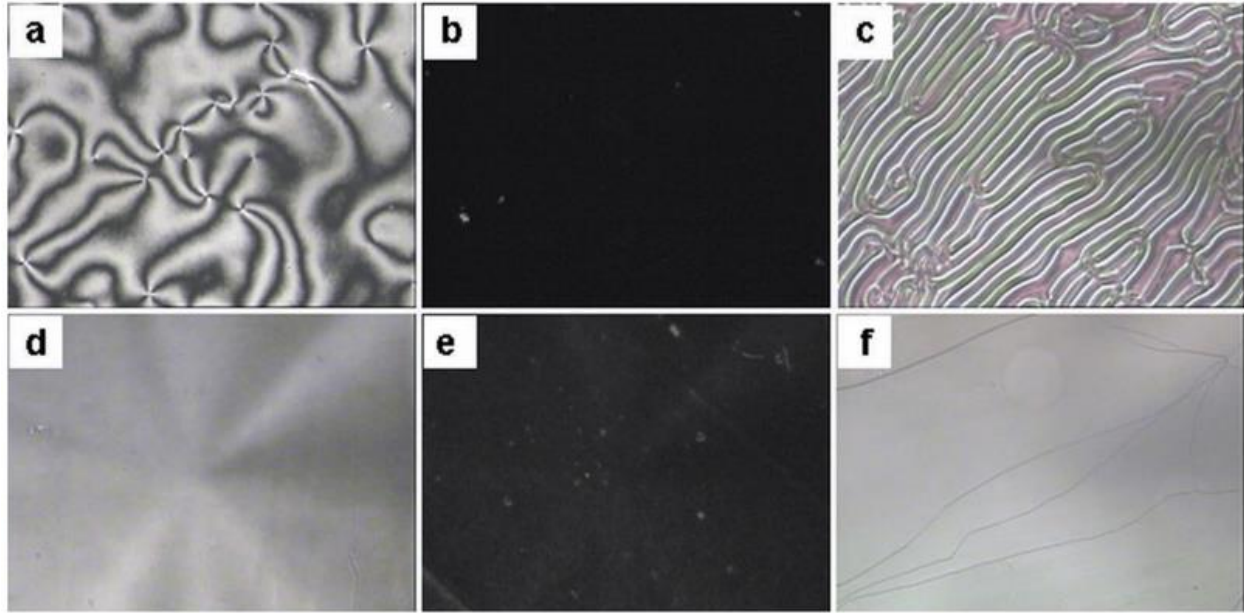


Figure 1-11: The effect nanoparticle morphology has on LC orientation; nanospheres vs nanobowls. (a) Unaligned nematic 5CB, (b) nanosphere doped 5CB with an  $89.4^\circ$  pretilt angle suggesting homeotropic alignment, (c) nanosphere doped cholesteric mixture. Fingerprint texture suggests homeotropic alignment. (d-e) Bright and dark field images of nanobowl doped 5CB. Pretilt angle was measured to be  $2.2^\circ$ , suggesting planar alignment. (f) Nanobowl doped cholesteric mixture; the oily streak texture suggests planar alignment, as the helical axis is parallel to the viewing angle.

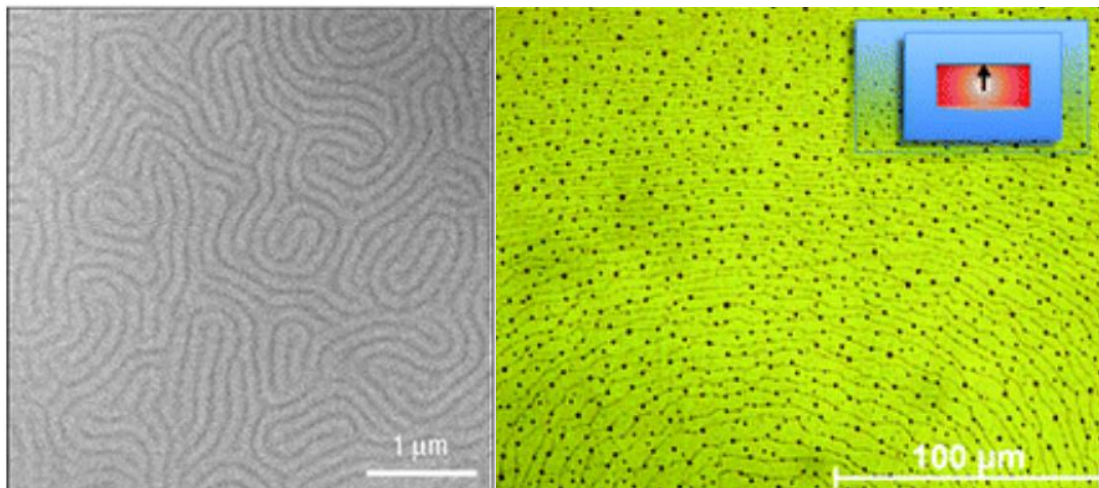


Figure 1-12: (Left) Cholesteric templating of platinum NPs, where the NPs are represented by the darkened region, which essentially maps out the cholesteric LC structure.<sup>111</sup> (Right) Dispersed

gold NPs within a smectic LC, dispersed gold NPs essentially represent the layer spacings within the smectic LCs.<sup>107</sup> Reproduced with permission.

### **1.3.2 Polymer-Dispersed Liquid Crystals and Other Polymer-LC composites**

In contrast to NPLCs, where the NPs are dispersed within an LC matrix, polymer-dispersed liquid crystals (PDLCs) are comprised of LC droplets embedded within a polymer matrix. The PDLC structure has been described as resembling “Swiss cheese” with the holes being replaced by the LC droplets (Figure 1-13).<sup>112</sup> The feature of this composite lies in the fact that two states are available: a cloudy/hazy “off” state and a transparent “on” state. In the absence of an electric field, the PDLC film will scatter light and appear hazy due to the non-aligned directors of each LC droplet and the spatially varied refractive index across the film. However, when an electric field is applied, the droplet directors become uniformly aligned and will instead transmit incident light, thereby giving a transparent appearance. Essentially, each LC droplet acts as an individual scattering center, thereby producing an overall hazy or transparent appearance when switched

off or on, respectively. For this reason, PDLCs have started seeing applications in smart/switchable windows, holography, flexible displays, as well as flat panel displays.<sup>113, 114</sup>

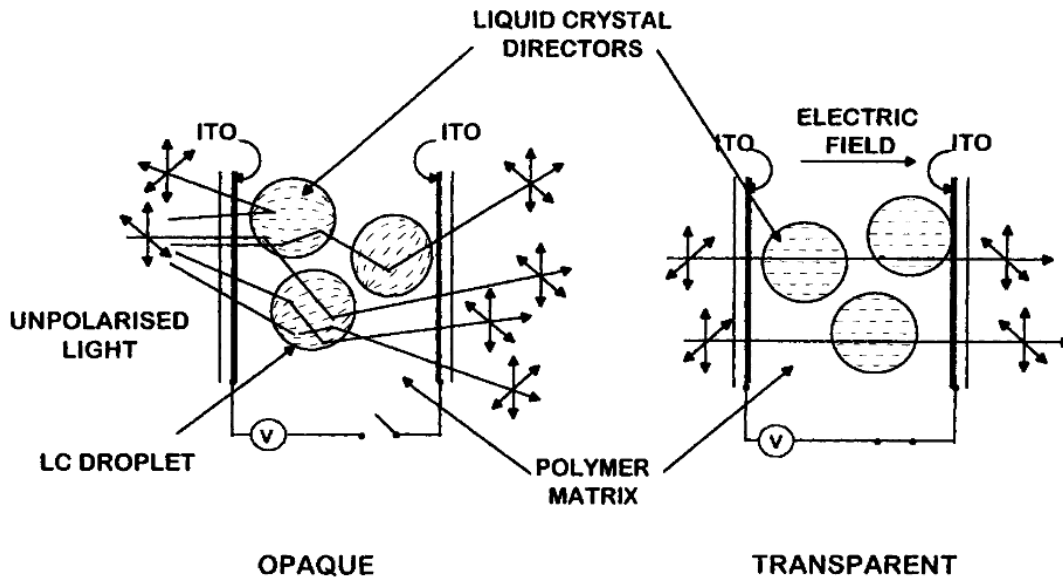


Figure 1-13 Schematic representation of LC droplets dispersed within a polymer matrix. Unpolarized light becomes scattered by unaligned LC droplets, however once an electric field is applied, alignment occurs within the LC domains and the unpolarized light is instead transmitted across the PDLC. Taken from ref.<sup>112</sup>

Typically, PDLCs are prepared either through polymerization induced phase separation (PIPS), solvent induced phase separation (SIPS) or temperature induced phase separation (TIPS). In essence, all three methods involve thorough mixing of the polymer and LC phases followed by some mechanism of phase separation as to trap the LC droplets in place.<sup>115-117</sup> As a result, polymer and LC are generally immiscible with each other, as miscible blends result in complex phase diagrams or non-birefringent/non-LC samples.<sup>118, 119</sup>

Discrete LC droplets occur when the LC fraction within the PDLC lies between 40–65%, however, other morphologies are possible at higher loadings. Coalesced droplets occur above 75% and polymer networks above 90%,<sup>115, 120</sup> which are undesirable for PDLC display applications

(due to the higher switching voltages and more transparent “off” states), however could still be a viable composite if mechanical strength is desired. In general, discrete droplets are desirable for display applications, with smaller droplets producing lower transmittance “off” states, improved contrast ratios, threshold voltages and response times.<sup>121, 122</sup>

Another polymer-LC design motif frequently mentioned are thermotropic LC polymers. Briefly, rigid LC functional groups may be covalently attached to a polymer chain (with several attachments possible as seen in Figure 1-15) thereby producing rubbery and elastic polymer networks with LC properties. Several types of actuators are possible, depending on the LC moieties used. For example, smectic, nematic and cholesteric LC phases are possible (Figure 1-14).

For this reason, these composite materials have tremendous potential (primarily) as heat-sensitive actuators, as heating the material will disturb LC organization, while cooling will return the original LC order.<sup>123, 124</sup> The key feature of these LC elastomer actuators are lightly crosslinked polymer networks, as the polymer network ensures the LC moieties return to their original positions prior to heating (which isn’t guaranteed in non-LCE materials).

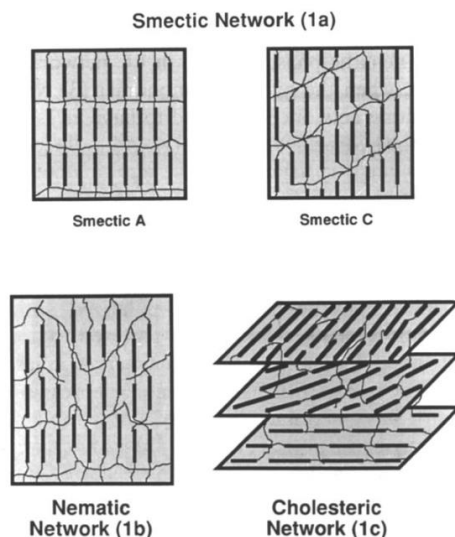


Figure 1-14: Schematic of several possible LC phases formed by LC elastomers including (1a) smectic, (1b) nematic, (1c) cholesteric. Here, the bolded rectangles represent the rigid LC

moieties while the lines which connect them represent the polymer network. Taken from Barclay and Ober, with permission.<sup>125</sup>

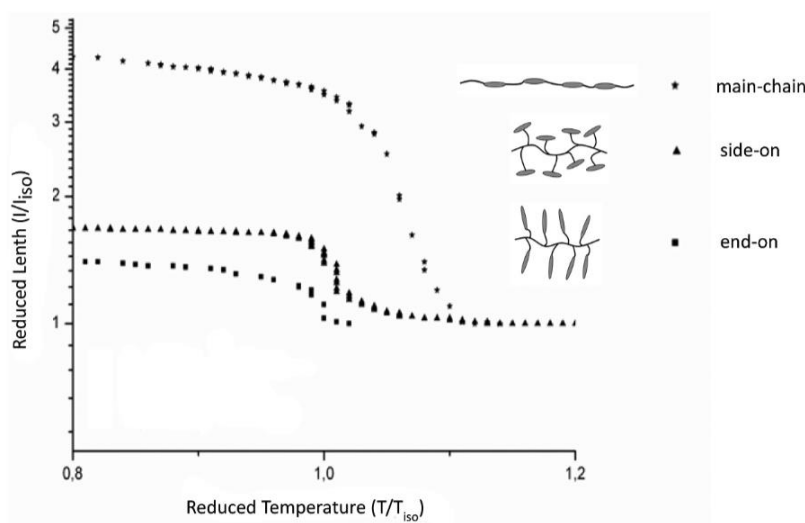


Figure 1-15: Within LC elastomers, several LC attachment methods are possible including main-chain, side-on, and end-on. The curves shown here represent contraction within LC elastomers relative to the smectic-to-isotropic transition. For example, main-chain elastomers exhibit the largest contraction upon heating, while side-on and end-on elastomers have marginal shape changes upon heating. Taken from Zentel, with permission.<sup>124</sup>

### 1.3.3 Liquid Crystalline Polymer Coated Nanoparticles

To summarize the two previous sections, PDLCs are advantageous in that the composites are relatively cheap to produce and enable large displays with high mechanical strength. In contrast, NPLCs provide quick response times, improved electro-optical properties and improved contrast ratios.<sup>127</sup> Ternary systems comprised of these components may be able to enhance the benefits and offset the drawbacks of each of these two-component systems. Generally, three component composites are prepared in the same manner as PDLC films via SIPS, PIPS, or TIPS, with an added step for the introduction of NPs. The resulting morphology of the composite is largely determined by the concentration and composition of the LC and polymer phases; the NPs have little effect on the overall morphology.<sup>126</sup>

Ternary systems have previously been reported; however, few systematic studies of these systems exist. One major drawback of such a complex system is that the properties of said system will largely depend on its constituents, composition, and morphology. In addition, the miscibility issue is further compounded by the fact that each constituent may reduce the predictability of the assembled morphologies. Gridyakina et al., summarizes the complex interactions in a flow chart in Figure 1-16 (with several exceptions).<sup>127</sup> As can be seen in Figure 1-16, when contemplating LC-NP-Polymer composites towards display applications, it becomes important to consider how composition and concentration of the system will affect LC droplet sizes, anchoring forces and LC alignment, which in turn will determine electro-optical properties.

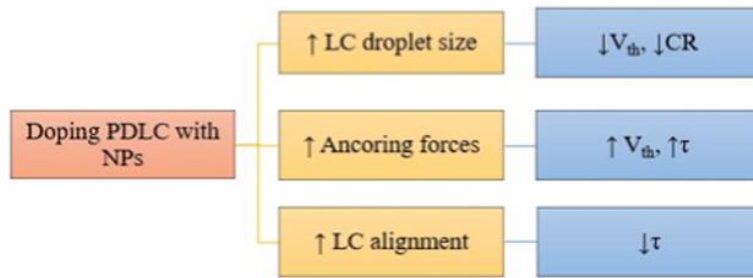


Figure 1-16: Flow chart summarizing the cause-and-effect nature of LC-NP-Polymer ternary composites. From top to bottom: Increased LC droplet sizes result in reduced threshold voltages and reduced contrast ratios, increased anchoring forces result in increased threshold voltages and increased response times, and increased LC alignment produces reduced response times.

Other component composites have been reported as well. For example, numerous chemically modified nanoparticles have been effectively dispersed into the LC phase, rather than the polymer matrix as seen in PDLCs.<sup>128</sup> Similarly, excluded droplets prepared from an aqueous/polymer-LC emulsion have been used to host/synthesize inorganic nanoparticles.<sup>129</sup>

## 1.4 Lyotropic Nanocomposites

Of all the LC nanocomposites listed previously, few have been lyotropic systems. While lyotropic LCs are highly abundant in the natural world, many LC systems discussed in literature have been thermotropic. Additionally, of the lyotropic LCs discussed in literature, several of these examples use nature-based LC molecules. For example, cellulose and cellulose nanocrystals,<sup>139, 140</sup> chitosan,<sup>141</sup> collagen,<sup>142</sup> and  $\alpha$ -helical polypeptides,<sup>143, 144</sup> and lipid based molecules,<sup>145</sup> to name a few. Reports of lyotropic LC nanocomposites have been rather sparse; perhaps this is due to the difficulty in chemical modification of these molecules owing to the numerous functional groups on the more complex biomolecules, in addition to the sensitivity to chemical modification if the biological activity were to be preserved.<sup>146, 147</sup>

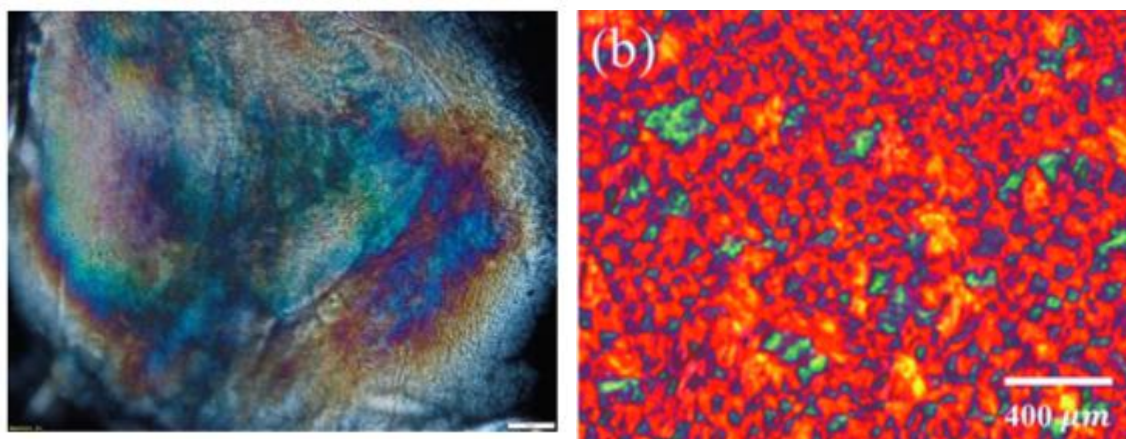


Figure 1-17: (Left) POM image of a nanocomposite comprised of hydroxypropylcellulose and cellulose nanocrystals.<sup>148</sup> (Right) POM image of single walled carbon nanotubes dispersed within a matrix of lyotropic LC surfactant molecules.<sup>149</sup>

In general, lyotropic LCs are generally comprised of NPs suspended within a matrix of one of the previous mentioned molecules. For example, carbon oxide NPs and cellulose nanocrystals have been successfully suspended within a matrix of hydroxypropylcellulose. However, lyotropic assembly was far from long range and the observed POM textures did not correspond to any LC textures.<sup>148</sup> Similarly, carbon nanotubes have been successfully dispersed into a hexagonal lyotropic LC, which did end up producing a focal conic texture (Figure 1-17).<sup>149</sup> Another commonly

seen lyotropic nanocomposite uses chemical modification of an NP core, as to disperse the NP within an LC matrix. This strategy has been effectively carried out by Russo et al., where poly( $\gamma$ -stearyl-L-glutamate) was successfully grafted onto silica NP cores. They were subsequently dispersed within a matrix of lyotropic cholesteric of the same polymer (Figure 1-18).<sup>150, 151</sup>

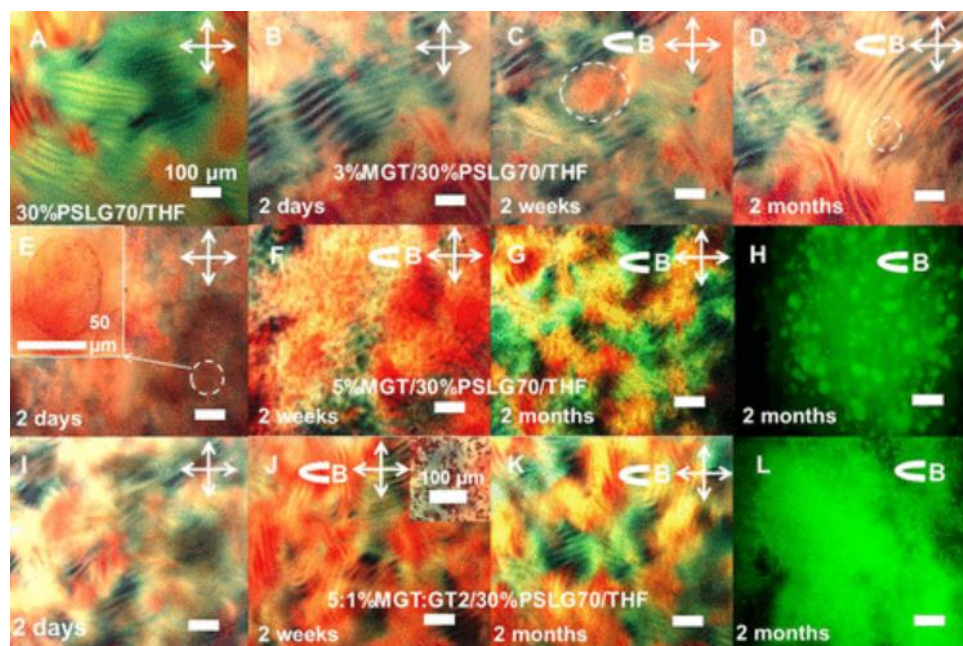


Figure 1-18: From top to bottom: Several ratios of PSLG functionalized NPs dispersed within a matrix of lyotropic cholesteric PSLG. From left to right: A ratio of the composite as measured over two months.

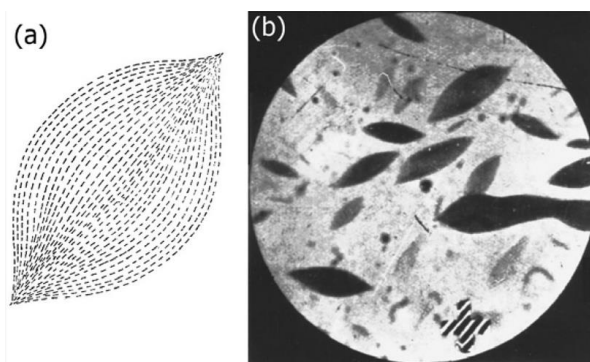


Figure 1-19: Suspensions of anisotropic  $V_2O_5$  crystallites. (left) Schematic of nematic director/ordering within a  $V_2O_5$  crystallite, (Right) Microscope image of the same crystallites. At sufficiently high concentrations, these crystallites achieve long-range order and self-assemble into lyotropic nematic LC phases.<sup>152</sup> Reproduced with permission.

Lyotropic nanocomposites can also be prepared from anisotropic colloidal particles. It follows that since all LC structures are anisotropic, the building blocks should be anisotropic as well. For example, columnar LCs are often comprised of disk-shaped molecules while nematic LCs are comprised of rod-shaped molecules. Generally, nanocomposites of this type are comprised of hard, inorganic particles, with the classic example of vanadium pentoxide,<sup>152, 153</sup> where suspensions of anisotropic crystallites self-assemble into lyotropic nematic LC phases (Figure 1-19).

In the context of this thesis, it is also important to discuss the self-assembly of isotropic particles as well. Spherical colloidal particles, including polymer grafted NPs, generally self-assemble into cubic lattices, as this type of organization represents the thermodynamic minimum.<sup>162</sup> In the case of 3D arrangements of spherical particles, this would be represented by face-centered cubic close-packing (fcc), whereas on 2D surfaces, the particles would adopt a hexagonal close-packing (hcp) arrangement.<sup>163</sup> Gold NPs (Figure 1-20),<sup>164</sup> polymer microspheres,<sup>165</sup> and block copolymer micelles<sup>166</sup> are a few examples of isotropic colloidal particles which self-assemble into cubic phases.

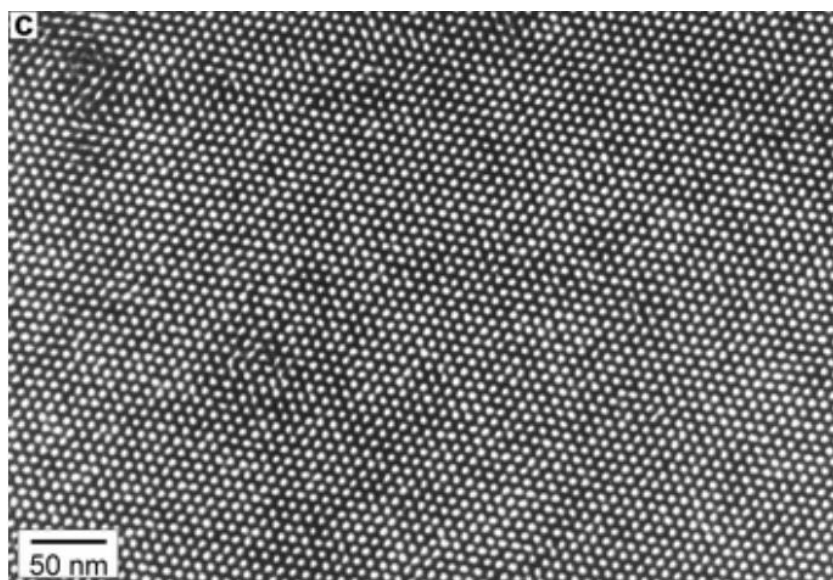


Figure 1-20: TEM micrograph of dodecane capped gold NPs, which adopts an hcp organization.<sup>164</sup>

Generally, synthesized anisotropic particles are used as dopants in existing LC phases, however it is also possible to impart LC behaviour towards these particles. For example, synthesized hematite ( $\alpha\text{-Fe}_2\text{O}_3$ ) nanorods were functionalized with polymethylmethacrylate, as to impart colloidal stability, which resulted in nematic-like ordering.<sup>154</sup> Similarly, nanodiscs were self-assembled by a ratio of a styrene-maleic acid-quaternary ammonium polymer and DMPC (a lipid), which in turn self-assembled into lyotropic nematic phases. The authors used this system towards residual dipolar coupling NMR experiments as to elucidate the structure of cytochrome c, a protein (Figure 1-21).<sup>155</sup>

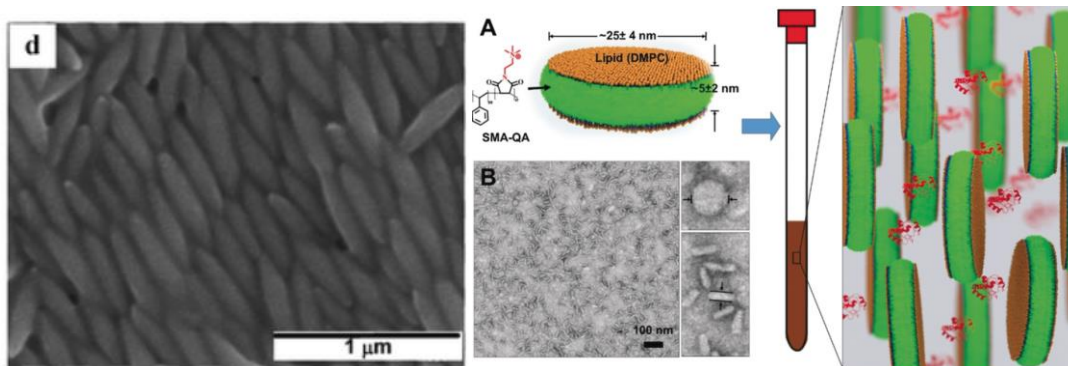


Figure 1-21: (left) Nematic-like ordering of PMMA functionalized  $\text{Fe}_2\text{O}_3$  nanorods. (right) Polymer/lipid based nanodiscs represented in (A) schematic diagram and (B) TEM images, which self-assemble into a lyotropic nematic phase towards NMR elucidation of biomolecules (rightmost schematic diagram).

## 1.5 Semi-Flexible Polymers and LC Formation

Semi-flexible polymers have properties which lie somewhere between fully flexible and fully rigid polymer systems. The flexibility/rigidity of the system is inherent to the molecular structure of the polymer. Traditionally rigid rod molecules have been quite successful in LC formation, as several methods exist towards self-assembly of these molecules i.e. the flexibility of its structure aids in self-assembly while the rigidity provides structure to the resulting architecture, both of which contribute to LC ordering.



Figure 1-22 Schematic representations of (left) flexible, (middle) semi-flexible, and (right) rigid polymers.

Formally, a polymer's flexibility is determined by its contour length relative to its persistence length, which is a measure of polymer stiffness and is inherent to the polymer's structure. In other words, whether the polymer is below, approximately equal to, or exceeds its persistence length will determine if the polymer is rigid, semi-flexible or flexible, respectively (Figure 1-22). Towards describing LC formation, many models have been proposed to varying degrees of success.

Onsager was the first to propose a model describing LC self-assembly, primarily via excluded volume effects.<sup>130</sup> In this model, the nematic molecules are described as infinitely long and infinitely rigid cylinders which will undergo phase transition from isotropic to nematic as to minimize the volume occupied by the cylinders. Upon entering the nematic phase, the increase in translational entropy is compensated for by a decrease in orientational entropy. One of the greatest successes of Onsager's theory is that the model provides an exact analytical solution while still accounting for both orientational and translational entropies upon phase transition,<sup>131</sup> which is why the model is still used and cited today.<sup>132, 133</sup> However, the largest drawback is that the theoretical treatment of polymers as infinitely long/rigid cylinders is not experimentally accurate in addition to the model not accounting for thermal effects, and consequently, Onsager's theory cannot be extended to thermotropic LCs.

In contrast, Maier and Saupe developed a model specifically for thermotropic LCs.<sup>134</sup> Through molecular mean field theory, it is possible to average all anisotropic interaction pair potentials between LC molecules and consequently, it becomes possible to locate the isotropic-

to-nematic transition temperature as well as describing the orientational order at the phase transition. Two major criticisms are often cited, firstly, the anisotropic interaction potential was experimentally confirmed to be much smaller than the value used in the theory.<sup>135</sup> Secondly, Maier-Saupe theory asserts that long-range attractive potentials are responsible for driving LC formation while disregarding short-range repulsive forces,<sup>136</sup> however, it may be possible that thermotropic LC formation is instead driven by repulsive forces.<sup>135</sup> Despite these major criticisms that have been raised, the theory continues to achieve a degree of success in explaining real nematic systems.

Towards semi-empirical solutions for lyotropic LCs, Flory describes LC structures formed by semi-flexible polymers as a cubic lattice comprised of polymer segments with axis ratio,  $x$ , described as a ratio between its polymeric length and its cross-sectional diameter (eq. 5).<sup>137</sup> This in turn, allows for an equation to determine the critical volume fraction required for LC formation ie. the isotropic-to-nematic phase transition (eq. 6).

$$x = L/d \quad (\text{eq. 5})$$

$$v_p^* \approx \left(\frac{8}{x}\right) \left(1 - \frac{2}{x}\right) \quad (\text{eq. 6})$$

Alternatively, Khoklov and Semenov,<sup>138</sup> describe semi-flexible polymers as a collection of short and stiff Kuhn segments, with a single polymer chain being comprised of  $N$  Kuhn segments (eq. 7), with the length of each Kuhn Segment being the ratio of a polymer's length to two times its persistence length. Essentially, a polymer's flexibility may be described in terms of  $N$ , where  $N > 1$  represents a semi-flexible polymer, while  $N < 1$  represents a rigid rod. From here, the critical volume fraction required for LC formation is entirely dependent on the polymer's flexibility and an analytical expression for it is shown in (eq. 8).

$$N = \frac{L}{2q} \quad (\text{eq. 7})$$

$$x_0 = \frac{12}{\left(1 - \frac{1 - \exp(-6N)}{6N}\right)} \quad (\text{eq. 8})$$

In summary, the Onsager and Maier-Saupe theory provides the most comprehensive understanding of LC formation and phase transitions. however, towards experimentally observed LC behaviour, Flory and Kohklov/Semenov's theories become more practical in the lab setting.

## 1.6 Conclusions and Future Outlook

This introduction chapter seeks to survey and summarize the abundance and diversity of literature on various LC composite systems. While the examples are by no means exhaustive, they serve to highlight common design motifs and structures of as well as potential applications that have previously been reported in literature.

The subsequent thesis chapters will discuss a new type of LC composite, where polymers with known LC behaviour are grafted onto spherical nanoparticles. To our knowledge, liquid crystalline behaviour has yet to be reported for polymer grafted isotropic nanoparticles. In this new composite, LC behaviour is derived from structural features inherent to the selected polymer, which is further aided upon anchoring onto the nanoparticles through efficient polymer packing and high grafting densities. The rationale is to circumvent the complexity of ternary, quaternary (and above) LC systems, which is why polymers with known LC behaviour were chosen rather than LC ligands, which are often expensive and synthetically complex (even more so if the LC molecule requires further chemical modifications). Additionally, this design scheme offers an alternative to NPs functionalized with LC ligands, which have the advantage of improved colloidal stability and the property of relatively simple chemical synthesis/modification inherent to polymers. To this end, semi-flexible polymers are great candidates toward these new nanoparticles due to the known and extensively researched LC behaviour.<sup>156, 157</sup>

To date, few semi-flexible polymer functionalized NPs have been synthesized and of the NPs that have been reported, the NPs often require other external factors to become LC. For example, single walled carbon nanotubes functionalized with poly( $\gamma$ -benzyl-L-glutamate) (PBLG) require that the PBLG coated nanotubes be dispersed in a PBLG solution with existing LC behaviour, which drastically lowered critical LC concentration.<sup>158</sup> Similarly, polyaniline functionalized cellulose nanocrystals exhibited cholesteric LC behaviour only when an aniline/HCl solution was added to aid in LC formation.<sup>159</sup> Furthermore, polymer functionalized anisotropic particles required anisotropy to be “pre-programmed” into the nanocomposite. Many examples of these NP-LC composites exist, however, NPs which generate LC behaviour without further

intervention have not been reported prior to our work. Additionally, to our knowledge, there have not been any reports of self-assembled anisotropic behaviour from isotropic building blocks.

Towards generating anisotropic architectures from isotropic building blocks, the premise of this thesis is the synthesis of semi-flexible polymer functionalized nanomaterials. The use of semi-flexible polymers is intuitive, as polymers in this regime are flexible enough for self-assembly, while having the rigidity to support complex anisotropic architectures.

In each subsequent chapter, several LC composites of this were designed, synthesized, and demonstrated to exhibit LC character using chosen polymers with LC properties. A special focus was given to semi-flexible polymers, which have been extensively discussed in literature.

Poly (hexyl-isocyanate) (PHIC) is one such polymer, where semi-flexibility arises due to partial double bond character across the main polymer chain and sterically bulky hexyl side chains. Overall, these two conflicting factors produce a semi-flexible polymer with a twisting along the polymer backbone. Lyotropic nematic LC systems have been reported for PHIC primarily in organic solvents, with cholesteric LCs also possible through chiral doping. **Chapter 2** will demonstrate the surprising LC behaviour of spherical zirconia nanoparticles grafted with PHIC.

Poly( $\gamma$ -benzyl-L-glutamate) (PBLG) is a polypeptide, where its semi-flexibility arises from its  $\alpha$ -helix structure. The twisting of the benzyl side chains about the  $\alpha$ -helix gives rise to chirality and consequently to lyotropic cholesteric LCs. Characterization of LC phases formed by PBLG functionalized nanoparticles are discussed in **Chapter 3**.

Poly( $\gamma$ -stearyl-L-glutamate) (PSLG) is similarly a semi-flexible polymer due to its polypeptide nature. However, the presence of the stearyl side chains enable “thermotropic” LC behaviour. Unlike traditional thermotropic LCs, where heating sends the material into an isotropic phase and LC behaviour is observed upon cooling, LC phases of PSLG assemble upon

heating. This is due to the melt behaviour of the paraffinic stearyl side chains. At sufficiently high temperatures, the stearyl side chains become liquid-like to solvate the polypeptide core, which in turn enables self-assembly of LC cholesteric phases. NP composites using PSLG will be further elaborated upon in **Chapter 4**.

Lastly, **Chapter 5** will overview a discussion of the findings of all the previous chapters together, along with potential future outlooks/perspectives. Overall, the present thesis seeks to demonstrate that a series of new nanoparticle composites comprised of polymers with known LC behaviour can achieve various desirable LC properties. By grafting LC polymers onto spherical nanoparticles, it thus becomes possible to mimic and tune LC behaviour over a wide range of interest to a variety of applications.

## 1.7 References

- (1) Feldman, D. Polymer History. *Designed Monomers and Polymers* **2008**, *11* (1), 1-15. DOI: 10.1163/156855508X292383.
- (2) Brydson, J. A. *Plastics materials*; Elsevier, 1999.
- (3) Alexander, M. Environmental and microbiological problems arising from recalcitrant molecules. *Microbial Ecology* **1975**, *2* (1), 17-27. DOI: 10.1007/BF02010378.
- (4) Eubeler, J. P.; Bernhard, M.; Knepper, T. P. Environmental biodegradation of synthetic polymers II. Biodegradation of different polymer groups. *TrAC Trends in Analytical Chemistry* **2010**, *29* (1), 84-100. DOI: <https://doi.org/10.1016/j.trac.2009.09.005>.
- (5) *Plastics - The Facts 2022*; PlasticsEurope Brussels, 2022.
- (6) Otake, Y.; Kobayashi, T.; Asabe, H.; Murakami, N.; Ono, K. Biodegradation of low-density polyethylene, polystyrene, polyvinyl chloride, and urea formaldehyde resin buried under soil for over 32 years. *Journal of Applied Polymer Science* **1995**, *56* (13), 1789-1796. DOI: <https://doi.org/10.1002/app.1995.070561309>.
- (7) Ekanayaka, A. H.; Tibpromma, S.; Dai, D.; Xu, R.; Suwannarach, N.; Stephenson, S. L.; Dao, C.; Karunarathna, S. C. A review of the fungi that degrade plastic. *Journal of fungi* **2022**, *8* (8), 772.
- (8) Zhu, B.; Wang, D.; Wei, N. Enzyme discovery and engineering for sustainable plastic recycling. *Trends in biotechnology* **2022**, *40* (1), 22-37.
- (9) Tournier, V.; Duquesne, S.; Guillaumot, F.; Cramail, H.; Taton, D.; Marty, A.; André, I. Enzymes' power for plastics degradation. *Chemical Reviews* **2023**, *123* (9), 5612-5701.
- (10) Ayre, D. Technology advancing polymers and polymer composites towards sustainability: A review. *Current Opinion in Green and Sustainable Chemistry* **2018**, *13*, 108-112.
- (11) Zhu, Y.; Romain, C.; Williams, C. K. Sustainable polymers from renewable resources. *Nature* **2016**, *540* (7633), 354-362.
- (12) Dubé, M. A.; Gabriel, V. A.; Pakdel, A. S.; Zhang, Y. Sustainable polymer reaction engineering: Are we there yet? *The Canadian Journal of Chemical Engineering* **2021**, *99* (1), 31-60.

- (13) Zhang, D.; del Rio-Chanona, E. A.; Shah, N. Screening synthesis pathways for biomass-derived sustainable polymer production. *ACS Sustainable Chemistry & Engineering* **2017**, *5* (5), 4388-4398.
- (14) Li, Y.; Wang, S.; Wang, Q.; Xing, M. A comparison study on mechanical properties of polymer composites reinforced by carbon nanotubes and graphene sheet. *Composites Part B: Engineering* **2018**, *133*, 35-41.
- (15) Liu, R.; Peng, Y.; Cao, J.; Chen, Y. Comparison on properties of lignocellulosic flour/polymer composites by using wood, cellulose, and lignin flours as fillers. *Composites Science and Technology* **2014**, *103*, 1-7.
- (16) Nambiar, S.; Yeow, J. T. Polymer-composite materials for radiation protection. *ACS applied materials & interfaces* **2012**, *4* (11), 5717-5726.
- (17) Das, A.; Stöckelhuber, K.; Jurk, R.; Saphiannikova, M.; Fritzsche, J.; Lorenz, H.; Klüppel, M.; Heinrich, G. Modified and unmodified multiwalled carbon nanotubes in high performance solution-styrene-butadiene and butadiene rubber blends. *Polymer* **2008**, *49* (24), 5276-5283.
- (18) Toriz, G.; Denes, F.; Young, R. Lignin-polypropylene composites. Part 1: Composites from unmodified lignin and polypropylene. *Polymer Composites* **2002**, *23* (5), 806-813.
- (19) Kim, K.; Zhu, W.; Qu, X.; Aaronson, C.; McCall, W. R.; Chen, S.; Sirbuly, D. J. 3D optical printing of piezoelectric nanoparticle-polymer composite materials. *ACS nano* **2014**, *8* (10), 9799-9806.
- (20) Chen, S.; Cao, Y.; Feng, J. Polydopamine as an efficient and robust platform to functionalize carbon fiber for high-performance polymer composites. *ACS Applied Materials & Interfaces* **2014**, *6* (1), 349-356.
- (21) Nee, A. Y. C. *Handbook of manufacturing engineering and technology*; Springer Publishing Company, Incorporated, 2014.
- (22) Jesson, D. A.; Watts, J. F. The Interface and Interphase in Polymer Matrix Composites: Effect on Mechanical Properties and Methods for Identification. *Polymer Reviews* **2012**, *52* (3), 321-354. DOI: 10.1080/15583724.2012.710288.
- (23) Testa, A. M.; Foglia, S.; Suber, L.; Fiorani, D.; Casas, L.; Roig, A.; Molins, E.; Grenèche, J. M.; Tejada, J. Unconventional magnetic behavior of iron-oxide nanoparticles in polymeric matrices.

*Journal of Applied Physics* **2001**, *90* (3), 1534-1539. DOI: 10.1063/1.1383019 (accessed 9/20/2023).

(24) Pirmoradi, F. N.; Cheng, L.; Chiao, M. A magnetic poly (dimethylesiloxane) composite membrane incorporated with uniformly dispersed, coated iron oxide nanoparticles. *Journal of Micromechanics and Microengineering* **2009**, *20* (1), 015032.

(25) Rankin, S. M.; Moody, M. K.; Naskar, A. K.; Bowland, C. C. Enhancing functionalities in carbon fiber composites by titanium dioxide nanoparticles. *Composites Science and Technology* **2021**, *201*, 108491.

(26) Sabir, A.; Islam, A.; Shafiq, M.; Shafeeq, A.; Butt, M. T. Z.; Ahmad, N. M.; Sanaullah, K.; Jamil, T. Novel polymer matrix composite membrane doped with fumed silica particles for reverse osmosis desalination. *Desalination* **2015**, *368*, 159-170.

(27) Corbierre, M. K.; Cameron, N. S.; Sutton, M.; Mochrie, S. G.; Lurio, L. B.; Rühm, A.; Lennox, R. B. Polymer-stabilized gold nanoparticles and their incorporation into polymer matrices. *Journal of the American Chemical Society* **2001**, *123* (42), 10411-10412.

(28) Ahmed, R.; El-Bashir, S. Structure and physical properties of polymer composite films doped with fullerene nanoparticles. *International Journal of Photoenergy* **2011**, *2011*.

(29) Nilagiri Balasubramanian, K. B.; Ramesh, T. Role, effect, and influences of micro and nano-fillers on various properties of polymer matrix composites for microelectronics: A review. *Polymers for Advanced Technologies* **2018**, *29* (6), 1568-1585. DOI: <https://doi.org/10.1002/pat.4280>.

(30) Pukanszky, B.; VÖRÖS, G. Mechanism of interfacial interactions in particulate filled composites. *Composite Interfaces* **1993**, *1* (5), 411-427.

(31) Kango, S.; Kalia, S.; Celli, A.; Njuguna, J.; Habibi, Y.; Kumar, R. Surface modification of inorganic nanoparticles for development of organic–inorganic nanocomposites—A review. *Progress in Polymer Science* **2013**, *38* (8), 1232-1261.

(32) Yang, H.; Zhang, Q.; Guo, M.; Wang, C.; Du, R.; Fu, Q. Study on the phase structures and toughening mechanism in PP/EPDM/SiO<sub>2</sub> ternary composites. *Polymer* **2006**, *47* (6), 2106-2115.

(33) Sato, A.; Kabusaki, D.; Okumura, H.; Nakatani, T.; Nakatsubo, F.; Yano, H. Surface modification of cellulose nanofibers with alkenyl succinic anhydride for high-density

polyethylene reinforcement. *Composites Part A: Applied Science and Manufacturing* **2016**, *83*, 72-79.

(34) Wang, L.; Okada, K.; Sodenaga, M.; Hikima, Y.; Ohshima, M.; Sekiguchi, T.; Yano, H. Effect of surface modification on the dispersion, rheological behavior, crystallization kinetics, and foaming ability of polypropylene/cellulose nanofiber nanocomposites. *Composites Science and Technology* **2018**, *168*, 412-419.

(35) Cao, J.-P.; Zhao, J.; Zhao, X.; Hu, G.-H.; Dang, Z.-M. Preparation and characterization of surface modified silicon carbide/polystyrene nanocomposites. *Journal of Applied Polymer Science* **2013**, *130* (1), 638-644. DOI: <https://doi.org/10.1002/app.39186>.

(36) Caragheorghopol, A.; Chechik, V. Mechanistic aspects of ligand exchange in Au nanoparticles. *Physical Chemistry Chemical Physics* **2008**, *10* (33), 5029-5041.

(37) Kamibayashi, M.; Ogura, H.; Otsubo, Y. Shear-thickening flow of nanoparticle suspensions flocculated by polymer bridging. *Journal of colloid and interface science* **2008**, *321* (2), 294-301.

(38) Surve, M.; Pryamitsyn, V.; Ganesan, V. Polymer-bridged gels of nanoparticles in solutions of adsorbing polymers. *The Journal of chemical physics* **2006**, *125* (6).

(39) Neouze, M.-A.; Schubert, U. Surface modification and functionalization of metal and metal oxide nanoparticles by organic ligands. *Monatshefte für Chemie-Chemical Monthly* **2008**, *139*, 183-195.

(40) Liu, B.; Liu, J. Surface modification of nanozymes. *Nano Research* **2017**, *10*, 1125-1148.

(41) Talebzadeh, S.; Queffélec, C.; Knight, D. A. Surface modification of plasmonic noble metal-metal oxide core-shell nanoparticles. *Nanoscale Advances* **2019**, *1* (12), 4578-4591.

(42) Ahangaran, F.; Navarchian, A. H. Recent advances in chemical surface modification of metal oxide nanoparticles with silane coupling agents: A review. *Advances in Colloid and Interface Science* **2020**, *286*, 102298.

(43) Chou, L. Y.; Chan, W. C. Fluorescence-tagged gold nanoparticles for rapidly characterizing the size-dependent biodistribution in tumor models. *Advanced healthcare materials* **2012**, *1* (6), 714-721.

(44) Cheon, J.; Lee, J.-H. Synergistically integrated nanoparticles as multimodal probes for nanobiotechnology. *Accounts of chemical research* **2008**, *41* (12), 1630-1640.

- (45) Ellairaja, S.; Krithiga, N.; Ponmariappan, S.; Vasantha, V. S. Novel pyrimidine tagged silver nanoparticle based fluorescent immunoassay for the detection of *Pseudomonas aeruginosa*. *Journal of Agricultural and Food Chemistry* **2017**, *65* (8), 1802-1812.
- (46) Mitomo, H.; Ijio, K. Controlled nanostructures fabricated by the self-assembly of gold nanoparticles via simple surface modifications. *Bulletin of the Chemical Society of Japan* **2021**, *94* (4), 1300-1310.
- (47) Song, C.; Sun, W.; Xiao, Y.; Shi, X. Ultrasmall iron oxide nanoparticles: Synthesis, surface modification, assembly, and biomedical applications. *Drug discovery today* **2019**, *24* (3), 835-844.
- (48) Storm, G.; Belliot, S. O.; Daemen, T.; Lasic, D. D. Surface modification of nanoparticles to oppose uptake by the mononuclear phagocyte system. *Advanced drug delivery reviews* **1995**, *17* (1), 31-48.
- (49) Berger, S.; Synytska, A.; Ionov, L.; Eichhorn, K.-J.; Stamm, M. Stimuli-responsive bicomponent polymer janus particles by “grafting from”/“grafting to” approaches. *Macromolecules* **2008**, *41* (24), 9669-9676.
- (50) Hansson, S.; Trouillet, V.; Tischer, T.; Goldmann, A. S.; Carlmark, A.; Barner-Kowollik, C.; Malmström, E. Grafting efficiency of synthetic polymers onto biomaterials: A comparative study of grafting-from versus grafting-to. *Biomacromolecules* **2013**, *14* (1), 64-74.
- (51) Boujemaoui, A.; Cobo Sanchez, C.; Engström, J.; Bruce, C.; Fogelström, L.; Carlmark, A.; Malmström, E. Polycaprolactone nanocomposites reinforced with cellulose nanocrystals surface-modified via covalent grafting or physisorption: A comparative study. *ACS applied materials & interfaces* **2017**, *9* (40), 35305-35318.
- (52) Wang, Y.; Quinsaat, J. E. Q.; Ono, T.; Maeki, M.; Tokeshi, M.; Isono, T.; Tajima, K.; Satoh, T.; Sato, S.-i.; Miura, Y. Enhanced dispersion stability of gold nanoparticles by the physisorption of cyclic poly (ethylene glycol). *Nature communications* **2020**, *11* (1), 6089.
- (53) Ueno, K.; Inaba, A.; Kondoh, M.; Watanabe, M. Colloidal stability of bare and polymer-grafted silica nanoparticles in ionic liquids. *Langmuir* **2008**, *24* (10), 5253-5259.
- (54) Kan, K. H.; Li, J.; Wijesekera, K.; Cranston, E. D. Polymer-grafted cellulose nanocrystals as pH-responsive reversible flocculants. *Biomacromolecules* **2013**, *14* (9), 3130-3139.

- (55) Perez-Potti, A.; Lopez, H.; Pelaz, B.; Abdelmonem, A.; Soliman, M. G.; Schoen, I.; Kelly, P. M.; Dawson, K. A.; Parak, W. J.; Krpetic, Z. In depth characterisation of the biomolecular coronas of polymer coated inorganic nanoparticles with differential centrifugal sedimentation. *Scientific Reports* **2021**, *11* (1), 6443.
- (56) Mittal, V.; Lechner, M. Size and density dependent sedimentation analysis of advanced nanoparticle systems. *Journal of colloid and interface science* **2010**, *346* (2), 378-383.
- (57) Stamatoiu, O.; Mirzaei, J.; Feng, X.; Hegmann, T. Nanoparticles in liquid crystals and liquid crystalline nanoparticles. *Liquid crystals: materials design and self-assembly* **2012**, 331-393.
- (58) Green, M. Solution routes to III–V semiconductor quantum dots. *Current Opinion in Solid State and Materials Science* **2002**, *6* (4), 355-363.
- (59) Murray, C.; Norris, D. J.; Bawendi, M. G. Synthesis and characterization of nearly monodisperse CdE (E= sulfur, selenium, tellurium) semiconductor nanocrystallites. *Journal of the American Chemical Society* **1993**, *115* (19), 8706-8715.
- (60) Green, M.; O'Brien, P. Recent advances in the preparation of semiconductors as isolated nanometric particles: new routes to quantum dots. *Chemical Communications* **1999**, (22), 2235-2241.
- (61) Darbandi, M.; Thomann, R.; Nann, T. Single quantum dots in silica spheres by microemulsion synthesis. *Chemistry of Materials* **2005**, *17* (23), 5720-5725.
- (62) Dubois, F.; Mahler, B.; Dubertret, B.; Doris, E.; Mioskowski, C. A versatile strategy for quantum dot ligand exchange. *Journal of the American Chemical Society* **2007**, *129* (3), 482-483.
- (63) Erathodiyil, N.; Ying, J. Y. Functionalization of inorganic nanoparticles for bioimaging applications. *Accounts of chemical research* **2011**, *44* (10), 925-935.
- (64) Ireland, P.; Jones, T. The response time of a surface thermometer employing encapsulated thermochromic liquid crystals. *Journal of Physics E: Scientific Instruments* **1987**, *20* (10), 1195.
- (65) Popov, P.; Mann, E. K.; Jáklí, A. Thermotropic liquid crystal films for biosensors and beyond. *Journal of Materials Chemistry B* **2017**, *5* (26), 5061-5078.
- (66) Abell, P. Improved laces for use with footwear, sports equipment and the like. Google Patents: 2011.

- (67) Efron, U.; Grinberg, J.; Braatz, P.; Little, M.; Reif, P.; Schwartz, R. The silicon liquid-crystal light valve. *Journal of applied physics* **1985**, *57* (4), 1356-1368.
- (68) Cupelli, D.; Nicoletta, F. P.; Manfredi, S.; Vivacqua, M.; Formoso, P.; De Filpo, G.; Chidichimo, G. Self-adjusting smart windows based on polymer-dispersed liquid crystals. *Solar Energy Materials and Solar Cells* **2009**, *93* (11), 2008-2012.
- (69) Gray, G. W.; Harrison, K. J.; Nash, J. New family of nematic liquid crystals for displays. *Electronics Letters* **1973**, *6* (9), 130-131.
- (70) Lucchetti, L.; Fraccia, T. P.; Ciciulla, F.; Simoni, F.; Bellini, T. Giant optical nonlinearity in DNA lyotropic liquid crystals. *Optics Express* **2017**, *25* (21), 25951-25959.
- (71) Lucchetti, L.; Fraccia, T. P.; Nava, G.; Turiv, T.; Ciciulla, F.; Bethge, L.; Klusmann, S.; Lavrentovich, O. D.; Bellini, T. Elasticity and viscosity of DNA liquid crystals. *ACS Macro Letters* **2020**, *9* (7), 1034-1039.
- (72) Garbovskiy, Y. A.; Glushchenko, A. V. Liquid Crystalline Colloids of Nanoparticles: Preparation, Properties, and Applications. In *Solid State Physics*, Camley, R. E., Stamps, R. L. Eds.; Vol. 62; Academic Press, 2010; pp 1-74.
- (73) Nagaraj, M. Liquid Crystals Templating. *Crystals* **2020**, *10* (8), 648.
- (74) Oldenbourg, R. Polarized light microscopy: principles and practice. *Cold Spring Harbor Protocols* **2013**, *2013* (11), pdb. top078600.
- (75) Carlton, R. A.; Carlton, R. A. Polarized light microscopy. *Pharmaceutical microscopy* **2011**, 7-64.
- (76) Color Plates. In *Textures of Liquid Crystals*, 2003; pp 167-212.
- (77) Anthamatten, M.; Zheng, W. Y.; Hammond, P. T. A morphological study of well-defined smectic side-chain LC block copolymers. *Macromolecules* **1999**, *32* (15), 4838-4848.
- (78) Freiburger, N.; Glatter, O. Small-Angle Scattering from Hexagonal Liquid Crystals. *The Journal of Physical Chemistry B* **2006**, *110* (30), 14719-14727. DOI: 10.1021/jp0559332.
- (79) Larsen, A. H.; Brookes, E.; Pedersen, M. C.; Kirkensgaard, J. J. K. Shape2SAS: a web application to simulate small-angle scattering data and pair distance distributions from user-defined shapes. *Journal of Applied Crystallography* **2023**, *56* (4), 1287-1294.

- (80) Pizzey, C.; Klein, S.; Leach, E.; van Duijneveldt, J. S.; Richardson, R. M. Suspensions of colloidal plates in a nematic liquid crystal: a small angle x-ray scattering study. *Journal of Physics: Condensed Matter* **2004**, *16* (15), 2479.
- (81) Toquer, G.; Porte, G.; Nobili, M.; Appell, J.; Blanc, C. Lyotropic structures in a thermotropic liquid crystal. *Langmuir* **2007**, *23* (7), 4081-4087.
- (82) Castelletto, V.; Squires, A.; Hamley, I.; Stasiak, J.; Moggridge, G. A SAXS study of flow alignment of thermotropic liquid crystal mixtures. *Liquid Crystals* **2009**, *36* (4), 435-442.
- (83) Kabata, D.; Ryoki, A.; Kitamura, S.; Terao, K. Chain Alignment of a Rigid Ring Polymer in the Lyotropic Liquid Crystal Phase: Cyclic Amylose Tris (n-butylcarbamate) in Tetrahydrofuran and Ethyl Lactate. *Macromolecules* **2021**, *54* (23), 10723-10729.
- (84) Prasad, S. K.; Kumar, M. V.; Shilpa, T.; Yelamaggad, C. Enhancement of electrical conductivity, dielectric anisotropy and director relaxation frequency in composites of gold nanoparticle and a weakly polar nematic liquid crystal. *RSC Advances* **2014**, *4* (9), 4453-4462.
- (85) Khatua, S.; Manna, P.; Chang, W.-S.; Tcherniak, A.; Friedlander, E.; Zubarev, E. R.; Link, S. Plasmonic nanoparticles– liquid crystal composites. *The Journal of Physical Chemistry C* **2010**, *114* (16), 7251-7257.
- (86) Podoliak, N.; Bartczak, D.; Buchnev, O.; Kanaras, A. G.; Kaczmarek, M. High Optical Nonlinearity of Nematic Liquid Crystals Doped with Gold Nanoparticles. *The Journal of Physical Chemistry C* **2012**, *116* (23), 12934-12939. DOI: 10.1021/jp302558c.
- (87) Vardanyan, K. K.; Walton, R. D.; Bubb, D. M. Liquid crystal composites with a high percentage of gold nanoparticles. *Liquid Crystals* **2011**, *38* (10), 1279-1287. DOI: 10.1080/02678292.2011.610469.
- (88) Hsu, C.-J.; Lin, L.-J.; Huang, M.-K.; Huang, C.-Y. Electro-optical effect of gold nanoparticle dispersed in nematic liquid crystals. *Crystals* **2017**, *7* (10), 287.
- (89) Kaur, S.; Singh, S. P.; Biradar, A. M.; Choudhary, A.; Sreenivas, K. Enhanced electro-optical properties in gold nanoparticles doped ferroelectric liquid crystals. *Applied Physics Letters* **2007**, *91* (2). DOI: 10.1063/1.2756136 (accessed 10/21/2023).

- (90) Krishna Prasad, S.; Sandhya, K.; Nair, G. G.; Hiremath, U. S.; Yelamaggad, C.; Sampath, S. Electrical conductivity and dielectric constant measurements of liquid crystal–gold nanoparticle composites. *Liquid crystals* **2006**, *33* (10), 1121-1125.
- (91) Liu, X.; Qi, G.; Park, A. M. G.; Rodriguez-Gonzalez, A.; Enotiadis, A.; Pan, W.; Kosma, V.; Fuchs, G. D.; Kirby, B. J.; Giannelis, E. P. Scalable synthesis of switchable assemblies of gold nanorod lyotropic liquid crystal nanocomposites. *Small* **2019**, *15* (22), 1901666.
- (92) Mishra, S.; V, M.; Gupta, R. K. Zinc Oleate Nanorod-Induced Vertical Alignment of Nematic Liquid Crystal. *ACS omega* **2022**, *7* (50), 46466-46474.
- (93) Mishra, S.; Sontakke, A.; Gupta, R.; Kumar, S.; Manjuladevi, V. Dielectric spectroscopy studies of silver nanorod doped nematic liquid crystal. *Materials Today: Proceedings* **2022**, *50*, 2587-2591.
- (94) Kumar, M.; Varshney, S.; Gowda, A.; Kumar, S. Silver nanodisks in soft discotic forest: Impact on self-assembly, conductivity and molecular packing. *Journal of Molecular Liquids* **2017**, *241*, 666-674.
- (95) Kamaliya, B.; Vijay Kumar, M.; Yelamaggad, C.; Krishna Prasad, S. Enhancement of electrical conductivity of a liquid crystal-gold nanoparticle composite by a gel network of aerosil particles. *Applied Physics Letters* **2015**, *106* (8).
- (96) Gowda, A.; Kumar, S. Recent advances in discotic liquid crystal-assisted nanoparticles. *Materials* **2018**, *11* (3), 382.
- (97) Sridevi, S.; Prasad, S. K.; Nair, G. G.; D'Britto, V.; Prasad, B. Enhancement of anisotropic conductivity, elastic, and dielectric constants in a liquid crystal-gold nanorod system. *Applied Physics Letters* **2010**, *97* (15).
- (98) Jiang, Z.; Zheng, J.; Liu, Y.; Zhu, Q. Investigation of dielectric properties in polymer dispersed liquid crystal films doped with CuO nanorods. *Journal of Molecular Liquids* **2019**, *295*, 111667.
- (99) Garbovskiy, Y. A.; Glushchenko, A. V. Liquid crystalline colloids of nanoparticles: preparation, properties, and applications. *Solid State Physics* **2010**, *62*, 1-74.
- (100) Haga, H.; Garland, C. W. Effect of silica aerosil particles on liquid-crystal phase transitions. *Physical Review E* **1997**, *56* (3), 3044.

- (101) Hourri, A.; Bose, T.; Thoen, J. Effect of silica aerosil dispersions on the dielectric properties of a nematic liquid crystal. *Physical Review E* **2001**, *63* (5), 051702.
- (102) Li, L.-s.; Walda, J.; Manna, L.; Alivisatos, A. P. Semiconductor nanorod liquid crystals. *Nano Letters* **2002**, *2* (6), 557-560.
- (103) García-Cámara, B.; Algorri, J. F.; Urruchi, V.; Sánchez-Pena, J. M. Directional scattering of semiconductor nanoparticles embedded in a liquid crystal. *Materials* **2014**, *7* (4), 2784-2794.
- (104) Qi, H.; Kinkead, B.; Hegmann, T. Effects of functionalized metal and semiconductor nanoparticles in nematic liquid crystal phases. In *Emerging Liquid Crystal Technologies III*, 2008; SPIE: Vol. 6911, pp 38-48.
- (105) Dierking, I.; Scalia, G.; Morales, P. Liquid crystal–carbon nanotube dispersions. *Journal of Applied Physics* **2005**, *97* (4).
- (106) Lagerwall, J. P.; Scalia, G. Carbon nanotubes in liquid crystals. *Journal of Materials Chemistry* **2008**, *18* (25), 2890-2898.
- (107) Millette, J.; Relaix, S.; Lavigne, C.; Toader, V.; Cowling, S. J.; Saez, I. M.; Lennox, R. B.; Goodby, J. W.; Reven, L. Reversible long-range patterning of gold nanoparticles by smectic liquid crystals. *Soft Matter* **2012**, *8* (24), 6593-6598.
- (108) Yoshida, H.; Kawamoto, K.; Kubo, H.; Tsuda, T.; Fujii, A.; Kuwabata, S.; Ozaki, M. Nanoparticle-Dispersed Liquid Crystals Fabricated by Sputter Doping. *Advanced Materials* **2010**, *22* (5), 622-626.
- (109) Pishnyak, O.; Tang, S.; Kelly, J.; Shiyankovskii, S.; Lavrentovich, O. Electrically induced dynamics of colloidal particles dispersed in nematic liquid crystal. *Ukr. J. Phys* **2009**, *54*, 101-108.
- (110) Mitov, M.; Bourgerette, C.; De Guerville, F. Fingerprint patterning of solid nanoparticles embedded in a cholesteric liquid crystal. *Journal of Physics: Condensed Matter* **2004**, *16* (19), S1981.
- (111) Mitov, M.; Portet, C.; Bourgerette, C.; Snoeck, E.; Verelst, M. Long-range structuring of nanoparticles by mimicry of a cholesteric liquid crystal. *Nature materials* **2002**, *1* (4), 229-231.
- (112) Coates, D. Polymer-dispersed liquid crystals. *Journal of Materials Chemistry* **1995**, *5* (12), 2063-2072.

- (113) Bronnikov, S.; Kostromin, S.; Zuev, V. Polymer-dispersed liquid crystals: progress in preparation, investigation, and application. *Journal of Macromolecular Science, Part B* **2013**, *52* (12), 1718-1735.
- (114) Liu, Y.; Sun, X. Holographic polymer-dispersed liquid crystals: materials, formation, and applications. *Advances in OptoElectronics* **2008**, *2008*.
- (115) West, J. L. Phase separation of liquid crystals in polymers. *Molecular Crystals and Liquid Crystals Incorporating Nonlinear Optics* **1988**, *157* (1), 427-441.
- (116) Serbutoviez, C.; Kloosterboer, J.; Boots, H.; Touwslager, F. Polymerization-induced phase separation. 2. Morphology of polymer-dispersed liquid crystal thin films. *Macromolecules* **1996**, *29* (24), 7690-7698.
- (117) Justice, R. S.; Schaefer, D. W.; Vaia, R. A.; Tomlin, D. W.; Bunning, T. J. Interface morphology and phase separation in polymer-dispersed liquid crystal composites. *Polymer* **2005**, *46* (12), 4465-4473.
- (118) Mucha, M. Polymer as an important component of blends and composites with liquid crystals. *Progress in Polymer Science* **2003**, *28* (5), 837-873. DOI: [https://doi.org/10.1016/S0079-6700\(02\)00117-X](https://doi.org/10.1016/S0079-6700(02)00117-X).
- (119) Patwardhan, A. A.; Belfiore, L. A. Thermodynamic miscibility of polymer-liquid crystal blends. *Polymer Engineering & Science* **1988**, *28* (14), 916-925.
- (120) Loudet, J.-C.; Barois, P.; Poulin, P. Colloidal ordering from phase separation in a liquid-crystalline continuous phase. *Nature* **2000**, *407* (6804), 611-613.
- (121) Shen, J.; Lin, H.; Ren, Y.; Sun, C.; Bao, J.; Xiao, J.; Gao, Y. Effect of Polymer Network Morphology on the Performance of Polymer Dispersed Liquid Crystal (PDLC) Composite Films. *Journal of Wuhan University of Technology-Mater. Sci. Ed.* **2022**, *37* (5), 1020-1024.
- (122) Drzaic, P. S. Droplet density, droplet size, and wavelength effects in PDLC light scattering. *Molecular Crystals and Liquid Crystals Science and Technology. Section A. Molecular Crystals and Liquid Crystals* **1995**, *261* (1), 383-392.
- (123) Kularatne, R. S.; Kim, H.; Boothby, J. M.; Ware, T. H. Liquid crystal elastomer actuators: Synthesis, alignment, and applications. *Journal of Polymer Science Part B: Polymer Physics* **2017**, *55* (5), 395-411. DOI: <https://doi.org/10.1002/polb.24287>.

- (124) Zentel, R. LC-elastomers: structure -property relations and concepts to improve applicability. *Liquid Crystals* **2023**, *50* (7-10), 1129-1142. DOI: 10.1080/02678292.2022.2142882.
- (125) Barclay, G. G.; Ober, C. K. Liquid crystalline and rigid-rod networks. *Progress in Polymer Science* **1993**, *18* (5), 899-945. DOI: [https://doi.org/10.1016/0079-6700\(93\)90021-4](https://doi.org/10.1016/0079-6700(93)90021-4).
- (126) Yaroshchuk, O. V.; Dolgov, L. O.; Kiselev, A. D. Electro-optics and structural peculiarities of liquid crystal–nanoparticle–polymer composites. *Physical Review E* **2005**, *72* (5), 051715.
- (127) Gridyakina, A.; Kasian, N.; Chychłowski, M. S.; Kajkowska, M.; Lesiak, P. Advances in multicomponent systems: Liquid crystal/nanoparticles/polymer. *Materials Today Physics* **2023**, *38*, 101258. DOI: <https://doi.org/10.1016/j.mtphys.2023.101258>.
- (128) Zhang, Y.; Liu, Q.; Mundoor, H.; Yuan, Y.; Smalyukh, I. I. Metal nanoparticle dispersion, alignment, and assembly in nematic liquid crystals for applications in switchable plasmonic color filters and E-polarizers. *Acs Nano* **2015**, *9* (3), 3097-3108.
- (129) Lee, G.; Park, G.; Park, J. G.; Bak, Y.; Lee, C.; Yoon, D. K. Universal Strategy for Inorganic Nanoparticle Incorporation into Mesoporous Liquid Crystal Polymer Particles. *Advanced Materials* **2023**, 2307388.
- (130) Onsager, L. The effects of shape on the interaction of colloidal particles. *Annals of the New York Academy of Sciences* **1949**, *51* (4), 627-659.
- (131) Frenkel, D. Onsager's spherocylinders revisited. *Journal of physical chemistry* **1987**, *91* (19), 4912-4916.
- (132) De Filippo, C. A.; Del Galdo, S.; Corsi, P.; De Michele, C.; Capone, B. On the role of polydispersity on the phase diagram of colloidal rods. *Soft Matter* **2023**, *19* (9), 1732-1738.
- (133) Xu, Y.; Atrens, A.; Stokes, J. R. A review of nanocrystalline cellulose suspensions: Rheology, liquid crystal ordering and colloidal phase behaviour. *Advances in colloid and interface science* **2020**, *275*, 102076.
- (134) Maier, W.; Saupe, A. Eine einfache molekulare Theorie des nematischen kristallinflüssigen Zustandes. *Zeitschrift für Naturforschung A* **1958**, *13* (7), 564-566.
- (135) Wulf, A. Difficulties with the Maier–Saupe theory of liquid crystals. *The Journal of Chemical Physics* **1976**, *64* (1), 104-109.

- (136) Luckhurst, G. R.; Zannoni, C. Why is the Maier–Saupe theory of nematic liquid crystals so successful? *Nature* **1977**, *267* (5610), 412-414. DOI: 10.1038/267412b0.
- (137) Flory, P. J. Molecular theory of liquid crystals. In *Liquid crystal polymers i*, Springer, 2005; pp 1-36.
- (138) Khokhlov, A.; Semenov, A. Liquid-crystalline ordering in the solution of partially flexible macromolecules. *Physica A: Statistical Mechanics and its Applications* **1982**, *112* (3), 605-614.
- (139) Lagerwall, J. P.; Schütz, C.; Salajkova, M.; Noh, J.; Hyun Park, J.; Scalia, G.; Bergström, L. Cellulose nanocrystal-based materials: from liquid crystal self-assembly and glass formation to multifunctional thin films. *NPG Asia Materials* **2014**, *6* (1), e80-e80.
- (140) Canejo, J.; Monge, N.; Echeverria, C.; Fernandes, S.; Godinho, M. Cellulosic liquid crystals for films and fibers. *Liquid Crystals Reviews* **2017**, *5* (2), 86-110.
- (141) Marin, L.; Popescu, M.-C.; Zabolica, A.; Uji, H.; Fron, E. Chitosan as matrix for bio-polymer dispersed liquid crystal systems. *Carbohydrate polymers* **2013**, *95* (1), 16-24.
- (142) Knight, D. P.; Vollrath, F. Biological liquid crystal elastomers. *Philosophical Transactions of the Royal Society of London. Series B: Biological Sciences* **2002**, *357* (1418), 155-163.
- (143) Marx, A.; Thiele, C. Orientational Properties of Poly- $\gamma$ -benzyl-L-glutamate: Influence of Molecular Weight and Solvent on Order Parameters of the Solute. *Chemistry—A European Journal* **2009**, *15* (1), 254-260.
- (144) Gupta, A.; Strazielle, C.; Marchal, E.; Benoit, H. Aggregation of poly ( $\gamma$ -benzyl-L-glutamate) in dioxane: Molecular-weight dependence of critical concentration. *Biopolymers: Original Research on Biomolecules* **1977**, *16* (5), 1159-1165.
- (145) Gin, D. L.; Pecinovsky, C. S.; Bara, J. E.; Kerr, R. L. Functional lyotropic liquid crystal materials. *Liquid Crystalline Functional Assemblies and Their Supramolecular Structures* **2008**, 181-222.
- (146) Schwartz, M. P.; Cunin, F.; Cheung, R. W.; Sailor, M. J. Chemical modification of silicon surfaces for biological applications. *physica status solidi (a)* **2005**, *202* (8), 1380-1384.
- (147) Sonawane, M. D.; Nimse, S. B. Surface modification chemistries of materials used in diagnostic platforms with biomolecules. *Journal of Chemistry* **2016**, 2016.

- (148) Basta, A. H.; Lotfy, V. F.; Micky, J. A.; Salem, A. M. Hydroxypropylcellulose-based liquid crystal materials. *Carbohydrate Polymer Technologies and Applications* **2021**, *2*, 100103.
- (149) Kasprzak, C. R.; Scherzinger, E. T.; Sarkar, A.; Miao, M.; Porcincula, D. H.; Madriz, A. M.; Pennewell, Z. M.; Chau, S. S.; Fernando, R.; Stefik, M. Ordered nanostructures of carbon nanotube–polymer composites from lyotropic liquid crystal templating. *Macromolecular Chemistry and Physics* **2018**, *219* (17), 1800197.
- (150) Rosu, C.; Balamurugan, S.; Cueto, R.; Roy, A.; Russo, P. S. Polypeptide-coated silica particles dispersed in lyotropic liquid crystals of the same polypeptide. *The Journal of Physical Chemistry B* **2016**, *120* (29), 7275-7288.
- (151) Balamurugan, S. S.; Soto-Cantu, E.; Cueto, R.; Russo, P. S. Preparation of organosoluble silica– polypeptide particles by “click” chemistry. *Macromolecules* **2010**, *43* (1), 62-70.
- (152) Zocher, H. Spontaneous structure formation in sols; a new kind of anisotropic liquid media. *Z Anorg Allg Chem* **1925**, *147*, 91-110.
- (153) Dierking, I.; Al-Zangana, S. Lyotropic liquid crystal phases from anisotropic nanomaterials. *Nanomaterials* **2017**, *7* (10), 305.
- (154) Huang, Y.; Sasano, T.; Tsujii, Y.; Ohno, K. Well-defined polymer-brush-coated rod-shaped particles: synthesis and formation of liquid crystals. *Macromolecules* **2016**, *49* (22), 8430-8439.
- (155) Ravula, T.; Ramamoorthy, A. Magnetic Alignment of Polymer Macro-Nanodiscs Enables Residual-Dipolar-Coupling-Based High-Resolution Structural Studies by NMR Spectroscopy. *Angewandte Chemie* **2019**, *131* (42), 15067-15070.
- (156) Sato, T.; Jinbo, Y.; Teramoto, A. Intermolecular interaction of stiff-chain polymers in solution. *Macromolecules* **1997**, *30* (3), 590-596.
- (157) Itou, T.; Teramoto, A. Isotropic-liquid crystal phase equilibrium in solutions of semiflexible polymers: poly (hexyl isocyanate). *Macromolecules* **1988**, *21* (7), 2225-2230.
- (158) Tang, H.; Zhang, D. Poly ( $\gamma$ -benzyl-L-glutamate)-functionalized single-walled carbon nanotubes from surface-initiated ring-opening polymerizations of N-carboxylanhydride. *Journal of Polymer Science Part A: Polymer Chemistry* **2010**, *48* (11), 2340-2350.

- (159) Zhang, D.; Zhang, L.; Wang, B.; Piao, G. Nanocomposites of polyaniline and cellulose nanocrystals prepared in lyotropic chiral nematic liquid crystals. *Journal of Materials* **2013**, *2013*, 1-6.
- (160) Allie, S.; Hegoburu, I.; Shin, M. J.; Jung, J. Y.; Toader, V.; Rey, A.; Soule, E. R.; Reven. R. Polymer functionalized nanoparticles in liquid crystals: combining PDLCs with LC nanocomposites. *Soft Matter* **2018**, *14*, 8580.
- (161) Agra-Kooijman, D.M. and Kumar, S. (2014). X-Ray Scattering Investigations of Liquid Crystals. In Handbook of Liquid Crystals (eds J.W. Goodby, C. Tschierske, P. Raynes, H. Gleeson, T. Kato and P.J. Collings).
- (162) Zhang, J.; Li, Y.; Zhang, X.; and Yang, B.. Colloidal Self-Assembly Meets Nanofabrication: From Two-Dimensional Colloidal Crystals to Nanostructure Arrays. *Adv. Mater* **2010**, *22*: 4249-4269.
- (163) Lotito, V. and Zambelli, T. Approaches to self-assembly of colloidal monolayers: A guide for nanotechnologists. *Adv. Colloid Interface. Sci* **2017**, *246*, 217-274.
- (164) Stoeva, S. I.; Prasad, B. L. V.; Uma, S.; Stoimenov, P. K.; Zaikovski, V.; Sorensen, C. M.; and Klabunde, K. J. *The Journal of Physical Chemistry B* **2003**, *107* (30), 7441-7448.
- (165) Bazin, G. and Zhu, X. X. Crystalline colloidal arrays from the self-assembly of polymer microspheres, *Prog. Polym. Sci.* **2013**, *38*(2), 406-419.
- (166) Abbas, S. and Lodge, T. P.. Superlattice Formation in Binary Mixtures of Block Copolymer Micelles, *Langmuir* **2008**, *24*(12), 6247-6253.
- (167) Cai, C.; Lin, L.; Zhuang, Z.; Zhu, W. Ordering of Polypeptides in Liquid Crystals, Gels and Micelles, *Adv. Polym. Sci.* **2013**, *259*, 159-200.
- (168) Singh, P.S. Small-Angle Scattering Techniques (SAXS/SANS). *Membrane Characterization.* **2017**, 95-111.
- (169) Liu, L.; Urquhart M.; Wang, X. Small and Wide X-ray Scattering Studies of Biological Macromolecules in Solution. *Journal of Visualized Experiments.* **2013**. (71):4160.
- (170) Smith, S. A.; Palke, W.E.; Gerig, J.T. The Hamiltonians of NMR. *Concepts in Magnetic Resonance.* **1992**, *4*, 181-204.

- (171) Li, G.W.; Wang, X. J.; Lei, X.; Liu, N. Wu, Z.Q. Self-Assembly of Helical Polymers and Oligomers to Create Liquid Crystalline Alignment for Anisotropic NMR Parameters. *Macromolecular Rapid Communications*. **2022**, 43 (14), 2100898.
- (172) Domenici, V. Nuclear Magnetic Resonance: a Powerful Tool to Study Liquid Crystals. *Liquid Crystals Today*. **2017**, 26(1), 2-10.
- (173) Seelig, J. and Niederberger, W. Deuterium-Labeled Lipids as Structural Probes in Liquid Crystalline Bilayers. A Deuterium Magnetic Resonance Study. *Journal of the American Chemical Society*. **1974**, 96(7), 2069-2072.
- (174) Zimmermann, H. Specifically Deuteriated Intermediates for the Synthesis of Liquid Crystals and Liquid-Crystalline Polymers. *Liquid Crystals*. **1989**, 4(6), 591-618.
- (175) Goldfarb, D.; Luz, Z.; Zimmermann, H. Deuterium NMR Studies of Discotic Liquid Crystals. *Israel Journal of Chemistry*. **1983**. 23(3), 341-352.
- (176) Voigt, J.; Bjorholm, T.; Jacobsen, J.P. Determination of Deuterium Quadrupole Coupling Constants in the Liquid Crystalline Phase -Values for Chloroform and Dichloromethane. *Israel Journal of Chemistry*. **1983**. 23, 291-294.
- (177) Jokisaari, J. and Hiltunen, Y. Deuteron quadrupole coupling constants of methyl iodide and chloroform determined by NMR in liquid-crystalline phases. *Journal of Magnetic Resonance*. **1984**. 60(2), 307-319.

# Chapter 2 : Lyotropic Nematic Phases of Isotropic Nanoparticles via Semiflexible Polymer Ligands

## Rationale for Chapter 2:

The first research chapter of this thesis reports the development of a novel lyotropic LC nanomaterial, based on semiflexible polymer grafted NPs, where anisotropic phases are formed from isotropic particles. To achieve this, a “grafting to” protocol to produce NPs with dense polymer coronas with higher molecular weights was employed, which provides Nematic rather than cubic phases to arise from the spherical NPs via splaying of the polymer ligand shell, notable because the LC phases observed had previously only been formed from rod- or disc-like NPs. Despite being attached to the NPs, the PHIC chains displayed a high degree of orientational order comparable to the free polymer solutions, yet the confinement of the PHIC chains to the NPs resulted in a lowering of the critical concentration for liquid crystallinity and a widening of the isotropic/nematic biphasic region. The PHIC grafted NPs can serve as a useful model for understanding the properties of semiflexible polymer brushes on curved surfaces, a feature of many biological structures, that has yet to be theoretically explored.

**Chapter 2** has been published as a manuscript in a peer-reviewed journal. Citation: J. Wong, V. Toader, L. Reven, “Lyotropic Nematic Phases of Isotropic Nanoparticles via Semiflexible Polymer Ligands” in *Macromolecular Rapid Commun.* **2023**, 44, 2200951

# Lyotropic Nematic Phases of Isotropic Nanoparticles via Semiflexible Polymer Ligands

*Jessie Wong, Violeta Toader and Linda Reven\**

Centre québécois sur les matériaux fonctionnels/Quebec Centre for Advanced Materials (CQMF / QCAM), Chemistry Department, 801 Sherbrooke St. W., Montreal, Qc H3A 0B8  
Canada

## 2.1 Abstract

Lyotropic liquid crystalline (LC) nanomaterials are normally achieved through particle shape anisotropy. Herein, it is shown that lyotropic nematic rather than cubic phases are produced from spherical nanoparticles (NPs) with semi-flexible polymer ligands.  $\text{ZrO}_2$  nanocrystals (4 nm dia.) are coated with a dense shell of poly(hexyl isocyanate) (PHIC), a helical rod-like polymer that forms lyotropic LC phases in a range of organic solvents. Solvent casted NPs with PHIC ligands above the persistence length form linear assemblies, separated by a characteristic distance related to the chain length while NPs with shorter, rigid rod PHIC ligands pack hexagonally. Concentrated NP-PHIC dispersions present nematic textures similar to the free PHIC nematic solutions but at lower critical concentrations, widening the isotropic-nematic biphasic region.  $^2\text{H}$  NMR spectra of the NPs dispersed in a deuterated solvent display quadrupolar splittings that increase with NP concentration, showing that the PHIC ligands are magnetically aligned. The high degree of orientation order is evidence that splaying of the ligand shell transforms the spherical NPs to rod-like shapes that assemble to produce nematic lyotropic LC phases and linear NP arrays. This approach to creating anisotropic assemblies can be extended to other types of spherical NPs and semiflexible polymers.

## 2.2 Introduction

Liquid crystals (LCs) have played a key role in nanotechnology serving as both synthetic templates and as dynamic stimuli-responsive matrices to improve and control the properties of nanomaterials. LCs can broadly be classified into two categories: thermotropic and lyotropic, driven through temperature and concentration dependent self-assembly, respectively. While thermotropic LC-based displays and electro-optical devices are widespread in everyday use, small molecule based lyotropic LCs are important for biomedical applications, primarily as drug delivery agents or templates for nanostructured materials.<sup>[1]</sup> Semi-flexible biopolymers such as DNA, polypeptides, actins, and glycopolymers, form lyotropic LC phases that are essential to their biological functions.<sup>[2]</sup> Given the relevancy to biological systems and colloid science, LC researchers are increasingly turning their attention to lyotropic LCs, generating new materials and applications such as active matter or living liquid crystals.<sup>[3]</sup> Organic or inorganic anisotropic nanomaterials such as carbon nanotubes, clays, chromonic liquid crystal, cellulose nanocrystals, and viruses, to name a few, can form lyotropic phases, primarily as aqueous dispersions.<sup>[4]</sup> Lyotropic nanomaterial LC phases in organic solvents are achieved by functionalizing anisotropic nanoparticles (NPs) with suitable ligands. Examples include ZnO nanowires<sup>[5]</sup> and CdSe nanorods<sup>[6]</sup> with alkyl ligands and metal oxide nanorods with polymer ligands.<sup>[7,8]</sup> Whereas anisotropic NPs form anisotropic LC phases (i.e., nematic, smectic, cholesteric), spherical NPs, with flexible polymer ligand shells, were shown by small angle X-ray diffraction (SAXS) to organize into cubic lyotropic LC phases.<sup>[9]</sup> Although NPs with flexible polymer ligands have been widely studied,<sup>[10]</sup> there are relatively few examples of NPs with semiflexible polymer ligands. As highlighted in a recent study of bioactive polymer brushes,<sup>[11]</sup> there is a lack of model synthetic semiflexible brushes on either flat or curved surfaces, despite the presence of biopolymer brushes frequently found in biological tissues whose stiffness is essential to their function. The majority of the nanoparticle studies with such brushes have concerned DNA<sup>[12]</sup> and polypeptide<sup>[13]</sup> functionalized NPs for sensor and drug delivery applications. Gold NPs with dense DNA coronas were shown under confinement to organize into solid super-lattices with the interparticle distances controlled by the ligand length.<sup>[14]</sup> Silica<sup>[15,16]</sup> and carbon nanotubes<sup>[17]</sup> with polypeptide ligands have been dispersed in lyotropic LCs formed by the same polypeptide.

However, to our knowledge, lyotropic phases formed by NPs with semiflexible polymer ligands have not yet been re-ported.

Semi-flexible polymers are defined by a persistence length and characteristic ratio between that of a flexible coil versus rigid rod polymer. Lyotropic LC phases are possible in concentrated semi-flexible polymer solutions through a combination of sufficiently high axis ratios and intermolecular forces promoting the formation of expanded coils in solution.<sup>[18–20]</sup> The orientational properties of lyotropic stiff polymers have been exploited for high-performance fibers, actuators, and electro-optical devices through their responses to electric fields and shear forces.<sup>[21]</sup> Poly (hexyl-isocyanate) (PHIC) is a semi-flexible helical polymer in which both thermotropic and lyotropic nematic LC phases (in chloroform, dichloromethane, and toluene) have been observed.<sup>[22]</sup> PHIC was selected as a semiflexible polymer ligand because its properties have been intensively studied, its solubility in various organic solvents, and chiral variants have been synthesized.<sup>[23]</sup> The similarity of the amide backbone of poly isocyanates to peptides has inspired investigations as more thermally stable alternatives to polypeptides.<sup>[24]</sup> The polymer persistence length,  $l_p$ , is a measure of the bending stiffness that varies with the solvent. For chain lengths below  $l_p$ , the polymer behaves as a rigid rod whereas for chain length well above  $l_p$ , the polymer is in the continuously flexible “wormlike” state. For PHIC,  $l_p$  ranges from  $\approx 20$  nm in chloroform or dichloromethane to  $\approx 40$  nm in toluene or n-hexane, allowing access to the rigid rod versus wormlike regimes at moderate molecular weights. Here we report the self-assembly of spherical NPs with PHIC ligand shells into nematic lyotropic LC phases and linear arrays. Dense PHIC coronas on 4 nm diameter  $ZrO_2$  NPs were produced using a “grafting to” approach that allows for more control over the molecular weight. In addition to determining the phase diagram, the origin of the nematic order was investigated by wide-line  $^2H$  NMR spectroscopy of the solvent, deuterated chloroform, to indirectly probe the orientational order of the PHIC ligands.

## 2.3 Results

### 2.3.1 Preparation of ZrO<sub>2</sub>-PHIC nanoparticles

There are only two previous reports of PHIC grafted NPs. Magnetic iron oxide NPs were functionalized with low molecular weight PHIC (4.4 to 7.8 K) using click chemistry.<sup>[25]</sup> A “grafting from” protocol was used to attach higher molecular weight PHIC (60K) to fumed silica using a titanium (IV) catalyst.<sup>[26]</sup> ZrO<sub>2</sub> nanocrystals were selected for this study as a convenient model system. Phosphonic acids bind very strongly to ZrO<sub>2</sub>NPs which can be prepared in large quantities with a relatively low size dispersity (4 nm±0.5 nm). Furthermore, the surface functionalization as developed here can be straightforwardly applied to other metal oxides such as TiO<sub>2</sub> or Fe<sub>2</sub>O<sub>3</sub> as well as semiconductor nanocrystals.

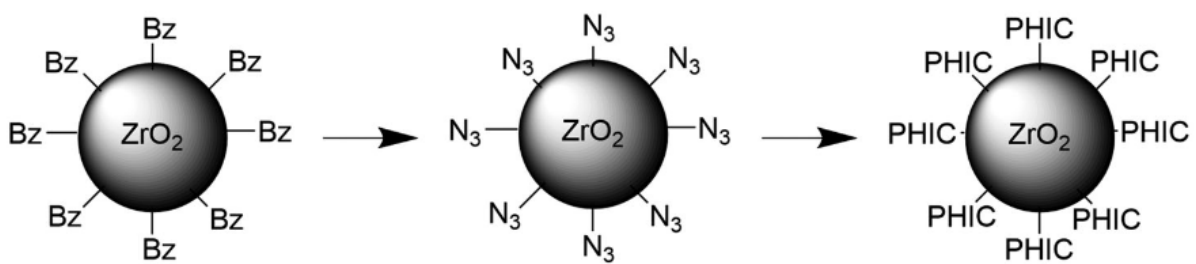
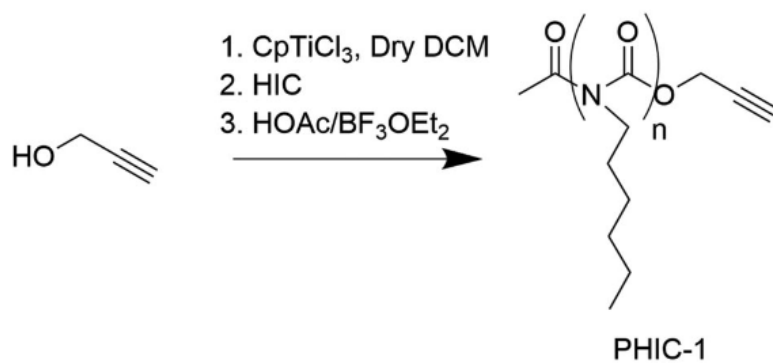
As our goal was to examine PHIC ligands with well-defined molecular weights above and below the persistence length,  $l_p$ , we designed various PHIC-functionalized phosphonic acid ligands for attachment to the ZrO<sub>2</sub> NPs.<sup>[25,27]</sup> Additionally, the ligand was designed such that the PHIC ligands would have some degree of flexibility near the ZrO<sub>2</sub> core, to impart flexibility upon the PHIC ligands toward liquid crystalline behavior as well as to maximize surface coverage. Initially, a click chemistry approach was utilized. (Scheme 2-1). However, this route produced lower grafting densities (<0.5 ch nm<sup>-2</sup>), cloudy suspensions and no observed liquid crystalline behavior.

Given the low coverages, the “grafting to” approach was adopted. A click reaction was used to first couple the alkyne terminated PHIC with the azide functionalized phosphonic ligand before attachment to the NPs. (Scheme 2-2) While this grafting to approach resulted in dense PHIC coronas, the click reaction was far from quantitative, and purification further lowered the yield.

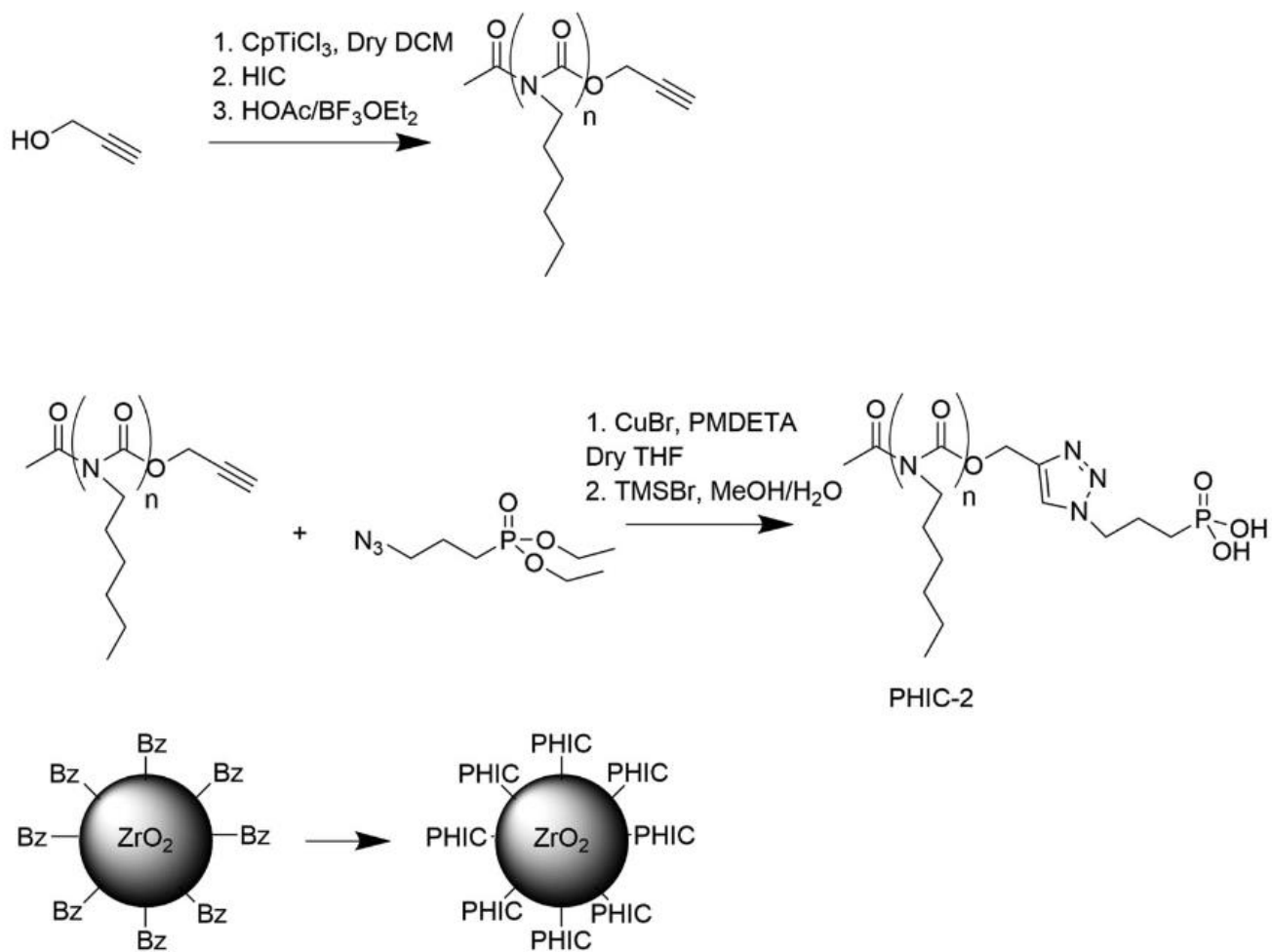
The organotitanium catalyst route to produce PHIC with end functional groups has the advantage of generating PHIC with well controlled molecular weights and low dispersities.<sup>[27]</sup> However, the maximum molecular weight is generally limited to <20K due to competing

depolymerization, a general problem for isocyanate polymerization reactions.<sup>[24]</sup> To address the problems listed above, a phosphonate functionalized initiator was de-signed, as to optimize the synthesis through reducing depolymerization and product loss through purification (Scheme 2-3).

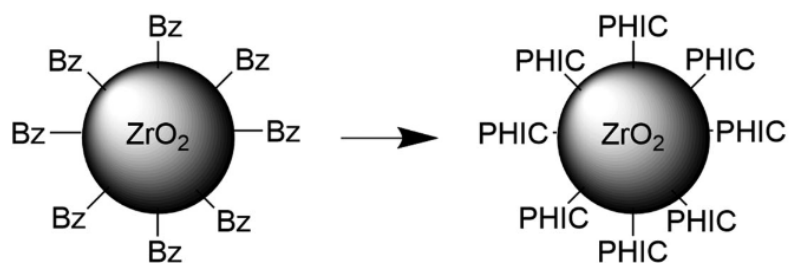
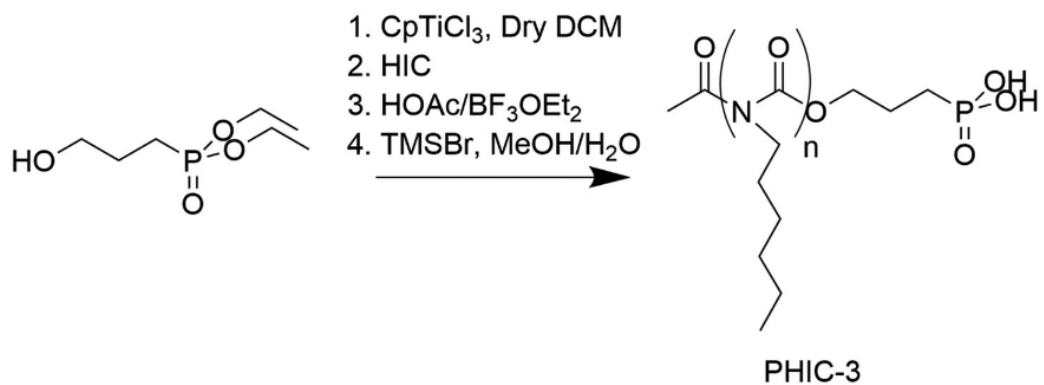
Three molecular weights of functionalized PHIC were synthesized and subsequently anchored onto ZrO<sub>2</sub> nanoparticles: PHIC<sub>24</sub> (MW=3K; N=24), PHIC<sub>55</sub> (MW=9000; N=55), and PHIC<sub>180</sub> (MW=23K; N=180). Assuming a repeat unit length of 0.2 nm,<sup>[28]</sup> the contour lengths of the prepared PHIC samples are as follows in increasing order of molecular weight: 4.8, 11.0, and 36.0 nm. This places PHIC<sub>24</sub> and PHIC<sub>55</sub> below the persistence length of PHIC in DCM ( $l_p=20$  nm) and PHIC<sub>180</sub> above the persistence length. The PHIC ligands were then attached to the benzyl alcohol stabilized ZrO<sub>2</sub> NPs through an exchange reaction followed by quantitative precipitation to remove unbound ligands. This approach yielded a dense polymer corona of 1.86 chains nm<sup>-2</sup> [for PHIC<sub>180</sub>] based on TGA analysis. Given the average surface area of a single ZrO<sub>2</sub> NP (50 nm<sup>2</sup>), each particle contains≈90 PHIC<sub>180</sub> chains.



Scheme 2-1: Attachment of alkyne terminated PHIC ligands to  $\text{ZrO}_2$ NPs by a click reaction.



Scheme 2-2: "Grafting to" functionalization of  $\text{ZrO}_2$ NPs with phosphonic acid terminated PHIC ligands produced by a click reaction.



Scheme 2-3: "Grafting to" functionalization of  $\text{ZrO}_2$  NPs with phosphonic acid terminated PHIC ligands synthesized via a phosphonate functionalized initiator.

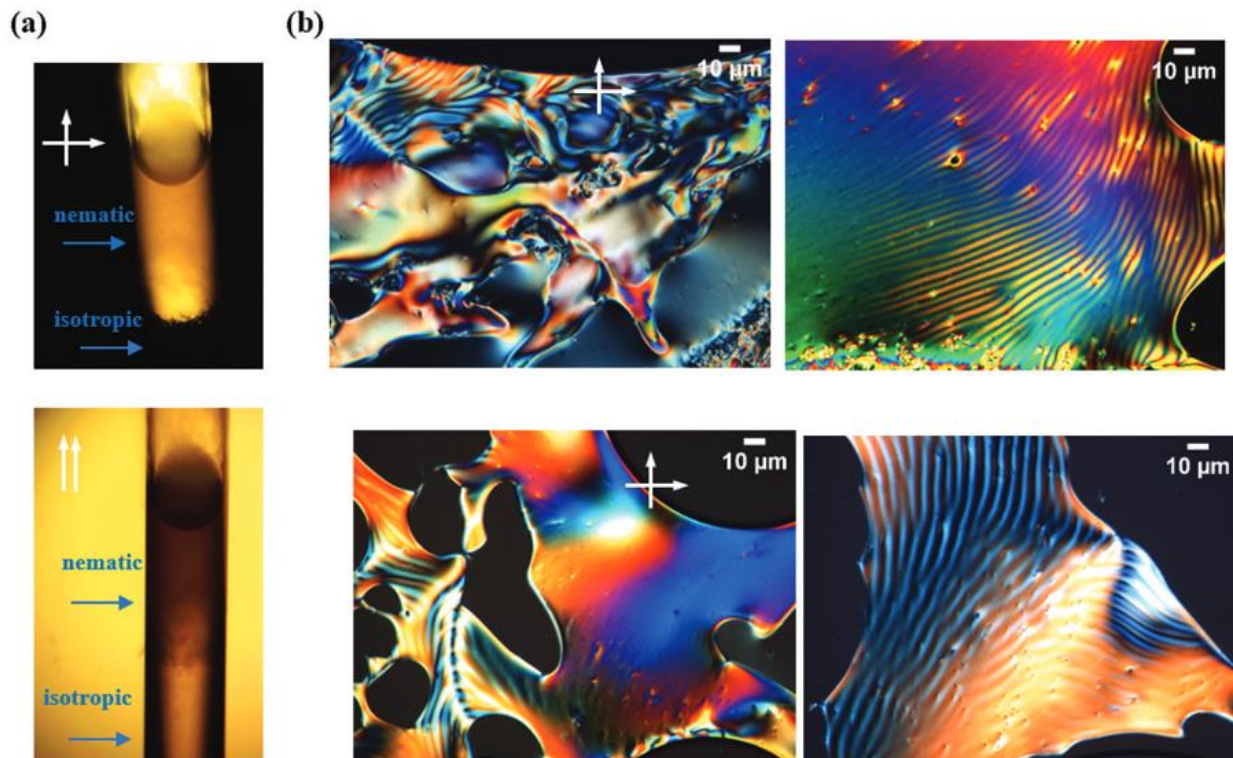


Figure 2-1: a) A solution of 25 wt.% ZrO<sub>2</sub>-PHIC<sub>180</sub> NPs in chloroform under cross polarizers (top) and uncrossed polarizers (bottom). The ZrO<sub>2</sub>-PHIC<sub>180</sub> NPs solution undergoes a phase separation of a hazy, highly concentrated anisotropic phase that is birefringent and a clear, dilute isotropic phase that appears black under cross polars. b) Polarized optical microscopy (POM) images of the lyotropic phases of 20.1 wt.% ZrO<sub>2</sub>-PHIC<sub>180</sub> NP (top) and PHIC<sub>180</sub> (bottom) solutions in DCM. The textures observed under POM are characteristic of the nematic phase.

### 2.3.2 Optical Microscopy

At concentrations below  $\approx 30$  wt.%, both the free PHIC and the PHIC grafted NPs solutions are biphasic and undergo a macroscopic phase separation as previously reported for PHIC.<sup>[29]</sup> In Figure 1a, a dispersion of the ZrO<sub>2</sub>-PHIC<sub>180</sub> NPs in chloroform shows a hazy birefringent anisotropic phase containing a high NP concentration on top and an isotropic phase with a lower NP concentration on the bottom of the sample tube. This phase separation is density driven due to the lower density of PHIC (0.87 g cc<sup>-1</sup>) as compared to CHCl<sub>3</sub> (1.5 g cc<sup>-1</sup>). Early studies of solutions of polydispersed PHIC found that the higher MW polymer is strongly partitioned into the anisotropic phase and shorter chains into the isotropic portion.<sup>[29,30]</sup> The PHIC ligands in this

study have PDIs of 1.2 to 1.5 so we would expect that the molecular weight based partitioning of PHIC between the two phases is present.

Figure 2-1 shows selected optical microscopy images of dichloromethane solutions of PHIC<sub>180</sub> and ZrO<sub>2</sub>-PHIC<sub>180</sub> NPs. Nematic droplets appeared for ZrO<sub>2</sub>-PHIC<sub>180</sub> NPs at concentrations above 9 wt.% whereas solutions of the unattached PHIC<sub>180</sub> ligand first showed birefringence at a higher concentration of 17 wt.%. Similar to previous studies, inclusions of isotropic liquid were present in the anisotropic phase, which is attributed to incomplete phase separation due to the very high viscosities.<sup>[30]</sup> For high concentrations (>20 wt.%), stripe textures were also observed in certain regions for both PHIC<sub>180</sub> and ZrO<sub>2</sub>-PHIC<sub>180</sub> NPs solutions. In general, such striped or banded patterns are formed in lyotropic semiflexible polymers under shear and/or flow.<sup>[31]</sup> In our case, these forces arise as the cover slip is placed on the drop of sample on the glass microscope slide. Stripe patterns for sheared lyotropic nematic PHIC solutions were first reported by Aharoni and co-workers.<sup>[30]</sup> While both ZrO<sub>2</sub>-PHIC<sub>24</sub> and ZrO<sub>2</sub>-PHIC<sub>55</sub> were prepared, neither lyotropic nematic textures nor macroscopic phase separation were observed in either sample.

### 2.3.3 Transmission Electron Microscopy

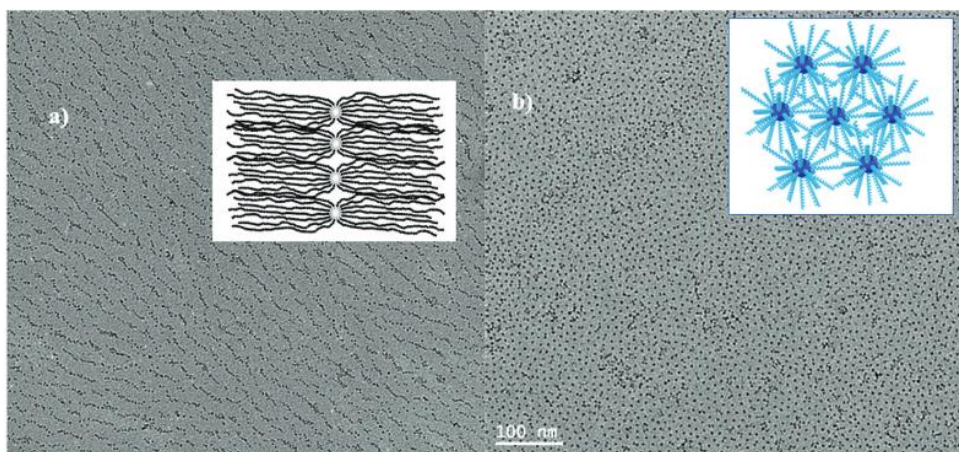


Figure 2-2. TEM images of a) ZrO<sub>2</sub>-PHIC<sub>180</sub> NP film formed at a dichloromethane/water interface and b) ZrO<sub>2</sub>-PHIC<sub>24</sub> NPs drop casted from a chloroform solution.

The spatial distributions of the ZrO<sub>2</sub>NPs functionalized with low(3k) and high (23k) MW PHIC were examined by transmission electron microscopy (TEM) (Figure 2-2). As we were not expecting lyotropic behavior solutions of the ZrO<sub>2</sub> NP-PHIC<sub>24</sub> were simply cast by putting a drop on a TEM grid. However, in the case of ZrO<sub>2</sub>-PHIC<sub>180</sub>, the TEM grids were instead drop-casted using both dilute and concentrated solutions of the nanoparticles. This was done to compare the well-dispersed and colloidally stable NPs to their self-assembled behavior (Figure 2-11, Supporting Information). To further confirm that the drop casting produced monolayers, thin films were also formed by depositing a drop of a dichloromethane ZrO<sub>2</sub> NP-PHIC<sub>180</sub> solution onto a water surface, and then transferred to the TEM grid by dipping, which revealed similar particle assemblies. As seen in Figure 2-2, the particle spatial distributions of ZrO<sub>2</sub>-PHIC<sub>24</sub> versus the ZrO<sub>2</sub>-PHIC<sub>180</sub> NPs are quite different. In the case of PHIC<sub>24</sub>, the average interparticle distance was measured to be  $\approx 8$  nm, and when compared to the calculated contour length, this suggests some degree of interpenetration of the neighboring PHIC<sub>24</sub> ligand shells.

In contrast, for ZrO<sub>2</sub>-PHIC<sub>180</sub>, spacings between the linear arrays were semi-regular with an average value of  $\approx 50$  nm. However, TEM grids of ZrO<sub>2</sub>-PHIC<sub>180</sub> prepared around the critical lyotropic concentration often resulted in thicker films, thereby making measurements of the interparticle distances within the linear assemblies difficult. Instead, the samples were dropped from a solution of ZrO<sub>2</sub>-PHIC<sub>180</sub> below the critical concentration such that suitable TEM resolution may be achieved. In these dropcast films from lowered NP concentrations, there are more isolated NPs, but linear assemblies are still present. (Figure 2-14, Supporting Information) The analysis of the higher resolution images of these thinner films yielded an average interparticle distance of  $\approx 5$  nm in the linear assemblies, however, the spread in values is large since the concentration and selection of the groups of NPs is somewhat arbitrary. In the rigid rod limit, the length of PHIC<sub>180</sub> with a degree of polymerization of 180 is 36 nm. Semiflexible polymer chain lengths greater than  $l_p$ , the persistence length, fall into the wormlike regime where the chains are modeled as continuously flexible rods.<sup>[32]</sup> In this model, the contour length is considered instead and is calculated from the molar mass  $M$ , and the molar mass per unit contour length for PHIC,  $M_L = 740 \text{ nm}^{-1}$ .<sup>[33]</sup> The calculated contour length  $L = M/M_L = 31 \text{ nm}$  for PHIC is only  $\approx 10 \text{ nm}$

greater than the persistence length,  $l_p=20$ . However, given the polydispersity of PHIC<sub>180</sub> (PDI=1.5) and the strong tendency of the longer chains to partition into the anisotropic phase, there should be a significant population of NPs with PHIC ligands well into the worm-like regime. Given the degree of irregularity, the measurement of the distances between the linear NP arrays has a wide spread of values. (Figure 2-13, Supporting Information). However, the calculated 50 nm average spacing between the linear NP assemblies is roughly equal to twice the PHIC<sub>180</sub> chain lengths, taking into consideration that there should be some chain flexibility and partial interpenetration of the PHIC<sub>180</sub> brushes.

### 2.3.4 Deuterium NMR Spectroscopy

The nematic ordering of the polymer ligands was confirmed by <sup>2</sup>H NMR spectroscopy of solutions of PHIC<sub>180</sub> and ZrO<sub>2</sub>-PHIC<sub>180</sub> NPs in deuterated chloroform. Lyotropic solutions of synthetic polypeptides like poly( $\gamma$ -benzyl-L-glutamate) (PBLG) are commonly used as alignment media for NMR studies of biomacromolecules. The first proof that lyotropic PHIC, despite its weak magnetic anisotropy, can be aligned by a magnetic field was demonstrated by a <sup>2</sup>H NMR study of PHIC in per deuterated toluene where the solvent becomes aligned along with the polymer.<sup>[34]</sup> The magnitude of the quadrupolar splittings suggested that the toluene solvent molecules are uniformly oriented parallel to the alkyl side chains of PHIC with the isocyanate back-bone aligned parallel to the applied magnetic field.

The degree of magnetic alignment of PHIC was directly determined from <sup>2</sup>H NMR of PHIC- $\alpha$ -d<sub>2</sub> as a function of concentration in chloroform and toluene.<sup>[35]</sup> In this study, the CH<sub>2</sub> group next to the isocyanate backbone was deuterated and the molecular weight (20k) was very close to that of the PHIC<sub>180</sub> used here. The critical order parameter at the onset of liquid crystallinity for PHIC was calculated to be  $S \approx 0.6$  at 20 wt.%. The order parameter  $S$  increased to 0.8 at 30 wt.% where the sample is fully nematic, showing that the PHIC is highly aligned by the magnetic field as theoretically predicted for semiflexible macromolecules.<sup>[36]</sup> Like the <sup>2</sup>H NMR study of PHIC in deuterated toluene,<sup>[34]</sup> the orientational order of the solvent, deuterated chloroform, was used hereto indirectly detect the alignment of the ZrO<sub>2</sub>-PHIC<sub>180</sub> NP ligands by a magnetic field.

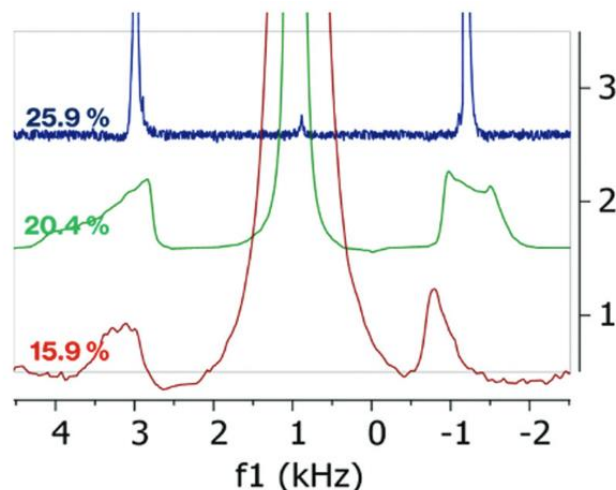


Figure 2-3. Representative  $^2\text{H}$  NMR experiments performed at 25.9, 20.4, and 15.9 wt.% in  $\text{CDCl}_3$ . Baselines were scaled up for clarity, as lower concentration samples had a smaller anisotropic volume, thereby decreasing the signal intensity.

Representative  $^2\text{H}$  NMR spectra of  $\text{ZrO}_2$ - $\text{PHIC}_{180}$  NP chloroform solutions are shown in Figure 2-3. At concentrations below 30 wt.% PHIC, the samples are biphasic and the  $^2\text{H}$  NMR spectra display both singlet and doublet signals from the isotropic and anisotropic phases respectively. All the samples displaying  $^2\text{H}$  NMR doublet signals were birefringent. Given that the prepared  $\text{ZrO}_2$ - $\text{PHIC}_{24}$  and  $\text{ZrO}_2$ - $\text{PHIC}_{55}$  NPs were not birefringent, solutions of these samples did not display any doublet signals. The integrated intensities of the isotropic versus the doublet  $^2\text{H}$  signals from the two phases are not quantitative in these spectra as it depended on the anisotropic volume inside the coil. For the biphasic samples at the lower PHIC concentrations, the anisotropic volume was smaller than the RF coil of the NMR spectrometer, resulting in a large isotropic peak. However, the focus here is on the size of the quadrupolar splitting which allows an estimate of the orientational order of the  $\text{CDCl}_3$  solvent molecules. The  $^2\text{H}$  quadrupolar splitting for a uniaxial nematic LC arising can be described by Equation (1). In the context of liquid crystals, the asymmetry parameter,  $\eta$ , may be assumed to be essentially zero,<sup>[37–39]</sup> simplifying the Equation (2). The order parameter,  $S$ , measures the extent of alignment of the molecule ( $\text{CDCl}_3$ ) with respect to the principal axis. The  $e^2qQ/h$  term is the deuterium quadrupolar

coupling constant, which was measured to be 167 kHz for deuterated chloroform.<sup>[37]</sup> Using this information, it was possible to calculate the order parameters of the solvent.

$$\delta\nu_Q = \frac{e^2qQ}{h} \left( \frac{3}{2}S_{aa} + \frac{1}{2}\eta(S_{cc} - S_{bb}) \right) \quad (1)$$

$$\delta\nu_Q = \frac{3}{2} \frac{e^2qQ}{h} S \quad (2)$$

Table 2-1 lists the quadrupole splittings and order parameters of CDCl<sub>3</sub> as a function of PHIC<sub>180</sub> concentration for solutions of the free polymer and the ZrO<sub>2</sub>-PHIC<sub>180</sub> NPs. In lyotropic systems that are being developed as alignment media for NMR studies of biomacromolecules, <sup>2</sup>H NMR of the CDCl<sub>3</sub> solvent is commonly used to monitor the concentration dependent isotropic to anisotropic phase transition. Given that weak alignment of the solute molecules is the goal for these NMR studies, the magnitudes of the quadrupole splittings of the CDCl<sub>3</sub> solvent are typically much smaller than those observed here for PHIC (<1000 Hz). Instead, the <sup>2</sup>H quadrupole splitting listed in Table 2-1 are comparable to those measured when CDCl<sub>3</sub> is employed as probe molecule for thermotropic liquid crystals.<sup>[37–39]</sup> Although the doublet for aligned CDCl<sub>3</sub> appears at lower concentrations for the ZrO<sub>2</sub>-PHIC<sub>180</sub> NP solutions, the magnitudes of the quadrupolar splittings and order parameters are slightly larger for the free PHIC<sub>180</sub>, indicating a greater degree of alignment. For the highest PHIC concentration, the quadrupole splittings are very similar, indicating that the NP tethered PHIC chains are highly aligned by the magnetic field.

Table 2-1: <sup>2</sup>H NMR quadrupole splitting and Order parameters.

PHIC <sub>180</sub>			ZrO <sub>2</sub> -PHIC <sub>180</sub> NPs		
[Wt.%]	$\Delta\nu_Q$	S	[Wt.%]	$\Delta\nu_Q$	S
9.5%	0	-	9.5%*	0	
13.0%	0	-	10.5%	3878	0.015
17.7%	4955	0.019	15.9%	3839	0.015
20.1%	4932	0.019	20.4%	3830	0.015
24.3%	5221	0.021	25.9%	4142	0.017
30.0%	5483	0.022	32.2%	5690	0.023

\*Birefringence was observed; however, no <sup>2</sup>H NMR doublet signal was detected.

## 2.4 Discussion

Given the polymer chain stiffness and the spherical core shape, the appearance of nematic textures, characteristic of rod shaped mesogens, was not expected. Only cubic lyotropic phases have been previously reported for spherical NPs with polymer ligand shells. However, the ligands in this study were polystyrene, a flexible polymer such that the NPs retain overall spherical shapes.<sup>[9]</sup> Another structural feature that would seem to preclude liquid crystallinity was the relatively dense polymer coronas of ZrO<sub>2</sub>-PHIC NPs produced here. The dense ligand shell density contrasts with the ligand shells of thermotropic liquid crystalline NPs. For this class of NPs, short alkyl-co-ligands are typically used as spacer groups between bulky mesogenic ligands to increase the available free volume within the ligand shell.<sup>[40–42]</sup> Increasing the spacing between the mesogenic ligands enhances the ability to form liquid crystalline phases as well as the miscibility of the NPs in liquid crystal solvents consisting of the same mesogens.<sup>[41]</sup>

Although the LC textures and the degree of orientational order as measured by <sup>2</sup>H NMR spectroscopy of the free and NP grafted PHIC<sub>180</sub> are very similar, the critical concentration for the onset of liquid crystallinity is significantly lower for the ZrO<sub>2</sub>-PHIC<sub>180</sub> NPs. While grafting the PHIC<sub>180</sub> to the NPs does not appear to greatly affect the chain order, the pinning of PHIC chains to the ZrO<sub>2</sub> cores increases the local chain densities in the solution and lowers the critical concentration for the onset of liquid crystallinity. The overall effect appears to be a widening the biphasic region. For the free polymer, the biphasic region can be quite narrow. In a study of the molecular weight dependence of the phase diagram of PHIC with low polydispersity (PDI=1.06), the onset of the nematic phase for a 20K PHIC in dichloromethane occurs at a 0.261 weight fraction and the sample is completely nematic above 0.296.<sup>[43]</sup> The different phase boundary weight fractions in our sample are mostly likely due to the higher polydispersity of the PHIC<sub>180</sub> (PDI=1.5). The different solvent, chloroform rather than dichloromethane, may also be a factor, although the PHIC persistence lengths in chloroform and dichloromethane are similar.<sup>[33]</sup>

We can compare the observed nematic order of the NP grafted PHIC chains to related PHIC brush systems. While the literature concerning the properties of flexible polymer brushes

on both flat and curved surfaces is very extensive, there are relatively few studies of semiflexible polymer brushes, despite the prevalence of these structures in biological systems.<sup>[10,44]</sup> As far as experimental studies, surface tethered PHIC rods at low and moderate grafting densities on flat surfaces have been produced by the adsorption of block copolymers where the short non-PHIC blocks selectively adhere to the surface.<sup>[45,46]</sup> The PHIC blocks align parallel to the surface with liquid crystalline order when annealed in solvent vapor due to the freedom of rotation of the end-grafted PHIC chains.<sup>[46]</sup> In regards to PHIC chains tethered to curved surfaces, micelles have been formed by adding a PHIC selective solvent to PHIC-b-P2VP block copolymers.<sup>[47]</sup> The degree of polymerization and thus lengths of the PHIC blocks were similar to the PHIC<sub>180</sub> ligands studied here. Rather than forming PHIC brush coronas, the PHIC blocks adopt a tangential chain conformation despite the surface curvature. The persistence length in the PHIC selective solvent used to form the micelles, toluene, is 40 nm, twice as long as that of chloroform or dichloromethane, yet the 38 nm PHIC chains were able to wrap around the 20–50 nm diameter P2VP cores.<sup>[47]</sup> The tangential rather than vertical LC nematic ordering of PHIC chains of the block copolymer assemblies on both flat and curved surfaces is made possible by the relatively low grafting densities.

The 4 nm ZrO<sub>2</sub> core is small compared to the ≈30 nm long PHIC<sub>180</sub> chains such that the ZrO<sub>2</sub>-PHIC<sub>180</sub> NPs can be compared to star polymers.<sup>[48]</sup> This analogy has been widely applied for theoretical studies of NPs with flexible polymer ligands through the Daoud-Cotton model.<sup>[10,48]</sup> Three arm PHIC star polymers were found to form nematic phases in toluene at higher critical concentrations than linear PHIC with similar molecular weights (44–50K).<sup>[49]</sup> The ability of the star polymer to form a nematic phase was attributed to the flexibility of the carbamate bonds connecting the PHIC arms to the cyclohexane core which can allow rotation of one arm to lie parallel to the second arm for a rod-like arrangement. The authors found that the branch point necessitated a higher critical concentration for the star PHIC to form a nematic phase. The reverse trend is true for the free versus NP grafted PHIC<sub>180</sub> since the solutions of ZrO<sub>2</sub>-PHIC<sub>180</sub> NPs show birefringence at half the concentration as the free polymer. This difference can be explained by considering the relative polymer chain lengths in the two systems. In the low MW PHIC region

(<≈50K) the molecule weight dependence of the critical concentration of PHIC increases very steeply with decreasing MW and hence chain lengths.<sup>[43]</sup> When comparing the star polymer with a linear polymer with an equivalent MW, the proposed rod-like arrangement by the authors would essentially lower the end-to-end chain length of PHIC thereby raising the critical concentration. Assuming a symmetric three-arm star polymer, this would mean an axis ratio roughly two-thirds of the linear polymer. In contrast, an equivalent linear polymer to the NP system would be twice that of the synthesized PHIC ligand. Combined with the dense polymer corona, this would essentially lower the lyotropic critical concentration.

Theoretical developments regarding the chain conformation of semiflexible polymer chains have evolved beyond the simple lattice models and single-chain behavior to wormlike and bead-and spring models that incorporate small angle bending de-formations, suitable for investigating the effects of shear forces or confinement.<sup>[32]</sup> Recent combined density functional theory (DFT) and molecular dynamics (MD) simulations of solutions of semiflexible polymers were used to calculate the LC phase diagrams as a function of chain length and stiffness.<sup>[50]</sup> This approach has recently been extended to explore the effect of applied magnetic or electric fields on lyotropic semiflexible polymer solutions.<sup>[51]</sup>

Tethering the PHIC chains to the nanoparticle surfaces is a form of confinement. The effect of confinement in polymer conformation and chain dynamics has been extensively studied for flexible polymers,<sup>[52]</sup> but confined semiflexible polymer have only recently been studied.<sup>[53]</sup> There have been relatively few theoretical studies of semiflexible polymer brushes. Simulations of semiflexible polymer brushes on flat surfaces reveal spontaneous transitions to liquid crystalline order.<sup>[53-57]</sup> Subsequent studies showed that with increasing chain density and stiffness, spontaneous tilting transitions occur to maximize the chain-chain interactions.<sup>[58,59]</sup> However, relevant to the polymer grafted NPs presented here, the effect of surface curvature on the properties of semiflexible brushes and interactions between such brushes has not yet been theoretically explored.<sup>[60]</sup>

The conformation of the NP tethered PHIC<sub>180</sub> chains should be consistent with both the formation of NP linear assemblies and nematic chain order. If the PHIC<sub>180</sub> chains with a grafting density of [1.9 ch nm<sup>-2</sup>] on the 4 nm dia. NPs were strictly behaving as rigid rods, then within the ligand shell, the polymer chains would occupy a volume fraction of only ≈0.05. In chloroform the onset of liquid crystallinity for PHIC<sub>180</sub> occurs at a polymer volume fraction of ≈0.30 (0.20 weight fraction). Extensive intercalation of the ligand shells of NPs with rigid rod PHIC chains would increase the polymer volume fraction but this should result in a cubic rather than nematic lyotropic LC phase.

To account for both the nematic order and the formation of linear arrays, we propose that the PHIC<sub>180</sub> ligands can tilt and bend about the inorganic core to splay the ligand shell and form rod-like rather than spherical shapes, as shown in the inset in Figure 2-2a. The hydroxypropyl phosphonate linkages connecting the PHIC chains to the NPs also provide some flexibility, similar to the rotation of the PHIC arms of the star polymer via the carbamate bonds.<sup>[49]</sup> Then the linear arrays assemble through lateral interactions between the PHIC ligands of neighboring NPs, resulting in interparticle distances of ≈5 nm within the chains of NPs which in turn are separated from neighboring chains by roughly twice the PHIC<sub>180</sub> brush lengths.

We report a new type of lyotropic LC nanomaterial, based on semiflexible polymer grafted NPs, where anisotropic phases are formed from isotropic particles. A “grafting to” protocol to produce NPs with dense polymer coronas with higher molecular weights was developed. Nematic rather than cubic phases arise from the spherical NPs via splaying of the polymer ligand shell. We note that anisotropic lyotropic nanomaterial phases have previously only been formed from rod- or disc-like NPs. Despite being attached to the NPs, the PHIC chains display a high degree of orientational order comparable to the free polymer solutions. However, the confinement of the PHIC chains to the NPs results in a lowering of the critical concentration for liquid crystallinity and a widening of the isotropic/nematic biphasic region. The nematic ordering of the PHIC ligands is also responsible for the formation of the linear NP assemblies. Ongoing work is extending this approach to plasmonic NPs and other semiflexible polymers such as synthetic polypeptides.

Other variables to be explored are the effect of particle size and grafting densities. Finally, the PHIC grafted NPs can serve as a useful model for understanding the properties of semiflexible polymer brushes on curved surfaces, a feature of many biological structures, that has yet to be theoretically explored.

## **2.5 Experimental Methods**

### **2.5.1 Materials**

All chemicals were commercially bought from Sigma-Aldrich. The hexyl isocyanate monomer was purified by initially drying over  $\text{CaH}_2$  overnight and distilled the following day. Commercial grade solvents were purified according to standard methods<sup>1,2</sup>

### **2.5.2 Synthesis of Initiator-functionalized 23K MW Poly-(hexyl isocyanate) (PHIC<sub>180</sub>)**

The one-pot synthesis of PHIC was adapted from Satoh et al<sup>28</sup>. Extra caution was taken as to exclude moisture from the reaction mixture. Initially, in a 50 mL Schlenk flask,  $\text{CpTiCl}_3$  (30 mg; 0.136 mmol) was allowed to homogenize with dry DCM (1.0 mL). Afterwards, the phosphonic acid initiator (26.6 mg; 0.136 mmol) was added and allowed to react 3H at room temperature. Afterwards, the Schlenk flask was put under vacuum overnight. The following day, HIC (9 mL; 0.0811 mol;  $[\text{HIC}]/[\text{CPTiCl}_3]=297.0$ ) was added to the Schlenk flask at 0°C and allowed to react for 24H. Afterwards, the mixture should be completely solidified and termination was achieved by adding acetic anhydride (56 mL; 594 mmol) and  $\text{BF}_3 \cdot \text{OEt}_2$  (2.20 mL; 17.8 mmol) and allowed to react for another 24H. The polymer was precipitated in methanol at 0°C; the filtrate was discarded while the precipitate was re-dissolved in the minimum amount of THF and subsequently precipitated another two times in cold methanol. The retrieved polymer was then dried under vacuum to obtain a white solid powder.

### 2.5.3 ZrO<sub>2</sub> Nanoparticle Synthesis

The synthesis of benzyl alcohol functionalized zirconia nanoparticles were adapted from Garnweitner et al.<sup>[61]</sup> Zirconium (IV) isopropoxide isopropanol complex (2.00 g) was weighed into a 30 mL glass vial within a sealed Teflon cup. Afterwards anhydrous benzyl alcohol (30 mL) was added into the glass vial under an inert atmosphere and the Teflon cup was sealed and subsequently placed inside a steel reactor which was then heated to 230°C for four days. After letting the reactor cool down to room temperature for an additional day, the nanoparticles were washed three times with anhydrous THF (discarding the supernatant) and the resulting nanoparticles were obtained via centrifugation.

### 2.5.4 PHIC Functionalization of ZrO<sub>2</sub> Nanoparticles

The required amount of PHIC ligand was stoichiometrically calculated based on the grafting density of the benzyl alcohol on the nanoparticle surface (quantified via TGA). Typically, in a 30 mL dram vial, phosphonic acid functionalized PHIC was dissolved in dry THF until homogenous. Afterwards, the suspension of benzyl alcohol stabilized ZrO<sub>2</sub> NPs in THF was added to the dissolved PHIC solution and allowed to react for three days to maximize surface functionalization. Purification was accomplished through quantitative precipitation, which initially involves the addition of methanol until the NP solution becomes cloudy followed by centrifugation. The resulting supernatant was discarded and the NPs were re-dissolved and precipitated with THF and methanol another three times and finally vacuum dried to afford a white powder.

### 2.5.5 Polarized Optical Microscopy

POM images were obtained using a Nikon model SMZ1500 stereomicroscope. Lyotropic samples were prepared by weighing the appropriate amounts of PHIC/ZrO<sub>2</sub>- PHIC and solvent into a 3 mL dram vial. The dram vial was subsequently homogenized using a stand mixer for a few hours up to overnight, depending on the viscosity of the lyotropic sample. A drop of the solution

was transferred to a microscope slide and secured with a cover slide then observed immediately under POM due to the volatility of DCM.

### **2.5.6 Molecular Weight Determination by GPC and $^1\text{H}$ NMR**

The MW was determined either through GPC using a Shimadzu instrument and through the NMR using a Varian VNMRS 500MHz spectrometer and polystyrene as the standard. MW calculated through NMR was done by calculating the ratio between the  $^1\text{H}$  NMR peaks at 2.28 ppm and from 3.10-4.20 ppm, corresponding to the terminal acetyl group and the repeating proton units along the side chains (adjacent to the nitrogen), respectively <sup>27</sup>.

### **2.5.7 $^2\text{H}$ NMR Spectroscopy**

In the case of a 20% w/w solution of  $\text{ZrO}_2\text{-PHIC}_{180}$  NPs, typically,  $\text{ZrO}_2\text{-PHIC}_{180}$  (100 mg) was added into a Norell heavy-walled NMR tube (2.20 mm inner diameter) as to withstand centrifugal forces. Afterwards, the NMR tube was centrifuged at 5000RPM for 20 minutes at room temperature as to simultaneously homogenize and maximize phase separation between the isotropic and liquid crystalline. As to minimize solvent evaporation and maintain the measured concentration, NMR was taken immediately following centrifugation.  $^2\text{H}$  NMR spectra were collected on a 800 MHz Bruker Avance III HD spectrometer. A standard 16-scan  $^2\text{H}$  NMR pulse sequence was used to obtain deuterium spectra and quadrupolar splittings. All other spectra were collected on a Varian VNMRS 500 MHz spectrometer.

### **2.5.8 Transmission Electron Microscopy (TEM)**

TEM images were obtained using a Talos F200X G2 (S)TEM instrument with an accelerating electron voltage of 200 kV.

### **2.5.9 Thermogravometric Analysis (TGA)**

TGA measurements were performed on a TA instruments Q500 instrument. Samples were heated at a rate of 20°C up to 800°C, with the atmosphere being exchanged from nitrogen to air at 600°C.

### **2.5.10 Acknowledgements**

This research was funded by a Discovery Grant from the National Sciences and Engineering Research Council of Canada (NSERC). The authors thank Dr. Robin Stein for experimental assistance.

## 2.6 References

- [1] R. Mezzenga, J. M. Seddon, C. J. Drummond, B. J. Boyd, G. E. Schröder-Turk, L. Sagalowicz, *Adv. Mater.* **2019**, *31*, 1900818.
- [2] I. W. Hamley, *Soft Matter*, **2010**, *6*, 1863.
- [3] I. Dierking, A. Martins Figueiredo Neto, *Crystals* **2020**, *10*, 604.
- [4] I. Dierking, S. Al-Zangana, *Nanomaterials* **2017**, *7*, 305.
- [5] S. Zhang, C. I. Pelligra, G. Keskar, P. W. Majewski, f. Ren, L. D. Pfefferle, C. O. Osuji, *ACS Nano* **2011**, *5*, 8357.
- [6] L. S. Li, J. Walda, L. Manna, A. P. Alivisatos, *Nano Letters* **2002**, *2*, 557.
- [7] S. Meuer, P. Oberle, P. Theato, W. Tremel, R. Zentel, *Adv. Mater.* **2007**, *19*, 2073.
- [8] M. Zorn, S. Meuer, M. N. Tahir, Y. Khalavka, C. Sönnichsen, W. Tremel, R. Zentel, *J. Mater. Chem.* **2008**, *18*, 3050.
- [9] S. M. Taheri, S. Fischer, M. Trebbin, S. With, J. H. Schröder, J. Perlich, s. V. Roth, S. S. Förster, *Soft Matter* **2012**, *8*, 12124.
- [10] M. J. Hore, *Soft Matter* **2019**, *15*, 1120.
- [11] D. Voerman, M. Schluck, J. Weiden, B. Joosten, L. J. Eggermont, T. van den Eijnde, B. Ignacio, A. Cambi, C. G. Figdor, P. H. Kouwer, *Biomacromolecules* **2019**, *31*, 2587.
- [12] B. Liu, J. Liu, *Matter* **2019**, *1*, 825.
- [13] J. Zong, S. L. Cobb, N. R. Cameron, *Biomater. Sci.* **2017**, *5*, 872.
- [14] W. Cheng, M. J. Campolongo, J. J. Cha, S. J. Tan, C. C. Umbach, D. A. Muller. D. Luo, *Nature Mater.* **2009**, *8*, 519.
- [15] C. Rosu, S. Balamurugan, R. Cueto, A. Roy, P. S. Russo, *J. Phys. Chem. B.* **2016**, *120*, 7275.
- [16] C. Rosu, S. Jacobeen, K. Park, E. Reichmanis, P. Yunker, P. S. Russo, *Langmuir* **2016**, *13*, 13137.
- [17] H. Tang, D. Zhang, *J. Poly. Sci. A: Poly. Chem.* **2010**, *1*, 2340.
- [18] P. J. Flory, *Proc. R. Soc. London, Ser. A* **1956**, *234*, 60.
- [19] W. Miller, *Ann. Rev. Phys. Chem.* **1978**, *29*, 519.
- [20] S. M. Aharoni, *J. Macromolecular Sci. B* **1982**, *21*, 105.

- [21] A. I. Barzic, R. Marinic Albu, L. I. Buruiana L.I. in *High Performance Polymers and Their Nanocomposites* (Eds: P. M. Visakh, A. O. Semkin) John Wiley & Sons, Hoboken NJ, **2018**, Ch. 2.
- [22] S. M. Aharoni, *J. Macromolecular Sci. B* **1982**, *21*, 105.
- [23] S. M. Aharoni, *Macromolecules* **1979**, *12*, 94.
- [24] S. Mayer, R. Zentel, *Prog. Polymer Sci.* **2001**, *26*, 973
- [25] I. G. Bak, C. G. Chae, J. S. Lee *Macromolecules* **2022**, *55*, 1923.
- [26] X. Liu, R. Cheng, J. Deng, Y. Wu, *RSC Advances*. **2014**, *4*, 48796.
- [27] F. Vatansever, M. R. Hamblin, *Macromol. Res.* **2017**, *25*, 97.
- [28] T. Satoh, R. Ihara, D. Kawato, N. Nishikawa, D. Suemasa, Y. Kondo, K. Fuchise, R. Sakai, T. Kakuchi, *Macromolecules* **2012** *45*, 3677.
- [29] S. M. Aharoni, E. K. Walsh *J. Polymer Sci. Polymer Lett.* **1979**, *17*, 321.
- [30] S. M. Aharoni, E. K. Walsh, *Macromolecules* **1979** *12*, 271.
- [31] A. D. Rey, T. Tsuji. *Macromol. Theory Simul.* [ **1998**, *7*, 623.
- [32] J. H. Kim, M. S. Rahman, J. S. Lee, J. W. Park, *J. Am. Chem. Soc.* **2007**, *129*, 7756.
- [33] K. Binder, S. A. Egorov, A. Milchev, A. Nikoubashman, *J. Phys. Mater.* **2020**, *3*, 032008.
- [34] T. Sato, A. Teramoto, A. *Adv. Polym. Sci.* **1996**, *126*, 85.
- [35] J. K. Moscicki, B. Robin-Lherbier, D. Canet, S. M. Aharoni S.M. *J. Phys. Lett.* **1984** *45*, 379.
- [36] H. Wang, R. J. Wittebort, D. B. DuPré, *J. Chem. Phys.* **1993** *99*, 7449.
- [37] G. Ronca, D. Y. Yoon, *J. Chem. Phys.* **1985** *83*, 373.
- [38] J. Voigt, T. Bjorholm, J. P. Jacobsen, *Israel J. Chem.* **1983**, *23*, 291.
- [39] J. Jokisaari, Y. Hiltunen, *J. Mag. Res.* **1984**, *60*, 307.
- [40] T. Barbara, B. P. Dailey, *Mol. Cryst. Liq. Cryst.* **1982**, *87*, 239.
- [41] W. Lewandowski, M. Wójcik, E. Górecka, *ChemPhysChem.* **2014**, *15*, 1283.
- [42] J. Milette, V. Toader, L. Reven, R. B. Lennox, *J. Mater. Chem.* **2011**, *21*, 9043.
- [43] J. Milette, V. Toader, E. R. Soulé, R. B. Lennox, A. D. Rey, L. Reven, *Langmuir* **2013**, *29*, 1258.
- [44] T. Itou, A. Teramoto, *Macromolecules* **1988**. *21*, 2225.
- [45] B. Zhao, W. J. Brittain, *Prog. Poly. Sci.* **2000**, *25*, 677.
- [46] J. H. Kim, M. S. Rahman, J. S. Lee, J. W. Park, *J. Am. Chem. Soc.* **2007** *129*, 7756.

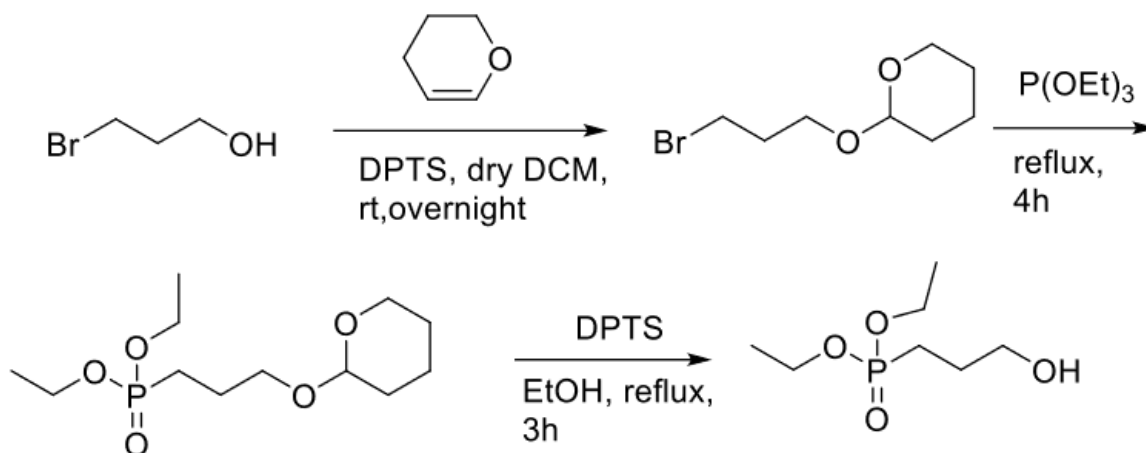
- [47] J. H. Kim, m. S. Rahman, J. S. Lee, J. W. Park, *Macromolecules* **2008** *41*, 3181.
- [48] H. D. Koh, J. W. Park, M. S. Rahman, M. Changez, J. S. Lee, *Chem. Commun.* **2009** *32*, 4824.
- [49] N. J. Fernandes, H. Koerner, E. P. Giannelis, R. A. Vaia. *MRS Commun.* 2013, 13.
- [50] S. H. Goodson, B. M. Novak, *Macromolecules* **2001**, *34*, 3849.
- [51] J. Midya, S. A. Egorov, K. Binder K, A. Nikoubashman *J. Chem. Phys.* **2019** *151*, 034902.
- [52] S. A. Egorov, *J. Phys. Chem. B.* **2021**, *125*, 1513.
- [53] L. Zhu, X. Wang, Q. Gu, W. Chen, P. Sun, G. Xue *Macromolecules* **2013** *46*, 2292.
- [54] A. Nikoubashman, *J. Chem. Phys.* **2021** *154*, 090901.
- [55] D. V. Kuznetsov, Z. Y. Chen, Z. Y. *J. Chem. Phys.* **1998** *109*, 7017.
- [56] A. Milchev, K. Binder, *J. Chem. Phys.* **2012**, *136*, 194901.
- [57] P. Benetatos, E. M. Terentjev, A. Zippelius, *Phys. Rev. E.* **2013** *88*, 042601.
- [58] S. A. Egorov, H. Hsu, A. Milchev, K. Binder, *Soft Matter* **2015**, *11*, 2604.
- [59] S. Blaber, N. M. Abukhdeir, M. W. Matsen, *Macromolecules* **2019**, *52*, 6988.
- [60] J. H. Huang, D. D. Sun, R. X. Lu, *Phys. Chem. Chem. Phys.* **2021**, *23*, 13895.
- [61] S. A. Egorov, *Polymers* **2021**, *13*, 2296.

## 2.7 Supporting Information

Jessie Wong, Violeta Toader and Linda Reven\*

### 2.7.1 Synthesis of diethyl (3-hydroxypropyl)phosphonate.

The synthesis of diethyl (3-hydroxypropyl)phosphonate was performed over three steps starting with 3-bromopropanol and following, with a slight modification, the procedure of Voight et al.<sup>1</sup> (Scheme 2-4)



Scheme 2-4 Synthesis of diethyl (3-hydroxypropyl)phosphonate).

#### *Step 1. Synthesis of 2-(3-bromopropoxy)tetrahydro-2H-pyran<sup>1</sup>*

1-bromopropanol (2.43 g, 17.5 mmol, 1 eq) was dissolved in 80 mL dry dichloromethane under an inert atmosphere. To the solution 3,4-dihydro-2H-pyran (2 mL, 25.78 mmol, 1.5eq) was added followed by dimethylamino pyridinium p-toluenesulfonate (880 mg, 3 mmol) was added to the solution and the reaction mixture was stirred overnight. Work up was performed following the procedure of Kier et al.<sup>2</sup> 0.5 g of  $\text{NaHCO}_3$  and 1.5g of  $\text{MgSO}_4$  were added and the reaction

mixture was stirred for 15 minutes and then filtrated through a Silica Gel – Celite pad (4 :1, w : w). The pad was washed with dichloromethane and the filtrate was concentrated under reduced pressure. The residue was further purified by column chromatography (SiO<sub>2</sub>, Hexanes : Ethyl Acetate, 9 : 1, (v : v), R<sub>f</sub> = 0.34). 3.42 g (87.62 %).

<sup>1</sup>H NMR (500 MHz, CDCl<sub>3</sub>) δ 4.60 (t, J = 4.5 Hz, 1H), 3.91-3.80 (m, 2H), 3.58-3.45 (m, 4H), 2.17 (quintet, J = 7.8Hz, 2H, CH<sub>2</sub>Br), 1.89-1.45 (m, 6H). <sup>13</sup>C NMR (126 MHz, CDCl<sub>3</sub>) δ 99.04, 77.41, 65.03, 62.40, 33.04, 30.81, 30.73, 25.55, 19.62

#### *Step 2. Synthesis of diethyl (3-((tetrahydro-2H-pyran-2-yl)oxy)propyl)phosphonate<sup>2</sup>*

A mixture of 2-(3-bromopropoxy)tetrahydro-2H-pyran (3.42 g, 15.4 mmol, 1eq.) and triethylphosphite (3.82 g, 3.95mL, 23 mmol, 1.5 eq.) was heated at 150 C for 4 hours. The reaction mixture was cooled down and the excess of triethylphosphite and by-products were removed by distillation under reduced pressure. The residue was purified by column chromatography (SiO<sub>2</sub>, Ethyl Acetate : Methanol, 10 : 1, (v : v), R<sub>f</sub> = 0.60). 3.1611 g of product was obtained as a colourless oil (73.20 %).

<sup>1</sup>H NMR (400 MHz, CDCl<sub>3</sub>) δ 4.56 (t, J = 3.6 Hz, 1H), 4.06 (q, J = 7.2 Hz, 4H), 3.86-3.59 (m, 2H), 3.54-3.34 (m, 2H), 1.94-1.44 (m, 10H), 1.29 (t, J = 6.9 Hz, 6H).

<sup>13</sup>C NMR (126 MHz, CDCl<sub>3</sub>) δ 98.88, 67.20 (d, J = 17.9 Hz), 62.41, 61.59 (J = 6.5 Hz), 30.76, 25.55, 23.11 (J = 4.7 Hz), 22.7 (J = 142.4 Hz), 19.64, 16.58 (J = 6.1Hz).

<sup>31</sup>P NMR (162 MHz, CDCl<sub>3</sub>) δ 32.30.

*Step 3. Synthesis of diethyl (3-hydroxypropyl)phosphonate.*

Diethyl 3-((tetrahydro-2H-pyran-2-yl)oxy)propylphosphonate (3.16 g, 11.27 mmol) was dissolved in 250 mL ethanol. DPTS (0.318 g, 1.27 mmol) was added and the reaction mixture was heated at reflux. The progress of the reaction was monitored by taking aliquots that were analyzed by  $^{31}\text{P}$  NMR. When the signal at 32.3 ppm was no longer detectable, the reaction mixture was cooled at room temperature. The solvent was removed under reduced pressure and the residue was purified by column chromatography ( $\text{SiO}_2$ , Dichloromethane:Methanol, 9:1, (v:v),  $R_f = 0.56$ ). 0.9464 g of product was obtained (42.70 %) as a colourless oil.

$^1\text{H}$  NMR (500 MHz,  $\text{CDCl}_3$ )  $\delta$  4.16-4.02 (m, 4H,  $\text{POCH}_2\text{CH}_3$ ), 3.68 (t,  $J = 5.5$  Hz, 2H,  $\text{HOCH}_2\text{CH}_2$ ), 1.90-1.78 (m, 4H,  $\text{BrCH}_2(\text{CH}_2)_2$ ), 1.31 (t,  $J = 7.05$  Hz,  $\text{POCH}_2\text{CH}_3$ )

$^{13}\text{C}$  NMR (126 MHz,  $\text{CDCl}_3$ )  $\delta$  62.51 (d,  $J = 12.95$  Hz), 61.86 (d,  $J = 6.57$  Hz), 25.79 (d,  $J = 6.22$  Hz), 22.67 (d,  $J = 142.30$  Hz), 16.55 (d,  $J = 5.92$  Hz).

$^{31}\text{P}$  NMR (203 MHz,  $\text{CDCl}_3$ )  $\delta$  33.24.

## 2.7.2 Thermogravimetric Analysis (TGA) for PHIC grafting densities

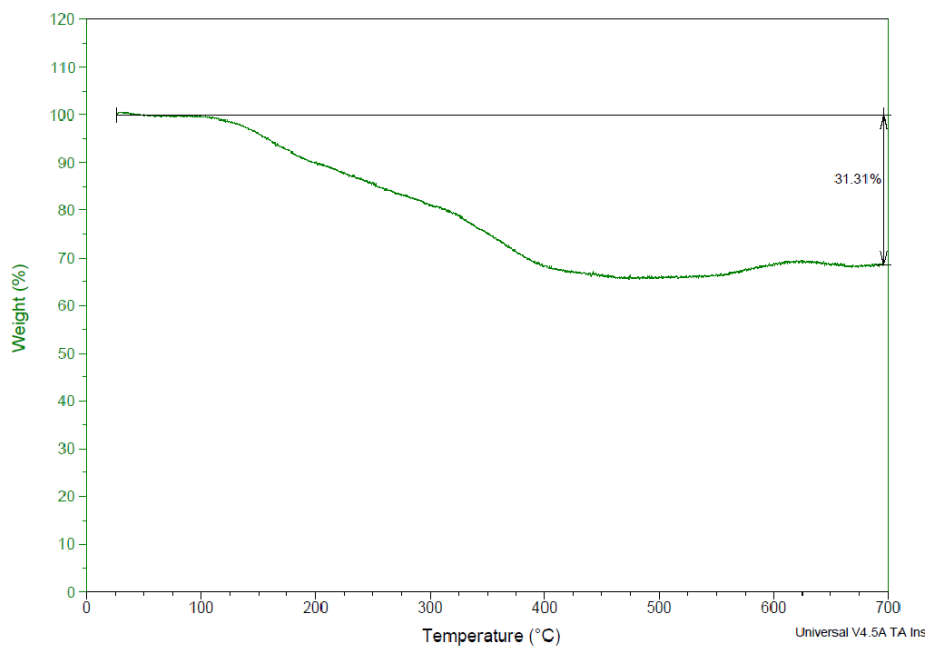


Figure 2-4 TGA Curve of ZrO<sub>2</sub> – PHIC<sub>24</sub> prepared using scheme 1.

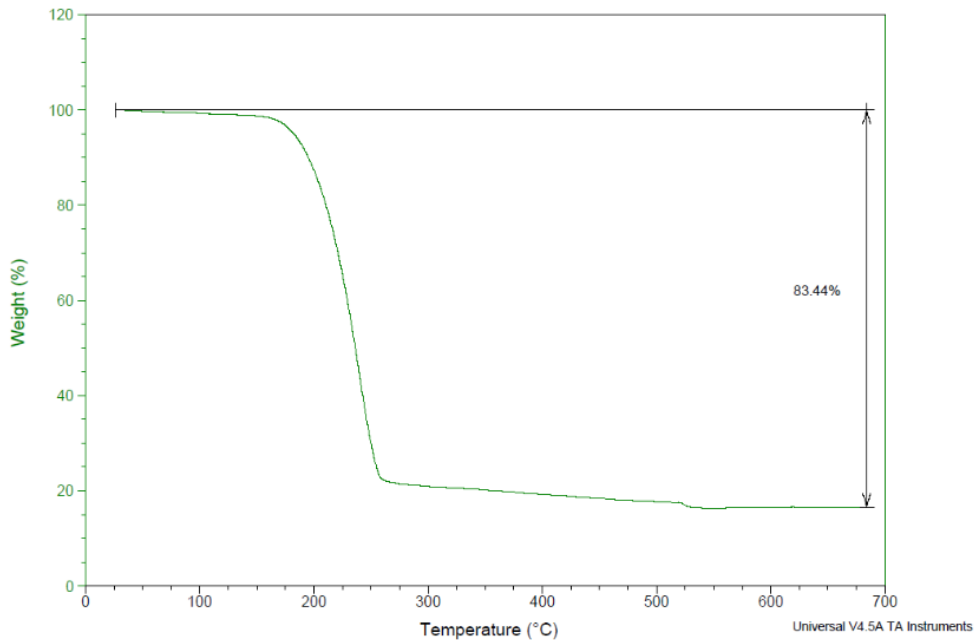


Figure 2-5 TGA Curve of ZrO<sub>2</sub> – PHIC<sub>55</sub> prepared using scheme 2.

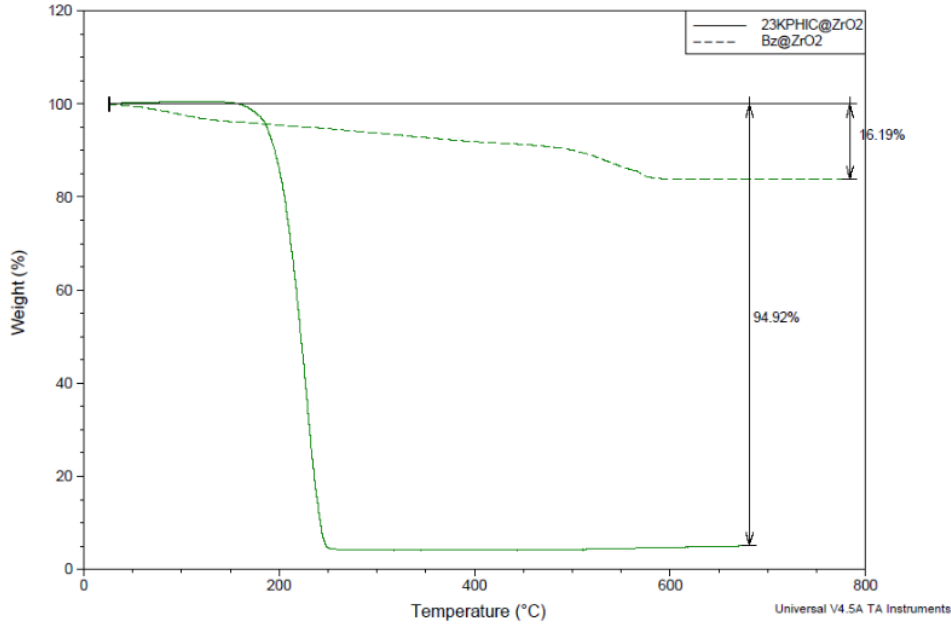


Figure 2-6 TGA Curve of  $ZrO_2$  –  $PHIC_{180}$  prepared using scheme 3.

**2.7.3 Sample calculation** for a 1.00 g sample of  $ZrO_2$ - $PHIC_{180}$  (2 nm core radius) prepared using scheme 3 with a TGA loss of 94.92%:

Organic Content:

$$0.9492 g_{PHIC_{180}} * \frac{1}{23000 \frac{g}{mol_{PHIC_{180}}}} * \left( 6.022 * 10^{23} \frac{molecules}{mol} \right)$$

$$= 2.485 * 10^{19} PHIC_{180} chains$$

Inorganic Content:

$$0.0508 g_{ZrO_2} * \frac{1}{5.63 \frac{g}{cm^3}} * \frac{1}{\frac{4}{3}\pi(2)^3 nm^3} = 2.692 * 10^{17} ZrO_2 nanoparticles$$

Chains per Nanoparticle:

$$\frac{2.485 * 10^{19} PHIC_{180} chains}{2.692 * 10^{17} ZrO_2 nanoparticles} = 92 chains/NP$$

Grafting Density:

$$\frac{92 chains}{4\pi(2)^2 nm^2} = 1.836 chains/nm^2$$

Surface Footprint:

$$\frac{1}{4.101 \frac{\text{chains}}{\text{nm}^2}} = 0.544 \text{ nm}^2/\text{chain}$$

**Table 2-2 Comparison of grafting densities between various PHIC coated NPs.**

	Bz@ZrO <sub>2</sub>	ZrO <sub>2</sub> -PHIC <sub>24</sub> NPs	ZrO <sub>2</sub> -PHIC <sub>55</sub> NPs	ZrO <sub>2</sub> -PHIC <sub>180</sub> NPs
Ligand MW	108	3000	13000	23000
Ligand Footprint (nm <sup>2</sup> /chain)	0.24	2.91	0.87	0.54
Ligand Density (chains/nm <sup>2</sup> )	4.07	0.34	1.41	1.84

#### 2.7.4 <sup>1</sup>H and <sup>31</sup>P NMR spectra

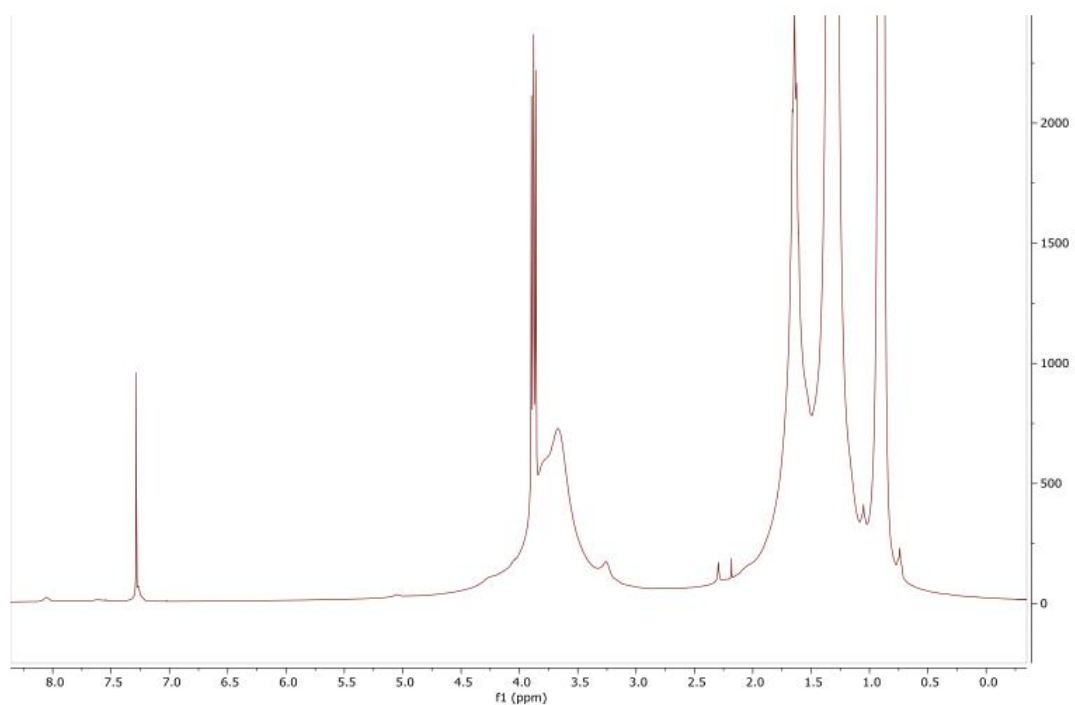


Figure 2-7 <sup>1</sup>H NMR spectrum of ZrO<sub>2</sub>-PHIC<sub>180</sub> NPs

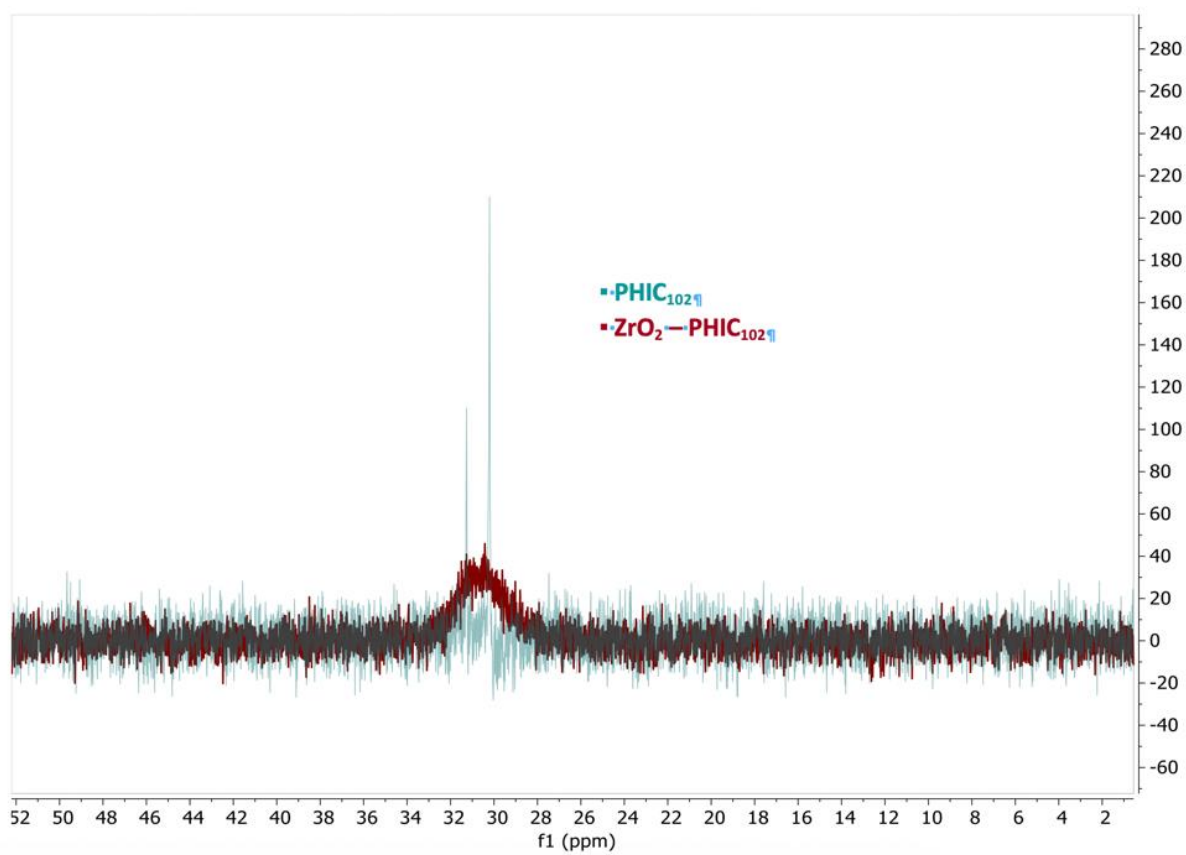


Figure 2-8  $^{31}\text{P}$  NMR of ZrO<sub>2</sub>-PHIC<sub>180</sub> NPs

## 2.7.5 <sup>1</sup>H NMR and GPC MW analyses

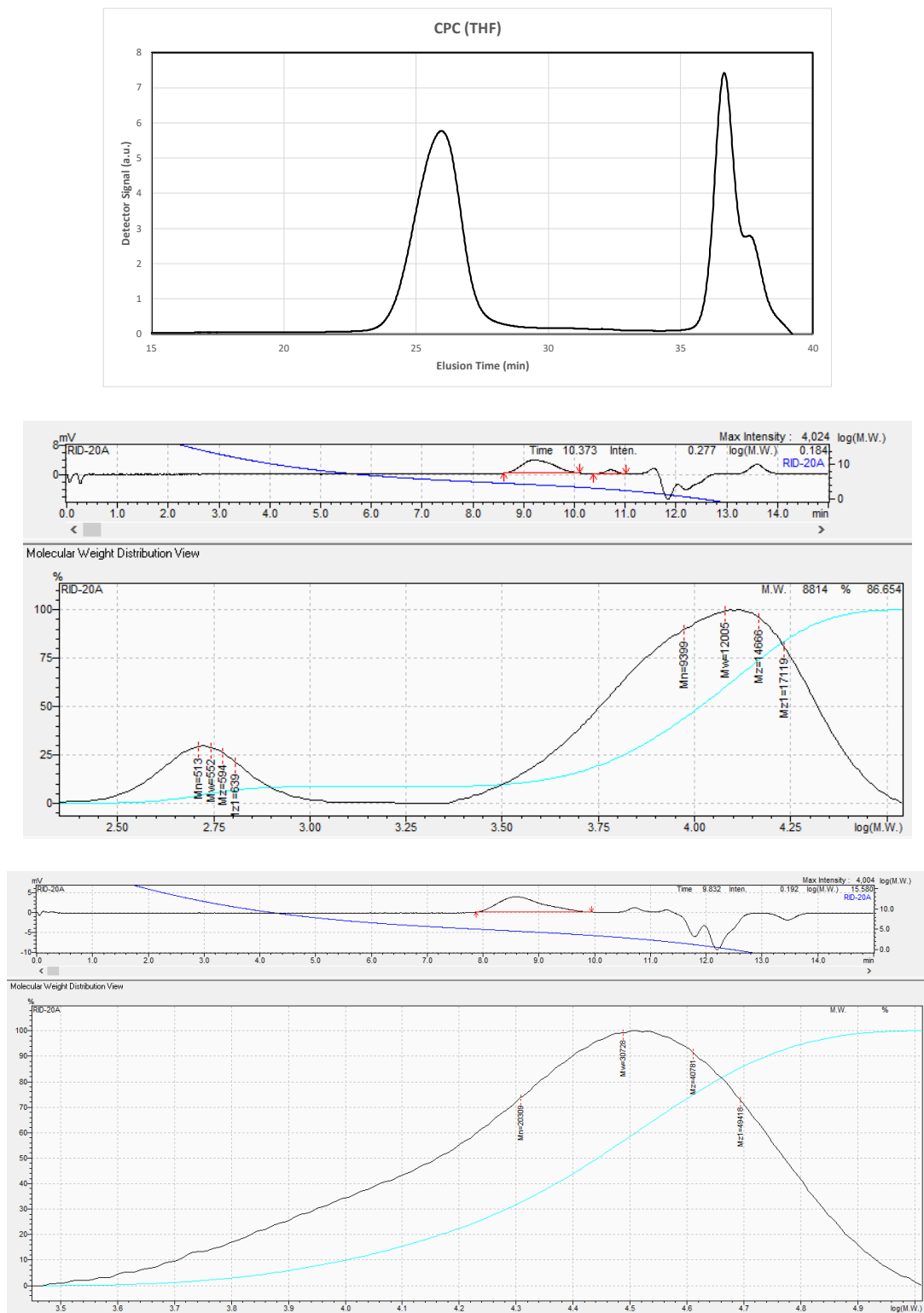


Figure 2-9 GPC of PHIC<sub>24</sub> (top), PHIC<sub>55</sub> (middle), PHIC<sub>180</sub> (bottom) from scheme 3.

**Table 2-3 Summarized molecular weight results**

	<b>NMR</b>	<b>GPC</b>	
	<b>M<sub>w</sub></b>	<b>M<sub>w</sub></b>	<b>PDI</b>
<b>PHIC<sub>24</sub></b>	3000	6800	1.18
<b>PHIC<sub>55</sub></b>	9000	12000	1.27
<b>PHIC<sub>180</sub></b>	22800	30100	1.51

The average molecular weight and molecular distribution ( $M_w / M_n$ ) were determined by GPC/SEC analyses run at 40°C using a Shimadzu instrument (Kyoto, Japan), equipped with a Shodex K-805L (300 x 8 mm, 10 μm) analytical column and a Shodex K-G 4A (10 x 4.6 mm, 8 μm) guard column. The mobile phase was HPLC grade chloroform (THF for PHIC<sub>24</sub>) that was delivered at a flow rate of 1 mL/min by a LC-20AR pump. 30 μL of 1mg/mL sample solution was injected and the signal of the RID detector (RID-20A) was analyzed and compared against the calibration curve. PS standards with narrow molecular weight in the range from 266 to 1 x 10<sup>6</sup> g/mol were used for calibration.

Data analyses was performed with Lab Solution –GPC Postrun software (Shimadzu, Kyoto, Japan).

### 2.7.6 TEM images and histograms of interparticle distances

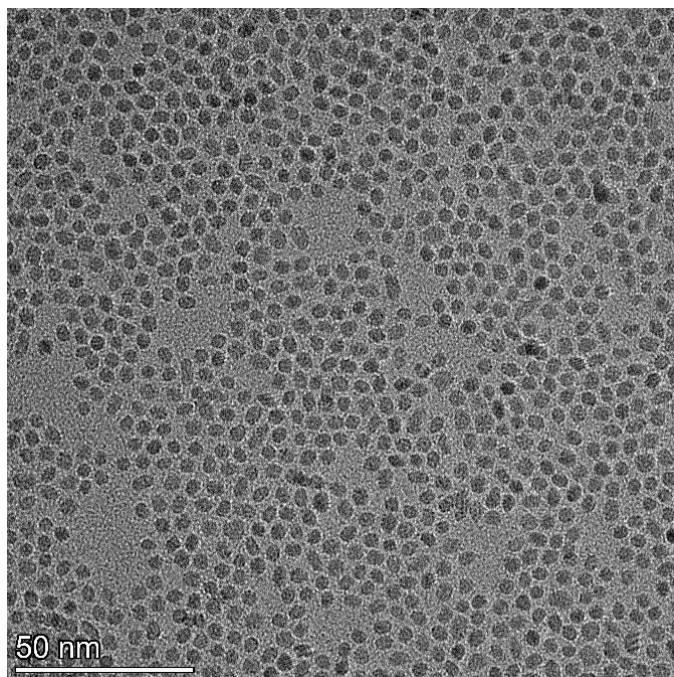


Figure 2-10: TEM of Benzyl alcohol stabilized  $ZrO_2$  NPs.

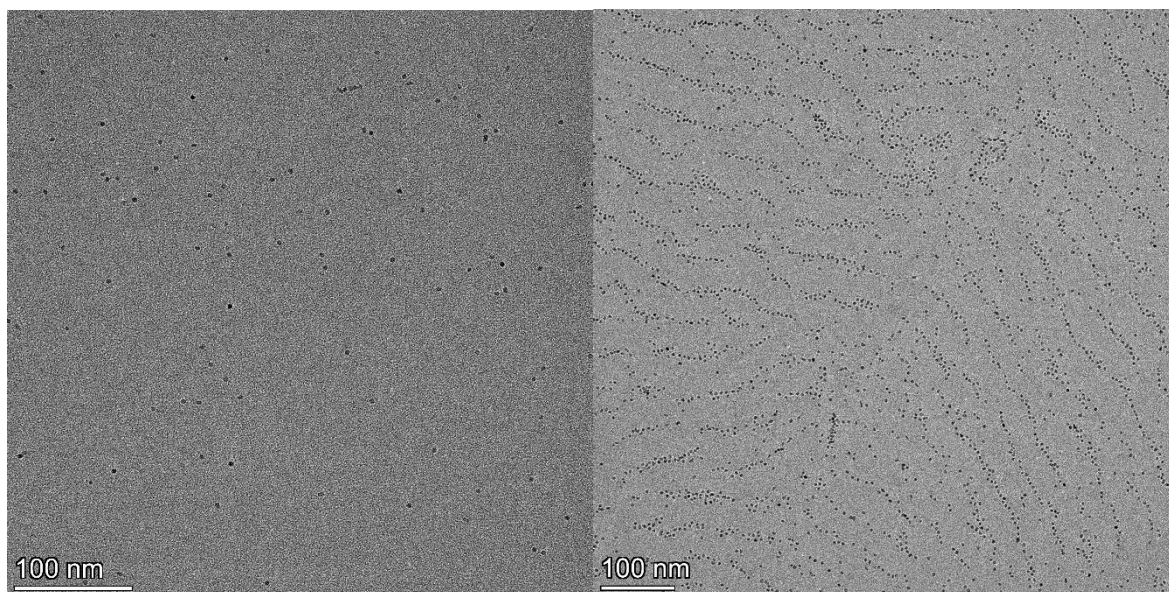


Figure 2-11 TEM of  $ZrO_2$ -PHIC<sub>180</sub> NPs drop casted from dilute (left) and concentrated (right) solutions.

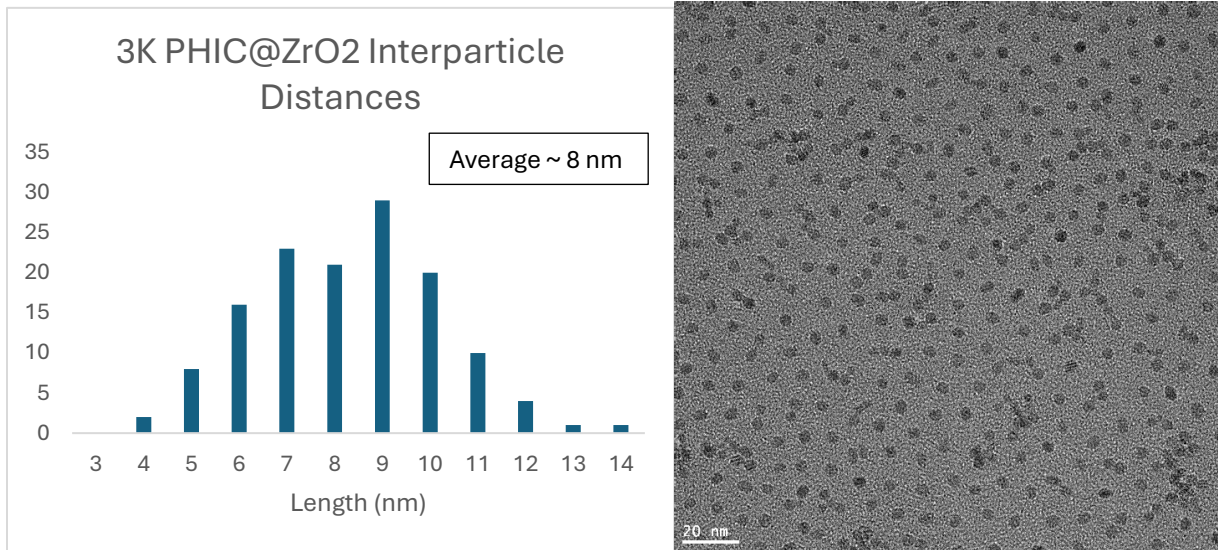


Figure 2-12 TEM and corresponding histogram of ZrO<sub>2</sub> – PHIC<sub>24</sub> NPs

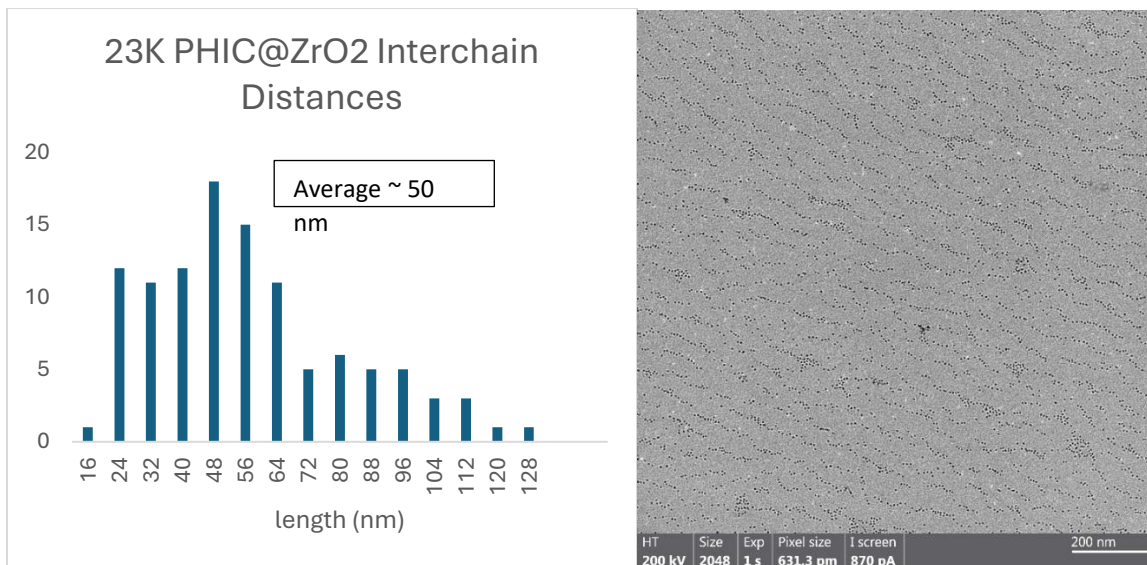


Figure 2-13 TEM and corresponding histogram of the inter-chain distances for ZrO<sub>2</sub> – PHIC<sub>180</sub> NPs.

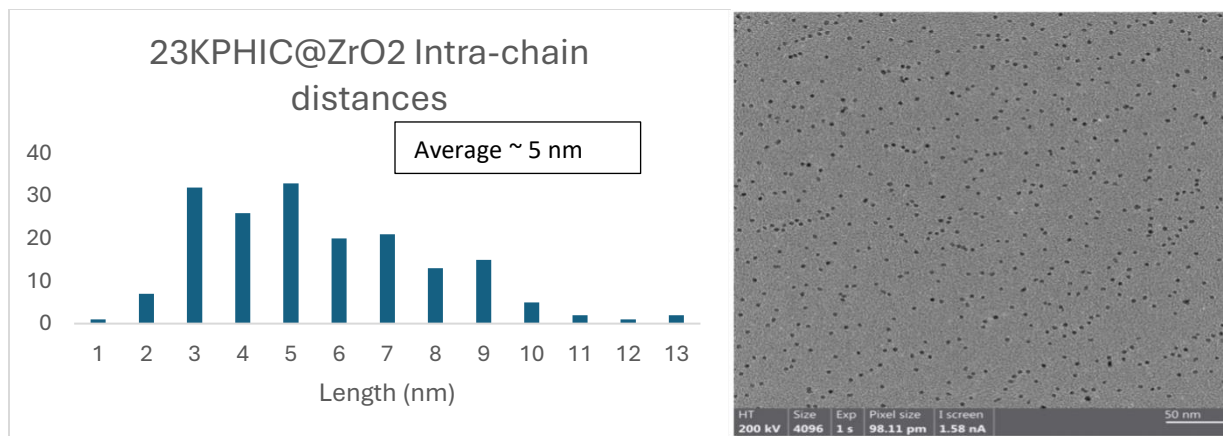


Figure 2-14 TEM and corresponding histogram of the intra-chain distances for  $\text{ZrO}_2$  – PHIC<sub>180</sub>

NPs.

### 2.7.7 POM images corresponding to the $^2\text{H}$ NMR samples.

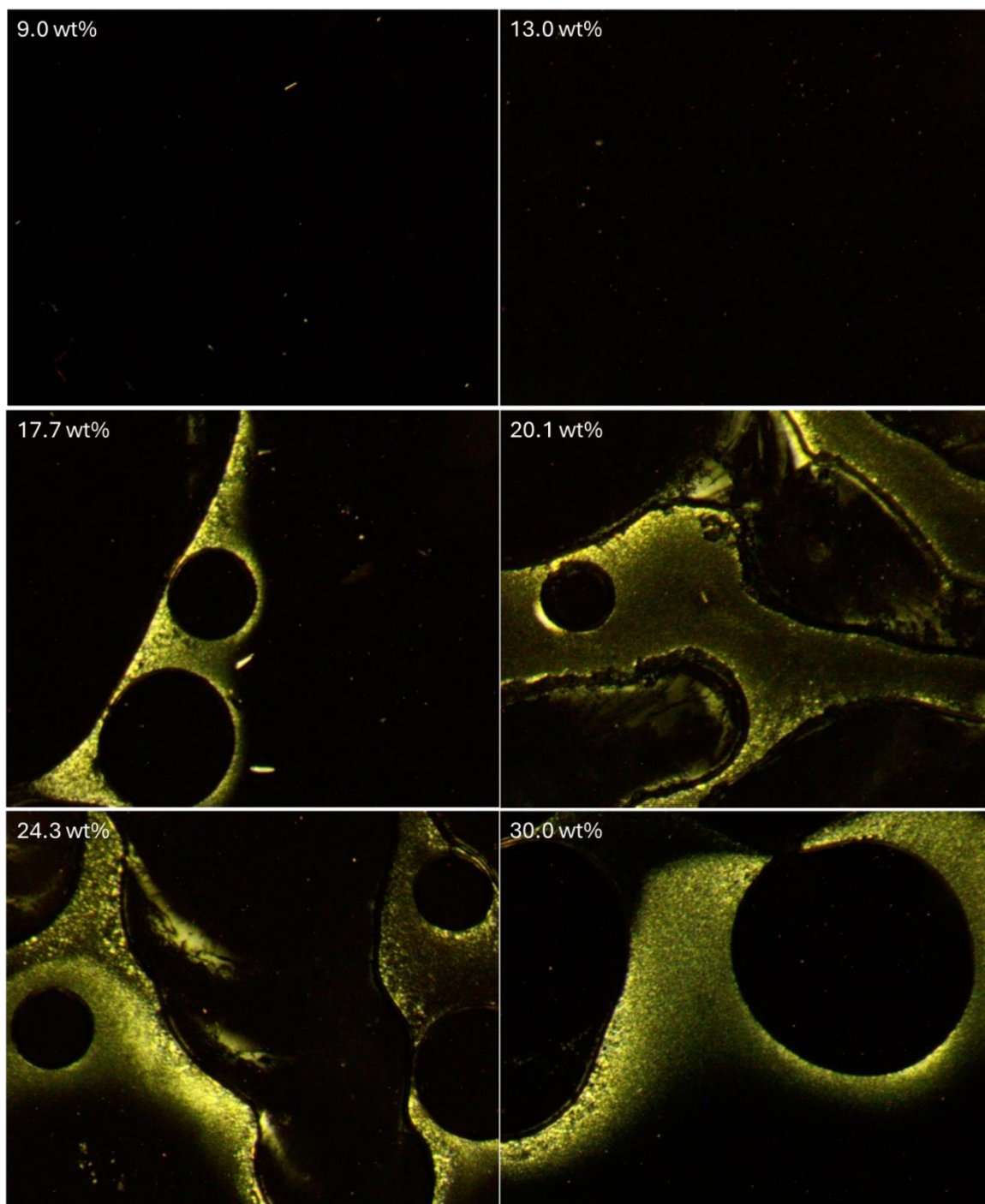


Figure 2-15 POM images corresponding to PHIC<sub>180</sub> at different concentrations: 9.0wt%, 13.0wt%, 17.7wt%, 20.1wt%, 24.3wt%, 30.0wt%. The black circular regions at higher concentrations correspond to air bubbles which are difficult to eliminate due to the very high viscosities.

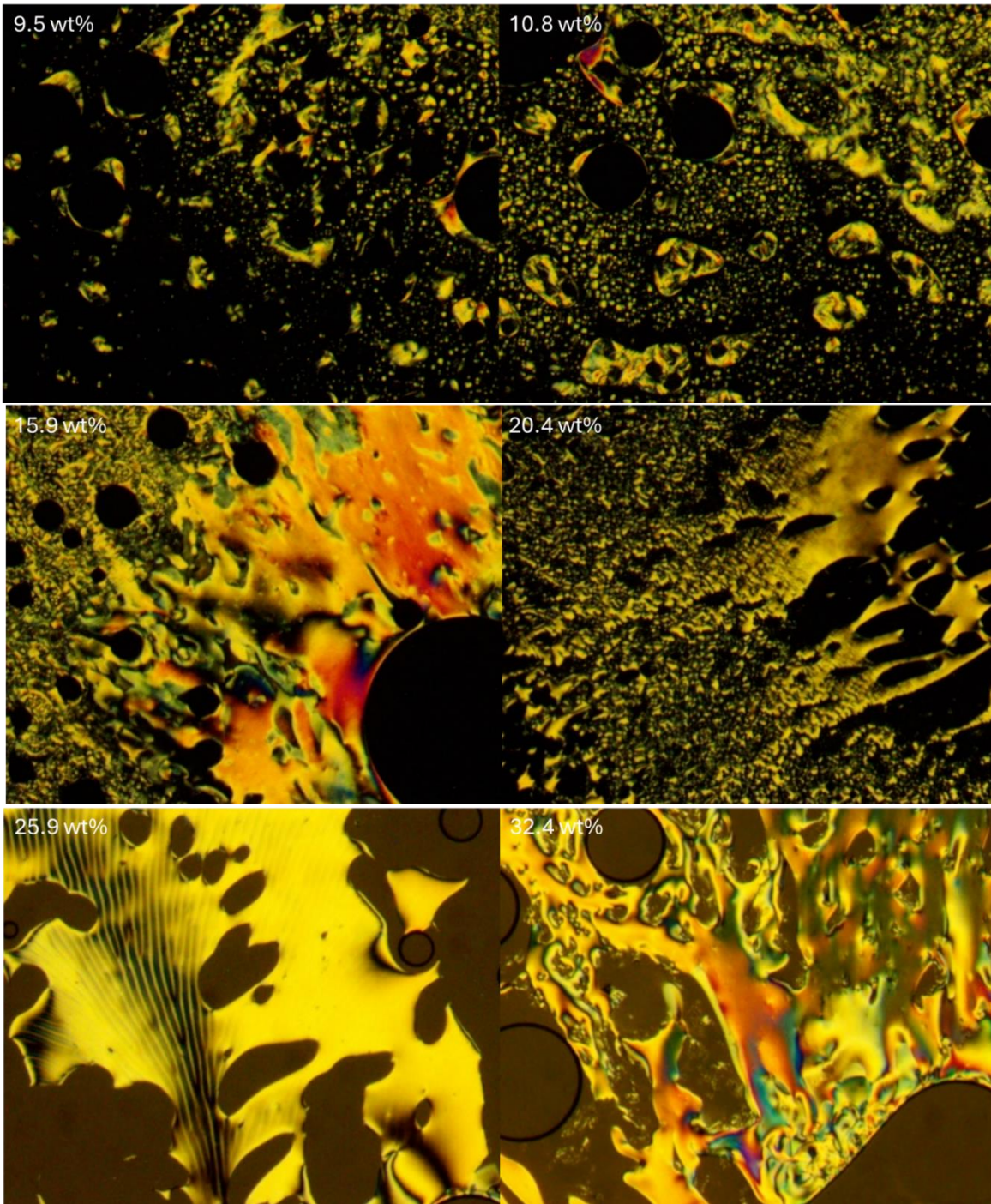


Figure 2-16 POM images corresponding to PHIC<sub>180</sub> at different concentrations (top to bottom): 9.5wt%, 10.8wt%, 15.9wt%, 20.4wt%, 25.9wt%, 32.2wt%. The black circular regions at higher concentrations correspond to air bubbles which are difficult to eliminate due to the very high viscosities.

### 2.7.8 Supplemental References:

1. M. Voigt, M. Klaumünzer, A. Ebel, F. Werner, G. Yang, R. Marczak, E. Spiecker, D. M. Guldi, A. Andreas Hirsch, W. Peukert, *J. Phys. Chem. C*, **2011**, *115*, 5561.
2. M. J. Kier, R. M. Leon, N. F. O'Rourke, A. L. Rheingold, C. Glenn, G. C. Micalizio, *J. Am. Chem. Soc.*, **2017**, *139*, 12374–12377.
3. X. Liu, R. Cheng, J. Deng, Y. Wu, *RSC Adv.*, **2014**, *4*, 48796.

# Chapter 3 : Cholesteric Behaviour of Poly( $\gamma$ -Benzyl-L-Glutamate) Functionalized Nanoparticles

*Jessie Wong, Linda Reven*

## Rationale for Chapter 3:

The third chapter of this thesis reports on the development of poly( $\gamma$ -benzyl-L-glutamate) (PBLG) functionalized nanoparticles. PBLG ligands were synthesized across a wide range of molecular weights to assess the role of molecular weight and grafting density on liquid crystal (LC) formation. Building on the work presented in **Chapter 2**, PBLG was chosen for its unique LC properties, as to expand the scope of the nanocomposite motif laid out in **Chapter 2**. In place of lyotropic nematic LCs, PBLG is well-known for its ability to self-assemble into lyotropic cholesteric LCs, and the justification for this chapter was to determine whether the same motif may be expanded to cholesteric LCs. It is now shown that low molecular weight PBLG-grafted NPs exhibited the most drastic reduction in the critical concentration required for LC assembly, while high molecular PBLG-grafted NPs exhibited minimal changes with respect to the critical concentration. Additionally, several precautions were taken to ensure that the PBLG-grafted NPs were entirely in the cholesteric state, as this phase competes simultaneously with gelation and molecular aggregation. Generally, the cholesteric structures formed from the synthesized PBLG-grafted NPs were enlarged compared to the cholesteric structures formed from the same molecular weight PBLG. This suggests that the presence of the NPs prevents optimal cholesteric ordering, which in turn enlarges the dimensions of the cholesteric structure.

**Chapter 3** is currently being prepared as a manuscript as J. Wong, L. Reven, "Cholesteric Behaviour of Poly( $\gamma$ -Benzyl-L-Glutamate) Functionalized Nanoparticles".

### 3.1 Abstract

Following earlier work showing that spherical nanoparticles with semiflexible polymer ligands can form an anisotropic lyotropic liquid crystal (LC) phase, this strategy was expanded to explore whether other LC phases are accessible. Poly( $\gamma$ -benzyl-L-glutamate) (PBLG) is a semiflexible polymer with well-known cholesteric LC properties. A wide molecular weight range of PBLG ligands were synthesized to graft onto spherical zirconia nanoparticles (NPs), and their corresponding LC properties were characterized. The anchoring of PBLG to NPs had the largest effect for low molecular weight PBLG with a significant drop in the critical concentration required for LC assembly. This trend diminished as the molecular weight of the PBLG ligands increased. Structure-wise, the NP contribution appeared to generally enlarge the cholesteric LCs formed, owing to the restricted movement of the tethered PBLG ligands.

### 3.2 Introduction

Traditionally, synthetic polypeptides have largely seen applications in biomedical fields due to a high degree of biocompatibility with, and biodegradability within the human body,<sup>1</sup> which in turn allows for medicinal applications such as drug delivery vessels<sup>2,3</sup> or scaffolds in tissue engineering.<sup>4,5</sup> In contrast to natural polypeptides, synthetic polypeptides have simpler compositions, typically with just a few amino acid residues, thereby enabling controlled self-assembly in the form of protein secondary structures such as  $\alpha$ -helices or beta sheets. A great advantage of these synthetic polypeptides (and polypeptoids) is their biodegradability, which becomes essential towards making materials science and related fields more sustainable. For example, hydrogels,<sup>6,7</sup> block copolymers,<sup>8,9</sup> films,<sup>10,11</sup> biosensors,<sup>12,13</sup> batteries,<sup>14</sup> and solar cells<sup>15</sup> are all materials that have traditionally used synthetic polymers and substituting these polymers with biodegradable synthetic polypeptides could provide a solution towards greener materials. For this reason, it becomes necessary to characterize the physical and material properties of these synthetic polypeptides, as to tailor their structure to targeted applications.

Poly( $\gamma$ -benzyl-L-glutamate) (PBLG), a modified polypeptide based on a glutamic acid homopolymer (PLGA), is the most studied and most widely applied synthetic polypeptide.

Sustainability-wise, PBLG (as well as PLGA) has low cytotoxicity and can be degraded using relatively mild conditions, rendering it a green material.<sup>16</sup> PBLG has previously been applied for tissue engineering,<sup>17-19</sup> gene therapy,<sup>20</sup> and drug delivery.<sup>21,22</sup> In materials science, PBLG has previously been used in films<sup>23</sup> and nano-fibers,<sup>24</sup> and composite systems.<sup>25-28</sup> PBLG is well known for its liquid crystalline (LC) properties, which is especially useful for NMR characterization of biomolecules via residual dipolar couplings.<sup>29,30</sup> Overall, PBLG is capable of forming an array of self-assembled architectures that provide unique characterization challenges.<sup>31</sup>

Due to the  $\alpha$ -helix conformation of PBLG, the polymer adopts a rod-like configuration in solution. In sufficiently concentrated solutions, PBLG primarily forms lyotropic cholesteric LC phases in various organic solvents,<sup>32-34</sup> that transform into a nematic phase in specific circumstances. If the PBLG sample is comprised of homo-chiral mixtures or subjected to magnetic field<sup>35</sup> or dissolved in a compensated solvent mixture, the cholesteric helix unwinds and becomes nematic instead.<sup>36</sup>

In previous work, we found that another semi-rigid rod-like polymer, poly (hexyl-n-isocyanate) (PHIC), was able to impart LC behaviour onto spherical zirconia nanoparticles, which resulted in nematic LC phases.<sup>37</sup> However, despite PHIC being a helical polymer, the rapid interconversion between the left- and right-handed screw sense essentially renders PHIC achiral, hence why only nematic LC phases are observed for unmodified PHIC. In contrast, the screw sense of PBLG is “locked in” by the alpha helix, allows for the formation of chiral LC phases, i.e. cholesterics.

An unanswered question from our previous work<sup>37</sup> was whether the linear NP arrays observed in films formed by casting a solution of the NPs are also present in the lyotropic solutions. Colloidal nanorods are known to self-assemble into nematic LC structures,<sup>38-40</sup> thereby suggesting that the linear NP arrays may self-assemble similarly. The LC behaviour originates from the PHIC and the observed reduced critical concentration may be explained through the effectively lengthened PHIC chains.<sup>41</sup> However, it may be possible that the PHIC provides colloidal

stability to the NP composite and the formation of NP arrays contributes to the reduced critical concentration. In addition to exploring the LC behaviour of PBLG coated NPs, this study seeks to expand our previous study as well. Characterization of the cholesteric LCs formed from the PBLG nanocomposites may help elucidate how spherical nanoparticles can produce anisotropic structures and perhaps explain the nematic phenomena as well.

### 3.3 Experimental

**3.3.1 Materials:** All solvents were obtained from a solvent purification system and were used immediately afterwards. Benzyl glutamate N-Carboxyanhydride (BLG-NCA) was purchased from Biosynth, which was purified using the approach suggested by Poché et al.<sup>42</sup> immediately prior to polymerization. All other chemical reagents were purchased from Millipore-Sigma. All reagents were used without further purification.

**3.3.2 Measurements:** MW measurements were carried out entirely using a Ubbelohde viscometer using  $[\eta] = KM_v^a$ , where  $\eta$  is the intrinsic viscosity as determined by the Ubbelohde viscometer,  $M_v$  is the viscosity-averaged molecular weight and  $K$  and  $a$  are the Mark-Houwink constants,  $1.58 \times 10^{-5}$  mL/g and 1.38, respectively. All measurements were carried out in DMF thermostated at 25 °C.<sup>43</sup> POM images were obtained using a Nikon model SMZ1500 stereomicroscope. TEM images were obtained using a ThermoScientific Talos 200X G2 TEM. SAXS profiles were obtained with the Anton Paar SAXSpoint 2.0 at the minimum sample-to-detector distance of 575 mm.

**3.3.3 Synthesis of [DPPA][TBA]:** Preparation tetrabutylammonium (TBA) salt procedure was adapted from Ossowicz et al.<sup>44</sup> In a 30 mL glass vial, diethylphosphonoacetic acid (DPPA) (500 mg) was dissolved in a 40% aqueous solution of tetrabutylammonium hydroxide[TBA][OH] (1.4 g). The mixture was allowed to stir at room temperature overnight. Afterwards, the solution was evaporated at 60 °C using a rotovap to remove water. Ethanol was used to precipitate excess

amino acid, which was filtered off. Afterwards, the ethanol was removed via rotovap and the product was dried in a vacuum at 60 °C to obtain a pale yellow oil.

**3.3.4 Synthesis of PBLG-PO(OEt)<sub>2</sub>:** Following an adapted procedure from Wu et al.<sup>45</sup> PBLG<sub>1237</sub> and PBLG<sub>2963</sub> were polymerized in DCM while PBLG<sub>89</sub> and PBLG<sub>228</sub> were prepared in THF, as to obtain a wide molecular weight range. BLG-NCA (2.00 g) was allowed to fully dissolve in dry DCM (at a concentration of 0.2 M) under N<sub>2</sub>. Afterwards, the corresponding amount of [DPPA][TBA] was quickly added into the reaction and the mixture was allowed to stir for up to three days. Afterwards, the viscous solution was precipitated into a beaker of cold methanol. The precipitation step was repeated twice more by re-dissolving the polymer product with DCM and subsequently precipitating it in cold methanol. High molecular weight samples appeared as white, solid, and fibrous. Lower molecular weight products appeared as white and flaky.

**3.3.5 Synthesis of PBLG-PO(OH)<sub>2</sub>:** The deprotection procedure was adapted from Mckenna et al.<sup>46</sup> After determining the MW of the synthesized PBLG product, the product (500 mg) was added to a flame dried round bottom flask under nitrogen. Dry DCM (10 mL) was added to the flask and the PBLG was allowed to dissolve completely while simultaneously cooling the flask down to 0°C. Bromotrimethylsilane (2.0 eq) was injected into the flask and the mixture was allowed to stir overnight while allowing the flask to warm up to room temperature. Afterwards, the flask was dried completely under vacuum and DCM (5 mL) and methanol (5 mL) were added sequentially and the mixture was again allowed to stir overnight. The mixture was then filtered and dried under vacuum to obtain PBLG-PO(OH)<sub>2</sub>.

**3.3.6 Functionalization of PBLG onto Bz@ZrO<sub>2</sub> – PBLG@ZrO<sub>2</sub>:** Highly monodisperse Bz@ZrO<sub>2</sub> nanoparticles with 4 nm diameters were synthesized according to the procedure from Garnweitner et al.<sup>47</sup> Initially, in a 30 mL dram vial capped with a septum, a measured amount of PBLG-PO(OH)<sub>2</sub> was added in a two-fold excess (with respect to monolayer coverage) and dissolved in dry DCM (20 mL). Solutions of high molecular PBLG ligands were highly viscous and up to 100 mL of dry DCM was used instead. Additionally, extra precautions were taken to ensure

these samples were entirely homogenized, primarily via periodic vortex mixing. Afterwards, the corresponding amount of Bz@ZrO<sub>2</sub> nanoparticles were injected into the dram vial. The solution was stirred for three days under nitrogen. Following the three days, the nanoparticles were precipitated using ethanol and centrifuged at 5K RPM, for ten minutes at room temperature. The supernatant was discarded, and the nanoparticles were centrifuged twice more. Afterwards, the precipitated solids were dissolved in DCM and transferred to a pre-weighed vial and dried under low air flow. The resulting product was vacuum dried overnight to obtain the PBLG@ZrO<sub>2</sub> nanoparticles.

**3.3.7 Liquid Crystal Sample Preparation:** Samples prepared for microscopy were dissolved a 3 mL Eppendorf tube and centrifuged to achieve homogeneity. The sample was spun at 12K RPM and rotated 180° between each centrifugation to ensure complete homogenization. The sample was then transferred to either a microscope slide or a capillary tube (sealed with Hemataseal clay sealant) to prevent solvent evaporation. The samples were left to stand overnight, and LC textures were observable the following morning.

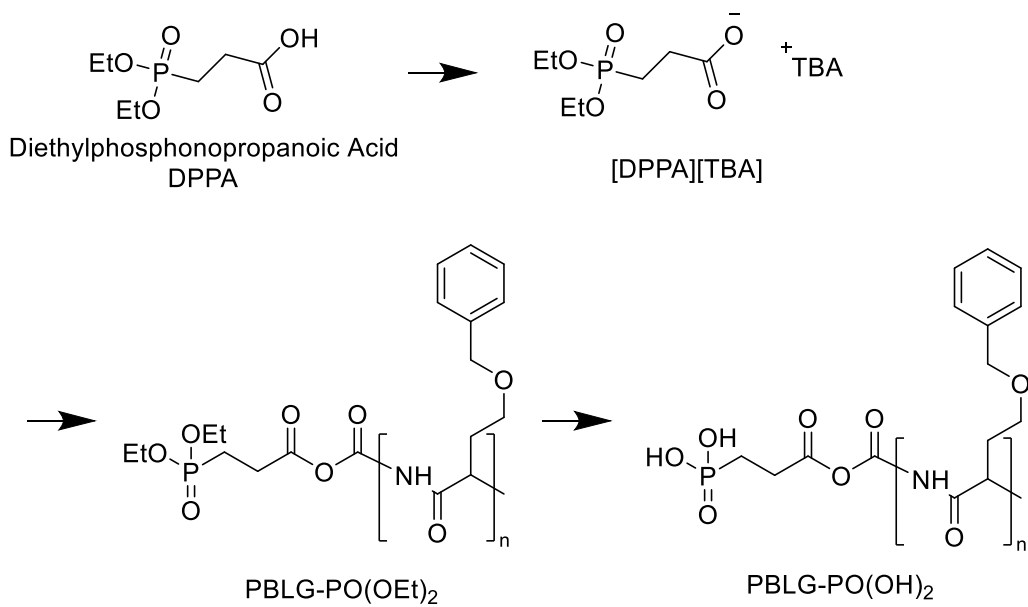
**3.3.8 SAXS Sample Preparation:** Samples of both PBLG<sub>228</sub> and PBLG<sub>228</sub>@ZrO<sub>2</sub> were prepared in 2 mL Eppendorf tubes by serial dilution and subsequently transferred to capillary tubes. Typically, ~50 mg of either sample was weighed in an Eppendorf tube and the corresponding amount of solvent was calculated and added to the Eppendorf tube as well. Due to the high viscosity of these samples, the mixtures were initially left on a vortex mixture for approximately 1 hour. Afterwards, the samples were centrifuged at 6000 RPM for 10 minutes at room temperature while rotating the Eppendorf tube 180° within the rotor between each session. Afterwards, the now-homogenized samples were transferred into soda lime glass capillary tubes via capillary action. To prevent solvent loss and to withstand the vacuum of the SAXS instrument, two layers of sealant were used to keep the samples inside. Firstly, Hematacrit clay sealant was used to plug either end of the capillaries. Afterwards, the capillary ends were dipped in epoxy and allowed to cure overnight. A second layer of epoxy was added and again allowed to dry overnight. The

samples were then left to stand vertically at 50 °C until the SAXS experiment was run (anywhere from one to three days).

## **3.4 Results**

### **3.4.1 Synthesis and Characterization of PBLG ligands:**

A synthetic scheme depicting the preparation of PBLG functionalized nanoparticles is shown in Scheme 3-1. PBLG was polymerized via a ring opening polymerization (ROP) of an N-carboxyanhydride through the normal amine mechanism (NAM); NAM was chosen such that the phosphonate functional group becomes incorporated into the polymer chain,<sup>16,48-50</sup> which in turn allows for phosphonate coupling to the zirconia surface. In contrast, in the other major polymerization pathway, the activated amine mechanism (AMM), the initiator does not become part of the PBLG chain<sup>51</sup> and is simply washed away during purification. To graft AMM-synthesized PBLG onto zirconia nanoparticles, the anchoring functional group must be coupled post-polymerization as the initiating species will only activate the monomer rather than participating in the polymerization reaction.<sup>52</sup> Furthermore, post-polymerization coupling is complicated by the large presence of side reactions and unpredictable terminal groups which renders further chemical modification difficult. For this reason, it was easier to design an initiator with dual functionality; one that will undergo NAM and will simultaneously anchor the resulting PBLG chain onto the zirconia surface. We also note that, while not used in the functionalized nanoparticles reported here, we have also successfully achieved high MW PBLG polymerization via NAM of PBLG using 18-crown-6.<sup>53</sup>



Scheme 3-1: Synthetic Scheme towards PBLG phosphonic acid ligands.

According to theory, the minimum degree of polymerization (DP) required for observed LC behaviour is 61. Several PBLG samples were prepared with DPs well above this threshold to ensure LC ordering. Additionally, PBLG samples are henceforth abbreviated as PBLG<sub>DP</sub>. The DP of the synthesized samples are summarized in Table 3-1 along with the dimensions of the polymer. The cross-section diameter and length per residue was assumed to be 1.6 nm and 0.15 nm,<sup>54</sup> respectively. Intrinsic viscosity was determined using an Ubbelohde Viscometer in DMF at 25 °C and the molecular weight was subsequently calculated using the following equation:  $[\eta] = 1.58 \times 10^{-5}(\text{MW})^{1.35}$ .<sup>55</sup>

Table 3-1 Summary some physical properties of synthesized PBLG samples.

Sample	[M]/[I]	Intrinsic Viscosity, $[\eta]$ mL/g	Molecular weight	Length (L), (nm)	Axial Ratio (L/D)
PBLG <sub>89</sub>	21.0	11.5±2.2	21.0±6.5 × 10 <sup>3</sup>	13.3	8.3
PBLG <sub>228</sub>	112	35.5±3.1	54.0±8.3 × 10 <sup>3</sup>	34.2	21
PBLG <sub>1237</sub>	114	341±15	293±27 × 10 <sup>3</sup>	186	12 × 10 <sup>1</sup>
PBLG <sub>2963</sub>	216	113±4.0 × 10 <sup>1</sup>	702±55 × 10 <sup>3</sup>	444	28 × 10 <sup>1</sup>

### 3.4.2 Functionalization of Zirconia Nanoparticles:

To confirm if the PBLG was successfully grafted onto the ZrO<sub>2</sub> surface, FTIR and TGA were performed (Supplemental Figures 3-7 and 3-8). Previously, working with lower molecular weight polymer ligands, the weight loss percentages from TGA could be used to determine the grafting density.<sup>37</sup> However with the much higher molecular weight PBLG ligands, the expected inorganic contribution to the weight is below the accuracy of the instrument. (Supplemental Table 3-4). The small weight loss differences that were detected did indicate that the surface coverage was inversely proportional to the DP of the PBLG ligands as expected. From FTIR, the amide I and II bands at 1650 cm<sup>-1</sup> and 1548 cm<sup>-1</sup> indicate that the functionalized PBLG ligands are in the  $\alpha$ -helix conformation.<sup>56</sup> In regards to the ZrO<sub>2</sub> NP core, the Zr-O-Zr band occurs at 740 cm<sup>-1</sup> owing to the ZrO<sub>2</sub> core, as well as a band expected around 1100 cm<sup>-1</sup> denoting a Zr-O-P band, which signifies successfully anchored PBLG ligands.<sup>57</sup> However, neither of these bands can be seen in the FTIR spectrum due to the low ZrO<sub>2</sub> content relative to the PBLG ligands.

To confirm successful polymer grafting of the PBLG ligands onto the ZrO<sub>2</sub> nanoparticles, TEM was performed. Initially, films were cast on carbon coated copper TEM grids from 1 wt% solutions of both PBLG and the NPs, however, polymer gel networks were observed in these samples despite the dilute concentration (Supplemental Figure 3-10). The observed textures in the PBLG gel networks resemble both PBLG nanofibers<sup>58</sup> and superhelical aggregates.<sup>59</sup> To confirm colloidal stability, the grids were instead cast from 0.1-0.5 wt% THF solutions at 50°C, which resulted in fewer gel networks and provided better contrast (Figure 2). However, gels were still observed in films of PBLG<sub>1237</sub>@ZrO<sub>2</sub> and PBLG<sub>2963</sub>@ZrO<sub>2</sub>, suggesting that PBLG gelation has a MW dependence. The higher contrast of the lower MW samples allowed for the interparticle distances to be measured but the spread in values is very wide for all the samples. (Supplemental Table 3-3) For PBLG<sub>89</sub>@ZrO<sub>2</sub>, this was determined to be  $(4\pm 1)\times 10^1$  nm, while PBLG<sub>228</sub>@ZrO<sub>2</sub> had average spacings of  $(5\pm 3)\times 10^1$  nm, averaging across a hundred measurements. Additionally, PBLG<sub>1237</sub>@ZrO<sub>2</sub> and PBLG<sub>2963</sub>@ZrO<sub>2</sub> had spacings of  $(6\pm 3)\times 10^1$  nm and  $(6\pm 3)\times 10^1$  nm. Although regular interparticle spacings were not observed, the TEM images were to confirm colloidal stability of the PBLG coated nanoparticles.

### 3.4.3 LC Behaviour

LC behaviour was initially explored in a variety of solvents. Typically, concentrated solutions of PBLG and the corresponding nanoparticles were packed into capillary tubes and allowed to sit for up to two days until cholesteric patterns were observed. LC samples were generally clear when observed through the capillary tube (without polarizers). Solutions using DCM were the easiest to prepare, due to the ease of solubility and the relatively low sample viscosities, as well as the consistency of cholesteric LCs without further intervention (Figure 3-2). In contrast, lyotropic solutions using other organic solvents, such as DMF and THF often appeared cloudy and faintly birefringent under crossed polarizers. The cloudiness and lack of LC textures is due to aggregation/gelation of PBLG in solution, which is a well-studied phenomenon.<sup>63-65</sup> Solvents in which PBLG can form cholesteric LC phases are known as ‘helicogenic’ solvents in literature. Of these helicogenic solvents, PBLG is molecularly dispersed in DMF, m-cresol and pyridine while being aggregated in other helicogenic solvents.<sup>61,62</sup> For this reason, DMF was chosen so as to ensure molecularly dispersed PBLG molecules. Despite the careful choice of solvent, gelation was frequently observed in concentrated samples, which appeared as white, turbid solutions (Supplemental Figure 3-9). Under POM, these gelled samples appear similar to the texture observed in Supplemental Figure 3-15. These properties can be attributed to the complex gelation behaviour, which has been extensively studied.<sup>63-65</sup>

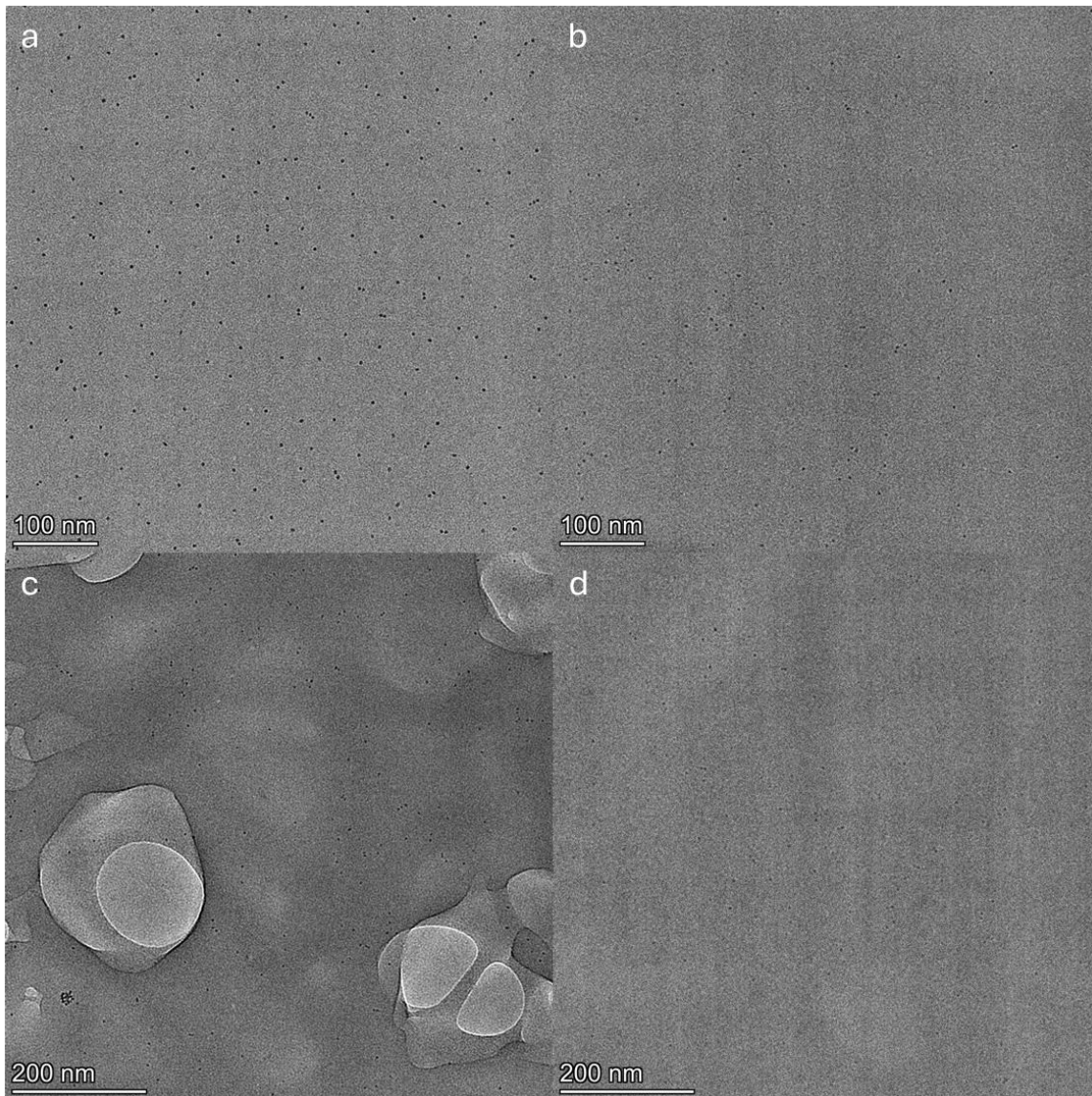


Figure 3-1: TEM images of (a) PBLG<sub>89</sub>@ZrO<sub>2</sub>, (b) PBLG<sub>228</sub>@ZrO<sub>2</sub>, (c) PBLG<sub>1237</sub>@ZrO<sub>2</sub>, and (d) PBLG<sub>2963</sub>@ZrO<sub>2</sub> cast from 0.1-0.5 wt% solutions in THF at 50°C. Average interparticle distances were calculated across a hundred measured points, using ImageJ.<sup>60</sup>

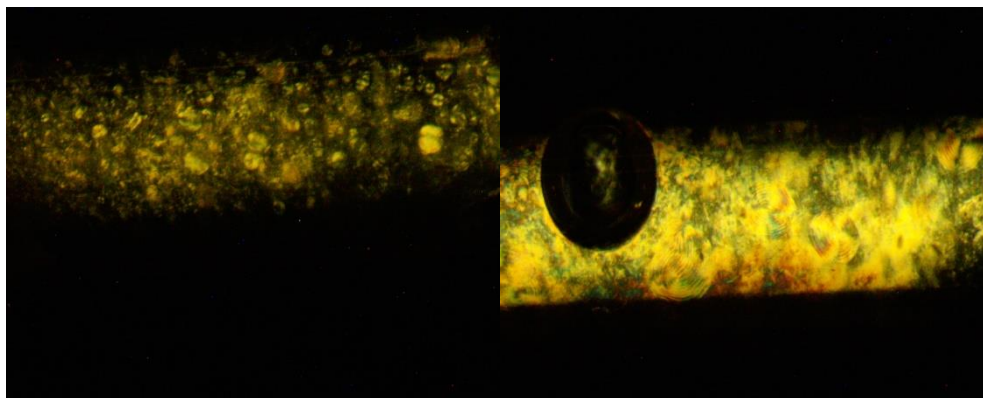


Figure 3-2: (left) PBLG228 and (right) PBLG228@ZrO<sub>2</sub> solutions in DCM at 10 wt%. PBLG<sub>228</sub> exhibits biphasic behaviour at this concentration while PBLG<sub>228</sub>@ZrO<sub>2</sub> exhibits cholesteric ordering, suggesting that the functionalized nanoparticles effectively lowered the LC critical concentration.

Since PBLG gelation behaviour is thermoreversible, samples of LC PBLG and PBLG@ZrO<sub>2</sub> in DMF were held at 50 °C (above the gel-sol transition temperature),<sup>65,66</sup> so as to ensure that the samples were entirely cholesteric prior to observation under POM. This way, a better comparison can be made between the LC behaviour of PBLG and its NPs. After thermally annealing the samples at 50 °C, the solutions appeared clear and strong birefringent LC textures were observed under the microscope. Cholesteric textures of a few representative NP samples, after thermally annealing the samples, are shown in Figure 3-3, and phase diagrams obtained using POM are available in the Supplementary Figures 3-11 to 3-14. A large critical concentration decrease occurs for PBLG<sub>89</sub>@ZrO<sub>2</sub> as compared to PBLG<sub>89</sub>. PBLG<sub>89</sub>@ZrO<sub>2</sub> appeared fully cholesteric at 30 wt%, while PBLG<sub>89</sub> exhibited biphasic behaviour at 40 wt%. However, the MW dependence of the onset of LC behaviour becomes diminished beyond this point, as PBLG<sub>228</sub>, PBLG<sub>1237</sub>, and PBLG<sub>2963</sub> had comparable critical concentrations to their corresponding NPs. Cholesteric half-pitch measurements are summarized in Table 3-2. As the fingerprint texture was not uniform (owing to the curvature of the capillary), pitch measurements were only obtained for visible fingerprints and were highly subject to sampling bias. Additionally, concentrated solutions of high MW PBLG did not exhibit fingerprint textures, perhaps due to the high viscosity of the solutions. For the gelled samples of PBLG<sub>228</sub> and PBLG<sub>228</sub>@ZrO<sub>2</sub> in THF, only PBLG<sub>228</sub> at 10 wt% sample exhibited

cholesteric fingerprints, while other samples were birefringent but did not display a liquid crystal texture. Additionally, samples diminished in birefringence as the sample concentration increased.

Table 3-2: Average cholesteric half-pitch measurements of PBLG and PBLG@ZrO<sub>2</sub> samples across several compositions in DMF. Measurements were averaged across at least fifty points.

	Cholesteric Half-Pitch ( $\mu\text{m}$ )			
	10 wt%	20 wt%	30 wt%	40 wt%
<b>PBLG<sub>89</sub></b>	-	-	-	0.3 $\pm$ 0.1
<b>PBLG<sub>89</sub>@ZrO<sub>2</sub></b>	-	-	0.5 $\pm$ 0.09	0.3 $\pm$ 0.09
<b>PBLG<sub>228</sub></b>	-	0.3 $\pm$ 0.08	0.2 $\pm$ 0.08	-
<b>PBLG<sub>228</sub>@ZrO<sub>2</sub></b>	-	0.4 $\pm$ 0.08	0.3 $\pm$ 0.08	-
<b>PBLG<sub>1237</sub></b>	0.3 $\pm$ 0.1	0.5 $\pm$ 0.06	0.5 $\pm$ 0.05	-
<b>PBLG<sub>1237</sub>@ZrO<sub>2</sub></b>	0.4 $\pm$ 0.08	0.3 $\pm$ 0.06	-	-
<b>PBLG<sub>2963</sub></b>	0.4 $\pm$ 0.07	0.4 $\pm$ 0.08	-	-
<b>PBLG<sub>2963</sub>@ZrO<sub>2</sub></b>	0.4 $\pm$ 0.1	0.4 $\pm$ 0.08	0.5 $\pm$ 0.06	-

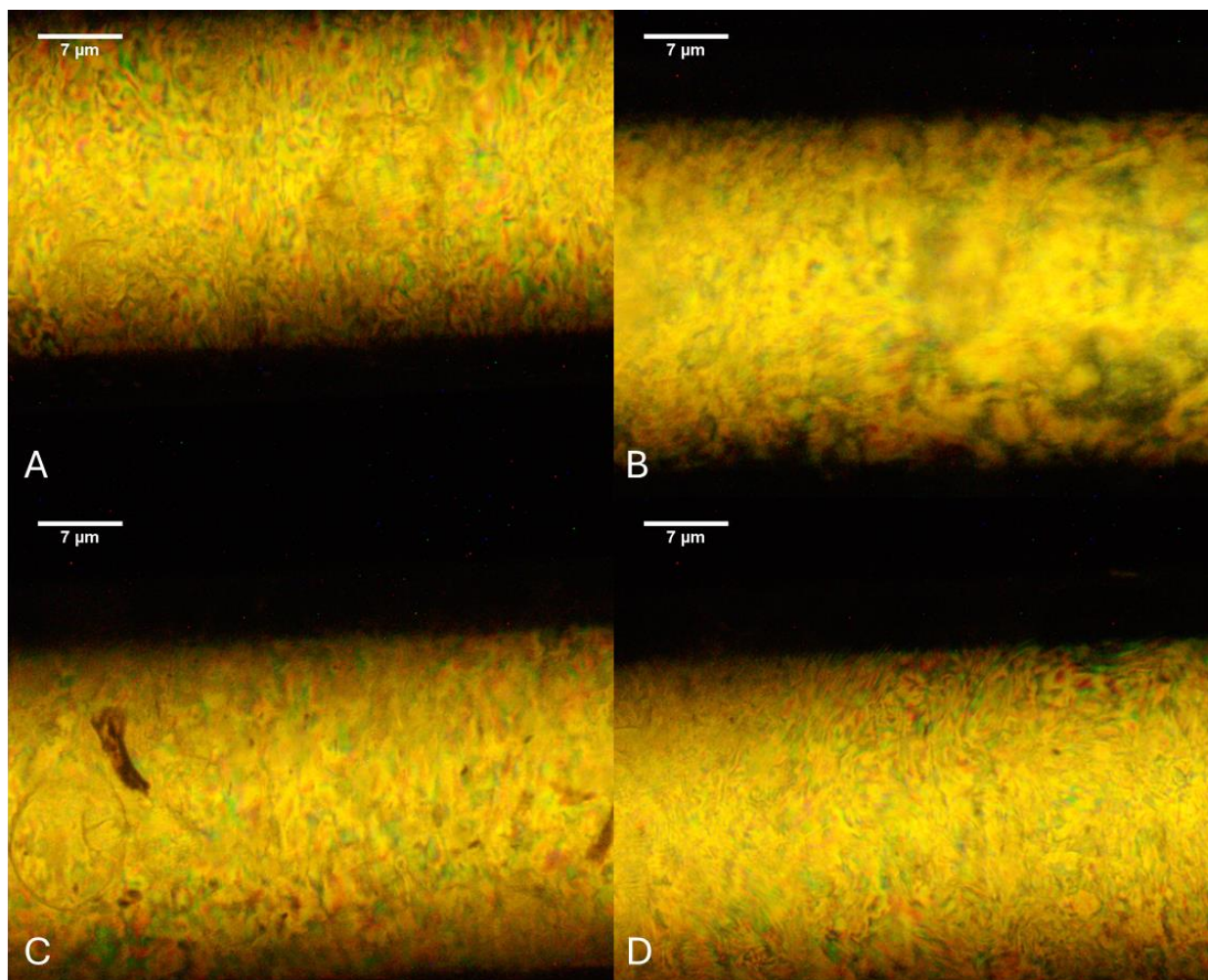


Figure 3-3: Representative samples of cholesteric LC phases of various MW PBLG-grafted NPs in DMF, after thermally annealing at 50°C. (A) 30 wt% DMF solution of PBLG<sub>89</sub>@ZrO<sub>2</sub>. (B) 20 wt% DMF solution of PBLG<sub>228</sub>@ZrO<sub>2</sub>. (C) 20 wt% DMF solution of PBLG<sub>1237</sub>@ZrO<sub>2</sub>. (D) 20 wt% DMF solution of PBLG<sub>2963</sub>@ZrO<sub>2</sub>.

#### 3.4.4 SAXS Experiments

To characterize the assembled LC structures, SAXS was employed at various polymer and NP compositions. To minimize molecular aggregation and gelation, SAXS was carried out on capillary tubes containing the lyotropic LC samples. Additionally, samples were stored in a 50 °C oven for up to two days prior to the SAXS experiments. LC samples appeared transparent while gelled/aggregated samples appeared white and cloudy. All samples were confirmed to be

transparent prior to the experiments. All cholesteric LC samples were in DMF, in addition to gelled samples of PBLG<sub>228</sub> and PBLG<sub>228</sub>@ZrO<sub>2</sub> in THF, which were prepared for comparison.

Fully cholesteric samples did not exhibit any significant reflections in the scattering region studied (Figure 3-4 and 3-5) other than broad peaks spanning from 2 nm<sup>-1</sup> to 4 nm<sup>-1</sup>, which intensify with increasing concentrations. While these peaks were broad, it also appears that in the NPs, the peaks shift to lower *q* values compared to their corresponding PBLG solution. In NP samples only (except for PBLG<sub>2963</sub>@ZrO<sub>2</sub>), a significant peak occurs between 0.1 nm<sup>-1</sup> and 1 nm<sup>-1</sup>, which similarly intensifies with increasing concentration. Since the samples studied were clearly cholesteric prior to the SAXS experiments, as evidenced by Figure 3-4, the presence of these broad peaks suggests scattering due to the cholesteric structure.

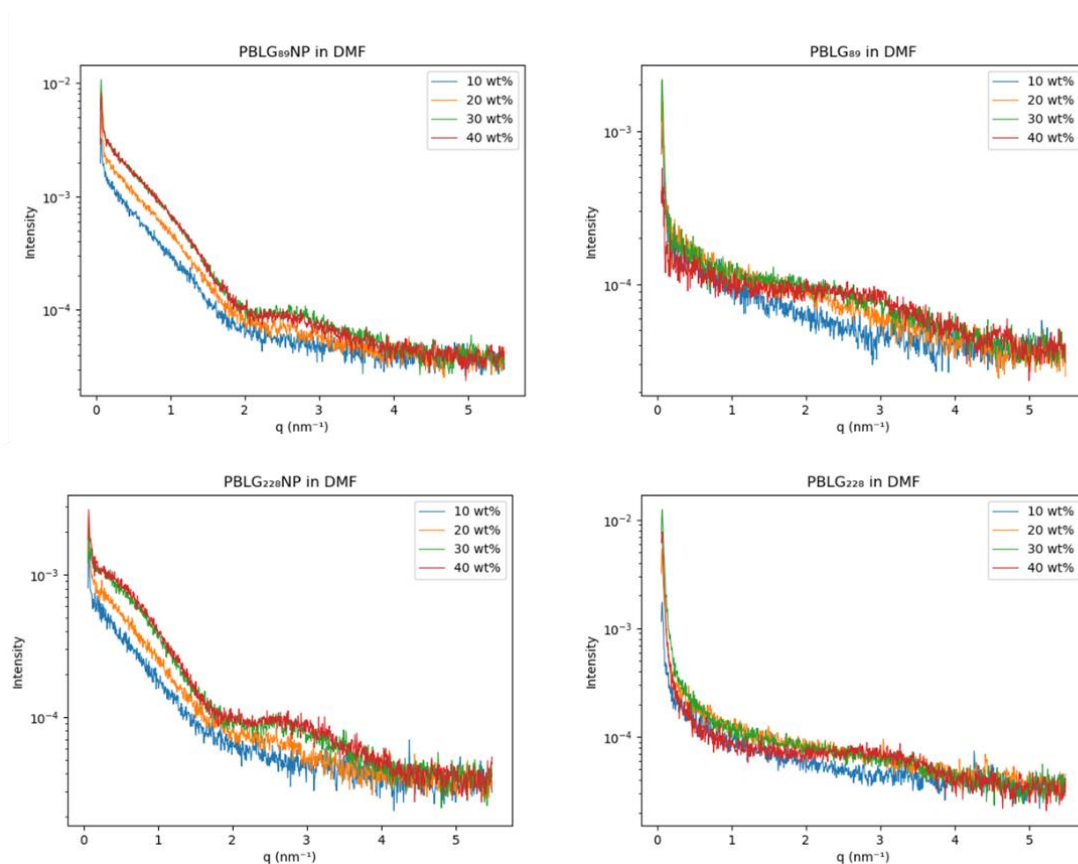


Figure 3-4 SAXS profiles of cholesteric LC solutions of PBLG<sub>89</sub> and PBLG<sub>228</sub> samples and their corresponding NPs. Samples were annealed overnight at 50 °C to ensure samples were entirely cholesteric.

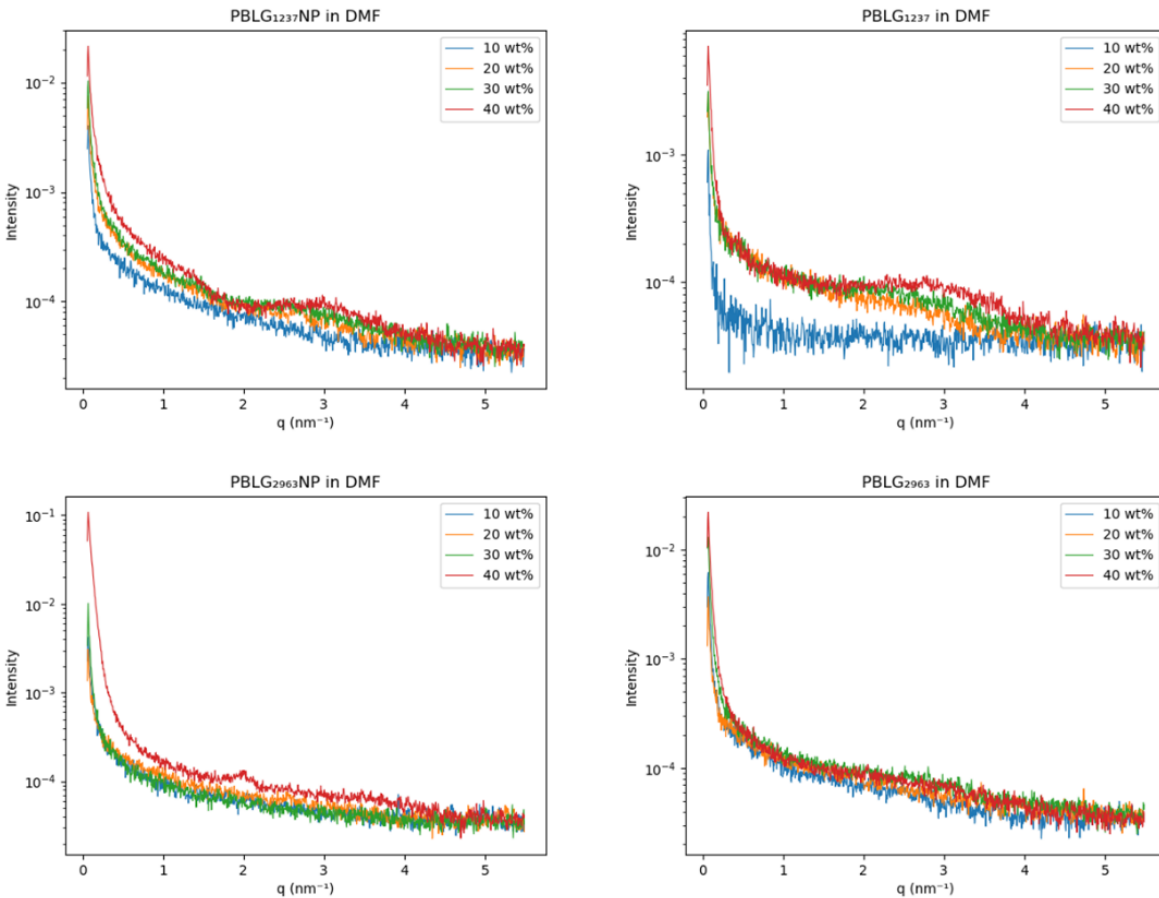


Figure 3-5 SAXS profiles of cholesteric LC solutions of PBLG<sub>1237</sub> and PBLG<sub>2963</sub> samples and their corresponding NPs. Samples were annealed overnight at 50 °C as to ensure samples were entirely cholesteric.

Exceptionally, the gelled samples of PBLG<sub>228</sub>@ZrO<sub>2</sub> in THF exhibited highly crystalline peaks at real  $d$  spacings of 1.35, 1.63, 1.77 and 1.63 nm, respectively (Figure 3-6). These reflections were assigned to the distances between densely packed  $\alpha$ -helices.<sup>58</sup> In contrast, PBLG<sub>228</sub> exhibited a much broader reflection in the same range, centered about 1.65 nm. Additionally, the broad peak, assigned to scattering from the ZrO<sub>2</sub> cores, was once again observed in the range of 0.1 nm<sup>-1</sup> to 1 nm<sup>-1</sup>.

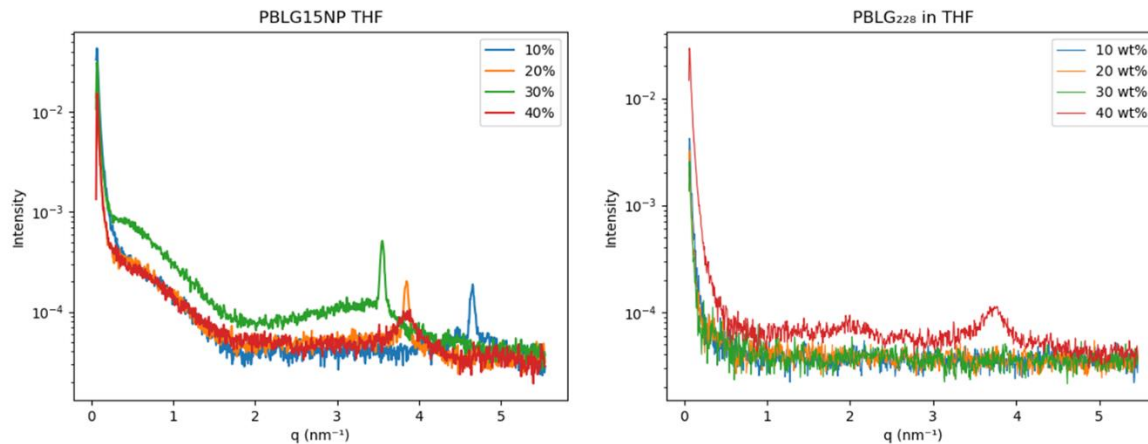


Figure 3-6: 1D SAXS curves corresponding to gelled samples of (Left) PBLG<sub>228</sub>@ZrO<sub>2</sub> and (Right) PBLG<sub>228</sub> in THF.

### 3.5 Discussion

While PBLG-coated nanoparticles have previously been reported,<sup>67-70</sup> few of these examples considered or reported on the LC character of the PBLG coated nanoparticles. The critical concentration required for semi-flexible polymers to exhibit LC behaviour is inversely related to the degree of polymerization (ie. a lower degree of polymerization results in a higher critical concentration).<sup>71</sup> The PBLG ligands used previously in literature would not be able to form lyotropic LC phase as the molecular weights were too low such that the critical concentration required for LC behaviour becomes impractically high. For a semi-flexible polymer of length,  $l$ , and cross-sectional diameter,  $D$ , LC behaviour can be predicted. According to Flory's theory of rigid rods, the relationship between the onset of LC behavior and a polymer's axis ratio,  $x = L/D$ , can be related by the following relation:  $v_p^* = (8/x)(1-2/x)$ .<sup>71</sup> From this relation, the minimum axis ratio of  $L/D = 6.417$  is required for LC phases,<sup>71-73</sup> which, in the case of PBLG, corresponds to a degree of polymerization,  $DP = 61$  (where  $L = 0.15\text{nm/monomer unit}$  and  $D = 1.42\text{ nm}$ ).<sup>74</sup> For this reason, the PBLG ligands here were synthesized such that the MW was above the minimum axis ratio as to guarantee LC behaviour. However, these PBLG samples were generally quite viscous and as a result, sample preparation and homogenization were difficult.

Qualitatively, concentrated solutions of high MW PBLG ligands were generally less viscous than solutions of low MW PBLG ligands at the same concentration. This is expected, since viscosity of LC samples generally peak near its critical concentration.<sup>75</sup> Concentrated solutions of high MW PBLG were beyond the corresponding critical concentration, whereas solutions of short PBLG ligands were closer to its critical concentration, resulting in more viscous solutions. In comparison, solutions of PBLG functionalized nanoparticles were generally less viscous than their corresponding unfunctionalized PBLG ligands.<sup>76</sup>

In the literature, there are examples of grafting PBLG ligands onto micron sized particles for stable dispersions in lyotropic PBLG matrices. Tang and Zhang showed that single-walled carbon nanotubes coated with PBLG<sub>151</sub> ligands can successfully be dispersed in lyotropic PBLG<sub>151</sub>/DMF solutions.<sup>77</sup> Rosu et al. functionalized domed silica microcylinders with another synthetic polypeptide, poly( $\gamma$ -stearyl-L-glutamate) for dispersions in a lyotropic cholesteric solutions of the same polypeptide.<sup>78</sup> The functionalization of these particles used a “grafting-from” polymerization and the MW was not reported. Here we report the first brush-like PBLG functionalized nanoparticles, where LC behavior is generated from the NPs, rather than dispersing the particles into a LC matrix. Additionally, the stability of the lyotropic nanocomposites listed above were also promoted by the anisotropic particle shape, whereas the present study is novel in that the anisotropic cholesteric LC phases were formed by isotropic, spherical NPs.

The present study is also the first in which the molecular weight of the polymer ligand was systematically varied. Unfortunately, the surface coverages could not be accurately determined since the contribution of the ZrO<sub>2</sub> NPs is below the TGA detection limit due to the relatively high MWs as compared to our earlier study with PHIC. Previously, our “grafting to” approach via ligand exchange produced high grafting densities,<sup>37</sup> however, using this procedure for high MW polymer ligands appeared to produce low grafting densities presumably due to steric hindrance. However, the ZrO<sub>2</sub> cores can be clearly seen in the TEM images and from the calculated estimates of interparticle distances, PBLG<sub>89</sub>@ZrO<sub>2</sub> and PBLG<sub>228</sub>@ZrO<sub>2</sub> both appear to

be “true” polymer brushes in that the PBLG ligands are fully extended outward.<sup>79</sup> In the case of PBLG<sub>89</sub>@ZrO<sub>2</sub>, the average interparticle distance was measured to be 40.3 nm, which is well above the contour length of PBLG<sub>89</sub>, 13.4 nm. For two non-interacting PBLG<sub>89</sub> NPs, the interparticle distance is expected to be 26.8 nm. Since the measured value is much higher than expected, this could be an indication of physisorbed PBLG within the polymer corona. However, given that the spread in values for the interparticle distances is very wide and the surface coverage cannot be measured accurately, this cannot be confirmed.

In agreement with past results,<sup>37</sup> LC behaviour generated by semi-flexible polymer coated NPs occurred at lower critical concentrations compared to the corresponding non-grafted polymer. This observation is most evident in the PBLG<sub>89</sub>@ZrO<sub>2</sub> and PBLG<sub>89</sub> samples, where cholesteric textures were observed in the PBLG-grafted NPs beginning at 30 wt% compared to the non-grafted PBLG<sub>89</sub>, where biphasic isotropic-LC behaviour occurs beginning at 40 wt%. Compared to literature, the onset of LC behaviour occurs around 40 wt% for PBLG<sub>89</sub>,<sup>83,84</sup> which agrees with our experimental results, however, the effects of NP polymer grafting effectively lowered the critical concentration to a value that would be consistent with PBLG<sub>150</sub>. For the higher MW NP, the effect of polymer grafting is minimal, since the relation between MW and the onset of LC assembly begins to plateau above a DP of ~400. It was also unclear whether the grafting density had an effect, as the high MW PBLG-grafted NPs presumably had reduced grafting densities as well. We note that functionalization of these NPs was challenging due to the high solution viscosities owing to the high MW of the PBLG ligands.

Several trends can be identified in relation to the cholesteric structure. Firstly, fingerprint structures were much more periodic in high MW PBLG/PBLG@ZrO<sub>2</sub> samples and half-pitch measurements were more consistent in these samples, as seen in the smaller uncertainties. Furthermore, cholesteric samples of the NPs had larger half-pitches than their corresponding MW PBLG. This is most likely due to confinement effects, as the restricted motion of the PBLG chains on the NP surface prevent optimal cholesteric ordering. Similarly, the cholesteric half-pitch measurements decreased as the concentrations increased, in agreement with other reports.<sup>85,86</sup>

Expectedly, the half-pitch was invariant to MW as well.<sup>86,87</sup> However, the cholesteric half-pitch measurements were generally smaller compared with other literature reports.<sup>85,86,88</sup> This could potentially be due to the short equilibrium time of our LC samples, as some previous studies report up to six weeks of equilibration time.<sup>89</sup> Alternatively, it could be due to temperature effects, as POM imaging was carried out at room temperature, rather than at 50 °C, due to equipment limitations. It is feasible that heating the lyotropic solutions expands the cholesteric helix, which is immediately collapsed upon rapid cooling resulting in the short, measured half-pitches. A previous study reports that rapidly quenched gels of PBLG contain 10 vol% of solvent in its aggregated state, whereas a slowly cooled gel contains 28 vol% of solvent in its aggregated state.<sup>90</sup> Additionally, the authors also note the emergence of an ordered, periodic structure upon rapidly quenching the gels, suggesting an LC transition, however the authors did not confirm if the structure was a cholesteric LC. Following this reasoning, it is possible that annealing the samples at 50°C followed by rapid quenching would produce broader distributions of cholesteric helices, and larger uncertainties in the measurements, owing to the excluded solvent molecules. For this reason, the differences between the measured pitches in the PBLG and NP samples are not statistically significant ( $p=0.56$ ), owing to the random variation of cholesteric fingerprint formation.

A few notable features were observed in the SAXS profiles of cholesteric LC solutions of PBLG and NPs. One study noted that below 25 wt%, it was “impossible to detect an X-ray spacing, even with very long exposures (24 h)”,<sup>91</sup> which was also confirmed by our experimentally obtained results. However, when concentrations were above 25 wt%, significant broad peaks appear between  $2 \text{ nm}^{-1}$  and  $4 \text{ nm}^{-1}$ . This is due to the molecular width of the PBLG chains becoming correlated. For nematic and cholesteric LCs, typically two broad peaks are expected, owing to the molecular length and width of the LC molecule.<sup>92</sup> Since LC structures are inherently less ordered than crystalline materials, these features arise as a distribution. For thermotropic LCs, this is a representation of short-range positional correlation between the molecular dimensions, however for lyotropic solutions, the correlation also includes the solvent molecules, which further broadens the distribution. For this reason, reflections owing to the molecular width

of PBLG appear broad in the scattering window observed, and only appear at sufficiently high concentrations once the molecules become correlated. The molecular correlation lengths of PBLG would similarly be expected in the ultra-small angle region, due to the large contour length of the synthesized PBLG ligands.

A significant, broad peak were observed in the cholesteric solutions of PBLG-grafted NPs. The peak spans  $0.1 \text{ nm}^{-1}$  to  $1 \text{ nm}^{-1}$ , and generally intensifies with concentration which indicates that the peak is due to scattering from the NPs.<sup>93</sup> This broad, low  $q$  peak was not observable highest MW sample most likely due to the relatively low NP content. Attempts were also made to fit the form factors of the PBLG coated NPs, however this proved quite difficult. Since the PBLG rods were anchored to the NP surface, the orientation of the rods is limited to an anchor at the point of attachment. For this reason, not all orientations become accessible, and fitting the profile to the scattering intensity function for randomly oriented cylinders, put forth by Guinier,<sup>94</sup> becomes impractical. Similarly, since the NPs were functionalized with high MW PBLG and presumably had low grafting densities (in the case of PBLG<sub>1237</sub> and PBLG<sub>2963</sub>), the 'spherical particle and its adsorbed polymer layer' model<sup>95</sup> would not be suitable either.

Several interesting features can be observed in the scattering profiles of gelled samples of PBLG<sub>228</sub> and PBLG<sub>228</sub>@ZrO<sub>2</sub> in THF. Firstly, in the case of PBLG<sub>228</sub>, the only sample with notable reflections is the solution of PBLG<sub>228</sub> at 40 wt%, which also coincides with diminished birefringence in POM (supplemental Figure 3-15). Additionally, the observed reflections can be indexed to a complex gel of form A, as originally put forth by McKinnon and Tobolsky,<sup>23</sup> where the unit cell is comprised of solvent molecules and between three to four  $\alpha$ -helices. If the structure is as the authors suggest, cholesteric LCs and gels of PBLG are incompatible, as the emergence of one structure disassembles the other.

Highly crystalline reflection peaks were also observed in gelled PBLG<sub>228</sub>@ZrO<sub>2</sub> solutions in THF, which correspond to the distances between densely packed  $\alpha$ -helices,<sup>58</sup> a feature not shared by the PBLG<sub>228</sub> samples in THF. Surprisingly, the distances between helices increase upon increasing the concentration, however, this phenomenon can be explained as the transition from

packed  $\alpha$ -helices to a gelled structure, as the reflections observed at 40 wt% once again coincides with the gel in form A. The crystalline peaks confirm that the high grafting densities of PBLG essentially mimic high concentration solutions of PBLG, however it is unclear why the same result was not also observed in DMF.

Despite the presence of the NP cores, the self-assembly behavior of all the synthesized NPs were primarily polymer driven and the structural features observed largely follow from PBLG properties. In comparison to untethered PBLG in solution, the cholesteric structure generated by the NPs exhibited longer cholesteric pitches and larger correlation lengths (as seen in SAXS). However, for lower MW PBLG ligands, the presence of NPs prompted early LC formation; this trend diminished with increasing MW.

### 3.6 Conclusion

Like PHIC-grafted NPs, the present study confirms that PBLG-grafted NPs generate LC behaviour from isotropic, spherical particles. PBLG ligands were synthesized across a wide range of molecular weights, via an ionic liquid-initiated polymerization. The use of ionic liquid catalyzed polymerizations enabled higher molecular weight PBLG ligands to be prepared that were subsequently grafted onto spherical zirconia nanoparticles through an efficient ligand exchange process. The most immediate observation of these PBLG-grafted NPs was the early onset of LC behavior, however this trend decreased with increasing MWs. The cholesteric LC structures of PBLG-grafted NPs were of larger dimensions in comparison to its untethered PBLG counterparts. This is most clearly seen in the general increase in cholesteric pitch measurements, as well as the shift of  $q$  values towards larger distances as seen in the SAXS data. On a practical basis, the lower molecular weight ligands with DP > 60, should be used to form liquid crystalline or gelled PBLG based nanocomposites. Future work will focus on the characterizing the spatial distribution of the NPs by ultra small angle X-ray scattering (USAXS), using NPs of larger sizes and different compositions and combining the PBLG ligands with flexible polymer ligands such as polystyrene or poly(ethylene oxide) to mimic rod-coil block copolymer self-assembly. In conclusion, PBLG-grafted NPs can serve as an effective strategy towards LC nanocomposites, as the self-assembly behavior is largely polymer driven and not disrupted by attachment to the NPs.



### 3.7 References

- (1) Deming, T. J. Synthetic polypeptides for biomedical applications. *Progress in Polymer Science* **2007**, 32 (8-9), 858-875.
- (2) Gombotz, W. R.; Pettit, D. K. Biodegradable polymers for protein and peptide drug delivery. *Bioconjugate chemistry* **1995**, 6 (4), 332-351.
- (3) Yang, J.; An, H.-W.; Wang, H. Self-assembled peptide drug delivery systems. *ACS Applied Bio Materials* **2020**, 4 (1), 24-46.
- (4) Zhang, K.; Diehl, M. R.; Tirrell, D. A. Artificial polypeptide scaffold for protein immobilization. *Journal of the American Chemical Society* **2005**, 127 (29), 10136-10137.
- (5) Gould, A.; Ji, Y.; L Aboye, T.; A Camarero, J. Cyclotides, a novel ultrastable polypeptide scaffold for drug discovery. *Current pharmaceutical design* **2011**, 17 (38), 4294-4307.
- (6) Xuan, S.; Lee, C.-U.; Chen, C.; Doyle, A. B.; Zhang, Y.; Guo, L.; John, V. T.; Hayes, D.; Zhang, D. Thermoreversible and injectable ABC polypeptoid hydrogels: Controlling the hydrogel properties through molecular design. *Chemistry of Materials* **2016**, 28 (3), 727-737.
- (7) Zhang, N.; Dietrich, M. A.; Lopez, M. J. Therapeutic doses of multipotent stromal cells from minimal adipose tissue. *Stem Cell Reviews and Reports* **2014**, 10, 600-611.
- (8) Carlsen, A.; Lecommandoux, S. Self-assembly of polypeptide-based block copolymer amphiphiles. *Current Opinion in Colloid & Interface Science* **2009**, 14 (5), 329-339.
- (9) Wright, E. R.; Conticello, V. P. Self-assembly of block copolymers derived from elastin-mimetic polypeptide sequences. *Advanced drug delivery reviews* **2002**, 54 (8), 1057-1073.
- (10) Haynie, D. T.; Zhang, L.; Rudra, J. S.; Zhao, W.; Zhong, Y.; Palath, N. Polypeptide multilayer films. *Biomacromolecules* **2005**, 6 (6), 2895-2913.
- (11) Rosu, C.; Jang, Y.; Jiang, L.; Champion, J. Nature-inspired and "water-skating" paper and polyester substrates enabled by the molecular structure of poly ( $\gamma$ -stearyl- $\alpha$ , l-glutamate) homopolypeptide. *Biomacromolecules* **2018**, 19 (12), 4617-4628.
- (12) Kesik, M.; Akbulut, H.; Söylemez, S.; Cevher, Ş. C.; Hızalan, G.; Udum, Y. A.; Endo, T.; Yamada, S.; Çırpan, A.; Yağcı, Y. Synthesis and characterization of conducting polymers containing polypeptide and ferrocene side chains as ethanol biosensors. *Polymer Chemistry* **2014**, 5 (21), 6295-6306.

- (13) Chen, P.; Kong, J.; Wang, X.; Ma, W.; Yang, X.; Qin, Y.; Hu, X. Development of Light-Responsive Poly ( $\gamma$ -Benzyl-L-Glutamate) as Photo Switches by a One-Step NCA Method. *Frontiers in Chemistry* **2020**, 8, 591.
- (14) Liang, Z.; Nguyen, T. P.; Attanayake, N. H.; Easley, A. D.; Lutkenhaus, J. L.; Wooley, K. L.; Odom, S. A. Metal-free polypeptide redox flow batteries. *Materials Advances* **2022**, 3 (16), 6558-6565.
- (15) Gatto, E.; Lettieri, R.; Vesce, L.; Venanzi, M. Peptide Materials in Dye Sensitized Solar Cells. *Energies* **2022**, 15 (15), 5632.
- (16) Han, J.; Ding, J.; Wang, Z.; Yan, S.; Zhuang, X.; Chen, X.; Yin, J. The synthesis, deprotection and properties of poly ( $\gamma$ -benzyl-L-glutamate). *Science China Chemistry* **2013**, 56, 729-738.
- (17) Fang, J.; Yong, Q.; Zhang, K.; Sun, W.; Yan, S.; Cui, L.; Yin, J. Novel injectable porous poly ( $\gamma$ -benzyl-L-glutamate) microspheres for cartilage tissue engineering: preparation and evaluation. *Journal of Materials Chemistry B* **2015**, 3 (6), 1020-1031.
- (18) Ma, T.-L.; Yang, S.-C.; Cheng, T.; Chen, M.-Y.; Wu, J.-H.; Liao, S.-L.; Chen, W.-L.; Su, W.-F. Exploration of biomimetic poly ( $\gamma$ -benzyl-L-glutamate) fibrous scaffolds for corneal nerve regeneration. *Journal of Materials Chemistry B* **2022**, 10 (33), 6372-6379.
- (19) Bu, S.; Yu, M.; Chen, Q.; Chen, D.; Xia, P.; Li, G.; Zhang, K.; Yan, S.; Wu, H.; Yin, J. Construction of poly-( $\gamma$ -benzyl-L-glutamate) composite microcarriers with osteogenic and angiogenic properties for the restoration of alveolar bone defects. *Composites Part B: Engineering* **2022**, 242, 110085. DOI: <https://doi.org/10.1016/j.compositesb.2022.110085>.
- (20) Dekie, L.; Toncheva, V.; Dubruel, P.; Schacht, E. H.; Barrett, L.; Seymour, L. W. Poly-L-glutamic acid derivatives as vectors for gene therapy. *Journal of controlled release* **2000**, 65 (1-2), 187-202.
- (21) Markland, P.; Amidon, G. L.; Yang, V. C. Modified polypeptides containing  $\gamma$ -benzyl glutamic acid as drug delivery platforms. *International journal of pharmaceutics* **1999**, 178 (2), 183-192.
- (22) Upadhyay, K. K.; Bhatt, A. N.; Mishra, A. K.; Dwarakanath, B. S.; Jain, S.; Schatz, C.; Le Meins, J.-F.; Farooque, A.; Chandraiah, G.; Jain, A. K. The intracellular drug delivery and anti tumor activity of doxorubicin loaded poly ( $\gamma$ -benzyl L-glutamate)-b-hyaluronan polymersomes. *Biomaterials* **2010**, 31 (10), 2882-2892.

- (23) McKinnon, A. J.; Tobolsky, A. V. Structure and properties of poly ( $\gamma$ -benzyl-L-glutamate) cast from dimethylformamide. *The Journal of physical chemistry* **1968**, 72 (4), 1157-1161.
- (24) Pan, C.-T.; Yen, C.-K.; Liu, Z.-H.; Kuo, S.; Lu, Y.; Li, H.; Lai, Y.-C. Poly ( $\gamma$ -benzyl  $\alpha$ , L-glutamate) in Cylindrical Near-Field Electrospinning Fabrication and Analysis of Piezoelectric Fibers. *Sens. Mater* **2014**, 26, 63-73.
- (25) Lu, Y.; Liu, D.; Wei, X.; Song, J.; Xiao, Q.; Du, K.; Shi, X.; Gao, H. Synthesis and Thermoreversible Gelation of Coil&dash;Rod Copolymers with a Dendritic Polyethylene Core and Multiple Helical Poly( $\gamma$ -benzyl-L-glutamate) Arms. In *Polymers*, 2023; Vol. 15.
- (26) Spyridakou, M.; Tsimenidis, K.; Gkikas, M.; Steinhart, M.; Graf, R.; Floudas, G. Effects of Nanometer Confinement on the Self-Assembly and Dynamics of Poly( $\gamma$ -benzyl-L-glutamate) and Its Copolymer with Poly(isobutylene). *Macromolecules* **2022**, 55 (7), 2615-2626. DOI: 10.1021/acs.macromol.2c00077.
- (27) Sogawa, H.; Takamatsu, S.; Tsutsuba, T.; Takata, T. Nitrile N-oxide-terminated poly( $\gamma$ -benzyl L-glutamate) (PBLG): synthesis and catalyst-free grafting onto polybutadiene (PBD) and natural rubber (NR). *Polymer Journal* **2020**, 52 (9), 1165-1171. DOI: 10.1038/s41428-020-0370-5.
- (28) Nguyen, L. T.; Le Tran, H.; Mai, P. T.; Duong, V. B.; Nguyen, L.-T. T.; Nguyen, H. T. Poly(L-glutamic acid) via catalytical hydrogenation for the fabrication of carbon nanotube nanocomposites. *Materials Research* **2021**, 24.
- (29) Thiele, C. M. Residual dipolar couplings (RDCs) in organic structure determination. *European Journal of Organic Chemistry* **2008**, 2008 (34), 5673-5685.
- (30) Recchia, M. J. J.; Cohen, R. D.; Liu, Y.; Sherer, E. C.; Harper, J. K.; Martin, G. E.; Williamson, R. T. "One-Shot" Measurement of Residual Chemical Shift Anisotropy Using Poly- $\gamma$ -benzyl-L-glutamate as an Alignment Medium. *Organic Letters* **2020**, 22 (22), 8850-8854. DOI: 10.1021/acs.orglett.0c03225.
- (31) Jahanshahi, K.; Botiz, I.; Reiter, R.; Thomann, R.; Heck, B.; Shokri, R.; Stille, W.; Reiter, G. n. Crystallization of poly ( $\gamma$ -benzyl L-glutamate) in thin film solutions: structure and pattern formation. *Macromolecules* **2013**, 46 (4), 1470-1476.

- (32) Livolant, F. Cholesteric liquid crystalline phases given by three helical biological polymers: DNA, PBLG and xanthan. A comparative analysis of their textures. *Journal de physique* **1986**, 47 (9), 1605-1616.
- (33) Kishi, R.; Sisido, M.; Tazuke, S. Liquid-crystalline polymer gels. 1. Cross-linking of poly ( $\gamma$ -benzyl L-glutamate) in the cholesteric liquid-crystalline state. *Macromolecules* **1990**, 23 (16), 3779-3784.
- (34) Toriumi, H.; Yahagi, K.; Uematsu, I.; Uematsu, Y. Cholesteric structure of lyotropic poly ( $\gamma$ -benzyl L-glutamate) liquid crystals. *Molecular Crystals and Liquid Crystals* **1983**, 94 (3), 267-284.
- (35) Iizuka, E. The effects of magnetic fields on the structure of cholesteric liquid crystals of polypeptides. *Polymer Journal* **1973**, 4 (4), 401-408.
- (36) Bellomo, E. G.; Davidson, P.; Imp  rator-Clerc, M.; Deming, T. J. Aqueous Cholesteric Liquid Crystals Using Uncharged Rodlike Polypeptides. *Journal of the American Chemical Society* **2004**, 126 (29), 9101-9105. DOI: [10.1021/ja047932d](https://doi.org/10.1021/ja047932d).
- (37) Wong, J.; Toader, V.; Reven, L. Lyotropic Nematic Phases of Isotropic Nanoparticles via Semiflexible Polymer Ligands. *Macromolecular Rapid Communications* **2023**, 44 (8), 2200951. DOI: <https://doi.org/10.1002/marc.202200951>.
- (38) Uchida, J.; Kiguchi, R.; Kato, R.; Kato, T. Thermotropic Colloidal Liquid-Crystalline Hydroxyapatite Nanorod Hybrids Containing a Forklike Mesogen. *Helvetica Chimica Acta* **2023**, 106 (8), e202300053. DOI: <https://doi.org/10.1002/hlca.202300053> (accessed 2024/01/05).
- (39) Miyamoto, N.; Iijima, H.; Ohkubo, H.; Yamauchi, Y. Liquid crystal phases in the aqueous colloids of size-controlled fluorinated layered clay mineral nanosheets. *Chem Commun (Camb)* **2010**, 46 (23), 4166-4168. DOI: [10.1039/b927335b](https://doi.org/10.1039/b927335b) From NLM.
- (40) Gabriel, J. C. P.; Davidson, P. New Trends in Colloidal Liquid Crystals Based on Mineral Moieties. *Advanced Materials* **2000**, 12 (1), 9-20. DOI: [https://doi.org/10.1002/\(SICI\)1521-4095\(200001\)12:1<9::AID-ADMA9>3.0.CO;2-6](https://doi.org/10.1002/(SICI)1521-4095(200001)12:1<9::AID-ADMA9>3.0.CO;2-6) (accessed 2024/01/05).
- (41) Goodson, S. H.; Novak, B. M. Synthesis and Characterization of Wormlike Three-Arm Poly(n-hexyl isocyanate) Star Polymers. *Macromolecules* **2001**, 34 (12), 3849-3855. DOI: [10.1021/ma991692i](https://doi.org/10.1021/ma991692i).

- (42) Poché, D. S.; Moore, M. J.; Bowles, J. L. An Unconventional Method for Purifying the N-carboxyanhydride Derivatives of  $\gamma$ -alkyl-L-glutamates. *Synthetic Communications* **1999**, 29 (5), 843-854. DOI: 10.1080/00397919908086042.
- (43) Temyanko, E.; Russo, P. S.; Ricks, H. Study of Rodlike Homopolypeptides by Gel Permeation Chromatography with Light Scattering Detection: Validity of Universal Calibration and Stiffness Assessment. *Macromolecules* **2001**, 34 (3), 582-586. DOI: 10.1021/ma0013511.
- (44) Ossowicz, P.; Rozwadowski, Z.; Gano, M.; Janus, E. Efficient method for Knoevenagel condensation in aqueous solution of amino acid ionic liquids (AAILs). *Polish Journal of Chemical Technology* **2016**, 18 (4), 90-95.
- (45) Wu, Y.; Chen, K.; Wu, X.; Liu, L.; Zhang, W.; Ding, Y.; Liu, S.; Zhou, M.; Shao, N.; Ji, Z.; et al. Superfast and Water-Insensitive Polymerization on  $\alpha$ -Amino Acid N-Carboxyanhydrides to Prepare Polypeptides Using Tetraalkylammonium Carboxylate as the Initiator. *Angewandte Chemie International Edition* **2021**, 60 (50), 26063-26071. DOI: <https://doi.org/10.1002/anie.202103540>.
- (46) McKenna, C. E.; Higa, M. T.; Cheung, N. H.; McKenna, M.-C. The facile dealkylation of phosphonic acid dialkyl esters by bromotrimethylsilane. *Tetrahedron Letters* **1977**, 18 (2), 155-158.
- (47) Garnweitner, G.; Goldenberg, L. M.; Sakhno, O. V.; Antonietti, M.; Niederberger, M.; Stumpe, J. Large-Scale Synthesis of Organophilic Zirconia Nanoparticles and their Application in Organic-Inorganic Nanocomposites for Efficient Volume Holography. *Small* **2007**, 3 (9), 1626-1632.
- (48) Aliferis, T.; Iatrou, H.; Hadjichristidis, N. Living polypeptides. *Biomacromolecules* **2004**, 5 (5), 1653-1656.
- (49) Vacogne, C. D.; Schlaad, H. Controlled ring-opening polymerization of  $\alpha$ -amino acid N-carboxyanhydrides in the presence of tertiary amines. *Polymer* **2017**, 124, 203-209. DOI: <https://doi.org/10.1016/j.polymer.2017.07.062>.
- (50) Liu, Y.; Li, D.; Ding, J.; Chen, X. Controlled synthesis of polypeptides. *Chinese Chemical Letters* **2020**, 31 (12), 3001-3014. DOI: <https://doi.org/10.1016/j.cclet.2020.04.029>.

- (51) Candau, F.; Dufour, C.; François, J.; Levy, H.; Marchal, E.; Layec, Y.; Wolff, C. Anomalous behaviour of poly( $\gamma$ -benzyl-L-glutamate) in helicogenic solvents in relation to the polymerization conditions. *European Polymer Journal* **1980**, 16 (5), 447-449. DOI: [https://doi.org/10.1016/0014-3057\(80\)90151-2](https://doi.org/10.1016/0014-3057(80)90151-2).
- (52) Li, Y.; Chang, R.; Chen, Y.-X. Recent Advances in Post-polymerization Modifications on Polypeptides: Synthesis and Applications. *Chemistry – An Asian Journal* **2022**, 17 (14), e202200318. DOI: <https://doi.org/10.1002/asia.202200318>.
- (53) Xia, Y.; Song, Z.; Tan, Z.; Xue, T.; Wei, S.; Zhu, L.; Yang, Y.; Fu, H.; Jiang, Y.; Lin, Y.; et al. Accelerated polymerization of N-carboxyanhydrides catalyzed by crown ether. *Nature Communications* **2021**, 12 (1), 732. DOI: 10.1038/s41467-020-20724-w.
- (54) Temyanko, E.; Russo, P. S.; Ricks, H. Study of rodlike homopolypeptides by gel permeation chromatography with light scattering detection: validity of universal calibration and stiffness assessment. *Macromolecules* **2001**, 34 (3), 582-586.
- (55) Bu, Z.; Russo, P. S.; Tipton, D. L.; Negulescu, I. I. Self-diffusion of rodlike polymers in isotropic solutions. *Macromolecules* **1994**, 27 (23), 6871-6882.
- (56) Dousseau, F.; Pézolet, M. Determination of the secondary structure content of proteins in aqueous solutions from their amide I and amide II infrared bands. Comparison between classical and partial least-squares methods. *Biochemistry* **1990**, 29 (37), 8771-8779. DOI: 10.1021/bi00489a038 From NLM.
- (57) Heinrich, C.; Niedner, L.; Oberhausen, B.; Kickelbick, G. Surface-charged zirconia nanoparticles prepared by organophosphorus surface functionalization with ammonium or sulfonate groups. *Langmuir* **2019**, 35 (35), 11369-11379.
- (58) Niehoff, A.; Manton, A.; McAloney, R.; Huber, A.; Falkenhagen, J.; Goh, C. M.; Thünemann, A. F.; Winnik, M. A.; Menzel, H. Elucidation of the structure of poly( $\gamma$ -benzyl-L-glutamate) nanofibers and gel networks in a helicogenic solvent. *Colloid and polymer science* **2013**, 291, 1353-1363.
- (59) Fukuzawa, T.; Uematsu, I.; Uematsu, Y. Viscoelastic Properties of Poly( $\gamma$ -benzyl glutamate). *Polymer Journal* **1974**, 6 (5), 431-437. DOI: 10.1295/polymj.6.431.

- (60) Schneider, C. A.; Rasband, W. S.; Eliceiri, K. W. NIH Image to ImageJ: 25 years of image analysis. *Nature Methods* **2012**, 9 (7), 671-675. DOI: 10.1038/nmeth.2089.
- (61) Sakamoto, R. Phase separation of poly ( $\gamma$ -benzyl L-glutamate) to liquid crystal and isotropic solution in various helicogenic solvents. *Colloid and Polymer Science* **1984**, 262, 788-792.
- (62) Kihara, H. Dielectric Properties of Polypeptides in Solution. II. Aggregation of Poly ( $\Gamma$ -Benzyl L-Glutamate) in Various Helicogenic Solvents. *Polymer Journal* **1977**, 9 (5), 443-450.
- (63) Oikawa, H.; Nakanishi, H. Dynamics of probe particles during sol-gel transition of PBLG-DMF solution and the resulting gel structure. *The Journal of Chemical Physics* **2001**, 115 (8), 3785-3791.
- (64) Ginzburg, B.; Siromyatnikova, T.; Frenkel, S. Gelation in the poly ( $\gamma$ -benzyl-L-glutamate)-dimethylformamide system. *Polymer Bulletin* **1985**, 13, 139-144.
- (65) Sasaki, S.; Hikata, M.; Shiraki, C.; Uematsu, I. Molecular Aggregation and Gelation in Poly ( $\gamma$ -benzyl L-glutamate) Solutions. *Polymer Journal* **1982**, 14 (3), 205-213.
- (66) Miller, W. G.; Wee, E. L. Liquid crystal-isotropic phase equilibria in the system poly ( $\gamma$ -benzyl-L-glutamate)-methylformamide. *The Journal of Physical Chemistry* **1971**, 75 (10), 1446-1452.
- (67) Higashi, N.; Kawahara, J.; Niwa, M. Preparation of helical peptide monolayer-coated gold nanoparticles. *Journal of colloid and interface science* **2005**, 288 (1), 83-87.
- (68) Marcelo, G.; Munoz-Bonilla, A.; Rodríguez-Hernández, J.; Fernández-García, M. Hybrid materials achieved by polypeptide grafted magnetite nanoparticles through a dopamine biomimetic surface anchored initiator. *Polymer Chemistry* **2013**, 4 (3), 558-567.
- (69) Cui, Y.; Deng, R.; Li, X.; Wang, X.; Jia, Q.; Bertrand, E.; Meguellati, K.; Yang, Y.-W. Temperature-sensitive polypeptide brushes-coated mesoporous silica nanoparticles for dual-responsive drug release. *Chinese Chemical Letters* **2019**, 30 (12), 2291-2294.
- (70) Bouchara, A.; de AA Soler-Illia, G. J.; Chane-Ching, J.-Y.; Sanchez, C. Nanotectonic approach of the texturation of CeO<sub>2</sub> based nanomaterials. *Chemical communications* **2002**, (11), 1234-1235.
- (71) Flory, P. J. Molecular theory of liquid crystals. In *Liquid crystal polymers I*, Springer, 2005; pp 1-36.

- (72) Wissbrun, K. F. Rheology of rod-like polymers in the liquid crystalline state. *Journal of Rheology* **1981**, 25 (6), 619-662.
- (73) Flory, P. J.; Ronca, G. Theory of systems of rodlike particles: I. Athermal systems. *Molecular Crystals and Liquid Crystals* **1979**, 54 (3-4), 289-309.
- (74) Wu, L.; Müller, E. A.; Jackson, G. Understanding and describing the liquid-crystalline states of polypeptide solutions: a coarse-grained model of PBLG in DMF. *Macromolecules* **2014**, 47 (4), 1482-1493.
- (75) Onogi, S.; Asada, T. Rheology and rheo-optics of polymer liquid crystals. In *Rheology: Volume 1: Principles*, Springer, 1980; pp 127-147.
- (76) Mor/Moshe Gottlieb, R.; Graham, A.; Mondy, L. VISCOSITY OF CONCENTRATED SUSPENSIONS OF SPHERE/ROD MIXTURES†. *Chemical Engineering Communications* **1996**, 148-150 (1), 421-430. DOI: 10.1080/00986449608936529.
- (77) Tang, H.; Zhang, D. Solid state self-assembly of the single-walled carbon nanotubes and poly ( $\gamma$ -benzyl-L-glutamate) s with different conformations. *Journal of Polymer Science Part A: Polymer Chemistry* **2013**, 51 (21), 4489-4497.
- (78) Rosu, C.; Jacobeen, S.; Park, K.; Reichmanis, E.; Yunker, P.; Russo, P. S. Domed Silica Microcylinders Coated with Oleophilic Polypeptides and Their Behavior in Lyotropic Cholesteric Liquid Crystals of the Same Polypeptide. *Langmuir* **2016**, 32 (49), 13137-13148. DOI: 10.1021/acs.langmuir.6b03165.
- (79) Brittain, W. J.; Minko, S. A structural definition of polymer brushes. *Journal of Polymer Science Part A: Polymer Chemistry* **2007**, 45 (16), 3505-3512.
- (80) Gharbi, K.; Salles, F.; Mathieu, P.; Amiens, C.; Collière, V.; Coppel, Y.; Philippot, K.; Fontaine, L.; Montembault, V.; Smiri, L. S. Alkyl phosphonic acid-based ligands as tools for converting hydrophobic iron nanoparticles into water soluble iron-iron oxide core-shell nanoparticles. *New Journal of Chemistry* **2017**, 41 (20), 11898-11905.
- (81) Daou, T. J.; Begin-Colin, S.; Grenèche, J. M.; Thomas, F.; Derory, A.; Bernhardt, P.; Legaré, P.; Pourroy, G. Phosphate Adsorption Properties of Magnetite-Based Nanoparticles. *Chemistry of Materials* **2007**, 19 (18), 4494-4505. DOI: 10.1021/cm071046v.

- (82) Wang, Z.; Zheng, Z.; Liu, J.; Wu, Y.; Zhang, L. Tuning the mechanical properties of polymer nanocomposites filled with grafted nanoparticles by varying the grafted chain length and flexibility. *Polymers* **2016**, 8 (9), 270.
- (83) Flory, P. J. Phase changes in proteins and polypeptides. *Journal of Polymer Science* **1961**, 49 (151), 105-128.
- (84) Robinson, C. The cholesteric phase in polypeptide solutions and biological structures. *Molecular Crystals and Liquid Crystals* **1966**, 1 (4), 467-494.
- (85) DuPré, D. B.; Duke, R. W. Temperature, concentration, and molecular weight dependence of the twist elastic constant of cholesteric poly- $\gamma$ -benzyl-L-glutamate. *The Journal of Chemical Physics* **1975**, 63 (1), 143-148. DOI: 10.1063/1.431066 (accessed 4/27/2024).
- (86) Sato, T.; Nakamura, J.; Teramoto, A.; Green, M. M. Cholesteric pitch of lyotropic polymer liquid crystals. *Macromolecules* **1998**, 31 (4), 1398-1405.
- (87) Itou, S. Lyotropic Liquid Crystalline Structures of Synthetic Polypeptides I: Molecular Weight Dependence of the Cholesteric Pitch on Poly ( $\gamma$ -benzyl L-glutamate) Solutions. *Molecular Crystals and Liquid Crystals* **1989**, 172 (1), 201-210.
- (88) Toriumi, H.; Kusumi, Y.; Uematsu, I.; Uematsu, Y. Thermally induced inversion of the cholesteric sense in lyotropic polypeptide liquid crystals. *Polymer Journal* **1979**, 11 (11), 863-869.
- (89) Russo, P. S.; Miller, W. G. Coexistence of liquid crystalline phases in poly ( $\gamma$ -benzyl  $\alpha$ , L-glutamate)-dimethylformamide. *Macromolecules* **1983**, 16 (11), 1690-1693.
- (90) Tadmor, R.; Dagan, A.; Cohen, Y. Polymer-solvent co-crystallization during thermoreversible gelation in solutions of the helical polypeptide PBLG. *Macromolecular Symposia* **1997**, 114 (1), 13-22. DOI: <https://doi.org/10.1002/masy.19971140104>.
- (91) Russo, P. S.; Miller, W. G. On the nature of the poly ( $\gamma$ -benzyl glutamate)-dimethylformamide" complex phase". *Macromolecules* **1984**, 17 (7), 1324-1331.
- (92) Agra-Kooijman, D. M.; Kumar, S. X-ray scattering investigations of liquid crystals. *Handbook of liquid crystals* **2014**, 8.

(93) Chevigny, C.; Dalmas, F.; Di Cola, E.; Gimes, D.; Bertin, D.; Boué, F.; Jestin, J. Polymer-grafted-nanoparticles nanocomposites: dispersion, grafted chain conformation, and rheological behavior. *Macromolecules* **2011**, 44 (1), 122-133.

(94) Guinier, A.; Fournet, G.; Walker, C. B.; Yudowitch, K. L. *Small-angle Scattering of X-rays*; Wiley New York, 1955.

(95) King, S.; Griffiths, P.; Hone, J.; Cosgrove, T. SANS from adsorbed polymer layers. In *Macromolecular Symposia*, 2002; Wiley Online Library: Vol. 190, pp 33-42.

### 3.8 Supplementary Information

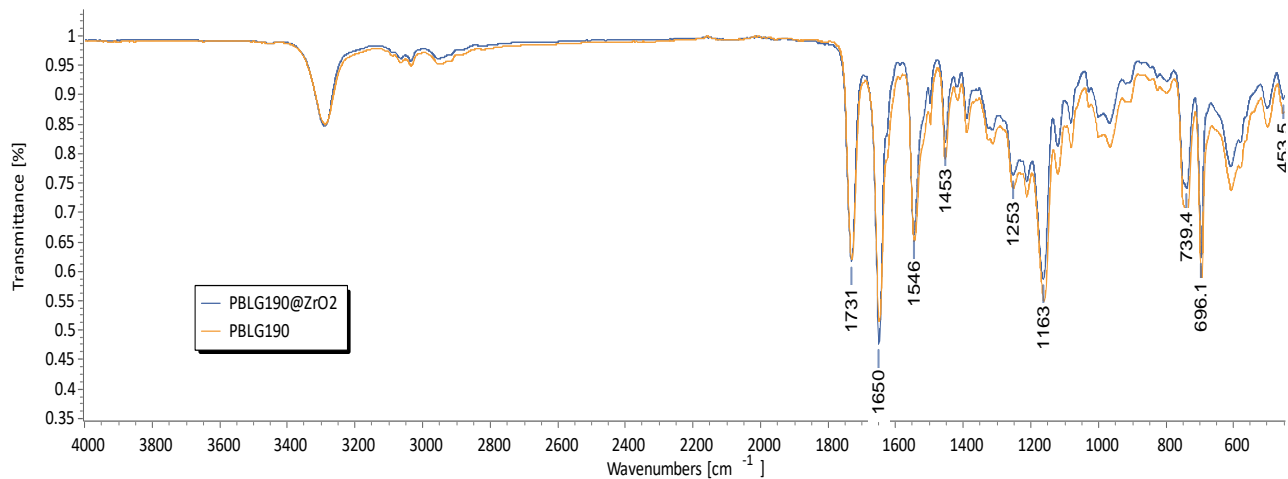


Figure 3-7: FTIR spectra of PBLG<sub>189</sub>@ZrO<sub>2</sub> and PBLG<sub>189</sub>. Location of amide I and II bands indicate  $\alpha$ -helix conformation.

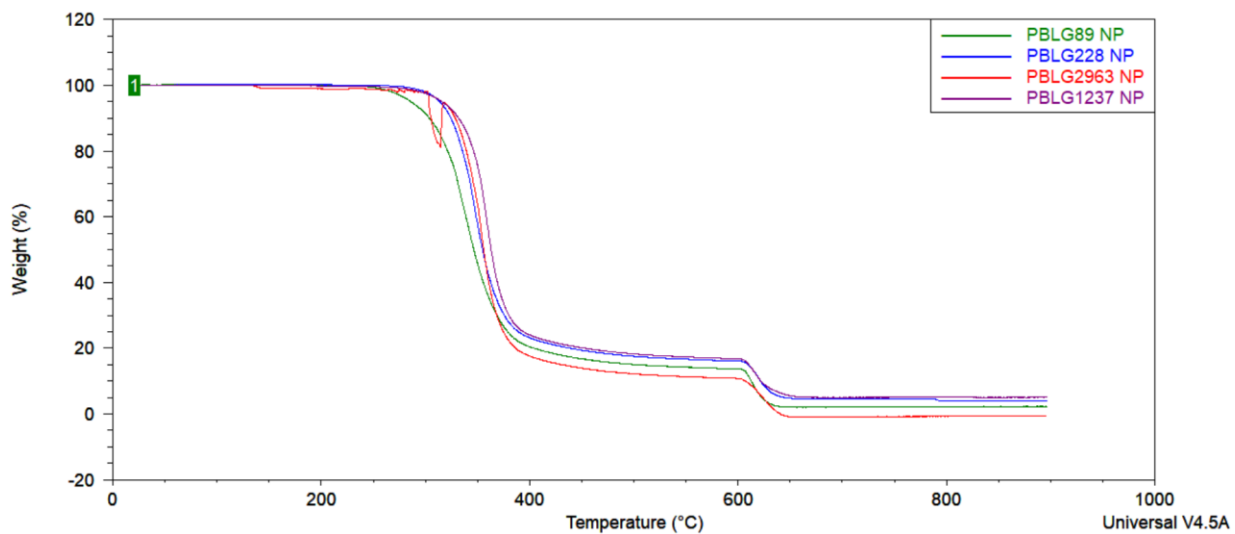


Figure 3-8: TGA weight loss curves for functional PBLG@ZrO<sub>2</sub> NPs.

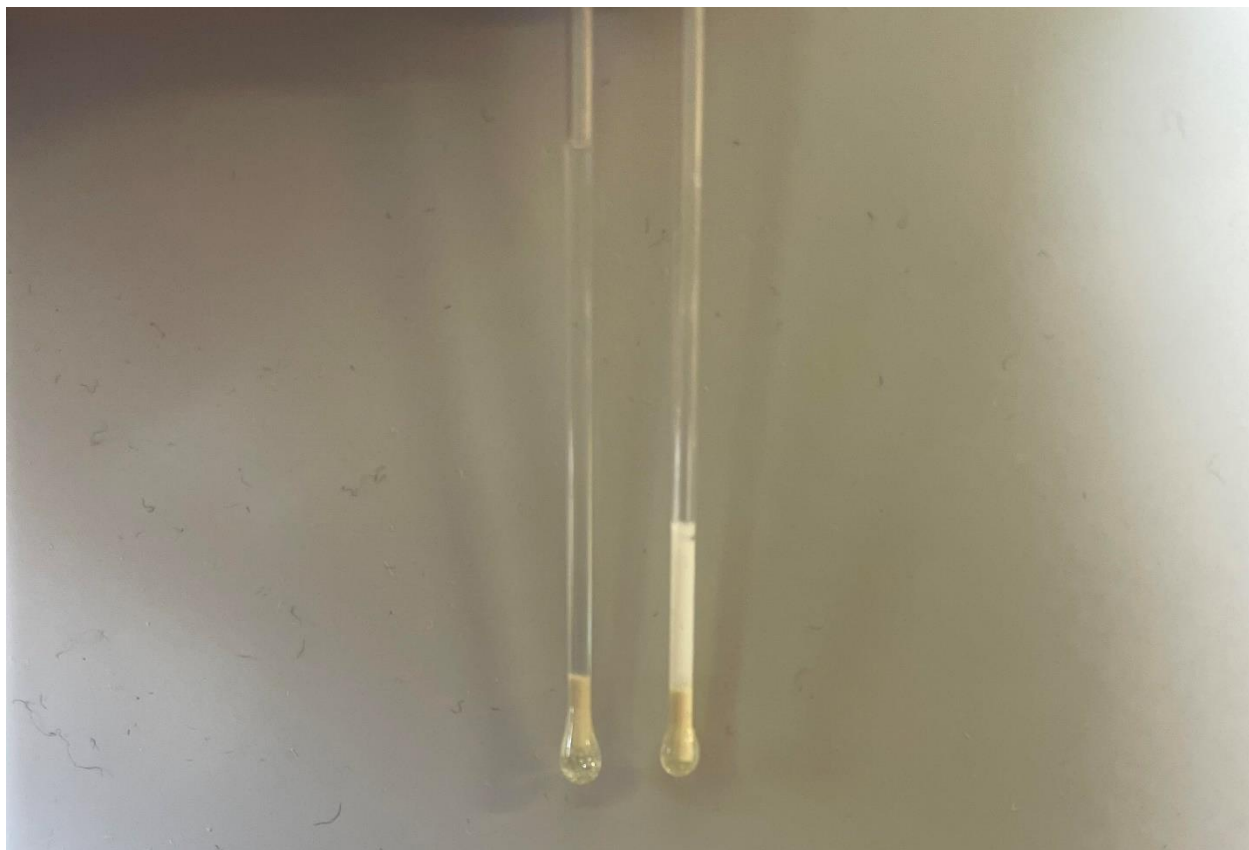


Figure 3-9: Comparison between transparent LC sample (left) and white and cloudy gel/aggregate sample (right).

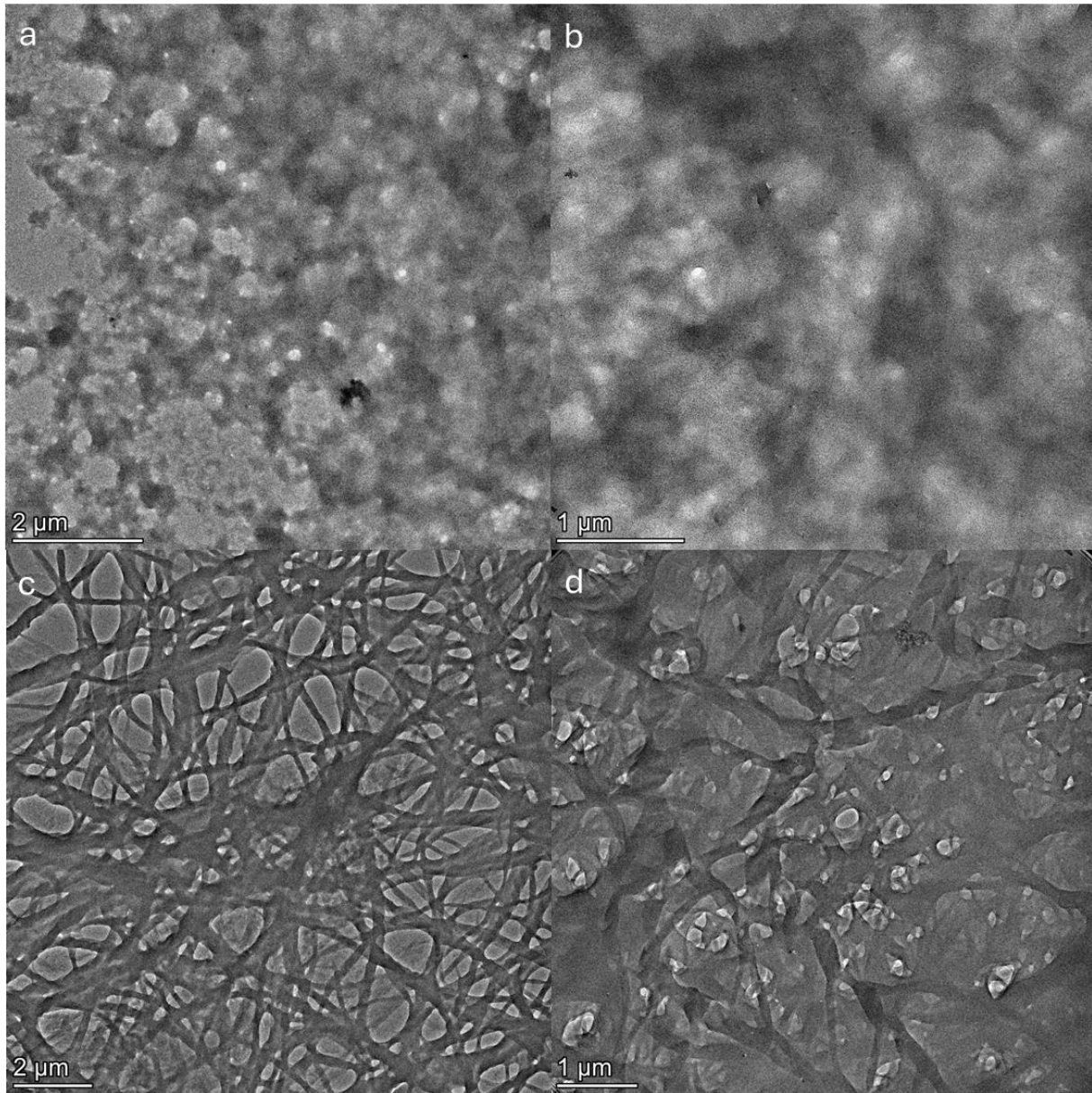


Figure 3-10: TEM images of polymer gel networks formed from (a) PBLG<sub>89</sub>@ZrO<sub>2</sub>, (b) PBLG<sub>228</sub>@ZrO<sub>2</sub>, (c) PBLG<sub>1237</sub>@ZrO<sub>2</sub>, and (d) PBLG<sub>2963</sub>@ZrO<sub>2</sub>. Films casted from 1.0 wt% DMF solutions at 50°C.

Table 3-3: Average interparticle distances measured from TEM images. Mean and standard deviation was calculated across a hundred measurements.

Sample	Mean ( $\times 10^1$ nm)	Standard Deviation ( $\times 10^1$ nm)
PBLG <sub>89</sub> @ZrO <sub>2</sub>	4	1
PBLG <sub>228</sub> @ZrO <sub>2</sub>	5	3
PBLG <sub>1237</sub> @ZrO <sub>2</sub>	6	3
PBLG <sub>2963</sub> @ZrO <sub>2</sub>	6	3

Table 3-4 Summary of TGA results. Calculated surface coverages from experimental TGA weight loss and expected weight loss, assuming a phosphonic acid footprint of 0.24 nm<sup>2</sup>.

Sample	Expected Weight Loss	Experimental Weight Loss	Calculated Surface Coverage (PBLG/nm <sup>2</sup> )
PBLG <sub>89</sub> @ZrO <sub>2</sub>	97.50%	97.75%	5.1
PBLG <sub>228</sub> @ZrO <sub>2</sub>	98.89%	95.95%	1.1
PBLG <sub>1237</sub> @ZrO <sub>2</sub>	99.79%	94.93%	0.16
PBLG <sub>2963</sub> @ZrO <sub>2</sub>	99.91%	100.6%	-

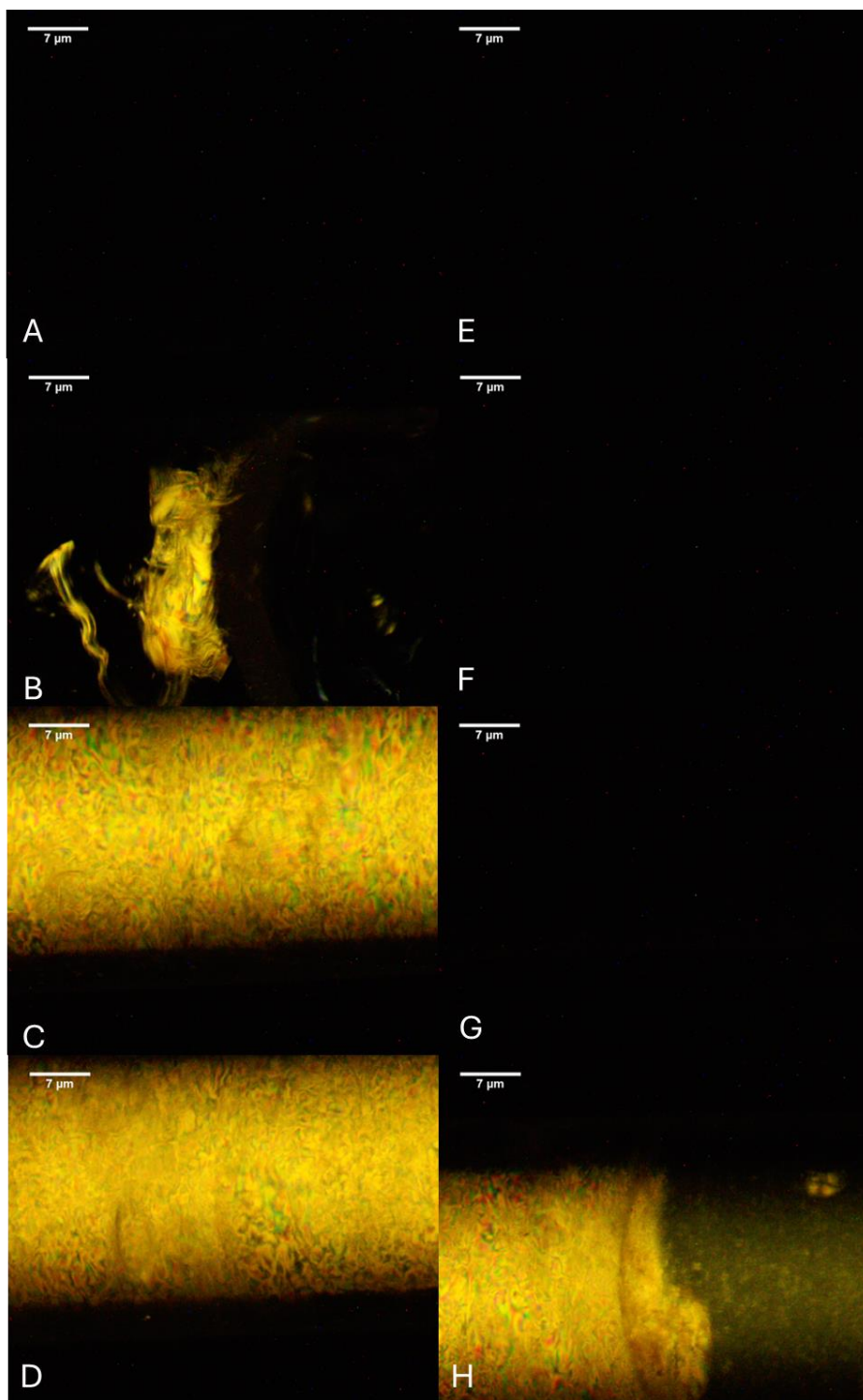


Figure 3-11: Lyotropic DMF solutions of (A-D) PBLG<sub>89</sub>@ZrO<sub>2</sub> and (E-H) PBLG<sub>89</sub>, in increasing concentration (10 wt%, 20 wt%, 30 wt%, 40 wt%). Samples were annealed overnight at 50°C prior to POM imaging.

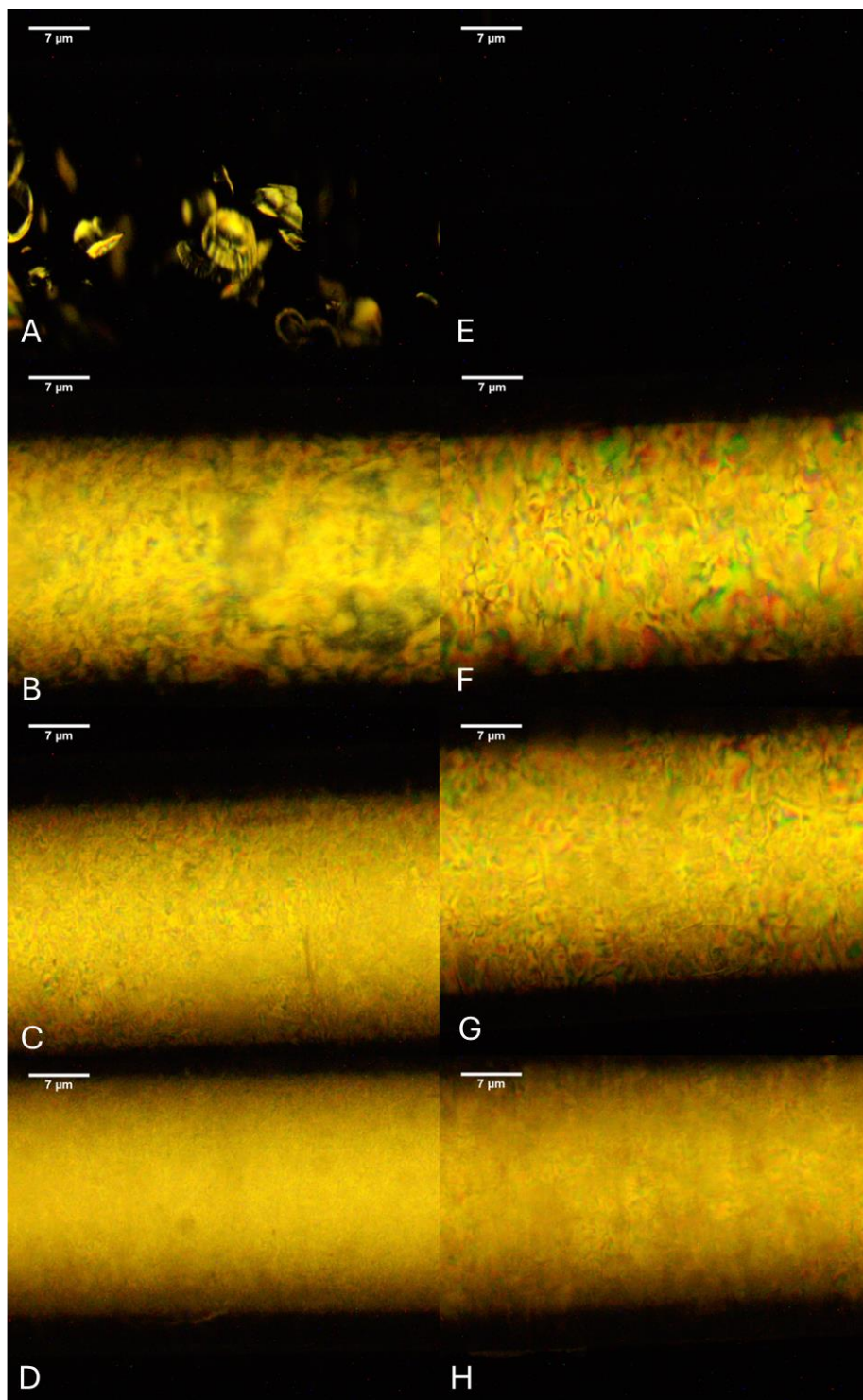


Figure 3-12: Lyotropic DMF solutions of (A-D) PBLG<sub>228</sub>@ZrO<sub>2</sub> and (E-H) PBLG<sub>228</sub>, in increasing concentration (10 wt%, 20 wt%, 30 wt%, 40 wt%). Samples were annealed overnight at 50°C prior to POM imaging.

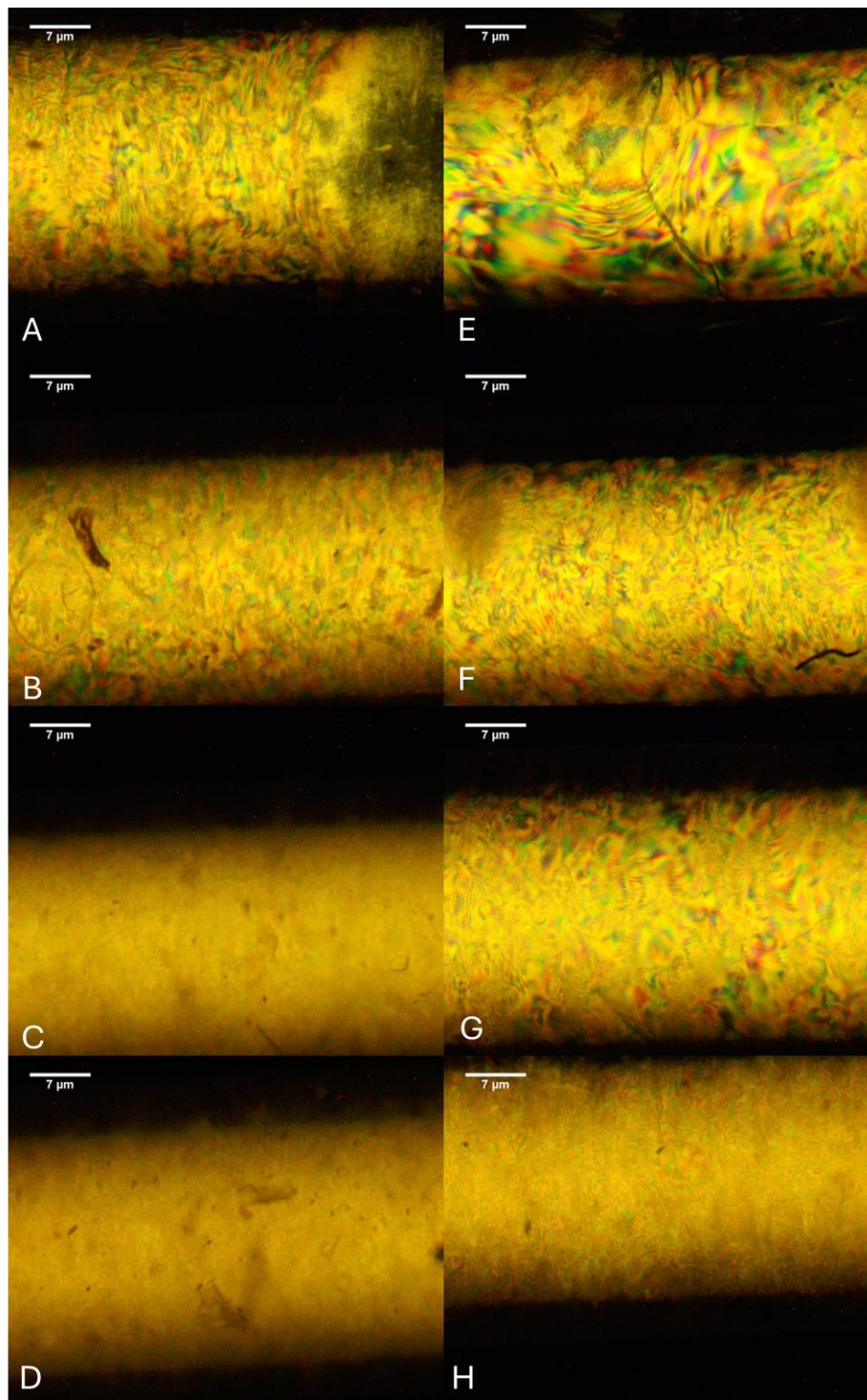


Figure 3-13: Lyotropic DMF solutions of (A-D) PBLG<sub>1237</sub>@ZrO<sub>2</sub> and (E-H) PBLG<sub>1237</sub>, in increasing concentration (10 wt%, 20 wt%, 30 wt%, 40 wt%). Samples were annealed overnight at 50°C prior to POM imaging.

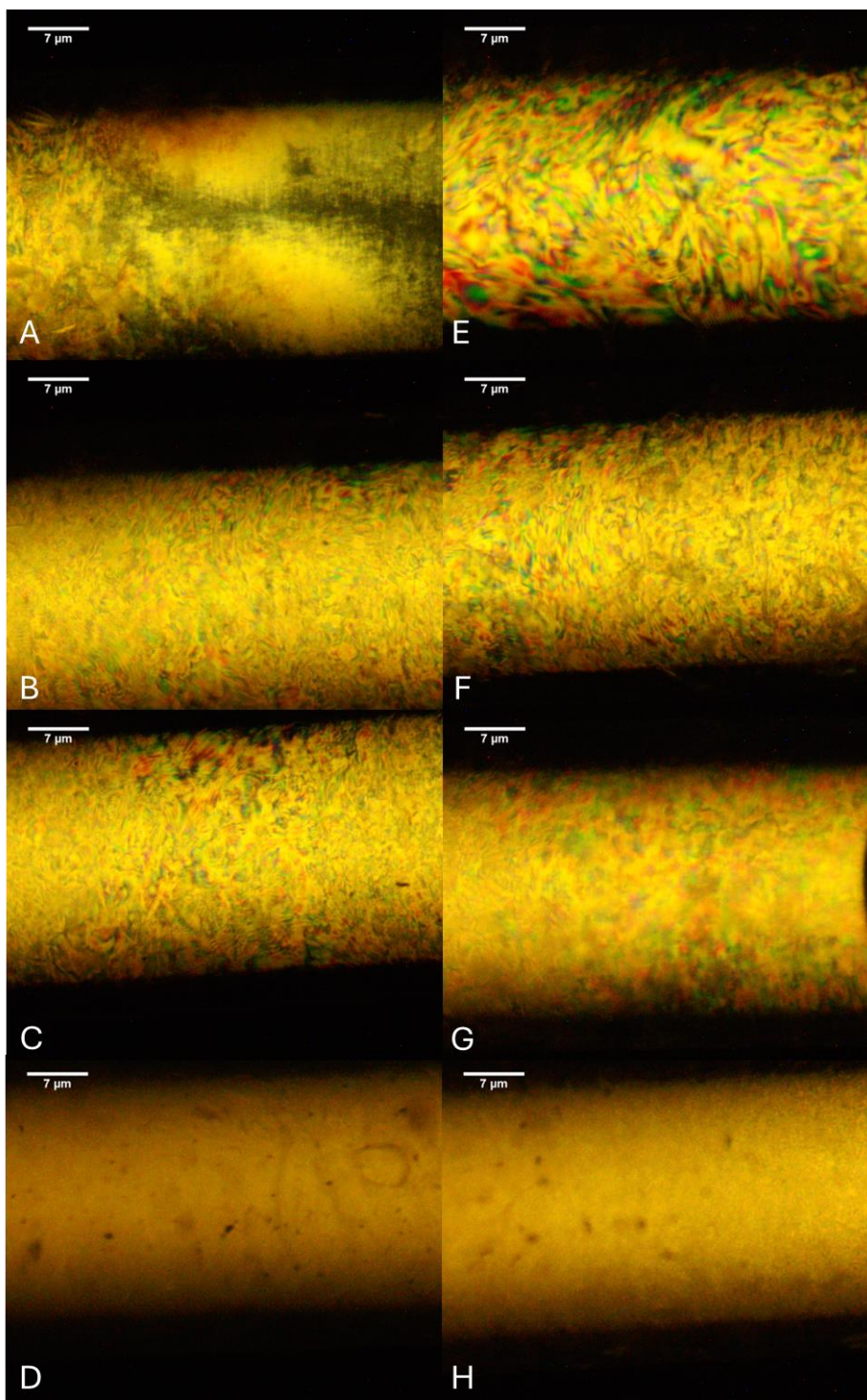


Figure 3-14: Lyotropic DMF solutions of (A-D) PBLG<sub>2963</sub>@ZrO<sub>2</sub> and (E-H) PBLG<sub>2963</sub>, in increasing concentration (10 wt%, 20 wt%, 30 wt%, 40 wt%). Samples were annealed overnight at 50°C prior to POM imaging.

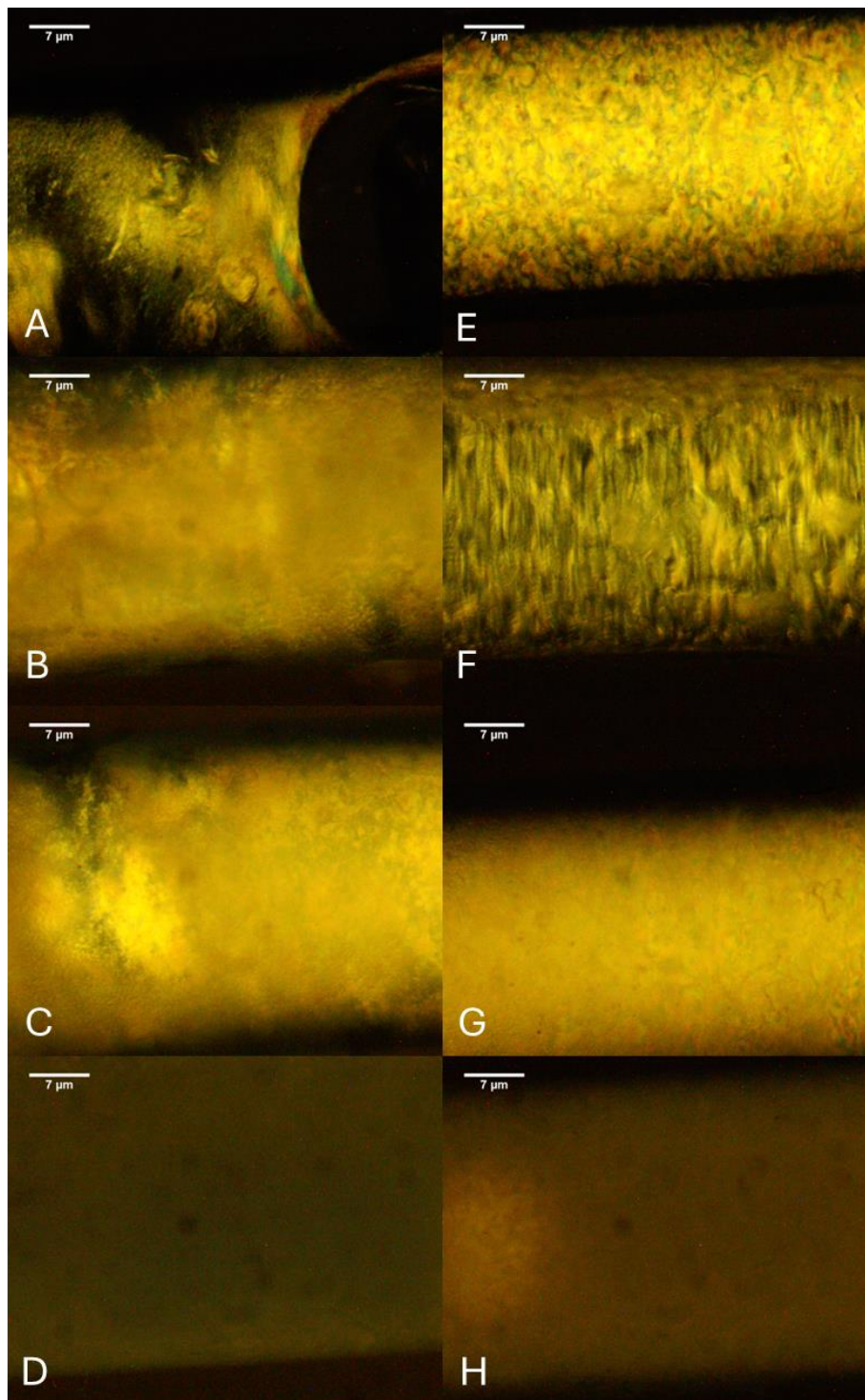


Figure 3-15: Gelled samples in THF of (A-D) PBLG<sub>228</sub>@ZrO<sub>2</sub> and (E-H) PBLG<sub>228</sub>, in increasing concentration (10 wt%, 20 wt%, 30 wt%, 40 wt%). Samples were allowed to sit undisturbed on the bench overnight prior to POM imaging.

# Chapter 4 Thermotropic and Lyotropic Phase Behavior of Cholesteric Poly( $\gamma$ -Stearyl-L-Glutamate) Functionalized Nanoparticles

Jessie Wong, Violeta Toader and Linda Reven

## Rationale for Chapter 4:

The fourth chapter of this thesis describes a novel polymer nanocomposite based on poly( $\gamma$ -stearyl-L-glutamate) (PSLG). To further expand upon the results seen in **Chapter 2**, PSLG was chosen due to its thermotropic liquid crystalline properties (as well as its lyotropic properties), in addition to its unique thermal structures. High molecular weight PSLG ligands were synthesized following a similar synthetic scheme outlined in **Chapter 3**. These ligands were then modified and subsequently attached to the surface of zirconia nanoparticles. The present chapter describes characterization of the synthesized PSLG ligands, their corresponding functionalized nanoparticles as well as the lyotropic and thermotropic liquid crystal structures, in addition to self-assembled thermal structures. Additionally, the present chapter seeks to consolidate decades of PSLG research, to distinguish physical properties owing to PSLG prepared through ester exchange and PSLG synthesized through N-carboxyanhydride polymerization. The results reveal that surface anchoring of the PBLG ligands do not significantly alter the self-assembling properties of the liquid crystals nor the thermal structures. Furthermore, PSLG and its functionalized PSLG particles were found to organize into a biphasic cholester/columnar liquid crystal.

Chapter 4 is currently being prepared as a manuscript as J. Wong, V. Toader, C. J. Barrett, L. Reven, "Thermotropic and Lyotropic Phase Behavior of Poly( $\gamma$ -Stearyl-L-Glutamate) Functionalized Nanoparticles".

## 4.1 Abstract

Poly( $\gamma$ -stearyl-L-glutamate) (PSLG) is a semiflexible synthetic polypeptide that forms both thermotropic and lyotropic liquid crystal (LC) phases. We previously showed that spherical nanoparticles decorated with another semiflexible helical polymer, poly(hexyl isocyanate), forms lyotropic nematic rather than cubic LC phases. In this work, PSLG ligands for functionalizing 4nm ZrO<sub>2</sub> nanoparticles (NPs) were prepared via N-carboxyanhydride polymerization. The structural changes of PSLG upon surface anchoring and the effect on its ability to form thermotropic and lyotropic LCs were studied by differential scanning calorimetry (DSC), optical microscopy and small angle X-ray scattering (SAXS). Surface anchoring of PSLG did not significantly change the lyotropic or thermotropic self-assembly behavior. However, for both free and tethered PSLG, X-ray scattering combined with optical microscopy revealed the co-existence of cholesteric and columnar hexagonal lyotropic phases over a wide concentration range rather than the expected pure cholesteric phase. Whereas low molecular weight mesogenic ligands have been widely used, polymer ligands have not been previously exploited to produce thermotropic liquid crystalline NPs.

## 4.2 Introduction

Cholesteric liquid crystals (CLCs) are one of the most studied LC systems in part due to their abundance in nature.<sup>1,2</sup> Cellulose, collagen,  $\alpha$ -helical polypeptides, DNA are a few examples of biological materials that exhibit cholesteric LC phases.<sup>3,4</sup> These chiral biopolymers are natural candidates as soft matter materials for optical and biomedical applications. By modulating the helical pitch,  $p$ , CLCs can be used as photonic crystals with selective reflection occurring in the visible light range.

Semi-flexible polymers can form liquid crystal phases in either thermotropic or lyotropic environments. One such polymer, poly( $\gamma$ -stearyl-L-glutamate) (PSLG), is known to do both. Traditionally,  $\alpha$ -helical polypeptides have been known to form lyotropic LCs, with poly( $\gamma$ -benzyl-L-glutamate) (PBLG) acting as a model rigid rod in solution. In sufficiently concentrated solutions,

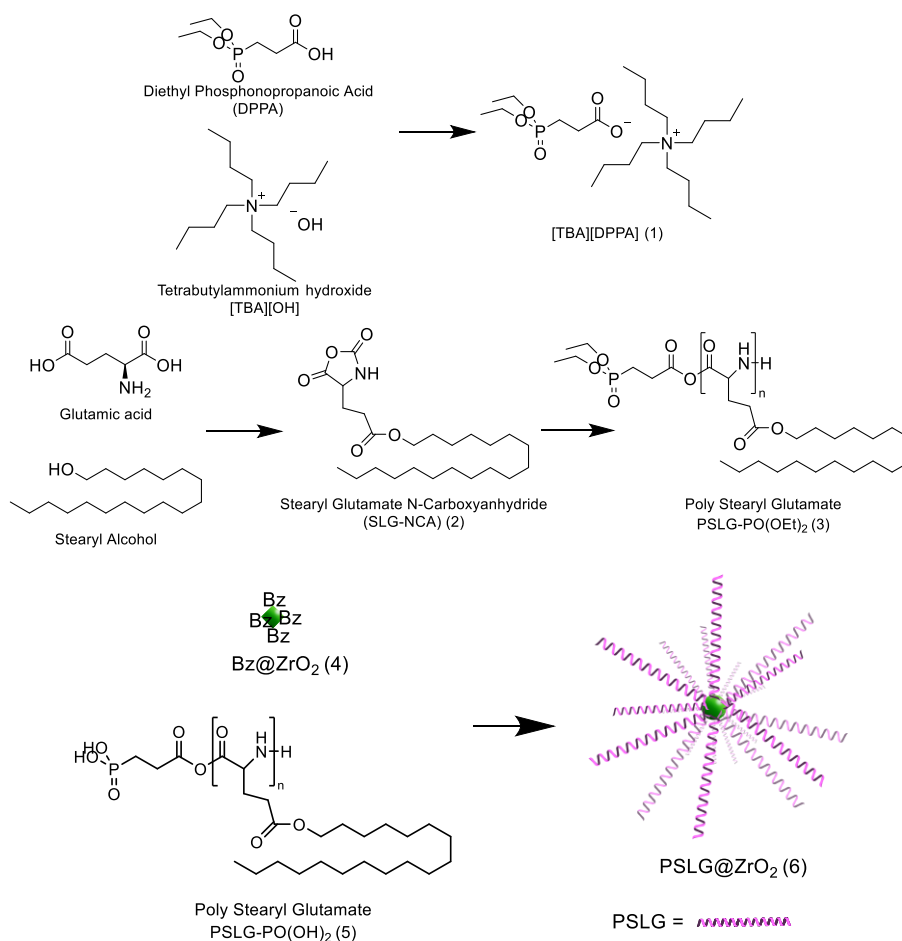
LC organization of PBLG become spontaneous, with several models existing to describe LC formation.<sup>5,6</sup> PSLG is a similar  $\alpha$ -helical polypeptide with the replacement of the benzyl moieties with stearyl side chains giving rise to temperature dependent properties.

It is known that for poly(alkyl glutamates), with linear alkyl chains comprised of 1 – 10 carbons, the  $\alpha$ -helices pack in hexagonal-like arrangement.<sup>7, 8</sup> In contrast, organization of poly(alkyl glutamates) with side chains of more than 10 carbons, is largely driven by crystallization of the alkyl side chains. At sufficiently high temperatures, the alkyl chains form a paraffin-like melt, which in turn solvates the  $\alpha$ -helices.<sup>9,10</sup> Previous literature on the thermotropic LC behavior of PSLG and its co-polymers with (and related poly alkyl glutamates) has been inconsistent as far as the presence and temperatures of different phase transitions. PSLG exhibits LC ordering on heating above the melting transition of the stearyl side chains.<sup>8,11-14</sup> In the case of copolymers of alkyl and benzyl glutamates, cholesteric or columnar hexagonal ordering occurs above the temperature at which thermal movement becomes accessible for the  $\alpha$ -helix core.<sup>15-17</sup> Additional studies have indicated the coexistence of thermotropic LC phases.<sup>14</sup>

Intuitively, cholesteric ordering should require thermal movement of the polypeptide rods to arrange into a supramolecular helix. However, only stearyl side chain mobility has been studied and it is still unclear whether the polypeptide backbone motion is coupled or uncoupled to the mobility of its side chains with literature examples suggesting both coupled<sup>8, 18</sup> and uncoupled motion.<sup>11, 19, 20</sup> Conversely, similar poly alkyl glutamates (and aspartates)<sup>19</sup>, with side chains less than 18 carbons exhibit two thermal transitions, owing to the melting of the side chains and rearranging of the polypeptide backbones, respectively. Unfortunately, many of these statements have been made without clear polarized optical microscopy (POM) images/distinguishable LC textures to elucidate the LC phase formed. Furthermore, several studies report birefringent behavior but without specifying if a cholesteric LC phase was formed.

A review of poly( $\gamma$ -alkyl-L-glutamates) (PALGs) by Daly and co-workers<sup>21</sup> pointed out that differences in the thermal behavior likely arise from the two main synthetic routes used to

produce these polymers: ionic polymerization of N-carboxy amino acid anhydrides (NCA) versus transesterification of poly( $\gamma$ -methyl-L-glutamate) with long-chain alcohols. The latter route often results in co-polymers as high degrees of substitution requires extended reaction times. In early work by Poché, the thermal behavior of PSLG-NCA across several molecular weight ranges, up to 248K g/mol, was studied by optical microscopy and DSC.<sup>22</sup> While cholesteric pitches were observed initially at room temperature for the solvent casted PSLG films, presumably due to passing through a lyotropic LC phase as the sample dried, only birefringence rather than cholesteric ordering was reported upon heating.<sup>23</sup> The present work seeks to both clarify the thermal behavior of PSLG and the related PSLG coated nanoparticles (NPs).



Scheme 4-1: Preparation of PSLG functionalized NPs

The organization of NPs into lyotropic LC phases is normally based on the particle shape anisotropy and in the case of spherical NPs, only cubic phases had been previously reported. In our prior work, we found that a semiflexible helical poly(hexyl isocyanate) (PHIC), that forms lyotropic nematic phases, is able to impart similar LC behavior when grafted onto spherical nanoparticles (NPs).<sup>24</sup> Naturally, the next step following this result, was to expand the scope of this design motif by using polymers that form other anisotropic LC phases. As in our previous work, ZrO<sub>2</sub> NPs were used since these relatively monodispersed NPs can be made in gram quantities and the same surface attachment using phosphonic acid end groups can be applied to other metal oxide and semiconductor NPs. PSLG is capable of thermotropic and lyotropic LC assembly in addition to cholesteric ordering, whereas our previous results for NPs with PHIC ligands only exhibited nematic order. For this reason, PSLG is a good candidate to determine whether other lyotropic phases and thermotropic liquid crystalline NPs can also be formed by this approach.

## **4.3 Experimental**

### **4.3.1 Materials**

All chemical reagents were bought from Millipore-Sigma, without further purification. Solvents were dispensed from a solvent purification system and were used immediately.

### **4.3.2 Synthesis of tetrabutylammonium-diethylphosphonopropanoic acid (TBA-DPPA) (1):**

Preparation tetrabutylammonium (TBA) salt procedure was adapted from Ossowicz et al.<sup>25</sup> In a 30 mL glass vial, diethylphosphonoacetic acid (DPPA) (500 mg) was dissolved in a 40% aqueous solution of tetrabutylammonium hydroxide[TBA][OH] (1.4 g). The mixture was allowed to stir at room temperature overnight. Afterwards, the solution was evaporated at 60°C using a rotovap to remove water. Ethanol was used to precipitate excess amino acid, which was filtered off. Afterwards, the filtrate was concentrated, and the product was further dried in a vacuum at 60°C to obtain a pale-yellow oil.

### 4.3.3 Synthesis of Stearyl glutamate N-carboxyanhydride (SLG-NCA) (2):

The procedure was adapted from Wasserman et al.<sup>26</sup> Initially, in a 2 L three-arm flask, L-glutamic acid (8 g) and stearyl alcohol (52 g) were dissolved in t-butanol resulting in a cloudy white suspension. Afterwards, the reaction mixture was heated to 40°C and concentrated sulfuric acid (6 mL) was slowly added. The reaction mixture was increased to 65°C until the mixture became clear and allowed to stir for an additional hour. Afterwards, the heat was turned off and triethylamine (6 mL) was quickly added to the mixture followed by water (10 mL) and ethanol (150 mL). Another portion of triethylamine (17 mL) was then added and the reaction was allowed to mix again for thirty minutes. The resulting crude product was quickly filtered while still hot and subsequently dissolved in 65°C methanol. The new hot mixture was once again filtered, and the product was washed several times with diethyl ether. The product appeared as a white powder at this stage and was dried in a vacuum oven overnight. Afterwards, the product was recrystallized at 25°C from a boiling solvent mixture of water: n-butanol to afford a pure white powder.

After drying, the product obtained in the previous step was used immediately in the N-carboxyanhydride procedure adapted from Poché et al.<sup>22</sup> Special precautions were taken as triphosgene is highly toxic. A three-arm flask was fitted with a condenser and vented directly into a solution of ammonium hydroxide, to immediately quench generated HCl or phosgene gases in addition to continuous nitrogen purging through one arm of the flask. Stearyl-glutamate (4.2 g) and THF (75 mL) were added to the three-arm flask and heated up to 50°C. Triphosgene (1.13 g) was added quickly in one portion and the reaction mixture allowed to stir for an hour. Afterwards, the solution was placed under vacuum and the solution's volume was reduced to a third of its original volume. The reaction mixture was poured into twice its volume of dry hexane and allowed to sit in a -20°C freezer overnight. While still cold, the white solid was filtered out of the mixture and subsequently re-dissolved in dry THF and precipitated in dry hexane yet again. The recrystallization process was arbitrarily carried out three more times to afford solid white crystals of the N-carboxyanhydride.

#### 4.3.4 Synthesis of PSLG-PO(OEt)<sub>2</sub> from SLG-NCA (3):

Following an adapted procedure from Wu et al.<sup>27</sup> SLG-NCA (2.00 g) was allowed to fully dissolve in dry DCM (at a concentration of 0.2 M) under N<sub>2</sub>. Afterwards, the initiator [TBA][DPPA] (M/I=300) was quickly added into the reaction and the mixture was allowed to stir for up to three days. Afterwards, the viscous solution was precipitated into cold methanol. The precipitation step was repeated twice more by re-dissolving the polymer product with DCM and subsequently precipitating it in cold methanol. The product appeared as a white, flaky solid.

#### 4.3.5 Preparation of Benzyl Alcohol Functionalized ZrO<sub>2</sub> Nanoparticles, Bz@ZrO<sub>2</sub> (4):

Initially, zirconium (IV) isopropoxide isopropanol complex (2 g) was weighed into a glass vial. Anhydrous benzyl alcohol (30 mL) was then added to the vial under inert atmosphere. The vial was then transferred into a sealed teflon cylinder which was subsequently transferred to a steel reactor. The reactor was heated at 230°C for four days and allowed to cool to room temperature on the fifth day. While under an inert atmosphere, the contents of the reactor were transferred to two 30 mL centrifuge tubes. Afterwards, the sample was spun at 9000 RPM at 10°C for 15 minutes and the supernatant was discarded. The NPs were washed three more times with dry THF (discarding the supernatant each time) and finally, the NPs were suspended in approximately 10 mL of THF for storage.

#### 4.3.6 Deprotection of PSLG (5) and Functionalization of ZrO<sub>2</sub> Nanoparticles, PSLG@ZrO<sub>2</sub> (6):

**Deprotection (5):** Typically, the synthesized PSLG-PO(OEt)<sub>2</sub> ligand (1.00 g) was dissolved in dry DCM (10 mL) at 0°C under an inert atmosphere. Bromotrimethylsilane was then added to the solution via 1-2 drops and the reaction was allowed to stir overnight. Afterwards, the volatile compounds were removed via rotovap leaving a white solid substance. The white solid was re-dissolved in DCM (5 mL) and then an excess of methanol was added. After stirring overnight, the solvents were evaporated via rotovap and the product was then vacuum dried at room temperature overnight.

**Ligand Exchange (6):** The amount of Bz@ZrO<sub>2</sub> NPs that can be functionalized with the yield obtained in the previous step was calculated by assuming the surface footprint of phosphonic acid head group to be 0.24 nm.<sup>28</sup> The deprotected PSLG ligands were fully dissolved in dry THF (10 mL) under an inert atmosphere at room temperature. From a suspension of the NPs obtained in (4), the corresponding amount of the Bz@ZrO<sub>2</sub> NPs was quickly injected into the reaction mixture and allowed to stir for three days. Afterwards, the solution was transferred to a centrifuge tube and precipitated with ethanol to be spun at 9K RPM at 10°C for five minutes. The sample was spun a total of three times, with the supernatant discarded between each spin. Afterwards, the sample was redissolved in DCM and transferred to a pre-weighed vial and most of the DCM was evaporated via a low air stream. Finally, the PSLG functionalized nanoparticles were dried in a vacuum oven at room temperature to obtain a solid, dried film.

#### **4.3.7 LC and NP/LC Sample Preparation:**

For both optical microscopy and SAXS measurements, a concentrated solution (40 wt%) of either the PSLG or PSLG@ZrO<sub>2</sub> was typically prepared. More dilute solutions were obtained through successive serial dilutions of the original concentration solution. The corresponding amount of PSLG/PSLG@ZrO<sub>2</sub> and the chosen organic solvent (toluene) was weighed in an Eppendorf tube. The sample was thoroughly homogenized for approximately 30 minutes in a mixer, followed by centrifugation at 9K RPM several times. Between each centrifugation step, the Eppendorf tube was rotated 180 degrees to ensure homogenization. Afterwards, the sample was transferred to a capillary tube such that the sample filled about half of the capillary. For viscous samples, the sample was packed into the capillary tube, while for more dilute solutions (10 wt%) it was possible to transfer by injecting the solution directly into the capillary via syringe.

#### **4.3.8 Measurements**

POM images were obtained using a Nikon model SMZ1500 stereomicroscope. TEM images were obtained using a ThermoScientific Talos 200X G2 TEM. SAXS profiles were obtained with the Anton Paar SAXSpoint 2.0 at the minimum sample-to-detector distance of 575 mm.

## 4.4 Results

### 4.4.1 Synthesis of PSLG ligands

The synthesis of LC PSLG ligands and their subsequent attachment onto 4 nm ZrO<sub>2</sub> NPs are shown in Scheme 4-1. Previously reported NMR assignments were used to confirm the presence of PSLG (Supplemental Figure 4-8).<sup>22</sup> Additionally, the molecular weight can be determined using  $[\eta]=K[MW]^\alpha$ , where  $\eta$  is the intrinsic viscosity (as measured by viscometry), while K and  $\alpha$  represent the Mark-Houwink constants, which are  $1.58 \times 10^{-5}$  mL/g and 1.35, respectively, for PSLG solutions in DMF at 25°C.<sup>53</sup> Analysis was primarily carried out on a batch of PSLG with the molecular weight of 54K (g/mol) and a degree of polymerization of 141, which will henceforth be abbreviated as PSLG<sub>141</sub>.

### 4.4.2 Characterization

#### 4.4.2.1 Nanoparticle Characterization

**Fourier Transform Infrared Spectroscopy (FTIR).** The secondary structure of the synthesized PSLG ligands can be determined by FTIR (Supplemental Figure 4-10), as the  $\alpha$ -helix or  $\beta$ -sheet conformations both exhibit characteristic bands. Both conformations exhibit the amide I and II bands, which occur at 1650-1658 cm<sup>-1</sup> and 1548-1550 cm<sup>-1</sup> for  $\alpha$ -helices and at 1626-1630 cm<sup>-1</sup> and 1520 cm<sup>-1</sup> for  $\beta$ -sheets.<sup>29, 30</sup> In the case of the synthesized PSLG ligands, the bands occur at 1653 cm<sup>-1</sup> and 1548 cm<sup>-1</sup>. Similarly, for PSLG@ZrO<sub>2</sub>, the bands occur at 1653 cm<sup>-1</sup> and 1546 cm<sup>-1</sup> (Supplemental Figure 4-10). In both cases, this shows that the synthetic polypeptide primarily adopts an  $\alpha$ -helical conformation.

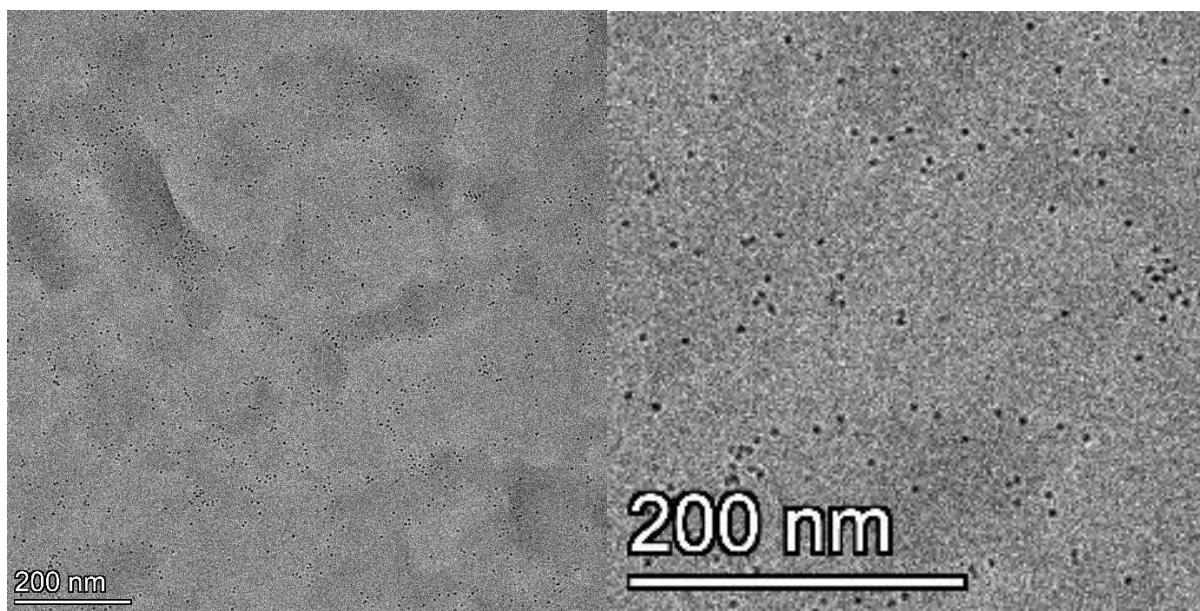


Figure 4-1. (Left) TEM image of PSLG<sub>141</sub>@ZrO<sub>2</sub> NPs to confirm colloidal stability. (Right) Zoomed image for clarity. TEM grids were drop-cast from semi-dilute DCM solutions.

**Transmission Electron Microscopy (TEM).** To confirm the colloidal stability of our PSLG@ZrO<sub>2</sub> NPs, TEM was performed (Figure 4-1). Since the method of preparation for the ZrO<sub>2</sub> NPs is known to produce highly monodisperse NPs, the diameters of the NPs were assumed to be 4 nm (which was also corroborated using TEM). However, the organization of the PSLG ligands cannot be discerned from TEM.

**Thermogravimetric Analysis (TGA).** TGA was used to determine the surface coverage of the functionalized nanoparticles (supplemental 4-9). A percentage weight loss of 93.04% represents a grafting density of 0.56 PSLG chains/nm<sup>2</sup>, or a footprint of 1.8 nm<sup>2</sup>/PSLG chain. Compared to larger particles with grafted polymer ligands, this is a relatively high coverage arising from the small particle size and the high surface curvature.

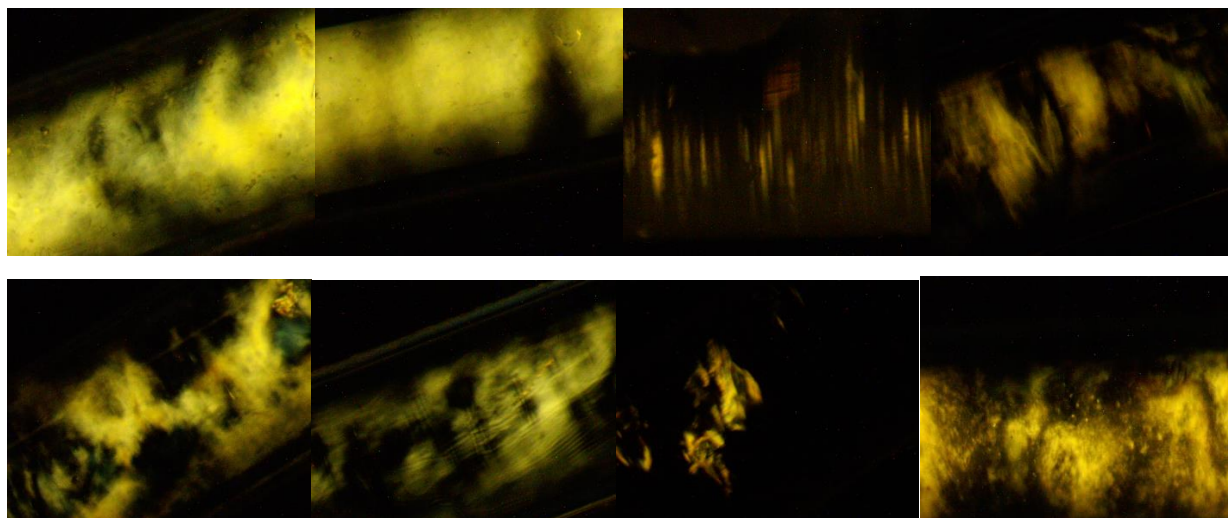


Figure 4-2: (Top) PSLG<sub>141</sub> and (bottom) PSLG<sub>141</sub>@ZrO<sub>2</sub> solutions in toluene with images taken via optical microscopy. Concentrations are as follows from left to right: 10 wt%, 20 wt%, 30 wt% and 40 wt%. These solutions were not annealed but were allowed to rest overnight prior to optical microscope imaging.

Table 4-1: Summary of cholesteric pitches of lyotropic samples of PSLG<sub>141</sub> and PSLG<sub>141</sub>@ZrO<sub>2</sub> prepared in toluene. Samples were annealed overnight at 70°C.

PSLG <sub>141</sub>		PSLG <sub>141</sub> @ZrO <sub>2</sub>	
Concentration	Pitch (μm)	Concentration	Pitch (μm)
10 wt%	Isotropic	10 wt%	Onset
20 wt%	1.89±0.1	20 wt%	2.84±0.3
30 wt%	2.58±0.3	30 wt%	3.78±0.5
40 wt%	-	40 wt%	-

#### 4.4.2.2 Lyotropic LC Characterization

**Polarized Optical Microscopy (POM).** Polarized Optical Microscopy (POM). To investigate the lyotropic LC behavior, PSLG<sub>141</sub> and PSLG<sub>141</sub>@ZrO<sub>2</sub> dispersions in toluene were analyzed by polarized optical microscopy (POM) (Figure 4-2). The samples were prepared in sealed capillary tubes to allow the same samples to be characterized by SAXS as well as to prevent solvent loss.

Toluene was the solvent of choice to allow comparisons to previous literature. Due to the high viscosity of the dispersions, samples were annealed to promote the formation of the LC phase (Figure 4-3). For samples that were not thermally annealed, the POM textures generally appeared cloudy, however, cholesteric fingerprints were still observed in some of these samples. For the cholesteric phases, the half-pitch was measured directly from the bands seen in the fingerprint texture. For comparison, the measurements are presented as a full pitch and are given in Table 4-1.

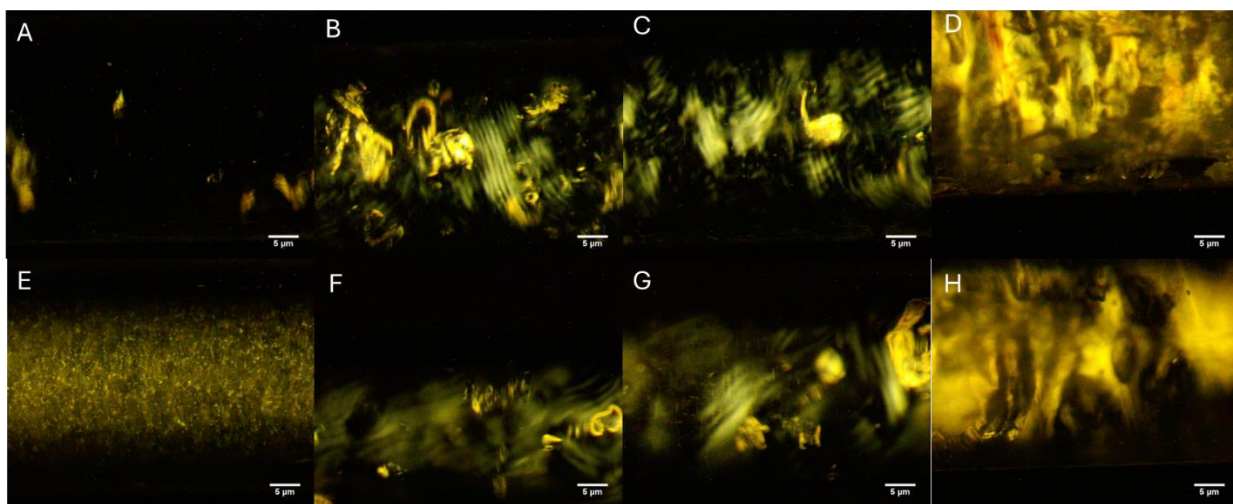


Figure 4-3: PSLG<sub>141</sub> (A-D) and PSLG<sub>141</sub>@ZrO<sub>2</sub> (E-H) samples in order of increasing concentration (10 wt%, 20 wt%, 30 wt%, 40 wt%). Samples were the same as the ones presented in Figure 2, however they were annealed overnight at 70°C.

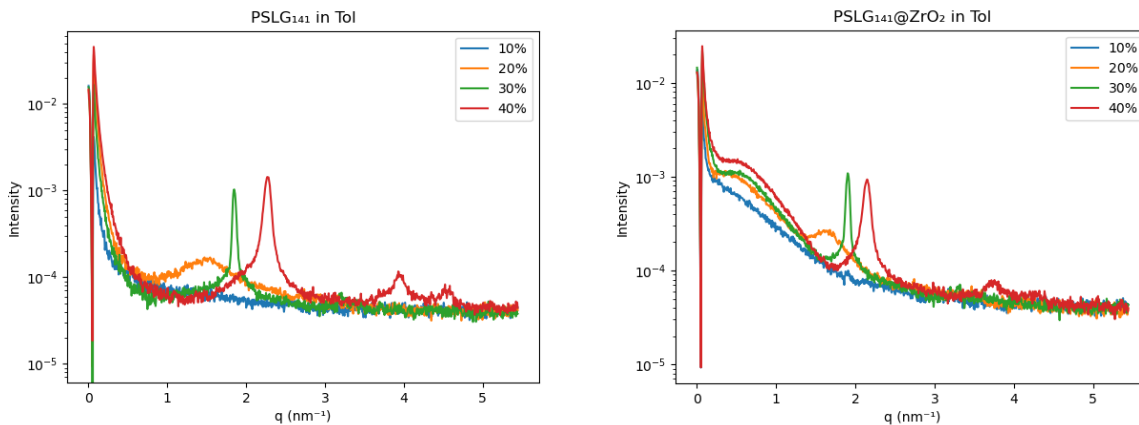


Figure 4-4: SAXS profiles of different concentrations of (Left) PSLG<sub>141</sub> and (Right) PSLG<sub>141</sub>@ZrO<sub>2</sub> obtained with a sample-to-detector distance of 575 mm and CuK $\alpha$  as the radiation source.

Table 4-2: Summary of observed SAXS reflections as well as calculated lattice parameters for PSLG<sub>141</sub> and PSLG<sub>141</sub>@ZrO<sub>2</sub> in toluene as a function of concentration.

	(hk)	10		11		20		Average
	Wt %	q (nm <sup>-1</sup> )	a (nm)	q (nm <sup>-1</sup> )	a (nm)	q (nm <sup>-1</sup> )	a (nm)	a (nm)
<b>PSLG<sub>141</sub></b>	<b>10</b>	-	-	-	-	-	-	-
	<b>20</b>	1.5	4.8	2.7	5.3	-	-	5.0±0.4
	<b>30</b>	1.9	4.0	3.3	4.4	3.8	3.8	3.4±0.3
	<b>40</b>	2.3	3.2	3.9	3.7	4.6	3.2	3.3±0.3
<b>PSLG<sub>141</sub>@ZrO<sub>2</sub></b>	<b>10</b>	-	-	-	-	-	-	-
	<b>20</b>	1.6	4.4	3.4	4.2	4.2	4.0	4.0±0.5
	<b>30</b>	1.9	3.9	3.3	4.4	4.1	4.0	4.0±0.4
	<b>40</b>	2.1	3.4	3.7	3.9	4.3	3.6	3.6±0.3

**Small Angle X-ray Scattering (SAXS).** The SAXS data comparing the lyotropic LC phases of PSLG and PSLG<sub>141</sub>@ZrO<sub>2</sub> samples are presented in Figure 4-4 and Table 4-2 (individual scattering profiles are provided in Figures S11 and S12). Two major observations can be made. First, sharp Bragg peaks occur in both PSLG<sub>141</sub> and PSLG<sub>141</sub>@ZrO<sub>2</sub>, with the onset of these sharp peaks

appearing at 30 wt% for PSLG<sub>141</sub> and 20 wt% for PSLG<sub>141</sub>@ZrO<sub>2</sub>. The relative peak positions follow ratios of 1,  $\sqrt{3}$ , and 2 indicating hexagonal cylinder packing, in agreement with other lyotropic polypeptide LC systems.<sup>31-34</sup> In the case of PSLG<sub>141</sub> at 30 wt%, the peaks can be indexed to a two dimensional unit cell, with  $a = b = 3.4 \pm 0.3$  nm. Similarly, for PSLG<sub>141</sub> at 40 wt%, the lattice parameter was found to be  $3.3 \pm 0.3$  nm. Additionally, for 20 wt%, a broad but significant peak occurs around the same  $q$  value as the primary peaks observed in 30 wt% and 40 wt%, in addition to a faint (11) reflection, suggesting the onset of hexagonal packing for PSLG<sub>141</sub>. In contrast, for PSLG<sub>141</sub>@ZrO<sub>2</sub>, the lattice parameters were measured to be  $4.0 \pm 0.5$ ,  $4.0 \pm 0.4$ ,  $3.6 \pm 0.3$  nm, at 20 wt%, 30 wt%, and 40 wt%, respectively. This suggests that surface anchoring of the PSLG ligand enables hexagonal packing at a lower critical concentration, which in turn may also be responsible for the reduced critical concentration required for LC assembly. In addition to the hexagonal peaks, another broader peak occurs in PSLG<sub>141</sub>@ZrO<sub>2</sub> (which did not appear for PSLG<sub>141</sub>) at  $\sim 0.5 \text{ nm}^{-1}$ , which would correspond to a real  $d$ -spacing of  $\sim 12.5$  nm. This broad peak was only seen in the NP samples and not in the PSLG<sub>141</sub> alone, which suggests that it is scattering from the 4 nm ZrO<sub>2</sub> NPs. Furthermore, the broad peak becomes more pronounced in the LC state suggesting it could arise from NP organization.

Table 4-3: Transition temperatures for PSLG<sub>141</sub> and PSLG<sub>141</sub>@ZrO<sub>2</sub>.

Sample	First Heating	First Cooling	Second Heating
PSLG141	61°C	39°C, 50°C	61°C
PSLG141@ZRO2	60°C, 65°C	55°C, 42°C	60°C, 65°C
PSLG-NCA	59°C, 67°C <sup>(a)</sup>		59°C, 67°C <sup>(a)</sup>
PSLG-EX	61 °C <sup>(a)</sup> 63°C, 89°C <sup>(a)</sup>		

(a) Daly, William H., Drew Poché, and Ioan I. Negulescu. "Poly ( $\gamma$ -Alkyl- $\alpha$ , l-glutamate) s, derived from long chain paraffinic alcohols." *Progress in polymer science* 19.1 (1994): 79-135.

#### 4.4.2.3 Thermotropic LC Characterization

**Differential Scanning Calorimetry (DSC).** Several techniques were applied to characterize the thermal behavior of PSLG<sub>141</sub> and PSLG<sub>141</sub>@ZrO<sub>2</sub> in the solid state. DSC was used to locate thermal transitions as well as to identify structural differences between the PSLG itself and PSLG anchored onto the NPs (Supplemental Figure 4-9). The transition temperatures, along with literature values that will be discussed later, are presented in Table 4-3. Whereas the initial heating step showed a single peak for PSLG<sub>141</sub>, two broad endothermic peaks were observed for PSLG<sub>141</sub>@ZrO<sub>2</sub>, at 60°C and 65°C suggesting two separate phase transitions. Upon cooling, PSLG<sub>141</sub> exhibited a large exothermic peak at 50°C and a smaller second exothermic peak at 39°C. For PSLG<sub>141</sub>@ZrO<sub>2</sub>, the size trend was reversed, where the large and small peaks occur at 42° and 55°C, respectively.

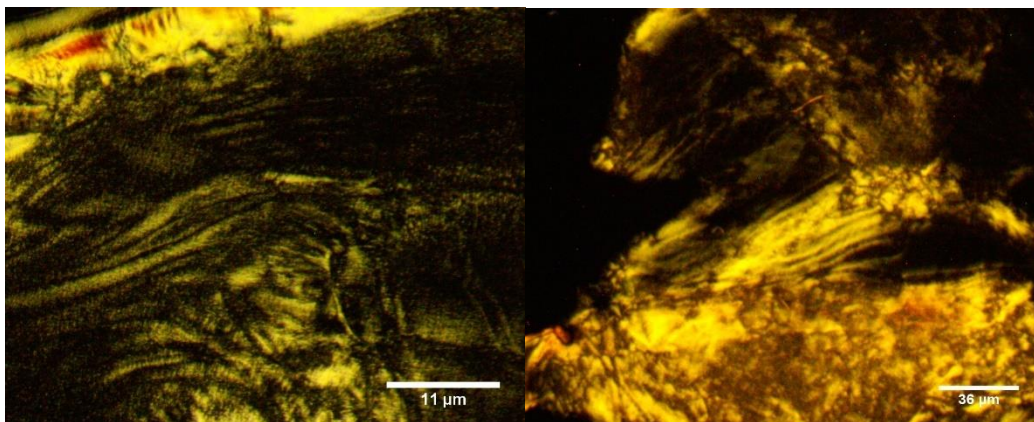


Figure 4-5: POM images taken from thermally annealed samples of PSLG<sub>141</sub> and PSLG<sub>141</sub>@ZrO<sub>2</sub> at 150°C. Films were annealed until cholesteric patterns were observed which varied anywhere from 1-5 days. To prepare the films, dilute solution of the PSLG or NP samples in DCM were air dried in a 3 mL vial and the subsequent film was transferred to a glass slide for POM imaging.

**Optical Microscopy.** The POM images show that PSLG<sub>141</sub> and PSLG<sub>141</sub>@ZrO<sub>2</sub> form thermotropic LCs. Films were annealed until cholesteric patterns were observed which varied anywhere from 1-5 days. To prepare the films, dilute solution of the PSLG or NP samples in DCM were air dried in a 3 mL vial and the subsequent film was transferred to a glass slide for POM imaging. While the samples are indeed birefringent, most of the observed textures do not correspond to any LC textures. However small cholesteric-like domains were observed throughout the sample, and

areas which exhibited fingerprint textures were chosen to be representative of the cholesteric domains for the purposes of pitch measurements (Figure 4-5). It is also important to note that not all films formed cholesteric domains and that it may be possible that some films were primed to become cholesteric at some point during the film preparation process. The cholesteric pitch was measured from the fingerprint pattern using the most periodic regions. This produces pitch measurements of  $8.1 \pm 4 \mu\text{m}$  and  $3.0 \pm 1 \mu\text{m}$  for PSLG<sub>141</sub> and PSLG<sub>141</sub>@ZrO<sub>2</sub>, respectively.

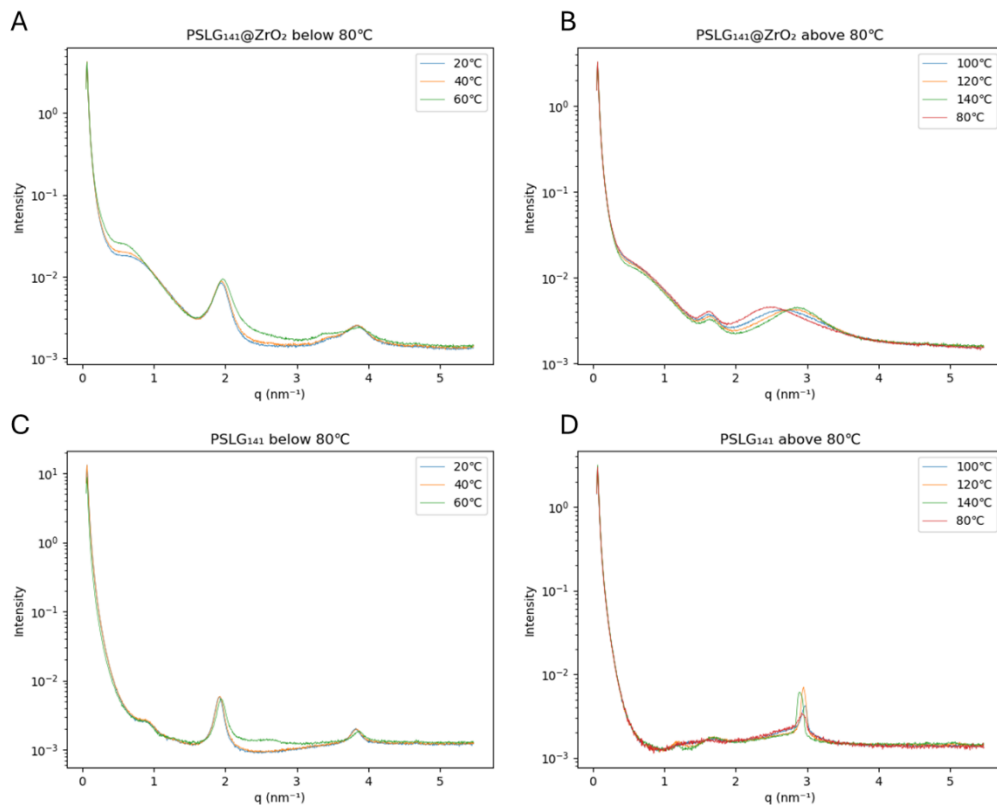


Figure 4-6: SAXS profiles of the thermal behavior of PSLG<sub>141</sub>@ZrO<sub>2</sub> below 80°C (A) and above 80°C (B) as well as PSLG<sub>141</sub> below 80°C (C) and above 80°C (D). Data was split above and below 80°C for clarity.

**SAXS.** Radial SAXS profiles were obtained for both PSLG<sub>141</sub> and PSLG<sub>141</sub>@ZrO<sub>2</sub> (Figure 4-6) as a function of temperature. It is important to note that of the collected SAXS data, the samples were not necessarily in the cholesteric LC phase, as there was no guarantee that the cholesteric domains were within the beam path. However, SAXS peaks corresponding to ordered thermal structures were clearly visible and appeared to persist across the capillary tube. Below 80°C, d

spacings of 3.3 and 1.64 nm for PSLG<sub>141</sub> were assigned to (100) and (200) indices based on the literature (Table 4-4).<sup>7, 8</sup> When PSLG<sub>141</sub> was heated to 80 °C, the 100 and 200 peaks broaden and disappeared and a new peak appears at  $d = 2.2 \pm 0.04$  nm, arising from somewhat disordered lateral packing of the  $\alpha$  helices, characteristic of the cholesteric phase.<sup>12, 35, 36</sup> The SAXS profile of PSLG<sub>141</sub>@ZrO<sub>2</sub> showed a somewhat different temperature dependence with the appearance at 80 °C of a broad peak at  $q \sim 2.9 \pm 0.5 \text{ nm}^{-1}$  ( $d \sim 2.2 \pm 0.2$  nm) that shifted to the same  $d$  spacing as PSLG<sub>141</sub> to  $2.2 \pm 0.04$  nm but remained broad. A small broad peak at  $\sim q = 2 \text{ nm}^{-1}$  ( $d = 4$  nm) appeared and remained unchanged as the sample was heated up to 150 °C.

**Table 4-4: Summary of SAXS data for Thermotropic PSLG<sub>141</sub> and PSLG<sub>141</sub>@ZrO<sub>2</sub>.**

<b>PSLG<sub>141</sub></b>			
<b>&lt; 80°C</b>		<b>80 to 150 °C</b>	
(hkl)	q (nm <sup>-1</sup> )	d(nm)	
100	1.9±0.02	3.3±0.03	q (nm <sup>-1</sup> ) 2.9±0.05
200	3.8±0.07	1.6±0.03	d(nm) 2.2±0.04

<b>PSLG<sub>141</sub>@ZrO<sub>2</sub></b>			
<b>&lt; 80°C</b>		<b>80 to 150 °C</b>	
(hkl)	q (nm <sup>-1</sup> )	d(nm)	
100	1.9±0.2	3.3±0.3	q (nm <sup>-1</sup> ) 2.9±0.4
200	3.8±0.5	1.6±0.3	d(nm) 2.2±0.2

**Literature values for PSLG (prepared via ester exchange)**

<b>25°C</b>	<b>90°C</b>	<b>150°C</b>	<b>210°C</b>
(hkl) q (nm <sup>-1</sup> )* d(nm)	q (nm <sup>-1</sup> )* d(nm)	q (nm <sup>-1</sup> )* d(nm)	(hkl) q (nm <sup>-1</sup> )* d(nm)
100 1.92 3.27	2.56 2.45	3.14 2.0	100 2.98 2.11
200 3.83 1.64			110 5.19 1.21
			200 5.93 1.06

\*q values were calculated from the real distances reported in literature.

## 4.5 Discussion

#### 4.5.1 Synthesis of the PSLG ligands.

To our knowledge, only two previous instances have been reported where PSLG has been grafted onto particles prepared via either grafting-to or grafting from. In the first example, click chemistry was used to covalently graft PSLG,<sup>37</sup> with a degree of polymerization of 17, onto pre-functionalized large (140 nm) silica particles, however no liquid crystallinity was reported with these materials. In the second example, the PSLG coated silica micro-bullets (HemiSil), were prepared via a grafting-from approach,<sup>38</sup> and dispersed into a cholesteric PSLG matrix. These same microparticles functionalized with PSLG were recently used to promote the formation of highly ordered crystalline assemblies of semiconducting poly(3-hexylthiophene) (P3HT).<sup>39</sup> While no molecular weight was reported in the second example, due to the nature of grafting-from surface polymerizations, it can be assumed that the molecular weight is relatively low as this is one of the drawbacks of primary amine initiation.<sup>40, 41</sup> Flory theory provides a relationship to describe rod-like lyotropic LC self-assembly (equation 1), where the critical volume fraction,  $V_c$ , is expressed in terms of the polymer's axial ratio,  $x$ .<sup>6</sup>

$$\text{Equation 1: } V_c \approx \left(\frac{8}{x}\right) \left(1 - \frac{2}{x}\right)$$

In addition to the large sizes of the silica particles of the two systems, LC behavior from the particles alone would also not be expected due to the low axis ratio of the PSLG ligands which would require very high concentrations to form a lyotropic phase.

Here, a nanocomposite comprised of high molecular weight PSLG ligands was combined with small(er) zirconia nanoparticles to achieve liquid crystallinity. The simplest method to produce high MW homo-polypeptides is through N-carboxyanhydride (NCA) polymerization. In this method, polymerization may undergo one of two pathways, either the normal amine mechanism (NAM) or the activated monomer mechanism (AMM). NAM is the more attractive option towards functional materials as this pathway incorporates the primary amine initiator into the polypeptide backbone,<sup>42, 43</sup> which in turn enables chemical modification. However, the major drawback of this pathway is that polymerization kinetics for NAM is slow and often produces low molecular weight polypeptides. In contrast, the other pathway, AMM, is much faster and

produces high molecular weights with broad distributions,<sup>41</sup> however, the drawback here is that the synthesized polypeptides here are highly subject to side reactions which produces diverse terminal groups. For this reason, only NAM is viable for producing PSLG ligands with molecular weights that are high enough to form lyotropic phases. Several approaches exist to enhance the NAM polymerization, including using metal mediation,<sup>44</sup> and high vacuum techniques.<sup>45</sup> However, tetrabutylammonium carboxylate initiation<sup>27</sup> stood out as the most promising candidate. This is due to the relative economy and ease at which the initiator can be synthesized. Crown ether catalyzed polymerizations were also possible.<sup>46</sup> However, in our experience, the tetrabutylammonium carboxylate method proved to have better molecular weight control.

#### **4.5.2 Characterization of PSLG and PSLG@ZrO<sub>2</sub>**

FTIR confirmed that in both PSLG and PSLG@ZrO<sub>2</sub>, the PSLG was primarily in the  $\alpha$ -helix conformation. The coexistence of  $\alpha$ -helices and  $\beta$ -sheets are only seen in PBLG, a synthetic polypeptide, with degrees of polymerization below 18,<sup>47</sup> whereas the polymer samples prepared here had a degree of polymerization of 141, which is above this threshold. This observation allows for PSLG to be approximated as rod-like.

In contrast to the previous study of the same ZrO<sub>2</sub> NPs with poly(hexyl isocyanate) (PHIC) ligands, which were observed by TEM to assemble into linear arrays upon casting as films, the NPs with PSLG ligands did not form periodic structures upon simple casting from a dilute solution. The spatial distribution of the ZrO<sub>2</sub> NPs in the TEM image shown in Figure 4-1 likely results from particle aggregation via stearyl crystallization. It has been reported that upon solvent evaporation, solutions of PSLG aggregate due to converging stearyl domains.<sup>48</sup> The formation of periodic structures in casted films of PSLG<sub>141</sub>@ZrO<sub>2</sub> NPs would likely require solvent/thermal annealing as discussed below.

#### **4.5.3 Lyotropic Behaviour**

Lyotropic LC solutions of both PSLG<sub>141</sub> and PSLG<sub>141</sub>@ZrO<sub>2</sub> in toluene are difficult to prepare without thermal annealing or prolonged aging. Of the concentrations explored, only one sample of PSLG<sub>141</sub>@ZrO<sub>2</sub> at 20 wt% had visible cholesteric patterning without further treatment,

whereas the rest of the samples were birefringent which does not necessarily indicate LC behavior. This is largely due to two competing forces at the critical PSLG concentration: the onset of LC behavior and the very high viscosity. In general, randomly oriented rod-like particles experience larger increases in viscosity at increasing concentrations as compared to spherical particles.<sup>49</sup> While birefringence was observed at 10 wt%, it is possible that this concentration was still below the critical concentration. At 20 wt%, the onset of LC behavior is facilitated by the relatively low viscosity at this concentration. Above this concentration, the diffusion of rod-like molecules becomes hindered and prevents formation of LCs within the allotted amount of time.<sup>50</sup> Fortunately, the slow diffusion can be easily overcome through heating. Apart from 10 wt% and the 40 wt% dispersions, which are below the critical concentration and highly viscous respectively, the PSLG<sub>141</sub> and PSLG<sub>141</sub>@ZrO<sub>2</sub> samples displayed cholesteric fingerprints after overnight annealing at 70°C (Figure 4-3).

The cholesteric half-pitch may be measured directly from the bands seen in the fingerprint texture. For comparison, the measurements are presented as a full pitch in Table 4-1. These values are smaller than those reported in the earlier literature for lyotropic PSLG. There can be a wide variation of the pitch of lyotropic polypeptides as it depends on the solvent, thermal history, boundary conditions and other variables. However, there is only a weak dependence on molecular weight. A half pitch of 2.36  $\mu\text{m}$ <sup>23</sup> was originally reported for 26 wt% PSLG (MW 40K g/mol) in toluene at 70°C. Larger half pitch values of 8.3 and 22.5  $\mu\text{m}$  for 25% wt PSLG (MW 40K g/mol) in toluene at 25°C were later reported.<sup>21</sup> In THF, a half pitches of 20  $\mu\text{m}$ <sup>51</sup> and 27 $\mu\text{m}$ <sup>38</sup> were measured for 30%wt PSLG (MW 70). Contrary to lyotropic PBLG, a variable temperature study of 25% wt PSLG (MW 129K) in toluene reported that the pitch decreased rather than increase with heating.<sup>31-33</sup> Given this temperature dependence of the pitch, it is possible that annealing the samples at 70°C, rather than aging at room temperature, is responsible for the smaller pitch values that more closely match cholesteric pitches of thermotropic polypeptide LCs which typically range between 1-10  $\mu\text{m}$ .<sup>12,35,36</sup>

Although the fingerprint texture observed by optical microscopy indicated the presence of the cholesteric phase, the X-ray scattering of the same samples surprisingly revealed columnar

hexagonal packing of the polymer chains. Characterization of lyotropic solutions of PSLG by X-ray scattering has only been reported for PSLG in long chain ( $C_{18}$ ) solvents.<sup>14</sup> In amphiphilic solvents like octadecylamine, PSLG formed columnar hexagonal phases that transformed into the cholesteric phase upon heating.<sup>14</sup> However PSLG in octadecane only displayed the cholesteric phase. The stabilization of the columnar hexagonal phase was attributed to compartmentalization of the polar head groups of the solvents out of the octadecyl aliphatic regions. A later study of a series of poly( $\gamma$ -alkyl-L-glutamates) in *m*-cresol revealed cholesteric phases that transformed to columnar phases through a wide co-existence region at high concentrations. The lyotropic samples in the Ch + Colm biphasic regions revert to the pure cholesteric phase upon heating, to I + Chol upon cooling, and to the pure columnar phase at a critical concentration.<sup>52</sup> PSLG was not studied specifically, but increasing the alkyl chains up to  $C_6$  showed that the critical columnar concentration increases with chain length. Similar to our conditions, the samples were heated to 70-80 °C. Based on the results for poly( $\gamma$ -hexyl-L-glutamate) (PHexLG, MW 90K), which has a critical columnar concentration of 50 wt%, the 30 and 40 wt% PSLG in toluene studied here should both be within the Ch + Colm biphasic region.

The calculated lattice parameters from the SAXS analysis of the lyotropic LC solutions,  $a = b = 3.4 \pm 0.3$ , and  $3.3 \pm 0.3$  nm for 30 and 40 wt% respectively, are smaller than PSLG in the solid state, which was reported to be  $a = 4.37$  nm and  $b = 4.79$  nm.<sup>8</sup> This is presumably due to the rearrangement in the lyotropic solutions, which allows for optimal packing of the  $\alpha$ -helices and smaller lattice parameters. For 20 wt% solutions of PSLG<sub>141</sub> the lattice parameters are  $a = b = 5.0 \pm 0.4$  nm, suggesting the onset of hexagonal packing. In previous reports, the diameter of PSLG in solution is typically given as 3.6 nm with high variation,<sup>22, 53</sup> depending on the degree of outward extension of the stearyl chains. For both PSLG<sub>141</sub> and PSLG<sub>141</sub>@ZrO<sub>2</sub>, at the onset of lyotropic LC behavior, hexagonal packing of the PSLG roughly begins at the solution limit ( $\sim 3.6$  nm). Further concentration increases result in contraction of the stearyl chains and convergence of the  $\alpha$ -helix cores. The hexagonal order is higher in the PSLG<sub>141</sub> as compared to PSLG<sub>141</sub>@ZrO<sub>2</sub> NPs since the higher order (20) reflection were more easily observed. In comparison, a smaller  $d_{10}$  value of 2.39 nm was reported for a 70% wt% solution of PSLG in an amphiphilic solvent<sup>14</sup> and  $d_{10} = 2.0$  nm for a 50 wt% solution of PHexLG in *m*-cresol.<sup>52</sup> Interestingly, similar results were

determined for PSLG<sub>141</sub>@ZrO<sub>2</sub>, which was surprising given the small size of the zirconia NPs and consequently, the high curvature. Of the most concentrated solutions prepared for both systems (30 and 40 wt%), PSLG<sub>141</sub> was determined to have smaller lattice parameters of 3.4±0.3 and 3.3±0.3 nm while the lattice parameter for PSLG<sub>141</sub>@ZrO<sub>2</sub> was determined to be 4.0±0.4 and 3.3±0.3 nm. The decrease in lattice parameters in concentrated solutions (for both systems) make sense, as the hexagonal lattices are expected to converge due to crowding. Furthermore, the hexagonal unit was generally larger in the PSLG<sub>141</sub>@ZrO<sub>2</sub> system. This could potentially be due to enlargement of the unit cell due to the PSLG being grafted onto the NPs, which is less optimal for hexagonal packing and further reaffirmed by the broadening of observed reflections for PSLG<sub>141</sub>@ZrO<sub>2</sub>. Interestingly, at the onset of LC behaviour, at 20 wt%, the concentration dependent behaviour was reversed, where the PSLG<sub>141</sub>@ZrO<sub>2</sub> system instead exhibited the smaller lattice parameters (4.0±0.5 nm) compared to PSLG<sub>141</sub> (5.0±0.4 nm). This may perhaps be due to close confinement of the PSLG chains on the NP surface, which may trigger early onset liquid crystallinity, however more detailed studies on effects of grafting density on this nanocomposite design could conclusively confirm this claim.

#### 4.5.4 Thermotropic Behavior

The thermal behavior of poly( $\gamma$ -alkyl-L-glutamates) is complex in general and depends on many variables. Previous literature reports the existence of three possible structures upon heating/cooling, simply referred to as phases A, B and C where C is the liquid crystalline phase.<sup>8, 19, 20</sup> The polarity of the casting solvent effects the structure, crystallinity and transition temperatures. In phase A, the structure is lamellar-like, where the interlayer spacings between the polypeptide  $\alpha$ -helices are comprised of the alkyl side chains and is periodically interrupted by the  $\alpha$ -helices. On heating, the sample transitions into phase B, where the interlayer spacings become more compact through rearrangement due to melting of the alkyl sidechains which occurs at  $T_1$ . Upon further heating, the  $\alpha$ -helices become mobile, which allows further rearrangement of the polypeptide backbone and smaller interlayer spacings. The transformation to the liquid crystal phase occurs at  $T_2$  which is slightly higher than  $T_1$ . The difference between  $T_1$  and  $T_2$  decreases with chain length. The reported thermal transitions between the three phases

vary depending on whether PSLG was synthesized from the monomer (PSLG-NCA) or by ester exchange (PSLG-EX) and the characterization method. Poché reported using DSC a single transition for PSLG-EX at 61 °C and two peaks at 59 and 67 °C for PSLG-NCA that remained after multiple heating cycles. The second transition at 67°C was attributed to an additional crystalline state. Depending on the thermal history, the side chains melt and can recrystallize to form crystallites of different dimensions. The transition to the liquid crystal phase was also found to increase if annealed at temperatures above  $T_1$ , with  $T_2$ , the onset of liquid crystallinity, ranging between 60 and 90°C.<sup>54</sup> Watanabe and Takashina later reported that PSLG-EX forms a cholesteric mesophase from 60 to 150 °C and a hexagonal columnar phase above 150 °C which is the reverse to what is observed for lyotropic PSLG.<sup>12, 35, 36 °C</sup>

We observe here a single transition at 61°C for PSLG<sub>141</sub> corresponding to sidechain melting. However, PSLG<sub>141</sub>@ZrO<sub>2</sub> has an endotherm with two transitions at 60 and 65°C where the second transition may be due to different crystallites sizes. Another possibility that should be considered is two separate populations of PSLG within the sample, the confined PSLG ligands anchored onto the NP surface, as well as PSLG ligands that may remain intercalated within the polymer corona despite the purification steps to remove free ligands. Generally, higher temperatures would be required to melt the grafted polymer chains anchored onto a NP surface,<sup>55, 56</sup> so for this reason, this population could be attributed to the peak at 65°C. The other peak at 60 °C then would correspond to the melting of the stearyl side chains of the physisorbed PSLG, owing to the broadness as well as its proximity to the bulk melting temperature (59°C). The anchored versus intercalated PSLG ligands could also have different crystallite sizes of the octadecyl side chains which would also give rise to two transitions.

Although films of PSLG<sub>141</sub> and PSLG<sub>141</sub>@ZrO<sub>2</sub> were annealed at 150 °C for up to 5 days, the cholesteric fingerprint texture was observed only in small regions at this temperature by optical microscopy. This probably limited the measurements of the pitches which were estimated to be 8.1±4 and 3.0±1 μm for PSLG<sub>141</sub> and PSLG<sub>141</sub>@ZrO<sub>2</sub> respectively as compared to the literature value of ~ 2 μm for PSLG-EX.<sup>12, 35, 36</sup> However, the variable temperature SAXS data is consistent

with the literature. At 25 °C, the observed lattice spacings for both PSLG<sub>141</sub> and PSLG<sub>141</sub>@ZrO<sub>2</sub> match those assigned to the 100 and 200 reflections of PSLG-EX.<sup>7, 8</sup> In that study of a series of poly( $\gamma$ -alkyl-L-glutamates) with different length sidechains, the wide angle region was indexed to a two-dimensional unit cell arising from the crystalline sidechains with lattice parameters similar to the sublattice attained by the *c* projection of triclinic unit cell of low molecular weight alkanes. The small angle region of PSLG-EX only contained a series of reflections with indices *h*00 where the *d* spacing of 3.27 nm is the distance between  $\alpha$  helices. Given that the length of the octadecyl chain is  $\sim$  2.28 nm, there is intercalation of the side chains between the  $\alpha$  helices and the size of the side chain crystal lattice was estimated to be  $\sim$ 18 side chains. However, this peak in the SAXS profile of PSLG<sub>141</sub>@ZrO<sub>2</sub> is extremely broad, indicating that the ability to form the cholesteric phase is hindered. The small broad peak at  $\sim d = 4$  nm that remains unchanged with temperature may arise from chain segments close to the nanoparticle surface with restricted mobility. As in the lyotropic samples, the broad peak at a low *q* value is due to scattering from the ZrO<sub>2</sub> nanoparticles.

## 4.6 Conclusion

The formation of anisotropic lyotropic phases by spherical NPs with semiflexible polymer ligands was expanded to include chiral and thermotropic LC phases. Metal oxide NPs functionalized with poly( $\gamma$ -stearyl-L-glutamate), (PSLG) brushes form LC phases similar to the free PSLG. In concentrated solutions, both PSLG and the nanoparticles are in a Chol + Colm biphasic state rather than a pure cholesteric phase as previously assumed. Confinement of the PSLG ligands to the NP surface results in closer packing of the  $\alpha$  helices but somewhat more disordered LC phases as compared to the free polypeptide. The degree of disorder for the NPs is larger for the thermotropic cholesteric phase that already requires for PSLG alone, long annealing times to reach equilibrium due its high intrinsic viscosity. Pinning the PSLG chains to the NPs further reduces the low mobility of the  $\alpha$ -helices along with limiting their ability to spatially rearrange to form the cholesteric phase.

The use of polymer ligands as first demonstrated here, rather than the traditional low molecular weight mesogenic ligands, to produce thermotropic liquid crystalline NPs, offers some advantages such as synthetic simplicity and tunability through variation of the molecular weight and sidechain groups. Future studies will include ultra-small angle X-ray scattering (USAXS) to determine the NP spatial arrangement and other thermotropic polypeptide ligands such as poly( $\gamma$ -oleyl-L-glutamate) which is liquid crystalline at room temperature.

## 4.7 References

- (1) Lagerwall, J. P. F.; Scalia, G. A new era for liquid crystal research: Applications of liquid crystals in soft matter nano-, bio- and microtechnology. *Current Applied Physics* **2012**, *12* (6), 1387-1412. DOI: <https://doi.org/10.1016/j.cap.2012.03.019>.
- (2) Mitov, M.; Dessaud, N. Going beyond the reflectance limit of cholesteric liquid crystals. *Nature Materials* **2006**, *5* (5), 361-364. DOI: 10.1038/nmat1619.
- (3) Livolant, F.; Bouligand, Y. Liquid crystalline phases given by helical biological polymers (DNA, PBLG and xanthan). Columnar textures. *Journal de physique* **1986**, *47* (10), 1813-1827.
- (4) Deniset-Besseau, A.; De Sa Peixoto, P.; Mosser, G.; Schanne-Klein, M.-C. Nonlinear optical imaging of lyotropic cholesteric liquid crystals. *Opt. Express* **2010**, *18* (2), 1113-1121. DOI: 10.1364/OE.18.001113.
- (5) Onsager, L. The effects of shape on the interaction of colloidal particles. *Annals of the New York Academy of Sciences* **1949**, *51* (4), 627-659.
- (6) Flory, P. J. Molecular theory of liquid crystals. In *Liquid crystal polymers i*, Springer, 2005; pp 1-36.
- (7) Watanabe, J.; Sasanuma, Y.; Endo, A.; Uematsu, I. Crystalline complex between poly ( $\gamma$ -methyl L-glutamate) and dimethyl phthalate. *Polymer* **1984**, *25* (5), 698-705.
- (8) Watanabe, J.; Ono, H.; Uematsu, I.; Abe, A. Thermotropic polypeptides. 2. Molecular packing and thermotropic behavior of poly (l-glutamates) with long n-alkyl side chains. *Macromolecules* **1985**, *18* (11), 2141-2148.
- (9) Katoh, E.; Kurosu, H.; Ando, I. Conformation and molecular motion of poly(l-glutamate) with long n-alkyl side chains in the solid state and the liquid crystalline state as studied by high-resolution  $^{13}\text{C}$  NMR spectroscopy. *Journal of Molecular Structure* **1994**, *318*, 123-131. DOI: [https://doi.org/10.1016/0022-2860\(93\)07917-L](https://doi.org/10.1016/0022-2860(93)07917-L).
- (10) Sakamoto, R.; Osawa, A. Liquid Crystal Formation of Poly( $\gamma$ -n-Alkyl D-Glutamate)S Having Long Alkyl Side Chains. *Molecular Crystals and Liquid Crystals Incorporating Nonlinear Optics* **1987**, *153* (1), 385-394. DOI: 10.1080/00268948708074553.
- (11) Yamaguchi, M.; Tsutsumi, A. Investigation of molecular motion and structures of side chains in poly ( $\gamma$ -methyl L-glutamate-co- $\gamma$ -stearyl L-glutamate) by spin-probe technique and  $^{13}\text{C}$

cross-polarization magic angle spinning nuclear magnetic resonance. *Polymer journal* **1990**, *22* (9), 781-792.

(12) Watanabe, J.; Takashina, Y. Columnar liquid crystals in polypeptides. 1. A columnar hexagonal liquid crystal observed in poly ( $\gamma$ -octadecyl L-glutamate). *Macromolecules* **1991**, *24* (11), 3423-3426.

(13) Watanabe, J.; Sakajiri, K.; Okoshi, K.; Kawauchi, S.; Magoshi, J. Columnar Liquid Crystals in Polypeptides, 1. Columnar Hexagonal Phase Observed in Lyotropic Solutions of Poly ( $\gamma$ -octadecyl-L-glutamate) Dissolved in Amphiphilic Solvents, Such as Octadecylamine, Octadecyl Alcohol, and Octadecanoic Acid. *Macromolecular Chemistry and Physics* **2001**, *202* (7), 1004-1009.

(14) Watanabe, J.; Takashina, Y. Thermotropic Polypeptides VIII. Anomalous Phase Behavior in Low Molecular-Weight Poly( $\gamma$ -octadecyl L-glutamate). *Polymer Journal* **1992**, *24* (7), 709-713. DOI: 10.1295/polymj.24.709.

(15) Watanabe, J.; Goto, M.; Nagase, T. Thermotropic polypeptides. 3. Investigation of cholesteric mesophase properties of poly ( $\gamma$ -benzyl L-glutamate-co- $\gamma$ -dodecyl L-glutamates) by circular dichroic measurements. *Macromolecules* **1987**, *20* (2), 298-304.

(16) Watanabe, J.; Nagase, T. Thermotropic polypeptides. 5. Temperature dependence of cholesteric pitches exhibiting a cholesteric sense inversion. *Macromolecules* **1988**, *21* (1), 171-175.

(17) Watanabe, J.; Nagase, T.; Ichizuka, T. Thermotropic Polypeptides. VII. Temperature Dependence of Cholesteric Pitches in Poly[( $\gamma$ -benzyl L-glutamate)-co-( $\gamma$ -dodecyl L-glutamate)s]. *Polymer Journal* **1990**, *22* (11), 1029-1033. DOI: 10.1295/polymj.22.1029.

(18) Tsujita, Y.; Ojika, R.; Takizawa, A.; Kinoshita, T. Thermal and transport properties of copoly ( $\gamma$ -stearyl l-glutamate- $\gamma$ -methyl l-glutamate). *Journal of Polymer Science Part A: Polymer Chemistry* **1990**, *28* (6), 1341-1351.

(19) López-Carrasquero, F.; Montserrat, S.; Martínez de Ilarduya, A.; Muñoz-Guerra, S. Structure and Thermal Properties of New Comblike Polyamides: Helical Poly ( $\beta$ -L-aspartate) s Containing Linear Alkyl Side Chains. *Macromolecules* **1995**, *28* (16), 5535-5546.

- (20) Colomer, F. J. R.; Ribelles, J. L. G.; Maciá, J. L.; Guerra, S. M. Side-chain crystallization and mobility of poly( $\gamma$ -stearyl-L-glutamate). *Polymer* **1991**, *32* (9), 1642-1646. DOI: [https://doi.org/10.1016/0032-3861\(91\)90400-D](https://doi.org/10.1016/0032-3861(91)90400-D).
- (21) Daly, W. H.; Poché, D.; Negulescu, I. I. Poly ( $\gamma$ -Alkyl- $\alpha$ , L-glutamate)s, derived from long chain paraffinic alcohols. *Progress in Polymer Science* **1994**, *19* (1), 79-135. DOI: [https://doi.org/10.1016/0079-6700\(94\)90038-8](https://doi.org/10.1016/0079-6700(94)90038-8).
- (22) Poche, D.; Daly, W.; Russo, P. Synthesis and Some Solution Properties of Poly ( $\gamma$ -stearyl- $\alpha$ , L-glutamate). *Macromolecules* **1995**, *28* (20), 6745-6753.
- (23) Poche, D. S. *Synthesis and characterization of linear and star-branched poly ( $\gamma$ -stearyl-L-glutamate)*; Louisiana State University and Agricultural & Mechanical College, 1990.
- (24) Wong, J.; Toader, V.; Reven, L. Lyotropic Nematic Phases of Isotropic Nanoparticles via Semiflexible Polymer Ligands. *Macromolecular Rapid Communications* **2023**, *44* (8), 2200951. DOI: <https://doi.org/10.1002/marc.202200951>.
- (25) Ossowicz, P.; Rozwadowski, Z.; Gano, M.; Janus, E. Efficient method for Knoevenagel condensation in aqueous solution of amino acid ionic liquids (AAILs). *Polish Journal of Chemical Technology* **2016**, *18* (4), 90-95.
- (26) Wasserman, D. G., John D. . Monoalkyl Esters of Glutamic Acid and Aspartic Acid and Process for Producing Same. 3,285,953, 1966.
- (27) Wu, Y.; Chen, K.; Wu, X.; Liu, L.; Zhang, W.; Ding, Y.; Liu, S.; Zhou, M.; Shao, N.; Ji, Z.; et al. Superfast and Water-Insensitive Polymerization on  $\alpha$ -Amino Acid N-Carboxyanhydrides to Prepare Polypeptides Using Tetraalkylammonium Carboxylate as the Initiator. *Angewandte Chemie International Edition* **2021**, *60* (50), 26063-26071. DOI: <https://doi.org/10.1002/anie.202103540>.
- (28) Pawsey, S.; McCormick, M.; De Paul, S.; Graf, R.; Lee, Y. S.; Reven, L.; Spiess, H. W.  $^1\text{H}$  fast MAS NMR studies of hydrogen-bonding interactions in self-assembled monolayers. *Journal of the American Chemical Society* **2003**, *125* (14), 4174-4184.
- (29) Ambrose, E. J.; Elliott, A.; Wilson, A. H. The structure of synthetic polypeptides. II. Investigation with polarized infra-red spectroscopy. *Proceedings of the Royal Society of London*.

*Series A. Mathematical and Physical Sciences* **1951**, 205 (1080), 47-60. DOI:

doi:10.1098/rspa.1951.0016.

(30) Doty, P.; Holtzer, A. M.; Bradbury, J. H.; Blout, E. R. POLYPEPTIDES. II. THE CONFIGURATION OF POLYMERS OF  $\gamma$ -BENZYL-L-GLUTAMATE IN SOLUTION<sup>1</sup>. *Journal of the American Chemical Society* **1954**, 76 (17), 4493-4494. DOI: 10.1021/ja01646a079.

(31) Sasaki, S.; Hikata, M.; Shiraki, C.; Uematsu, I. Molecular Aggregation and Gelation in Poly ( $\gamma$ -benzyl L-glutamate) Solutions. *Polymer Journal* **1982**, 14 (3), 205-213.

(32) Chakrabarti, S.; Miller, W. G. Aggregation of poly ( $\gamma$ -benzyl- $\alpha$ , l-glutamate). *Biopolymers: Original Research on Biomolecules* **1984**, 23 (4), 719-734.

(33) Matsushima, N.; Hikichi, K.; Tsutsumi, A.; Kaneko, M. X-ray scattering of synthetic poly ( $\alpha$ -amino acid) s in the solid state. I. Transition of poly ( $\gamma$ -benzyl L-glutamate) and poly ( $\gamma$ -methyl L-glutamate). *Polymer Journal* **1975**, 7 (1), 44-49.

(34) Yen, C.-C.; Edo, S.; Oka, H.; Tokita, M.; Watanabe, J. Phase diagram for solutions of  $\alpha$ -helical poly (l-glutamate) s in m-cresol including isotropic, cholesteric, and columnar phases.

*Macromolecules* **2008**, 41 (10), 3727-3733.

(35) Okoshi, K.; Sano, N.; Suzaki, G.; Tokita, M.; Magoshi, J.; Watanabe, J. Smectic Liquid Crystal Observed in Thermotropic System of Rigid-Rod Poly( $\gamma$ -octadecyl L-glutamate). *Japanese Journal of Applied Physics* **2002**, 41 (6B), L720. DOI: 10.1143/JJAP.41.L720.

(36) Watanabe, J. Thermotropic liquid crystals in polypeptides. In *Ordering in Macromolecular Systems: Proceedings of the OUMS'93 Toyonaka, Osaka, Japan, 3-6 June 1993*, Springer, 1993; pp 99-113.

(37) Balamurugan, S. S.; Soto-Cantu, E.; Cueto, R.; Russo, P. S. Preparation of Organosoluble Silica-Polypeptide Particles by "Click" Chemistry. *Macromolecules* **2010**, 43 (1), 62-70. DOI: 10.1021/ma901840n.

(38) Rosu, C.; Jacobeen, S.; Park, K.; Reichmanis, E.; Yunker, P.; Russo, P. S. Domed Silica Microcylinders Coated with Oleophilic Polypeptides and Their Behavior in Lyotropic Cholesteric Liquid Crystals of the Same Polypeptide. *Langmuir* **2016**, 32 (49), 13137-13148. DOI: 10.1021/acs.langmuir.6b03165.

- (39) Rosu, C.; Chu, P.-H.; Tassone, C. J.; Park, K.; Balding, P. L.; Park, J. O.; Srinivasarao, M.; Reichmanis, E. Polypeptide composite particle-assisted organization of  $\pi$ -conjugated polymers into highly crystalline "coffee stains". *ACS applied materials & interfaces* **2017**, *9* (39), 34337-34348.
- (40) Han, J.; Ding, J.; Wang, Z.; Yan, S.; Zhuang, X.; Chen, X.; Yin, J. The synthesis, deprotection and properties of poly ( $\gamma$ -benzyl-L-glutamate). *Science China Chemistry* **2013**, *56*, 729-738.
- (41) Deming, T. J. Living polymerization of  $\alpha$ -amino acid-N-carboxyanhydrides. *Journal of Polymer Science Part A: Polymer Chemistry* **2000**, *38* (17), 3011-3018.
- (42) Blout, E.; Karlson, R. Polypeptides. III. The synthesis of high molecular weight poly- $\gamma$ -benzyl-L-glutamates<sup>1</sup>. *Journal of the American Chemical Society* **1956**, *78* (5), 941-946.
- (43) Goodman, M.; Hutchison, J. The mechanisms of polymerization of n-unsubstituted n-carboxyanhydrides<sup>1</sup>. *Journal of the American Chemical Society* **1966**, *88* (15), 3627-3630.
- (44) Deming, T. J. Living polymerization of  $\alpha$ -amino acid-N-carboxyanhydrides. *Journal of Polymer Science Part A: Polymer Chemistry* **2000**, *38* (17), 3011-3018. DOI: [https://doi.org/10.1002/1099-0518\(20000901\)38:17<3011::AID-POLA10>3.0.CO;2-Z](https://doi.org/10.1002/1099-0518(20000901)38:17<3011::AID-POLA10>3.0.CO;2-Z).
- (45) Habraken, G. J.; Wilsens, K. H.; Koning, C. E.; Heise, A. Optimization of N-carboxyanhydride (NCA) polymerization by variation of reaction temperature and pressure. *Polymer Chemistry* **2011**, *2* (6), 1322-1330.
- (46) Xia, Y.; Song, Z.; Tan, Z.; Xue, T.; Wei, S.; Zhu, L.; Yang, Y.; Fu, H.; Jiang, Y.; Lin, Y.; et al. Accelerated polymerization of N-carboxyanhydrides catalyzed by crown ether. *Nature Communications* **2021**, *12* (1), 732. DOI: 10.1038/s41467-020-20724-w.
- (47) Papadopoulos, P.; Floudas, G.; Klok, H. A.; Schnell, I.; Pakula, T. Self-Assembly and Dynamics of Poly( $\gamma$ -benzyl-L-glutamate) Peptides. *Biomacromolecules* **2004**, *5* (1), 81-91. DOI: 10.1021/bm034291q.
- (48) Sohn, D.; Yu, H.; Nakamatsu, J.; Russo, P. S.; Daly, W. H. Monolayer properties of a fuzzy rod polymer: Poly ( $\gamma$ -stearyl  $\alpha$ , L-glutamate). *Journal of Polymer Science Part B: Polymer Physics* **1996**, *34* (17), 3025-3034.

- (49) Powell, R. L.; Morrison, T. G.; Milliken, W. J. Apparent viscosity of suspensions of rods using falling ball rheometry. *Physics of Fluids* **2001**, *13* (3), 588-593. DOI: 10.1063/1.1345717 (accessed 2/18/2024).
- (50) Rosu, C.; von Meerwall, E.; Russo, P. S. Diffusion of Rodlike Polymers: Pulsed Gradient Spin Echo NMR of Poly( $\gamma$ -stearyl- $\alpha$ ,L-glutamate) Solutions and the Importance of Helix Stability. *The Journal of Physical Chemistry B* **2018**, *122* (50), 12194-12200. DOI: 10.1021/acs.jpccb.8b08974.
- (51) Rosu, C.; Balamurugan, S.; Cueto, R.; Roy, A.; Russo, P. S. Polypeptide-coated silica particles dispersed in lyotropic liquid crystals of the same polypeptide. *The Journal of Physical Chemistry B* **2016**, *120* (29), 7275-7288.
- (52) Yen, C.-C.; Edo, S.; Oka, H.; Tokita, M.; Watanabe, J. Phase Diagram for Solutions of  $\alpha$ -Helical Poly(L-glutamate)s in m-Cresol Including Isotropic, Cholesteric, and Columnar Phases. *Macromolecules* **2008**, *41* (10), 3727-3733. DOI: 10.1021/ma701971f.
- (53) Temyanko, E.; Russo, P. S.; Ricks, H. Study of Rodlike Homopolypeptides by Gel Permeation Chromatography with Light Scattering Detection: Validity of Universal Calibration and Stiffness Assessment. *Macromolecules* **2001**, *34* (3), 582-586. DOI: 10.1021/ma0013511.
- (54) Daly, W. H.; Negulescu, I. I.; Russo, P. S.; Poche, D. S. Side-Chain Crystallinity and Thermal Transitions in Thermotropic Liquid-Crystalline Poly ( $\gamma$ -alkyl- $\alpha$ , L-glutamate) s. ACS Publications, 1992.
- (55) Francis, R.; Joy, N.; Aparna, E.; Vijayan, R. Polymer grafted inorganic nanoparticles, preparation, properties, and applications: a review. *Polymer Reviews* **2014**, *54* (2), 268-347.
- (56) Sunday, D. F.; Green, D. L. Thermal and rheological behavior of polymer grafted nanoparticles. *Macromolecules* **2015**, *48* (23), 8651-8659.

## 4.8 Supporting Information

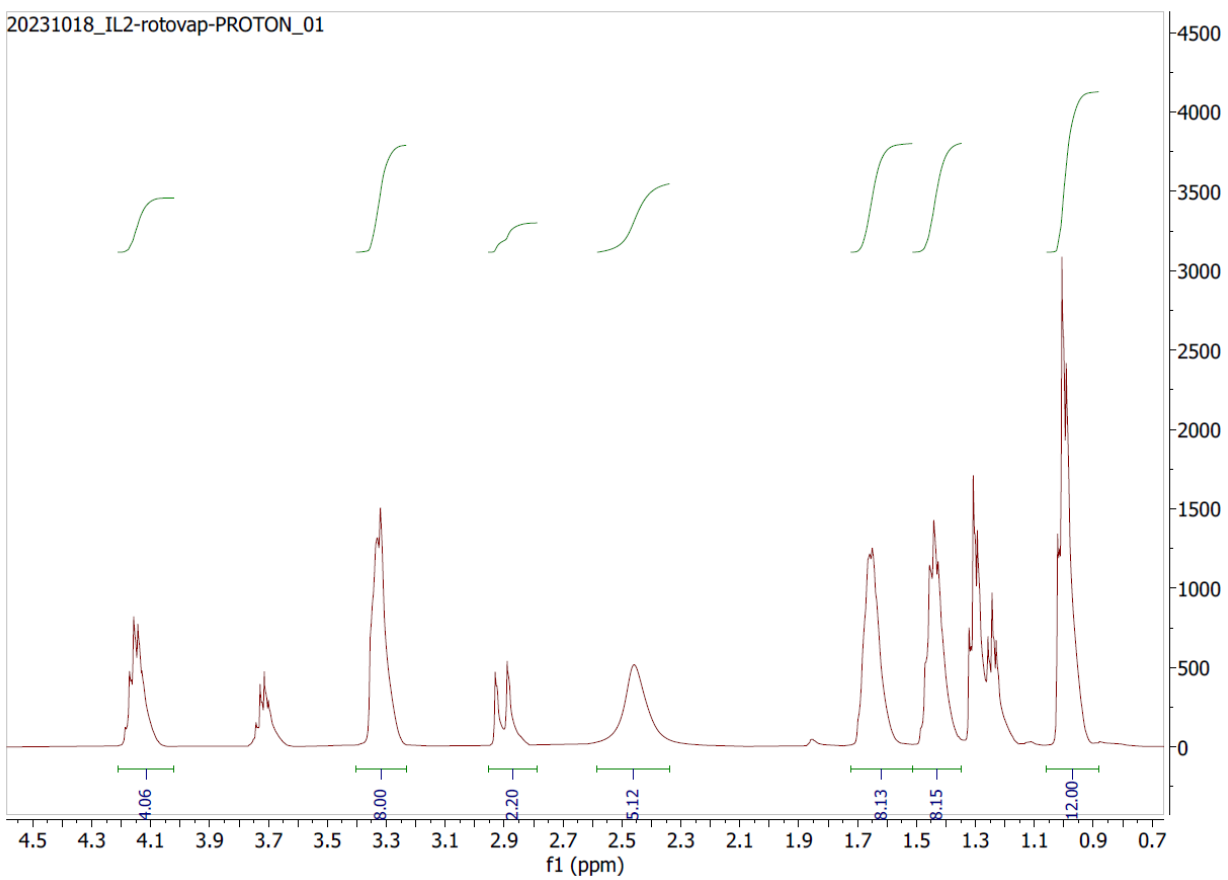


Figure 4-7:  $^1\text{H}$  NMR Spectrum of [DPPA][TBA] in  $\text{CDCl}_3$ .

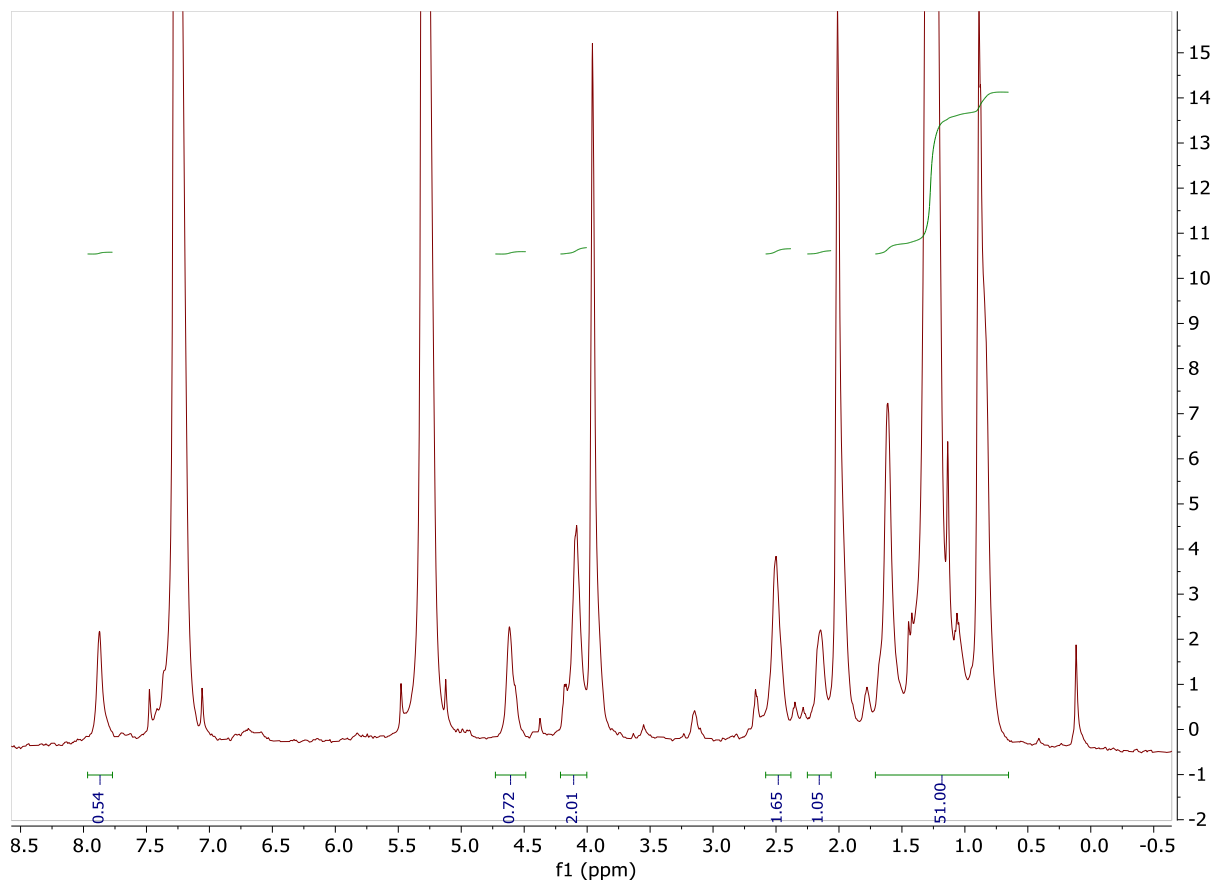
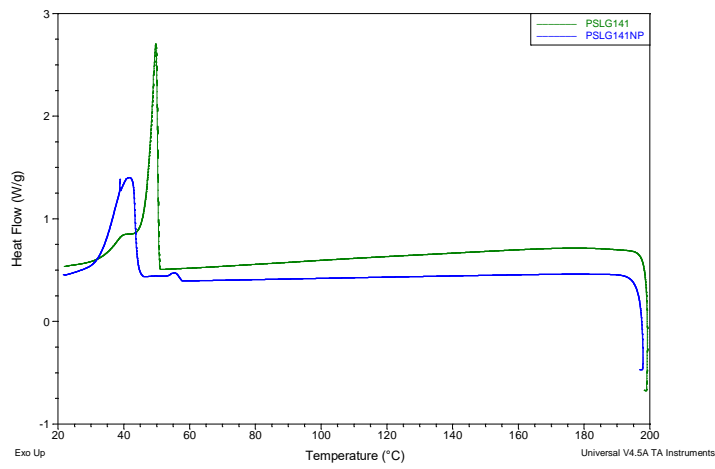
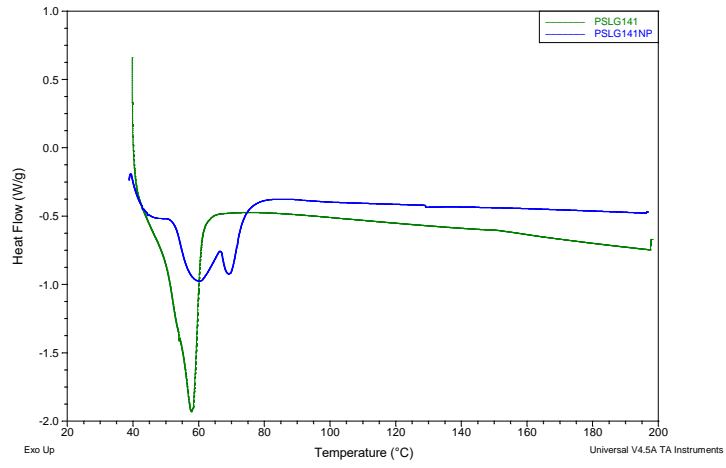


Figure 4-8: <sup>1</sup>H NMR Spectrum of PSLG<sub>141</sub> taken in CDCl<sub>3</sub> with 10% trifluoroacetic acid.



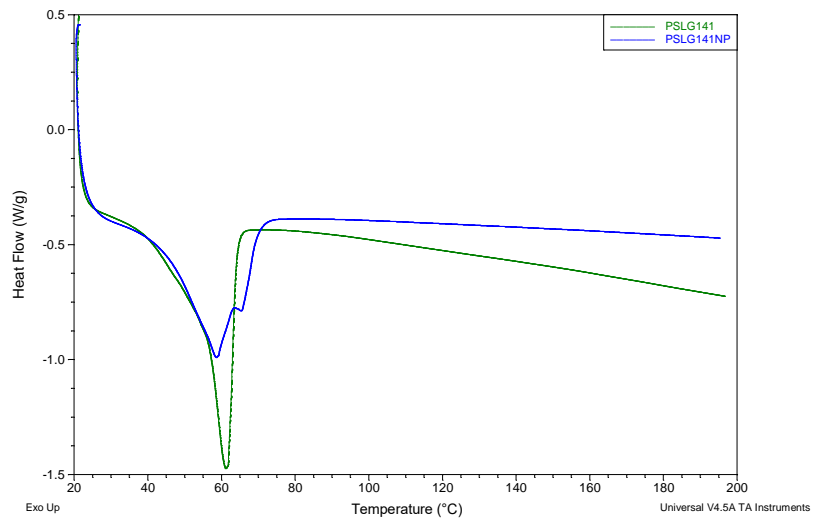


Figure 4-9: DSC curves of PSLG<sub>141</sub> and PSLG<sub>141</sub>@ZrO<sub>2</sub> taken at a heating rate of 10°C/min. The two curves have been split into heating/cooling steps: (Top) First Heating step, (Middle) First cooling, and (Bottom) second heating.:

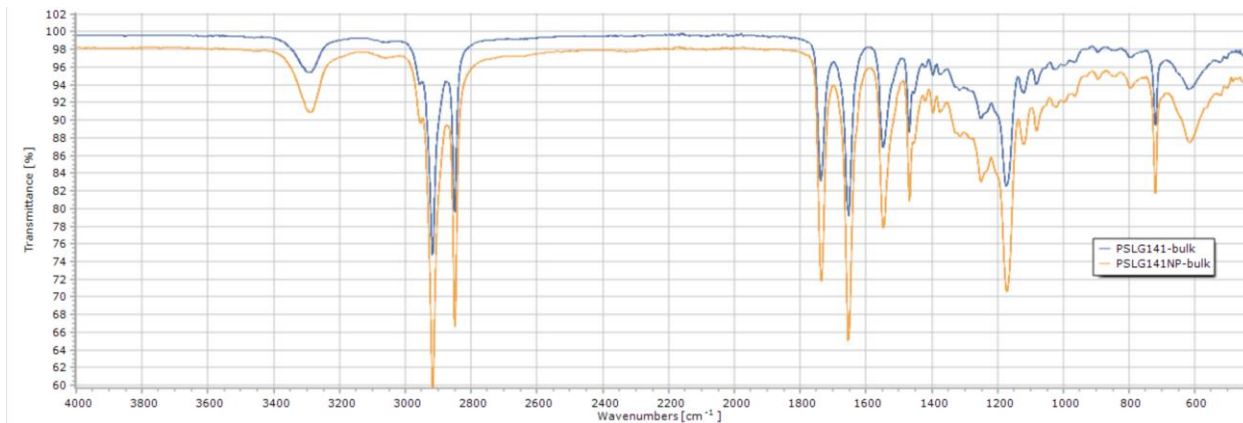


Figure 4-10: FTIR Spectrum of PSLG<sub>141</sub> and PSLG<sub>141</sub>@ZrO<sub>2</sub>

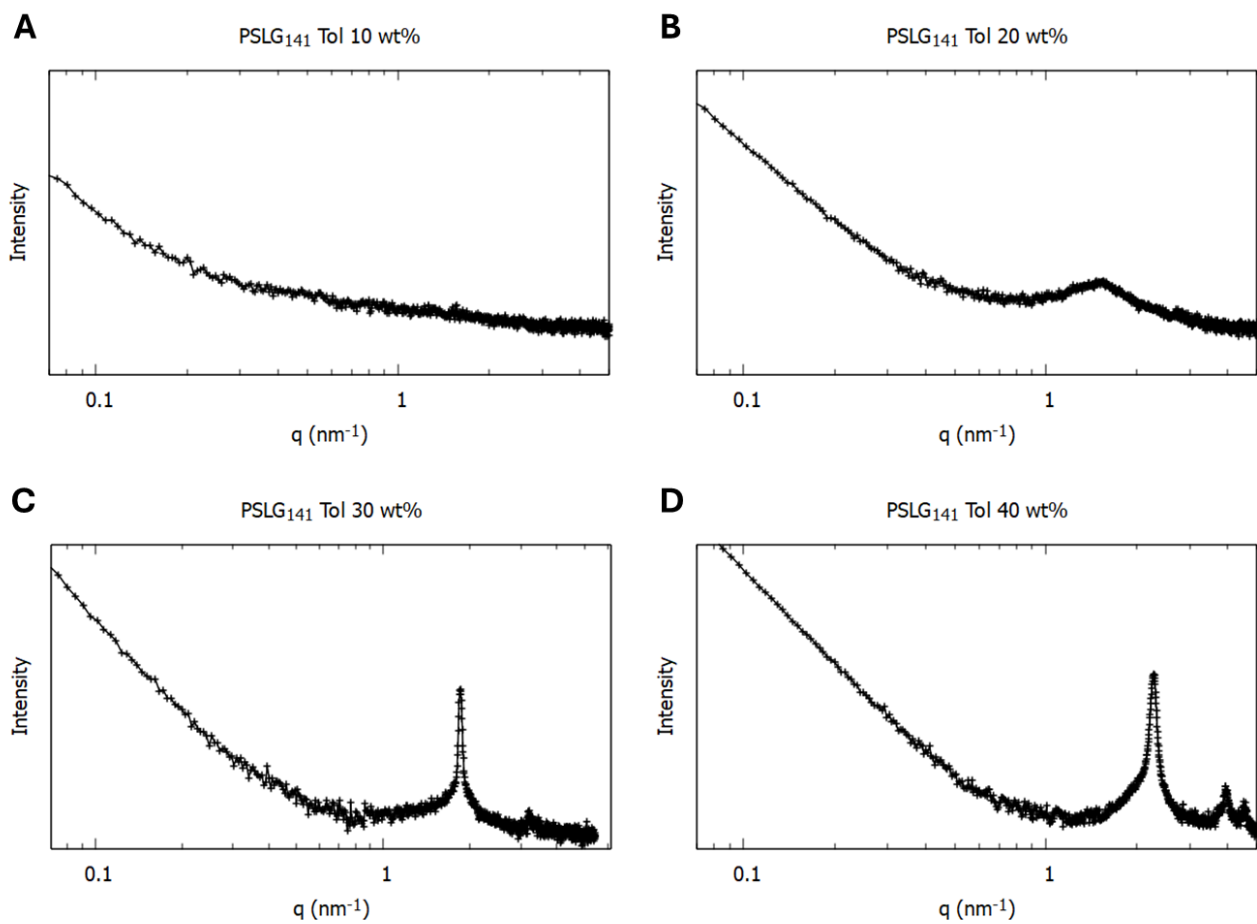


Figure 4-11: 1D SAXS profiles of various concentrations of PSLG<sub>141</sub> prepared in toluene; separated for clarity.

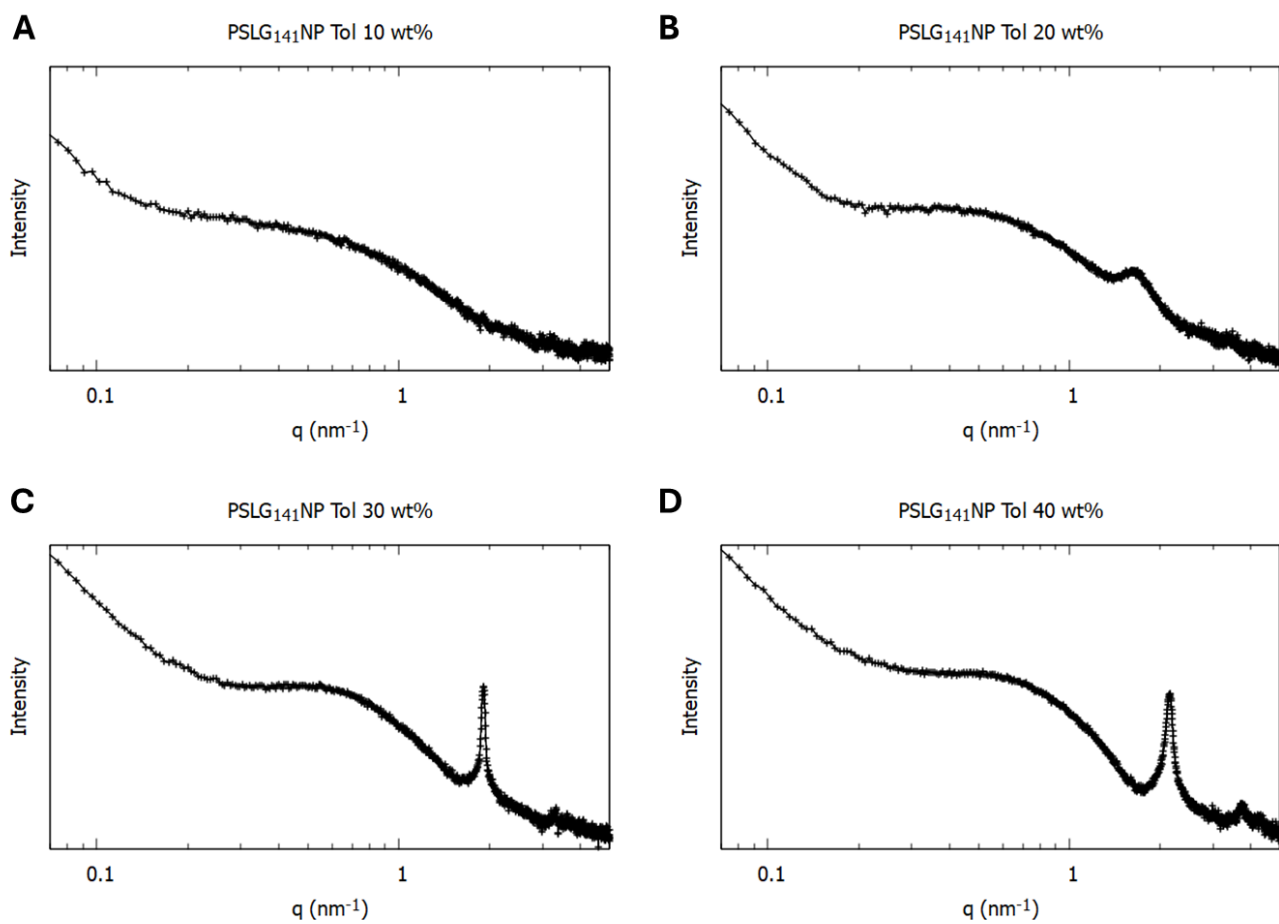


Figure 4-12: 1D SAXS profiles of various concentrations of PSLG<sub>141</sub>NP prepared in toluene; separated for clarity.

# Chapter 5 Discussions, Conclusions and Future Outlook

## 5.1 Discussion

This thesis outlines several methods in synthesizing semi-flexible polymer-grafted spherical nanoparticles, in addition to the preparation and characterization of their liquid crystal (LC) assemblies. In each chapter, a different semi-flexible polymer was chosen for its unique LC properties, which was imparted onto spherical nanoparticles following surface grafting of these ligands. Fabrication of these semi-flexible polymer-grafted NPs reveals a new motif towards LC nanocomposites.

In **Chapter 2**, poly (hexyl isocyanate) (PHIC) ligands were functionalized onto spherical zirconia nanoparticles. PHIC ligands were designed and synthesized using a phosphonic acid-based initiator, which enabled high molecular weights surpassing previous literature reports for PHIC ligands. Additionally, a highly efficient ligand exchange process was carried out to obtain high molecular weight PHIC-grafted NPs with high grafting densities. The surprising result of these NPs was that their organization was concentration dependent. Dilute solutions of these NPs revealed discrete particles suggesting effective dispersion, owing to the PHIC functionalization. Conversely, semi-dilute solutions of these NPs arranged into linear arrays, where the NPs formed long correlated chains. This assembly suggests deformation of the polymer corona, to enable close contact of the NP cores while simultaneously retaining colloidal stability. For contrast, low molecular weight PHIC-grafted NPs organized efficiently into hexagonally packed lattices, due to the more rigid nature of low molecular weight ligands. Towards characterizing LC behavior, it was found that the high molecular weight PHIC-grafted NPs exhibited an early onset of lyotropic nematic state. Compared to the untethered PHIC (of the same molecular weight), the critical concentration required for LC formation was observed to be around 7-8 wt% lower for PHIC-grafted NPs. In addition, textures resembling zebra stripes were observed, a feature previously only observed in biological fibrils and other long rod-shaped molecules. This lends further credence to the concentration dependent rod-like behavior of the PHIC-grafted NPs. Towards

elucidating the LC structure,  $^2\text{D}$  NMR was carried out on the solvent molecules ( $\text{CDCl}_3$ ) as to determine the quadrupolar splitting, which in turn can be used to determine experimental order parameters of the nematic structure formed from PHIC-grafted NPs as well as the non-grafted PHIC chains. It was concluded from these experiments that the order parameter was slightly larger in the NPs compared to the non-grafted PHIC chains, which was attributed to distortion of the nematic director by the presence of the NP cores. For this reason, LC structures formed from PHIC-grafted NPs were slightly less ordered compared to PHIC of the same molecular weight. We proposed that the semi-flexible nature of the polymer corona allows for splaying as to transform the NP into a more rod-like conformation, as to enable lyotropic nematic states.

**Chapter 3** features poly( $\gamma$ -benzyl-L-glutamate) (PBLG), a synthetic polypeptide that has seen widespread in biological applications as well as for its LC behavior. Homo polypeptides of sufficiently high MWs adopt an  $\alpha$ -helical conformation, which enables PBLG to become the 'model' semi-flexible rod. Like PHIC-grafted NPs, **Chapter 3** confirms that PBLG-grafted NPs may similarly generate LC behaviour from isotropic, spherical particles. PBLG ligands were synthesized across a wide range of molecular weights, via an ionic liquid-initiated polymerization. The use of ionic liquid catalyzed NCA polymerizations enabled high molecular weight functional PBLG ligands. Traditionally, PBLG ligands were carried out using NCA polymerization via the NAM mechanism (initiated by primary amine initiators), however, the largest drawback of this method is the long reaction times and the molecular weight ceiling, which empirically appears to occur around 20K MW. PBLG ligands with four different molecular weights were synthesized: PBLG<sub>89</sub>, PBLG<sub>228</sub>, PBLG<sub>1237</sub> and PBLG<sub>2963</sub>. The PBLG ligands were subsequently grafted onto spherical zirconia nanoparticles through a highly efficient ligand exchange process, producing densely covered NPs, with grafting densities of 5.0, 1.1, and 0.16 PBLG chains/nm<sup>2</sup>, in order of increasing molecular weight. Unfortunately, the grafting density could not be determined for PBLG<sub>2963</sub>. The most immediate observation of these PBLG-grafted NPs was the early onset of LC behavior, consistent with the PHIC-grafted NPs, however this trend decreased with increasing MWs. Towards characterization of the lyotropic cholesteric phase, LC behavior was obfuscated by gelation and molecular aggregation, which appeared to be competing processes towards LC

formation. For this reason, samples were annealed at 50°C to ensure that lyotropic solutions were entirely in the LC phase, with no contributions from gelation nor aggregation. While cholesteric structures are generally difficult to characterize, the LC structures self-assembled from PBLG-grafted NPs were observed to have larger dimensions in comparison to its untethered PBLG counterparts. This is most clearly seen in the general increase in cholesteric pitch measurements, as the pitch was generally larger in the NP samples. In addition, in SAXS, the molecular dimensions of the lyotropic phase appear enlarged as well, as seen in the broad cholesteric peaks which shifted towards larger distances. Drawing from these results, PBLG-grafted NPs were further confirmation that this new motif serves as an effective strategy towards LC nanocomposites.

**Chapter 4** compares the unique thermotropic and lyotropic properties of Poly( $\gamma$ -stearyl-L-glutamate) (PSLG), and the behavioural and structural changes upon surface grafting of PSLG onto spherical zirconia NPs. Like PBLG, PSLG is a synthetic polypeptide which adopts an  $\alpha$ -helical conformation, however, due to the stearyl shell coating the  $\alpha$ -helix, thermotropic LCs become accessible, owing to the melt/crystallization dynamics of the stearyl side chains. Surprisingly, the literature on homo polymers of PSLG has been sparse, as an extensive literature review of the field revealed that studies on PSLG self-assembly and properties have largely been performed on random copolymers of PSLG rather than homo polymers. Traditionally, PSLG has been prepared via ester exchange from poly( $\gamma$ -methyl-L-glutamate), however this method proves inefficient as the conversion is typically limited to around 90%. These random copolymers are then used in subsequent studies, which have been generalized to homo polymers of PSLG, prepared through NCA polymerization, as well. For this reason, **Chapter 4** serves to consolidate the structure and properties of homopolymers of PSLG, while discerning the results which are seen exclusively in copolymers of PSLG. PSLG ligands were synthesized following a similar procedure, where NCA polymerization was initiated by ionic liquids. Similarly, the same ligand exchange procedure was then carried out, however the procedure produced a grafting density of 0.56 chains/nm<sup>-2</sup>, which is high compared to other grafting-from/grafting-to procedures, but unexpectedly low for this procedure. Previous characterization methods were carried out on these PSLG-grafted NPs, to

elucidate the structure and properties of the NPs, as well as the homo polymers of PSLG. A comparison of the results revealed that despite surface anchoring of the PSLG chains onto the NP surface, the PSLG chain ordering is largely similar between the NPs and the unbound PSLG. Through DSC and SAXS, it was confirmed that stearyl side chain motion is coupled with  $\alpha$ -helix backbone mobility, a topic that has been contentious in the literature. In addition, homo polymers of PSLG revealed only one phase transition (ie. two thermal structures), whereas two phase transitions between three structures were reported in the literature. Literature reports cite decoupled side chain/main chain motion, which they attribute to the first and second transitions, respectively. PSLG-grafted NPs were similarly confirmed to exhibit the same thermal properties, despite the confinement of the PSLG ligands to an NP core. Furthermore, relative peak ratios of 1,  $\sqrt{3}$ , and 2, were observed in SAXS, suggesting that the PSLG ligands were ordered hexagonally on the NP surface; this was the first indication of polymer organization on the NP surface, out of all the semi-flexible polymer-grafted NPs studied. PSLG-grafted NPs were confirmed to exhibit both thermotropic and lyotropic cholesteric LC states, however, it appears that self-assembly is largely limited by the slow diffusion experienced by the PSLG ligands. Prior to thermal annealing, both thermotropic and lyotropic samples did not exhibit LC phases under POM, however the elevated temperatures aid in mobility/self-assembly, which in turn gives rise to visible LC textures after a few days. Consistent with the other semi-flexible polymer-grafted NPs studied, a reduction in critical concentration was observed, as cholesteric ordering was observed beginning at 10 wt% for the NPs compared to 20 wt% for the untethered PSLG. The functionalized NPs exhibited similar cholesteric pitches to the unbound polymer, however comparisons to the literature are difficult due to inconsistencies in the sample preparation. Towards thermotropic LC ordering, diffusion appears to be a significant obstacle, as cholesteric ordering of both PSLG and PSLG-grafted NP bulk films were observed after around five days. Additionally, thermotropic organization was largely inconsistent, as not all films prepared exhibited cholesteric ordering, despite the films being prepared from the same batch. This suggests that some films are primed such that cholesteric organization is more accessible. Towards LC nanocomposites, PSLG-grafted NPs serves as a possibility, however the slow diffusion of the PSLG ligands provides a significant obstacle to overcome towards material applications.

Several literature reports exist of the same semi-flexible polymer ligands grafted onto various NP cores (albeit through different design schemes). However, none of these reports attempt to prepare/characterize potential LC phases arising from the semi-flexible polymers, as LC properties arising from semi-flexible polymers have been known for several decades. Generally, only short molecular weight polymer ligands were used in the literature examples, as the goal of these studies was to provide proof of concept that the select polymer could provide colloidal stability to its NPs. However, according to theory, high axis ratios are generally required towards LC behavior. Consequently, this gap in knowledge was filled via synthesizing high molecular weight semi-flexible polymer ligands towards NP functionalization, as well as characterizing the LC properties of the resulting semi-flexible polymer-grafted NPs.

In addition, the present work also serves as one of the few examples of anisotropic structures self-assembled from isotropic building blocks (without further intervention). Previous studies on the self-assembly of spherical colloids report organization into cubic phases through repulsive interactions (which is taken advantage of in colloidal photonic crystals).<sup>1,2</sup> However, few literature examples report thermotropic organization from the self-assembly of isotropic NPs. One study reports hexagonal close packed and non-close packed, square and linear ordering from polystyrene microspheres dispersed in a poly(*N*-isopropylacrylamide) microgel owing to careful consideration of colloidal pair potentials (microgel-microgel, microgel-microsphere, microsphere-microsphere).<sup>3</sup> A second study reports thermotropic self-assembly via oppositely charged, dual-polymer coronas.<sup>4</sup> However, this report seems questionable, as intuitively, the oppositely charged polymer layers should produce an overall neutral particle, which would not be an adequate driving force in the self-assembly of any anisotropic structure. In summary, careful control and consideration is required in designing anisotropic structures self-assembled from isotropic building blocks and the present work would serve as another example in this field.

## 5.2 Conclusion

Overall, this thesis introduces a new type of LC nanocomposite, where the strategy is relatively simple. Firstly, a spherical NP core is functionalized with relatively high molecular

weight semi-flexible polymer ligands. These ligands would provide a sufficiently high axis ratio required for LC assembly, which is then imparted to the NP core. Secondly, high grafting densities can be achieved using a relatively efficient ligand exchange procedure. The dense coverage essentially aids in mimicking the tight packing in concentrated solutions, thereby resulting in drastic reductions in the critical concentration required for LC formation. Furthermore, this work provides validation that deformation of the polymer corona, where isotropic particles may adopt an anisotropic conformation, serves as a driving force towards LC assembly. In a broader context, this thesis not only serves as an example of anisotropic organization from isotropic building blocks, but it also serves as one of the first examples of concentration dependent LC behavior which is generated from the nanocomposite itself, rather than a composite comprised of two miscible phases.

In conclusion, this thesis outlines a new nanocomposite motif, where LC behavior can be generated from semi-flexible polymer-grafted NPs, a feat which has previously not been reported in literature. LC nanocomposites in literature largely consist of NP functionalization followed by dispersion of the NP in an LC matrix. To that end, this new motif provides an alternative to the precedent set by literature, with clear advantages. From the studies carried out, grafting density and molecular weight play a significant role in determining the critical concentration required for LC assembly. Similarly, the NPs provide an avenue for tailoring the size of the LCs, as the LC structures were characterized to be generally enlarged compared to LC structures assembled by the non-grafted polymers, owing to the presence of the NPs and the restricted movement experienced by the tethered polymer chains. This feature could potentially serve as another tool towards engineered materials, should the nanocomposite require anisotropic organization. The self-assembly of structures possessing properties such as directional conductivity, selective permeability, and controlled optical properties would expand the range of functionalities available in nanocomposite materials. Furthermore, many biological systems rely on the self-assembly of isotropic building blocks into anisotropic structures. By mimicking these natural processes, researchers can develop biomimetic materials and devices in addition to a better understanding of the natural world.

### 5.3 Future outlook

Towards LC nanocomposites, only PHIC appears to be a feasible candidate, owing to the complex behavior of the synthetic polypeptides. Since LC behavior competes with uncontrolled gelation and molecular aggregation in PBLG and PSLG, extra precaution should be taken as to ensure the resulting nanocomposite is in the LC structure. For comparison, designing PHIC based nanocomposite would be much simpler, due to a greater degree of control over its self-assembly behavior. However, the more significant conclusion of this work is that surface attachment of polypeptides, or more generally: semi-flexible polymers, to the NP surface did not disrupt the self-assembly behaviour of the polymer ligand. It can then be reasoned that the zirconia NP core can be swapped out for other NP functionalities, without altering the self-assembly behavior. For example, this motif could be expanded to include gold NPs, which would instead produce ordered plasmonic structures.

The source of LC behavior remains unclear in the PHIC-grafted NPs; it is plausible that nematic ordering in these samples could be attributed to either the grafted PHIC ligands, or the linear chains of NPs. When observing the NPs under POM, the linear NP chains appear to adopt nematic ordering (similar to the stereotypical representation of nematic phases), while ordering of the PHIC ligands appear layered and highly periodic, perpendicular to the NP chains. In other words, it is possible that the NP chains essentially self-assemble as lyotropic nematic colloidal rods. From appearances alone, semi-dilute solutions of PHIC-grafted NPs would suggest smectic ordering. It is also possible that the NPs adopt another structure in the nematic LC phase, however the semi-dilute image is the resolution limit using TEM. The source of LC behavior in PHIC-grafted NPs could easily be distinguished using USAXS by discerning whether the nematic correlation length closely matches the dimensions of a PHIC molecule or the linear chains.

While the only LC phases discussed in this thesis were nematic and cholesteric phases, it may be possible to design nanocomposites which feature other LC phases such as hexatic and smectic phases. Since polymers generally fall into the rod-like/calamitic geometry, it was interesting that of the semi-flexible polymer-grafted NPs explored, there was no evidence of

smectic organization. Generally, orientational order is easily accessible to rod-like polymers, however positional order (required for smectic ordering) requires highly monodisperse samples. In literature, there is precedence for smectic organization from polymeric building blocks, however, these samples were obtained either through successive fractionations or bacterial production.<sup>5,6</sup> A few examples even reports smectic behavior in PBLG, however these samples were highly monodisperse owing to bacterial production.<sup>7,8</sup> It is also unclear whether monodisperse semi-flexible polymer-grafted NPs would organize into smectic structures, as deformation of the polymer corona does not necessarily become a driving force towards positional order. Similarly, hexatic phases could also be feasible for the systems presented in this thesis. Since grafted PSLG ligands were revealed to exhibit hexagonal packing on the NP surface, it would also be feasible that the hexagonal packing could be extended to the NP core as well. An alternative structure that could be proposed would be where the polymer corona deforms in a disc-like manner, rather than rod-like, which would enable hexatic LC ordering. However, the conditions required for this type of deformation are unclear.

It is with hope that this thesis lays the groundwork towards more complex self-assembled structures. It has been shown that deformation of the polymer corona of isotropic particles produce rod-like particles, which in turn, allows for anisotropic organization. Furthermore, this thesis reveals that molecular geometry does not necessarily dictate the LC structure being formed and that its constituents do not need to be unnecessarily complicated. Perhaps future researchers may use this work in building more complex nanoscale architectures from basic building blocks.

## 5.4 References

- (1) Zhao, Y.; Shang, L.; Cheng, Y.; Gu, Z. Spherical colloidal photonic crystals. *Accounts of chemical research* **2014**, *47* (12), 3632-3642.
- (2) Dutta, J.; Hofmann, H. Self-organization of colloidal nanoparticles. In *Encyclopedia of nanoscience and nanotechnology*, Vol. 9; American Scientific Publishers California, 2004; pp 617-640.
- (3) Rey, M.; Law, A. D.; Buzza, D. M. A.; Vogel, N. Anisotropic self-assembly from isotropic colloidal building blocks. *Journal of the American Chemical Society* **2017**, *139* (48), 17464-17473.
- (4) Wan, S.; Cong, W.; Shao, B.; Wu, B.; He, Q.; Chen, Q.; Shen, J.; Chen, D.; Hu, H.-G.; Ye, F. A library of thermotropic liquid crystals of inorganic nanoparticles and extraordinary performances based on their collective ordering. *Nano Today* **2021**, *38*, 101115.
- (5) Onouchi, H.; Okoshi, K.; Kajitani, T.; Sakurai, S.-i.; Nagai, K.; Kumaki, J.; Onitsuka, K.; Yashima, E. Two-and three-dimensional smectic ordering of single-handed helical polymers. *Journal of the American Chemical Society* **2008**, *130* (1), 229-236.
- (6) Rubin, S. F.; Kannan, R. M.; Kornfield, J. A.; Boeffel, C. Effect of mesophase order and molecular weight on the dynamics of nematic and smectic side-group liquid-crystalline polymers. *Macromolecules* **1995**, *28* (10), 3521-3530.
- (7) Yu, S. M.; Soto, C. M.; Tirrell, D. A. Nanometer-Scale Smectic Ordering of Genetically Engineered Rodlike Polymers: Synthesis and Characterization of Monodisperse Derivatives of Poly( $\gamma$ -benzyl  $\alpha$ ,l-glutamate). *Journal of the American Chemical Society* **2000**, *122* (28), 6552-6559. DOI: 10.1021/ja000465p.
- (8) Yu, S. M.; Conticello, V. P.; Zhang, G.; Kayser, C.; Fournier, M. J.; Mason, T. L.; Tirrell, D. A. Smectic ordering in solutions and films of a rod-like polymer owing to monodispersity of chain length. *Nature* **1997**, *389* (6647), 167-170. DOI: 10.1038/38254.